

# **Forschungsbericht 2019-28**

## **A combined analytical and numerical analysis method for low-velocity impact on composite structures**

Raffael Bogenfeld

Deutsches Zentrum für Luft- und Raumfahrt  
Institut für Faserverbundleichtbau  
und Adaptronik  
Braunschweig

156 Seiten  
83 Bilder  
16 Tabellen  
205 Literaturstellen



DLR

Deutsches Zentrum  
für Luft- und Raumfahrt



TU Braunschweig – Niedersächsisches  
Forschungszentrum für Luftfahrt

Berichte aus der Luft- und Raumfahrttechnik

**Forschungsbericht 2019-15**

**A combined analytical and numerical analysis  
method for low-velocity impact on composite  
structures**

**Raffael Bogenfeld**

Deutsches Zentrum für Luft- und Raumfahrt  
Institut für Faserverbundleichtbau und Adaptronik  
Braunschweig

---

Diese Veröffentlichung wird gleichzeitig in der Berichtsreihe „NFL - Forschungsberichte“ geführt.

Diese Arbeit erscheint gleichzeitig als von der Fakultät für Maschinenbau der Technischen Universität Carolo-Wilhelmina zu Braunschweig zur Erlangung des akademischen Grades eines Doktor-Ingenieurs genehmigte Dissertation.



**A combined analytical and numerical analysis method for  
low-velocity impact on composite structures**

Von der Fakultät für Maschinenbau  
der Technischen Universität Carola-Wilhelmina zu Braunschweig

zur Erlangung der Würde

eines Doktor-Ingenieurs (Dr.-Ing.)

genehmigte Dissertation

*von:* Dipl.-Ing. Raffael BOGENFELD  
*aus (Geburtsort):* Filderstadt

*eingereicht am:* 5.9.2018  
*mündliche Prüfung am:* 27.2.2019

*Gutachter:*  
Prof. Dr.-Ing. Martin WIEDEMANN  
Prof. Dr.-Ing. Laura DE LORENZIS



## *Zusammenfassung*

Das Verständnis von Schlagschädigung ist eine essentielle Voraussetzung zur Konstruktion von Leichtbaustrukturen aus Faserverbundmaterialien. Die vorliegende Arbeit beschreibt hierzu die Entwicklung eines kombinierten Analyseverfahrens aus Numerik und Analytik. Diese Kombination erlaubt sowohl ein detailliertes Verständnis der Schädigungsvorgänge im Laminat als auch die effiziente Analyse von Luftfahrt-Strukturbauteilen.

Die Entwicklung eines numerischen Modells basiert auf verschiedenen bereits verfügbare Methoden. Ein hochaufgelöstes explizites FE Modell abstrahiert das Laminat auf der Meso-Skala. Dies ist nötig um die Schadensmodi Delamination, Faserbruch und Zwischenfaserbruch physikalisch plausibel abzubilden. Das Modell kombiniert dazu zwei bruchmechanische Ansätze: kohäsive Kontakte dienen der Vorhersage von Delamination, Kontinuumsschädigungsmechanik erfasst die Schäden innerhalb einer unidirektionalen Lage. Auf diesem Modell aufbauend wird im Rahmen der vorliegenden Arbeit eine Steifigkeits-Degradationsmethode für Zwischenfaserbrüche in schiefen Bruchebenen entwickelt. Basierend auf einem Schädigungstensor achter Stufe erlaubt diese Methode die Berücksichtigung der Kopplung von Schub und Normalverformung bei Ausbildung schiefer Risse. Durch Rotation des Steifigkeitstensors in die Bruchebene wird die Degradationsgleichung vereinfacht. Eine Validierung des so verbesserten progressiven Schädigungsmodells erfolgt anhand von Würfel-Druckversuchen und Coupon-Impacts.

Hochaufgelöste FE Modelle lassen sich kaum direkt auf Strukturbauteile anwenden, da der damit verbundene Berechnungsaufwand inadäquat hoch ist. Jedoch wird in dieser Arbeit der relevante Analysebereich auf einen kleinen Referenzcoupon reduziert. Diese Modellreduktion erlaubt hocheffiziente Simulation von Schlagschäden. Ein analytischer Transferansatz ermöglicht, dass der Schaden am reduzierten Modell dem an der Originalstruktur entspricht. Hierzu kommt ein neu entwickeltes Feder-Masse-Modell zum Einsatz. Dieses beschreibt Impactschäden für ein Laminat unabhängig der Randbedingungen und Einschlagposition. So kann von einem bekannten Impact das laminatabhängige Schädigungsverhalten für jedes ausreichend ähnliche Impactscenario abgeleitet werden. Die Impactenergie wird für die Übertragung des Schadens zwischen Struktur und Referenzcoupon skaliert. Im Rahmen der Validierung zeigt eine umfangreiche Versuchsreihe die Möglichkeiten und Einschränkungen dieser Methode.

Über die Skalierung einzelner Impacts hinaus ist die integrale Betrachtung der Impactgefährdung von weiten Bereichen eines Bauteils möglich. Durch die objektive Schadensbeschreibung können aus dem Feder-Masse-Modell Resultate für jeden ähnlichen Einschlagort ermittelt werden. Diese Herangehensweise ebnet den Weg für den Einbezug von Schlagschäden in die schadenstolerante Strukturauslegung von Flugzeugen.





## *Abstract*

Understanding impact damage is essential to building lightweight composite structures. The present doctoral thesis proposes a comprehensive impact analysis approach that combines analytical and numerical methods. This approach assists in understanding the details of laminate damage modes and in analyzing the impact scenarios of a typical aircraft structure. This thesis approaches numerical impact analysis through an examination of various existing methods. An explicit finite element model that captures the laminate on the meso-scale can be used to plausibly predict impact-induced delamination, inter-fiber failure, and fiber failure. This model involves two fracture-mechanical methods: first, cohesive surfaces catch the delamination damage while, second, continuum damage mechanics addresses the intra-ply failure modes. Building on this model, the present work describes the development of an appropriate degradation method for inter-fiber cracks in oblique fracture planes. Using a rank-eight damage tensor, this method enables the calculation of the resulting stiffness tensor including the coupling effects of shear and normal deformation. A simplified approach in fracture plane coordinates is derived on the basis of this tensorial degradation. Compression experiments with oblique fracture planes and coupon impacts serve as validation of this new progressive damage model. The computational cost of this high-fidelity approach impedes a direct application on the structural level. However, a typical property of damage resulting from impact with low velocity and large mass helps to reduce the scope of the structural model: as the impact damage is small in comparison to the full structure, the relevant zone for damage analysis is limited to a small cross-section around the impact location. This model reduction permits a very efficient analysis of structural impact. An analytical transfer approach allows the reduced model to comply with the original structural impact. A newly developed spring-mass model captures the damage that occurs. In this model, a damage element objectively describes the damage for a laminate configuration. Thus, the spring-mass model offers a method for transferring the damage behavior to any sufficiently similar impact configuration. Wherever qualitatively similar damage occurs, this model scales the impact energy for damage similarity. In this manner, a structural impact scenario can be analyzed on a numerical or experimental reference coupon of minimal size. Impact experiments validate the method and show its range of applicability. Finally, the transfer method enables impact analysis on sizeable structural areas through the areal evaluation of the damage description in the spring-mass model. This development allows for the establishment of a damage-tolerant design based on the actual impact threat to structures.



## *Danksagung*

Die vorliegende Dissertation entstand im Rahmen meiner Tätigkeit als wissenschaftlicher Mitarbeiter am Institut für Faserverbundeleichtbau und Adaptronik des Deutschen Zentrums für Luft- und Raumfahrt (DLR) in Braunschweig. Viele Menschen haben mich während der Zeit dieser Arbeit unterstützt und begleitet und somit maßgeblich zur erfolgreichen Fertigstellung beigetragen.

Meinem Doktorvater Professor Martin Wiedemann danke ich für die Betreuung und das Stellen der richtigen Fragen als Grundlage dieser Arbeit. Professor Laura De Lorenzis gebührt mein Dank für Ihren Einsatz als zweite Betreuerin und für wichtige Impulse aus einer neuen Perspektive. Ebenso danke ich Professor Peter Horst für die Übernahme des Vorsitzes in der Prüfungskommission.

Vielen Dank an Janko Kreikemeier für kritische wissenschaftliche Diskussionen, an Caroline Lüders für viele geduldige Überlegungen, an Tobias Wille für den wichtigen Rückhalt, und an all meine Kollegen der Abteilung Strukturmechanik, da ich von diesen in jeder scheinbaren Sackgasse Rat bekommen habe. Darüber hinaus bedanke ich mich bei Carmen Westphal und Bernd Friederichs für die Unterstützung bei den experimentellen Untersuchungen.

Die mit dieser Arbeit verbundene Forschung hätte ohne das Lufo-Projekt SCHACH nicht stattfinden können, daher danke ich ebenso dem BMWi als Förderer, und den Projektpartnern für die gute Zusammenarbeit. Besonders zu erwähnen sind dabei Patrik Schmiedel, Naren Kuruvadi und Alexander Kling mit denen ich in regelmäßigem Austausch stand. Auch danke ich Michael Mauersberger, Jan-Philipp Schmidt, Florentine Vilzmann und Filip Przybyło, die im Rahmen von Diskussionen während ihrer studentischen Arbeiten immer wieder interessante Anregungen für mich miteinbrachten.

Zu guter Letzt gilt mein Dank meiner gesamten Familie, da moralische Unterstützung die nötige Energie zum Abschluss dieser Arbeit verleiht.



*Meinen Eltern, Rita und Alfred.*



# Contents

<b>Abstract</b>	<b>v</b>
<b>Contents</b>	<b>xi</b>
<b>1 Introduction</b>	<b>1</b>
1.1 Motivation of impact analysis on composite structures . . . . .	1
1.2 Objectives and hypotheses . . . . .	2
1.3 Fiber-reinforced plastics . . . . .	3
1.3.1 Fiber reinforcement . . . . .	3
1.3.2 Damage modes of fiber-reinforced plastics . . . . .	4
1.3.3 Damage-tolerant design with fiber-reinforced plastics . . . . .	6
1.4 Failure analysis . . . . .	9
1.5 The finite element method . . . . .	16
1.5.1 Time integration . . . . .	17
1.5.2 Composite modeling with the finite element method . . . . .	18
1.5.3 Contact formulation in the finite element method . . . . .	19
1.5.4 Cohesive zone method . . . . .	19
1.5.5 Continuum damage mechanics in a finite element model . . . . .	21
1.6 Impact on composite structures . . . . .	22
1.6.1 Overview of impact analysis methods . . . . .	23
1.6.2 Existing reviews . . . . .	27
1.6.3 Impact analysis on the structural level . . . . .	27
<b>2 The Numerical Prediction of Low-Velocity Impact Damage</b>	<b>29</b>
2.1 General considerations . . . . .	29
2.2 Model building . . . . .	30
2.2.1 System boundary of an impact setup . . . . .	30
2.2.2 Abstraction scale of the laminate model . . . . .	31
2.2.3 Impactor model and contact formulation . . . . .	40
2.2.4 Interface model . . . . .	41
2.2.5 Intra-ply damage model . . . . .	44
2.2.6 Analysis of the impact process . . . . .	46
2.2.7 Identification of required improvement . . . . .	48
2.3 A tensorial-based progressive damage model . . . . .	50
2.3.1 Material degradation in oblique fracture planes . . . . .	50
2.3.2 Tensorial material degradation . . . . .	51
2.3.3 Derivation of a simplified tensorial-based degradation . . . . .	53
2.4 Validation of the tensorial-based damage model . . . . .	55
2.5 Validation of the impact model . . . . .	57
2.5.1 Validation setup . . . . .	57
2.5.2 Validation results . . . . .	58
2.5.3 Comparison with other methods . . . . .	62

2.6	Critical assessment of the numerical impact analysis model . . . . .	63
<b>3</b>	<b>Analytical Impact Scaling</b>	<b>69</b>
3.1	Analysis approaches for impact on the structural level . . . . .	69
3.1.1	General consideration of impact similarity . . . . .	70
3.2	Analytical impact analysis . . . . .	72
3.2.1	Elastic spring-mass models . . . . .	72
3.2.2	Damage description with spring-mass models . . . . .	75
3.2.3	Determination principle for the damage parameter $k_d$ . . . . .	77
3.3	Impact scaling . . . . .	79
3.3.1	Scaling for equivalent damage or same impact energy . . . . .	80
3.3.2	Unstable damage propagation . . . . .	82
3.3.3	Modal energy correction . . . . .	84
3.3.4	Obvious constraints and the characteristics of impact similarity	88
3.4	Application and validation of the methodology . . . . .	90
3.4.1	Description of experimental impact damage through $k_d$ . . . . .	90
3.4.2	Validation of the impact scaling . . . . .	94
3.4.3	Quantification of the uncertainty through scaling . . . . .	104
3.5	Critical assessment of the developed impact transfer method . . . . .	105
<b>4</b>	<b>Structural Assessment of Impact Damage</b>	<b>109</b>
4.1	Numerical impact analysis through a minimal reference coupon . . . . .	109
4.1.1	Determination of the minimal reference coupon size . . . . .	109
4.1.2	Numerical high-fidelity analysis of the minimal reference coupon	111
4.2	Integral assessment of impact-prone structures . . . . .	113
4.3	Integration for structural design . . . . .	117
4.3.1	Follow-up interface for residual strength analysis . . . . .	118
<b>5</b>	<b>Conclusion and Outlook</b>	<b>121</b>
<b>A</b>	<b>Experimental methods, results and material data</b>	<b>125</b>
A.1	Error analysis of the impact history data . . . . .	125
A.2	Ultrasonic scanning methods . . . . .	127
A.3	Material properties for numerical analyses . . . . .	129
A.4	Results of scaled impacts . . . . .	131
<b>B</b>	<b>Mathematical Methods</b>	<b>139</b>
B.1	Time integration methods . . . . .	139
B.2	Least squares (LSQ) function estimation . . . . .	140
B.3	Symmetry of tensors . . . . .	141
	<b>Bibliography</b>	<b>143</b>



## List of Figures

1.1	Damage modes of composite materials: fiber fracture, inter-fiber fracture, delamination (from left to right). . . . .	4
1.2	Interaction of delamination with an IFF shear crack (A) and an IFF tensile crack (B). . . . .	7
1.3	Applicability of damage tolerance and safe-life design philosophy for different damage sizes. . . . .	8
1.4	Schematics damage-tolerant design with damage growth under operation load. . . . .	8
1.5	Stress-strain schematics of material behavior in an elastic phase, a failure region, and a post-failure region. . . . .	9
1.6	Sketch of an oblique fracture plane and the coordinate systems of the material (1/2/3) and the fracture plane ( $L/N/T$ ). . . . .	11
1.7	IFF index of Puck's criterion depending on the fracture angle determined by iterative search (blue) and golden section search (red). . . . .	11
1.8	Schematics of a cracked material element according to the CDM. . . . .	13
1.9	Bilinear damage evolution law with an elastic phase (1), a degradation phase (2), and a post-failure region (3). . . . .	14
1.10	Sketch of the FEM applied to a tensile bar. . . . .	17
1.11	Illustration of a composite layup model on the macro-scale (A) and on the meso-scale (B). . . . .	19
1.12	Categories of impact according to Olsson: ballistic impact, low-mass impact, and large-mass impact ( $m_{i1} < m_{i2} < m_{i3}$ ). . . . .	22
1.13	Characterization of impact scenarios through the impactor mass and velocity. The graph illustrates the target regions of interest (BVID) and validity (blue) of the models developed in the present work. . . . .	23
1.14	Overview of impact analysis methods on different abstraction scales. . . . .	24
2.1	Impact test setup according to the CAI standard AITM 1.0010 [153]. . . . .	30
2.2	Test case for the assessment of methods and the trade-off analysis. . . . .	32
2.3	A central cross-section of three impact models shows the out-of-plane displacement $\Delta z$ at $t = 0.8$ ms. . . . .	33
2.4	The force-displacement history of the elastic impact simulations with the three models on different abstraction scales. . . . .	34
2.5	Sketch of the analytical derivation of out-of-plane stresses in a circular cross-section around the impact spot. . . . .	37
2.6	The stress distribution $\sigma_{zz}$ over the laminate thickness predicted by the analytical models, with parabolic shear (ana1) and half-parabolic shear (ana2) and the numerical stacked-solid model (FEM). . . . .	38
2.7	Load transfer behavior depending on the abstraction scale: layer-wise normalized stress and strain plots of a cross-section in a unidirectional laminate with a crack in ply three. . . . .	39

2.8	Force-displacement history of elastic impact simulations with three different contact formulations. . . . .	42
2.9	Force-displacement history of stacked-solid impact simulations with different cohesive zone methods. . . . .	42
2.10	Predictions of the delamination results, beginning from the lowermost (left) interface to the uppermost (right). . . . .	43
2.11	Penetration behavior of two adjacent plies depending on the master-slave choice of the contact partners. . . . .	44
2.12	Force history of impact simulations with different activated damage modes. . . . .	46
2.13	Damage energy dissipation history predicted with the model considering only delamination (blue) and the model taking into account intra-ply damage and delamination (black). . . . .	46
2.14	Predicted damage results of the numerical model with all damage modes. . . . .	47
2.15	Phases of an impact illustrated in the force history (black) and the energy dissipation (green) of the reference impact simulation with increased impact energy (15.5 J). . . . .	47
2.16	Predicted damage results of the numerical model with all damage modes. . . . .	48
2.17	Experimental setup (A) and the corresponding FE model (B) of a compression cube specimen with a 0° unidirectional laminate. . . . .	49
2.18	The predicted damage initiation (A) and the fully developed crack (B) of the compression specimen analyzed with a degradation mode in Cartesian planes in comparison with the experimental damage (C). The view is perpendicular to the fiber direction. . . . .	49
2.19	Force history of a single element under tensile load in 11-direction. After damage initiation, an asymmetrical material degradation is applied. . . . .	50
2.20	Overview of stress components and stress derivatives with respect to the strain of a fully developed material element with a crack. . . . .	52
2.21	Existing stress components and derivatives of the stress with respect to the strain for an open crack (a) and a closed crack (b). . . . .	55
2.22	Sketch (A), force history (B), and damage (C) in a numerical minimal tensile test with the tensorial-based degradation. . . . .	56
2.23	Application of the tensorial-based damage model for the prediction of the damage initiation (A) and the fully developed crack (B) under compression load in comparison with the experimental damage results (C) and (D). . . . .	56
2.24	Virtual test setups for the validation of the high-fidelity impact analysis model. . . . .	58
2.25	Numerical force time history (red) and force displacement history (blue) of the validation cases in comparison with the test results (grey). . . . .	61
2.26	Comparison of the each predicted delamination overlay plot with the ultrasonic D-Scan results of three exemplary coupon tests. . . . .	65
2.27	Comparison of the numerical prediction for FF in the top ply in comparison with the top view of three exemplary test coupons. . . . .	66
2.28	Energy dissipation by damage in comparison between the experiments and the high-fidelity simulation. . . . .	66
2.29	Comparison of different intra-ply damage models on the validation case CAI2.40. . . . .	67
2.30	Comparison of the numerically determined delamination overlay plots with four different damage models (CAI2.40). . . . .	67

3.1	Graphical explanation of the considered options for impact analysis on the structural level. . . . .	71
3.2	The elastic deformation under impact load is split up to a bending, a shear, and a membrane component. . . . .	73
3.3	Elastic spring-mass models in the idealized version (A) and the variant accounting for local indentation (B). . . . .	74
3.4	FE-predicted elastic force-displacement history and the spring-mass model fit for two test cases: a CAI coupon and a stiffened panel section. . . . .	75
3.5	Sketches of damage-capturing spring-mass models: the idealized version of the model by Olsson (A) and the spring-mass model newly introduced in this work (B). . . . .	76
3.6	Determination of the damage stiffness parameter $k_d(E)$ from the real impact response and the elastic response depending on the introduced energy $E_{total}$ . . . . .	78
3.7	Flow chart for the scaling of the impact energy/ the transfer of impact damage between the origin and the target. . . . .	80
3.8	Curve of the damage-equivalent impact energy for the transfer origin and the target. . . . .	82
3.9	Released energy of the global elastic structure of an impact configuration when the contact force drops from $F_{up}$ to $F_{drop}$ . . . . .	83
3.10	Spring-mass model illustration of the energy transfer during damage growth with decreasing contact force. . . . .	83
3.11	Model sketch of an impact system for a modal analysis. . . . .	86
3.12	Distribution of kinetic energy over the first 50 modes of a linearized impact setup. . . . .	87
3.13	Location of the four reference points for the derivation of check values of deformation similarity. . . . .	90
3.14	Validation schematics for the analytical spring-mass model, the impact scaling and the high-fidelity simulation. . . . .	91
3.15	Development of the damage parameter $k_d$ (blue) and the corresponding force-displacement history (black) on the example of a 30 J CAI impact (configuration <i>CAI1.30</i> in Section 2.5). . . . .	92
3.16	The spring-mass model's results for the force-time and force-displacement responses of a 30 J CAI impact (configuration <i>CAI1.30</i> in Section 2.5). . . . .	92
3.17	Comparison of the projected delamination area (black) with the values of $k_d$ (blue) for a set of CAI experiments with the continuous course of one exemplary 30 J experiment (dashed line). . . . .	93
3.18	Energy dissipation by damage in comparison between the experiments, the high-fidelity simulation and the analytical spring-mass model. . . . .	94
3.19	The spring-mass model's force-time and force-displacement history of the reference impact "REF" (B1) with 25 J. . . . .	95
3.20	Geometry of all five validation specimen types and the 18 chosen impact locations. . . . .	97
3.21	Force-displacement history of experimental impacts (grey) and prediction by the transfer (red) derived from the reference impact. . . . .	98
3.22	Maximum contact force, delamination area, crack length, and the energy absorption of all scaled impact experiments. . . . .	101
3.23	Experimentally determined values of $k_d$ for all tested impact configuration that shall result in a similar damage as the reference coupon (REF). . . . .	102

3.24	Dynamic energy dissipation by higher-order vibrations for each test configuration. . . . .	104
4.1	Laminate-level energy distribution of the validation laminate as calculated through an elastic analysis with 8 kN indentation force. . . . .	112
4.2	Numerical force-displacement history of the minimal reference coupon and its transfer prediction by the original reference coupon B1. . . . .	113
4.3	Delamination result predicted by the numerical analysis of the minimal reference coupon. . . . .	113
4.4	Areal impact transfer results for the stiffened panel section. The color scale is inverted, as small values of $E$ and $k_d$ indicate an impact-sensitive area (red) and high values an impact-firm zone (blue). . . . .	115
4.5	Areal impact transfer results for a generic aircraft door section. The color scale is inverted to emphasize that small values of $E$ and $k_d$ indicate an impact-sensitive area (red), high values stand for an impact-firm zone (blue). . . . .	116
4.6	The proposed procedure for the assessment of impact damage tolerance with the methods in this work. . . . .	118
5.1	Schematics of the comprehensive analysis process of impact damage on composite structures. . . . .	122
A.1	Ceast Fractovis impact drop tower that was used to conduct the experiments for this work. . . . .	126
A.2	Displacement magnitudes of the first two eigenmodes of the impactor that can participate in the impact. . . . .	127
A.3	Illustration of the evaluation of the sound waves for two ultrasonic scanning methods. . . . .	128
A.4	Cross-section of three equivalent laminates with different delamination patterns. . . . .	128
A.5	C-Scan and D-Scan of the same impact damage. . . . .	129
A.6	Legends of the false color scale representing the depth of a delamination damage in the laminate. . . . .	129
A.7	The force-displacement curves of all impact configurations in the test campaign: comparison of the spring-mass model's prediction (red) and the experimental result (gray). . . . .	132
B.1	Time integration by an explicit and an implicit procedure. . . . .	140

## List of Tables

2.1	Stress distribution and failure index for selected plies of the elastic impact test case at $t = 0.8$ ms. . . . .	35
2.2	Overview of the computational effort and its dependence on the number of plies $n_{plies}$ and the ply thickness $t_{ply}$ for each abstraction scale. . . .	40
2.3	Summary of the trade-off between a layered-shell model, a stacked-shell model, and a stacked-solid model. . . . .	40
2.4	Overview of the computational effort, degrees of freedom, and integration points for models with different cohesive zone methods. . . . .	43
2.5	Test parameters for the five validation experiments on three different laminates. . . . .	58
2.6	Validation results of the numerical prediction in comparison with the experimental results (average and standard deviation) in brackets. . .	60
3.1	Test setups (upper row) and finite element models (lower row) for all specimen types of the transfer validation. . . . .	96
3.2	Overview of all 18 impact configurations, including the impact position from the specimen center, the elastic stiffness, the impact energy, and the number of conducted tests. . . . .	106
3.3	Average result values and the respective standard deviation the reference impacts and the total of all validly scaled impacts. . . . .	107
A.1	Material properties for the simulations in this work. . . . .	130
A.2	D-scan delamination results of the impact experiments on specimen type B. . . . .	133
A.3	D-scan delamination results of the impact experiments on specimen type A and D. . . . .	134
A.4	D-scan delamination results of the impact experiments on the specimen type C. The dotted double line indicates the position of the stiffener on the backside. . . . .	135
A.5	D-scan delamination results of the impact experiments on the specimen type C. The dotted double line indicates the position of the stiffener on the backside. . . . .	136
A.6	D-scan delamination results of the impact experiments on the specimen type E. The dotted double line indicates the position of the stiffener on the backside. . . . .	137
B.1	Number of independent entries $e$ depending on the tensor order $n$ . . .	142



## List of Abbreviations

<b>AITM</b>	Airbus Industries Test Method
<b>ASTM</b>	American Society for Testing and Materials
<b>BC</b>	Boundary condition
<b>BVID</b>	Barely visible impact damage
<b>CDM</b>	Continuum damage mechanics
<b>CLT</b>	Classical laminate theory
<b>CPU</b>	Central processing unit
<b>CZM</b>	Cohesive zone method
<b>DIN</b>	Deutsches Institut für Normung
<b>DoF</b>	Degrees of freedom
<b>EASA</b>	European Aviation Safety Agency
<b>ERR</b>	Energy release rate
<b>FAA</b>	Federal Aviation Administration
<b>FEA</b>	Finite element analysis
<b>FEM</b>	Finite element method
<b>FF</b>	Fiber failure
<b>FRP(s)</b>	Fiber reinforced Plastic(s)
<b>IFF</b>	Inter-fiber failure
<b>LSQ</b>	Least squares
<b>REF</b>	Reference impact configuration
<b>RVE</b>	Reference volume element
<b>UD</b>	Unidirectional
<b>VCCT</b>	Virtual crack closure technique
<b>VID</b>	Visible impact damage
<b>XFEM</b>	Extended finite element method





## List of Symbols

### Scalar variables

$A_{dela}$	Projected delamination area	[mm]
$A_d$	Load carrying cross section of a cracked element	[mm]
$A_0$	Initial cross section of an element	[mm]
$a$	Crack length	[mm]
$b$	Crack width	[mm]
$c_d$	Compliance by damage in a laminate	$[\frac{mm^2}{N}]$
$c_{det}$	Coefficient of determination for a non-linear curve fit	[-]
$c_i$	Check values for the deformation symmetry of an impact location	[-]
$d$	Stiffness degradation variable for the damage evolution	[-]
$E_{ela}$	Elastic energy	[J]
$E_d$	Elastic energy in the local damage zone of an impacted laminate	[J]
$E_{global}$	Globally stored elastic energy in an impacted laminate	[J]
$E_{release}$	Globally released energy after a force drop during an impact	[J]
$E_i$	Impact energy of the impactor	[J]
$E_{ij}$	Young's moduli ( $i = j$ ) and shear moduli ( $i \neq j$ )	[MPa]
$E_{hertz}$	Combined modulus of contact partners	[MPa]
$F$	Contact force of the impactor and the laminate	[N]
$g_0$	Gravitational acceleration	m/s <sup>2</sup>
$G_{ij}$	Shear modulus	[MPa]
$G$	Energy release rate at the crack tip	$[\frac{mJ}{mm^2}]$
$G_c$	Critical energy release rate at the crack tip	$[\frac{mJ}{mm^2}]$
$g_c$	Volume-specific critical energy release rate	$[\frac{mJ}{mm^3}]$
$I_{ply}$	Number of integration points per ply	[-]
$K_{ij}$	Stiffness in a cohesive zone	$[\frac{N}{mm^3}]$
$k_m$	Membrane stiffness of a spring-mass model	$[\frac{N}{mm^3}]$
$k_{bs}$	Bending and shear stiffness of a spring-mass model	$[\frac{N}{mm}]$
$k_d$	Spring-mass model damage parameter of a laminate	$[\frac{N}{mm^3}]$
$l_f$	Fiber crack length on the impact side	[mm]
$l_m$	Interfiber crack length on the impact back side	[mm]
$l_c$	Characteristic element length for a damage mode	[mm]
$l_{crit}$	Critical element length for numerical stability	[mm]
$l_{max}$	Maximum allowed element length	[mm]
$m_i$	Impactor mass	[kg]
$m_1$	Modal mass in the first eigenmode of an impact system	[kg]

$m_s$	Modal mass in the first eigenmode of an impact specimen	[kg]
$n_{plies}$	Number of plies in a laminate	[-]
$R_i$	Impactor nose radius	[mm]
$r_c$	Radius of the contact area between the impactor and the laminate	[mm]
$s(x)$	Standard deviation of $x$	[ $x$ ]
$\Delta t$	Time increment in a numerical analysis	[s]
$t_{ij}$	Traction in a cohesive zone	[MPa]
$T_0$	Constitutive thickness of cohesive elements	[mm]
$T_{ply}$	Ply thickness	[mm]
$V_{char}$	Characteristic volume of a material element	[mm <sup>3</sup> ]
$w$	Indentation of the impactor into the laminate	[mm]
$w_d$	Addition impactor indentation through the compliance by damage	[mm]
$w_{global}, w_g$	Global (elastic) impactor indentation into laminate	[mm]
$w'$	Laminate bending angle	[rad]
$X_{ij}$	Material strengths for normal and shear stress	[MPa]
$\alpha$	Ratio of artificial stiffness by a cohesive zone and material stiffness	[-]
$\delta_{ij}$	Separation in a cohesive zone	[mm]
$\varepsilon_i$	Equivalent strain at damage initiation	[-]
$\varepsilon_u$	Equivalent strain at ultimate failure	[-]
$\zeta$	Damping ratio	[-]
$\eta$	Mixed mode coefficient	[-]
$\theta$	Radial coordinate	[rad]
$\Lambda$	Logarithmic decrement	[-]
$\nu_{ij}$	Poisson's ratio	[-]
$\xi$	Modal degree of freedom in a dynamic system	[mm]
$\sigma_i$	Equivalent stress at damage initiation	[MPa]
$\varphi$	Fracture angle for inter-fiber failure	[rad]

### Tensorial variables

${}_4\mathbf{C}$	Fourth-order stiffness tensor
${}_2\mathbf{C}$	Stiffness tensor in 6x6 Voigt notation
$\mathbf{C}^d$	Degraded stiffness tensor
$\mathbf{C}^r$	Rotated stiffness tensor
$\mathbf{D}$	Damping matrix of the equation of motion
${}_2\mathbf{D}$	Second-order degradation tensor
${}_8\mathbf{D}$	Eighth-order degradation tensor
$\mathbf{f}$	External forces in a dynamic system
${}_8\mathbf{I}$	Eighth-order identity tensor
$\mathbf{K}$	Stiffness matrix of the equation of motion
$\mathbf{M}$	Mass matrix of the equation of motion

$\mathbf{n}$	Normal vector in the fracture plane
$\mathbf{R}$	Rotation matrix
$\mathbf{x}$	Degrees of freedom in a dynamic system
$\sigma$	Stress tensor
$\varepsilon$	Strain tensor
${}_8\Omega$	Weighting tensor for the degradation

### Generic Variables

<i>DMG</i>	Impact damage
<i>IMP</i>	Impactor properties
<i>BC</i>	Boundary conditions
<i>MAT</i>	Material properties of a unidirectional ply and the ply interface
<i>LAY</i>	Laminate's layup

### Indexes

+	Tension
-	Compression
<i>m</i>	Matrix failure
<i>f</i>	Fiber failure
<i>n</i>	Fracture plane normal direction
<i>l</i>	Lateral direction in the fracture plane
<i>t</i>	Transverse shear direction in the fracture plane



*“Research is what I’m doing when I don’t know what I’m doing.”*

Wernher von Braun, space scientist (1912-1977)

# 1

## Introduction

Nature provides fiber reinforcement to organically grown materials. The human invention of fiber reinforcement copies this evolutionary approach. However, one crucial difference remains. While a tree can overgrow and repair damage, a human-made structure remains damaged. We thus have to deal with the damage.

### 1.1 Motivation of impact analysis on composite structures

Impact is the action of one object striking another. During this action, both objects deform, and kinetic energy is converted to internal energy in both objects. A deformation beyond the reversible capacity of an object deteriorates its mechanical integrity; damage results. The subject of this thesis is the striking of foreign objects against load-sustaining structures. Impact-induced damage reduces the structure’s capability to sustain load. If impact cannot be avoided, a structure becomes damage-prone. Consequently, impact damage has to be understood, and solutions for its mitigation have to be found.

Consideration of impact damage is crucial for designing aircraft structures, in particular. Aircraft are likely to be exposed to impact during their service life: hail, birds, and dropped tools are only some relevant impact scenarios. If massive damage occurs during flight, safe flight continuation has to be ensured until landing. Small damage that is unlikely to be recognized immediately has to be tolerated until its discovery; it may even need to be tolerated for the entire lifetime of the structure.

Impact scenarios are relatively simple to handle for metallic materials. Plastic deformation absorbs most kinetic energy, and the damage is visible. The corresponding damage-growth behavior is stable, well understood, and the guidelines for a safe, damage-tolerant design are long established. Conversely, fiber-reinforced plastics (FRPs) do not fit to this established system, based on their damage characteristics. For this reason, experiences from metal structures are not directly transferable to structures made of FRPs.

Fiber-reinforced plastics provide higher strength and stiffness than do conventional metallic materials. Indeed, the exploitation of FRPs’ anisotropic characteristics enhances the possibility of establishing load-path-optimized designs. Although the low mass density of FRPs provides a high potential for lightweight construction, the

practically achieved weight savings are not nearly as high as the pure numbers of strength and density suggest. One reason for this discrepancy is impact damage. The complex damage behavior of various interacting damage modes makes damage-tolerant design challenging. Damage is hardly visible and its growth easily becomes unstable. All this deprives FRPs of their advantageous lightweight properties. As a consequence, conservative design with high safety factors ensures the structure's airworthiness. Such safety factors increase the structural mass of the aircraft, however. Moreover, the conservative design demands for extensive qualification effort, increasing the corresponding costs associated with FRP structures.

The research in this thesis shall provide an improved understanding of impact damage. A combined analytical-numerical method is established for impact damage assessment on a structural level. An analytical scaling approach enables a transfer of a structural impact scenario and to a simplified coupon impact. A numerical coupon simulation provides the actual damage prediction. Advanced means of structural analysis represent the basic instruments for the developed methodologies in the present work.

Based on this approach, the risk of impact damage can be estimated, and the experimental qualification effort shall be reduced. This work will not directly result in better lightweight aircraft design, but in the increased safety for future lightweight aircraft and the reduction of the associated design costs.

## 1.2 Objectives and hypotheses

The objectives of this dissertation are formulated in three hypotheses from which the accomplished work steps derive. These hypotheses build on the primary goal of developing an analysis strategy for low-velocity impact on the structural level. The knowledge gaps that I discovered in currently available analysis methods and ideas for their solutions lead to the hypotheses' formulation. In the main part of the thesis, these solutions are developed, applied, and validated through experiments. The final part of this work involves an evaluation of each hypothesis.

Initially, an impact analysis method that can be implemented in a damage tolerance (DT) analysis according to industrial standards requires a reliable damage prediction for FRPs. Physical soundness of the phenomenological description and numerical robustness have to be ensured. This analysis includes the prediction of both the damage initiation and the postfailure behavior of the damaged material. A numerical model that is based on the published state of the art shall serve that purpose. The model shall be further improved where a lack of physical consistency is identified. This leads to the first hypothesis:

### **Hypothesis 1:**

The failure of unidirectional composite plies in multi-directional laminates can be captured by continuum damage mechanics (CDM) and a finite element solution.

For application in a DT analysis, the results of distinct impact scenarios are insufficient. A comprehensive approach, describing impact damage on an entire structure would be useful and would radically enhance the possibilities of structural impact assessment. Only a quickly solvable analytical model can provide this assessment. Therefore, a new damage description method is required to characterize both the structural state of damage and its effect on the mechanical behavior. Thus, the second hypothesis is derived:

**Hypothesis 2:**

The impact damage of a composite structure can be described through an analytical spring-mass model, capturing the state of damage and the structural indentation behavior.

An analytical description of the damage state is insufficient to predict impact damage. Instead of a prediction, the analytical model shall allow the transfer of a known impact damage to a different location. It has to permit the deduction of a laminate's generalized damage behavior from a known impact case. This deduction presumes that the impact damage behavior can be described objectively regarding the boundary conditions (BC) and the impact location. From the objective damage behavior, the results of specific impact scenarios shall be derived. Accordingly, a reduced, representative impact setup can represent large areas of an impact-prone structure. These aims are formulated in the third hypothesis:

**Hypothesis 3:**

A low-velocity impact on a composite structure is transferable to a more general reference case, the results of which can be inversely transferred to large areas of a structure.

In the course of the thesis, the Chapters 2, 3, and 4 comprise the analysis of all three hypotheses. The present introductory chapter provides the necessary theoretical background on the basis of the published literature.

## 1.3 Fiber-reinforced plastics

### 1.3.1 Fiber reinforcement

Fiber-reinforced plastics are composites of at least two materials: a fiber reinforcement and a matrix embedding the fibers. Fiber reinforcement is not a human invention but a basic principle evolved by nature. Nature applied fiber reinforcement to organic materials in plants and living organisms – wood, bone, and muscle are naturally fiber-reinforced materials. Human-built structures reinforced by plant fibers are known to have existed 3000 years ago in ancient Egypt [1]. In fact, the use of plant fibers is reported in many ancient applications, commonly in combination with loam or tree gum, both of which harden by drying; in that way, the increased material toughness by fiber reinforcement was early on exploited by man. Modern utilization has moved from natural to manufactured fibers made of carbon, glass, or aramid. Fibers are superior to a solid of the same material because they are free of notches and have identically oriented molecules.

A composite of fibers and matrix material has a clear distribution of tasks. Fibers provide high tensile stiffness and strength – excellent premises for load bearing. The disadvantages of pure fiber material include a lack of compression stability and a negligible shear stiffness. To overcome these disadvantages, fibers have to be combined with a second material component. This component has to provide cohesion and stability to the fiber reinforcement. These are the main tasks of the matrix material.

Fibers provide high strength and stiffness only in their longitudinal direction. The composite of fibers and matrix behaves similarly. This behavior results in a particular case of directional material properties called “orthotropy”. As such, there are three mutually orthogonal planes with symmetry of elasticity. For a fiber-reinforced

material, one of these three planes is very tough, while the other two are not. In some applications this characteristic fits perfectly to the load – a tree trunk is such an example in nature. Under multiaxial loading, however, an orthotropic behavior is not advantageous. A combination of differently orientated fibers resolves this deficiency. The most pragmatic solution for this problem is thus a layered composite. Individual orthotropic layers of unidirectional fibers are stacked to a multidirectional laminate. This arrangement in layers is another essential characteristic of today’s composites. It offers new opportunities to design load-path-optimized structures.

Each of these positive characteristics makes FRPs a promising material for present and future aircraft. Their properties of density, stiffness, and strength offer high potential for lightweight designs. In design, analysis, and manufacturing, many new difficulties arise, however. The damage behavior is complicated and hard to analyze [2]. Improved damage capture of FRPs is inevitable for future structures made from FRPs.

### 1.3.2 Damage modes of fiber-reinforced plastics

The damage behavior of FRP materials is driven by a diversity of various failure modes that involve the fibers, the matrix, and the interface region [3]. The composite itself, consisting of at least two different materials, is responsible for this variety. In addition, the layered design provides an additional property that influences the damage behavior. Depending on the laminate and the loading, different damage modes dominate the failure. Figure 1.1 illustrates the three crucial damage modes of composites [4].

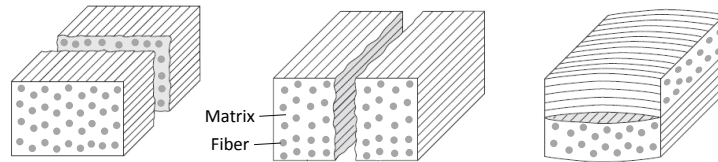


FIGURE 1.1: Damage modes of composite materials: fiber fracture, inter-fiber fracture, delamination (from left to right).

#### Fiber failure

In an FRP structure, the fiber reinforcement takes the bulk of the load. In consequence, the breakage of fibers is the most severe failure mode. It substantially attenuates structural strength and stiffness. Alfred Puck even calls fiber damage “the only desired failure mode of laminates” [5]. Being the load-carrying elements, fibers should be exploited to their utmost strength. If another failure mode occurs before fiber damage, the material potential is not fully exploited.

With fiber failure (FF) due to tensile load, usually fibers break, causing a crack to appear. Under compressive load, the FF is dominated by kinking. In this case, the fibers can lose their capability to bear a load without an actual crack [6, 7]. This behavior can be important if the loading condition changes between compression and tension. Fibers that broke on tensile load can still sustain compression, and the opposite is also true. Accordingly, the FF has to be captured as two separate damage modes.



The shear load is a minor factor for FFs. Due to the symmetry of the stress tensor [8], each shear component in a possible fiber fracture plane  $\sigma_{12}$  and  $\sigma_{13}$  equivalently acts in a possible plane of inter-fiber fracture by  $\sigma_{21}$  and  $\sigma_{31}$ . Accordingly, shear load usually results in a matrix failure mode before the fibers would be affected.

Fiber failure crack planes are usually perpendicular to the fiber orientation, as illustrated in Figure 1.1.

### Inter-fiber failure

We consider any ply damage orthogonal to the fiber orientation as inter-fiber failure (IFF). It results in a cracked laminate with intact fibers. As early as 1987, Liu et al. analyzed this damage type experimentally [9]. Inter-fiber failure can occur in two ways: either by a crack in the matrix material or by the debonding of fibers and matrix. Both ways can be summarized in one comprehensive IFF mode.

Depending on the state of stress that initiates the damage, the IFF has different damage characteristics. Tensile load in combination with shear results in one distinct crack. When this crack is closed, the compression load can still be sustained. In contrast to that, compression-shear damage results in a zone of crushed matrix material, after which neither compression nor tension nor shear can be carried in that section. However, in both cases the fibers remain undamaged. Consequently, load in the fiber direction can still be carried. Either way, the stability behavior of fibers under compression load can be affected negatively.

As the fibers remain intact, the fracture planes of IFF are usually in line with the fiber orientation. Hence, they can occur at different angles around the fiber axis. The exact orientation depends on the state of stress that leads to the failure.

### Delamination

In contrast to the previously described modes, delamination is an interlaminar failure mode [9] – the local debonding of two adjacent plies. This mode leads to an IFF surface parallel to the ply surfaces. Physically, the mechanisms are the same as for IFF; however, the delamination does not occur on the ply level but on the laminate level.

Delamination is not visible from the outside. Even when it occurs together with visible damage, delamination can span over a much larger area. It is often called the *predominant damage mode* in the failure of composites [9, 10, 11, 12]. This is true for certain damage causes, especially those that do not result in catastrophic failure, such as a low-velocity impact (LVI) [9]. Ballistic impacts and manufacturing defects are also common causes of delamination [13, 4]. Usually, exceeding a certain level of impact energy makes FF predominate over delamination.

The layup also influences the occurrence of failure types. As delamination appears only at interfaces between two plies with a different orientation, unidirectional laminates do not delaminate [14]. A larger number of delamination-prone ply interfaces results in smaller dimensions of the individual delaminations. The interface angle of two adjacent plies influences the delamination size as well [15].

The distribution of impact-induced delaminations over the laminate thickness direction shows a certain characteristic: The damage size varies with the damage depth. Commonly, a pine tree pattern of delamination damage occurs [16]. For thin laminates, the delamination size increases from the impact side to the reverse side. The lowermost delamination is commonly the largest. For thick laminates, the pine tree pattern reverses. The largest delamination occurs in the interface closest to the impact side.

To detect delamination damage in a structure, non-destructive inspection methods have to be applied; possible methods include ultrasonic inspection, X-ray analysis, and computer tomography, all of which require specialized test equipment. Ultrasonic inspection is the most important method for practical inspection of structures as well as for the validation of simulation results. The fundamental principle of the applied ultrasonic methods is explained in Appendix A.2.

### Damage interaction

The described failure modes can appear as separate phenomena. However, this is only true for generic exceptions, like homogeneous states of stress; by contrast, the damage modes usually interact [9]. Only by consideration of the modes' influence on each other can a plausible prediction be made. An essential interaction regarding impact analysis is the relation between delamination and IFF (Figure 1.2). Choi and Chang were the first to describe these effects in 1992 [17]. Shi and Yee enhanced the description in 1994 [18] through their analysis of the crack opening modes leading to the propagation of delamination. Additionally, Serge Abrate contributed to a better understanding of the delamination distribution over a laminate's interfaces with his comprehensive work about impact [16].

In common sense, an IFF is the first-occurring damage in a laminate. The bending load of the impact induces inter-fiber cracks by normal stress or by shear stress. According to the same principle, as for a beam [19], normal stress is linearly distributed over the thickness, with compression on the top and tension on the lower side. The largest tensile stress is located on the backside of the laminate. A tensile IFF is mostly located in the lower half of the laminate, while shear stress is quadratically distributed and reaches its maximum in the middle of the laminate [20]. In consequence, shear cracks accumulate in the laminate's inner plies.

An inter-fiber crack grows through a ply until it reaches an interface where the fiber orientation changes. The fibers of the next ply act as a crack stopper, and crack is deflected to the interface; delamination results. Once a delamination initiates, the Mode I crack opening significantly contributes to its propagation [18].

The shear-induced delamination in the middle of the laminate can also appear without a previous intra-ply crack. The symmetry of the stress tensor leads to an equivalence of out-of-plane shear and the shear in the ply interface. In contrast, the tension-induced delamination at the impact backside cannot arise separately. It is bound to the matrix crack. This coupling is crucial for the prediction of the delaminations close to the impact backside. In a damage analysis, this interaction has to be enabled by the damage model. Alternatively, it can be considered directly in the damage prediction, as Choi and Chang proposed in their delamination criterion [17].

### 1.3.3 Damage-tolerant design with fiber-reinforced plastics

Aircraft structures have to meet high safety standards that are defined by the aeronautical authorities European Aviation Safety Agency (EASA) and the Federal Aviation Administration (FAA). These safety standards result from an indispensable need for fail-safety in structures of vital importance. Describing his flying machine, Leonardo da Vinci said that "in constructing wings one should make one cord to bear the strain and a looser one in the same position so that if one breaks under the strain, the other is in the position to serve the same function" [21]. To comply with that need, design guidelines for aircraft structures have developed throughout aviation history. As those structures were originally made for metal alloys, the established guidelines

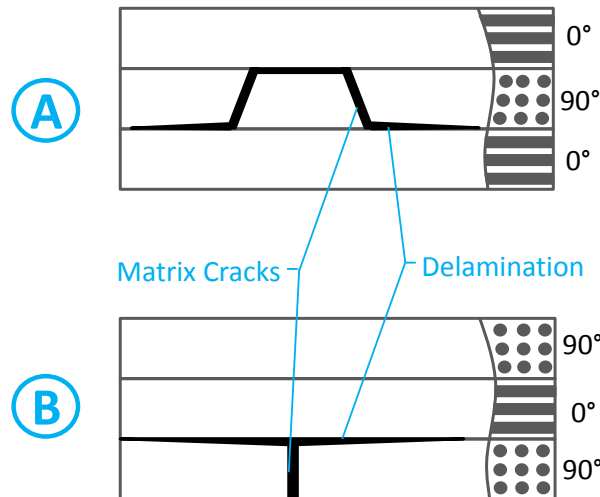


FIGURE 1.2: Interaction of delamination with an IFF shear crack (A) and an IFF tensile crack (B).

deal with metallic damage behavior and hence are not directly transferable to FRPs. Further developments are required in the field of dealing with impact damage. An FRP structure has to “equal or exceed” the same safety standards as a conventional metal structure [22]. For that purpose, the FAA guideline AC 20-107 [23] defines the permitted design principles for composite aircraft.

The first design concepts applied to ensure airworthiness were the safe-life and the fail-safe design philosophies. As the diagram in Figure 1.3 shows, a safe-life structure has to ensure that ultimate load can be sustained over the service life of the aircraft. This assurance includes any possible damage occurring, because an inspection has not been scheduled. Thus, safe-life design results in high structural mass. The fail-safe concept ensures airworthiness by a redundancy of load paths but does not formulate inspection requirements. The major difference in DT is the in the specification of inspections [24]. Regular inspections are scheduled to detect damage before it becomes critical. With this design philosophy, the structure has to provide only the capability to sustain the limit load over an inspection interval. Critically damaged components are repaired or replaced. This method permits lighter structures.

Aircraft structures are designed according to the concept of DT. This concept replaced the safe-life and the fail-safe concepts in the 1980s [24]. Damage tolerance provides a good compromise between safety and economic efficiency. The basic analysis principle of damage-tolerant design is shown in schematic damage-growth diagram in Figure 1.4 [25]. Damage is considered by assuming an initial crack exists in the structure. Under operational load, this damage begins to grow. Damage tolerance demands that the damage be detected and repaired before it reaches the maximum tolerable size [22]. The residual structural strength, needing to be higher than the limit load, defines the damage threshold. A damage growth analysis can obtain the safe interval between those two damages sizes. Required inspection interval are derived directly as a fraction of the interval of safe damage growth. This principle was established for aircraft made from metal materials.

In their work regarding DT concepts for composite structures Sierakowski and Newaz said, “A basic tenet in the design of structures composed of composite materials is that the structure should equal or exceed the damage tolerance requirement of metals” [22]. However, the damage behavior of FRP materials makes a direct transfer of the damage-tolerant design principle difficult. Observable crack propagation is

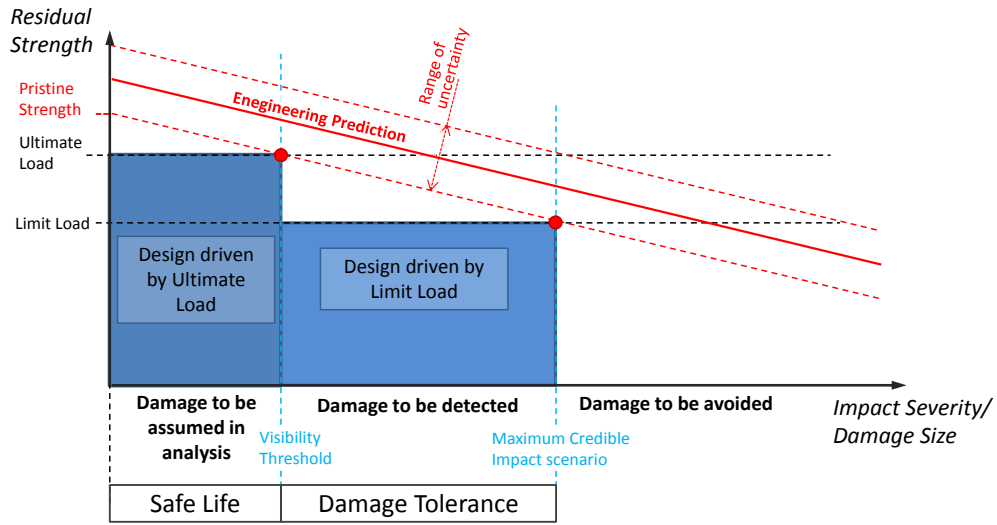


FIGURE 1.3: Applicability of damage tolerance and safe-life design philosophy for different damage sizes.

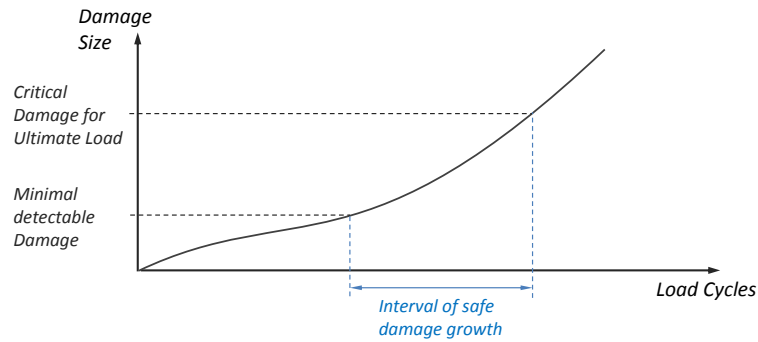


FIGURE 1.4: Schematics damage-tolerant design with damage growth under operation load.

fundamental to establishing the DT design principle. Unfortunately, damage detectability cannot be ensured for all relevant damage. Delamination must be considered nondetectable in a visual inspection. In addition, damage on the inner side of the structure is not necessarily observable from the outside. These damage modes are classified as barely visible impact damage (BVID). This term refers to a damage that is not detectable in a general visual inspection procedure according to the EASA and FAA [26]. This makes BVID likely to remain in the structure during its service life. Accordingly, the maximum possible BVID has to be considered in the design of this structure.

The interval of safe damage growth in FRPs is very small, since damage might not be visible even when it becomes critical. Accordingly, tight inspection intervals would be required. As a result, a no-growth approach is applied, not permitting any growth of possibly existing BVIDs. This is close to a safe-life design philosophy (Figure 1.3). The structure has to be capable of sustaining ultimate load after any possible impact scenario [27]. Capabilities to build lighter structures cannot be exploited, as the growth of damage is not permitted.

## 1.4 Failure analysis<sup>1</sup>

The analysis of material failure is an important engineering discipline. Impact analysis methods are founded on more general methods of failure analysis in materials. This section gives a brief introduction to the relevant fundamentals.

The behavior of most materials begins with an elastic phase that can be considered linear. In Figure 1.5, this linearity is represented by the first illustrated phase. In this phase, no damage occurs, and loading and unloading are fully reversible. Hooke's law [28] describes the linear correlation of load and displacement. Equation (1.1) shows the generalized law in stiffness form. The fourth-order stiffness tensor  ${}_4\mathbf{C}$  couples the stress tensor  $\sigma$  and the strain tensor  $\varepsilon$ .

$$\sigma = {}_4\mathbf{C}\varepsilon \quad (1.1)$$

When the loading exceeds a certain threshold, the linear phase ends, and damage initiates. Irreversible deformations occur. These can be either small cracks or plastic deformations by damage on the atomic scale. Both result in a reduction of the material's load-carrying capability. For engineering application, this second phase is crucial. The prediction of the threshold of damage initiation is the first point of interest. Secondly, the degradation behavior until total failure has to be described.

The third illustrated phase represents the post-failure behavior of a material. Under tensile load, the failure usually results in an open crack, and the load drops to zero. Under compression load, there is still a residual load-carrying capacity, as the material cannot physically move away. A failure analysis also has to capture this third phase.

The failure analysis in FRP usually requires a distinction of cases. The diversity of damage modes is hard to capture in a comprehensive approach, as each failure mode initiates differently and shows its own propagation behavior.

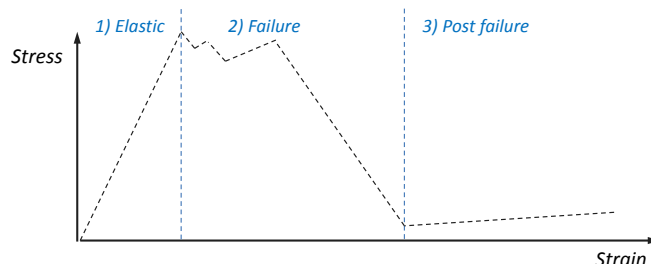


FIGURE 1.5: Stress-strain schematics of material behavior in an elastic phase, a failure region, and a post-failure region.

### Damage initiation

Engineering methods use stresses or strains for the prediction of damage initiation in isotropic materials. Methods like the von Mises yield criterion [29] or the maximum-normal stress theory of Rankine [30] are established and applied in design processes.

The prediction of damage initiation of FRP is challenging and is itself a topic of research. Many prediction methods – so-called failure conditions – are available. These conditions predict the damage initiation according to the states of stress and strain in the material. Many reviews of such conditions them have been established.

<sup>1</sup>Parts of this section have been published by the author in [RB1].

Additionally, international comparative studies have been conducted in the *World-Wide Failure Exercises* (WWFE) [31, 32, 33].

In this international exercise, many failure conditions were evaluated [32]. The homogenized criteria can be categorized by their association to failure modes [34]. For example, criteria like those of Tsai-Wu [35] or Chamis [36] simply indicate damage by a general failure index comprising all failure modes. Other conditions that consider different failure modes work with one failure index for each mode: Criteria of this kind can be distinguished in non-interactive methods, that limit every stress or strain component separately [33] and interactive criteria, taking into account several stress or strain components to predict distinct failure modes. Non-interactive criteria such as maximum-strain are usually straightforward but not necessarily conservative. Interactive models like the Hashin criterion [37] analyze each failure mode by taking into account all strains or stresses that influence this specific mode (compare [RB2]). In this category, there are simple geometrical models like the quadratic strain criterion in the Equation (1.2). This criterion can be interpreted as the normalized length of the strain vector in a fracture plane with the coordinates  $L/N/T$ . This normalized length indicates failure when it becomes larger than 1. The fracture planes are commonly the three orthogonal planes of the Cartesian material coordinates 1/2/3 in Figure 1.6. Some failure conditions determine the most likely fracture plane of IFF. In this case  $L/N/T$  is rotated by the angle  $\varphi$  around the 1-axis.

$$F_n = \sqrt{\left(\frac{\varepsilon_{nn}E_{nn}}{X_{nn}}\right)^2 + \left(\frac{\varepsilon_{nl}E_{nl}}{X_{nl}}\right)^2 + \left(\frac{\varepsilon_{nt}E_{nt}}{X_{nt}}\right)^2} \quad (1.2)$$

Failure conditions that determine the fracture plane are physically based. For example, such an approach was developed by Puck and Schürmann [38]. Puck assumes that IFF occurs in arbitrary fracture planes. According to the sketch in the Figure 1.6, this fracture plane is equipped with the coordinate system  $L/N/T$ , where  $L$  is the fiber direction and  $N$ , the normal vector of the fracture plane.

Equations (1.3) and (1.4) show the Puck failure conditions for tensile IFF ( $\Phi_{IFFt}$ ) and compressive IFF ( $\Phi_{IFFc}$ ) as it was formulated by Wiegand et al. [39]. The criterion builds on the physically based Mohr-Coulomb type of failure. Thus, shear stress determines the damage onset. The clue is the influence of the normal stress through a friction term [39, 40]. The friction coefficients  $p_{NT}$  and  $p_{NL}$  in Equations (1.5) and (1.6) quantify this influence. Compression stress increases the sustainable shear load, and tensile stress reduces it.

$$\Phi_{IFFt}(\varphi) = \left(\frac{\sigma_{NN}}{X_{NN}}\right)^2 + \left(\frac{\sigma_{NL}}{X_{NL} - p_{NL}\sigma_{NN}}\right)^2 + \left(\frac{\sigma_{NT}}{X_{NT} - p_{NT}\sigma_{NN}}\right)^2 \geq 1 \quad (1.3)$$

$$\Phi_{IFFc}(\varphi) = \left(\frac{\sigma_{NL}}{X_{NL} - p_{NL}\sigma_{NN}}\right)^2 + \left(\frac{\sigma_{NT}}{X_{NT} - p_{NT}\sigma_{NN}}\right)^2 \geq 1 \quad (1.4)$$

$$p_{NT} = -\frac{1}{2 \tan(2\varphi_0)} \quad (1.5)$$

$$p_{NL} = p_{NT} \frac{X_{NL}}{X_{NT}} \quad (1.6)$$

According to the evaluation in WWFE-II, especially those criteria that consider oblique fracture planes provide good predictions (Puck [38], Cuntze [41], Pinho [7]). The model of Puck and Schürmann includes a determination of the most likely fracture

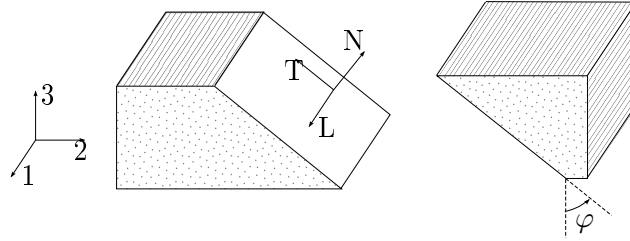


FIGURE 1.6: Sketch of an oblique fracture plane and the coordinate systems of the material (1/2/3) and the fracture plane (L/N/T).

angle to predict initiation more precisely. Another approach with oblique but fixed fracture planes was proposed by Maimí, Camanho et al. in 2007 [42, 43]. They assume compression fracture to occur in the typical angle of  $\phi_0 = 53^\circ$  [44]. Apart from Maimí and Camanho, many researchers report a similar fracture angle for compression failure of unidirectional composites [45, 46, 47]. Based on the idea of Camanho, further development by Catalanotti et al. [48] also lead to a criterion that determines of the fracture angle.

For two-dimensional analysis, the most likely fracture angle can be computed directly by an analytic formula [5, 49]. In a three-dimensional case, the determination of the fracture angle  $\varphi$  has to be established as an iterative process. Wiegand et al. have published an algorithm for efficient determination of the fracture plane [39]. Through a golden section search and quadratic interpolation, the fracture plane is determined in very few iterative steps. Evaluation of the failure conditions in the fracture plane for approximately ten angles is required to compute a value that is comparably reliable to an iterative search with 180 steps (cf. Figure 1.7). Wiegand's algorithm is suitable for any criterion that requires the determination of a fracture plane [38, 48, 50].

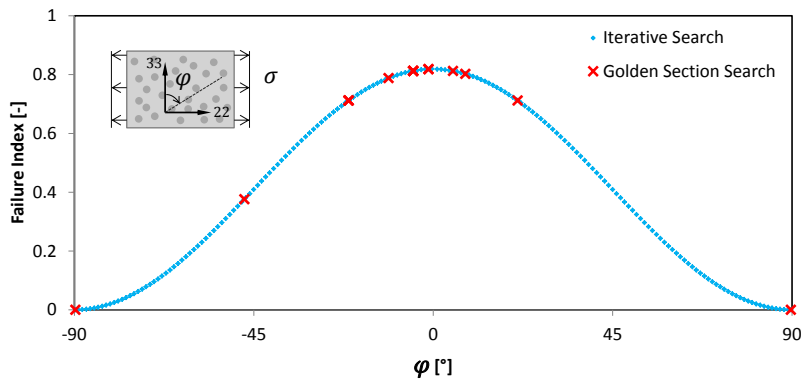


FIGURE 1.7: IFF index of Puck's criterion depending on the fracture angle determined by iterative search (blue) and golden section search (red).

## Damage propagation

For analysis of a strength- or stiffness-based design, the consideration of the damage initiation is sufficient. A safety factor ensures an adequate structural reserve until the point of damage initiation that the failure condition predicts. However, for DT design the damaged case becomes essential – propagating cracks and existing damage have to be considered. Damage evolution describes what happens after the failure

initiation, when Hooke's law according to the Equation (1.1) no longer describes the material behavior.

At sharp crack tips, the assumptions of continuum mechanics would result in infinitely high stresses. As such levels of stress are physically implausible, the continuum theory reaches its limits. Inglis described this insufficiency as early as 1913 [51]. It is an insufficiency from which a new branch of mechanics arose. Suitable methods to deal with cracked structures belong to the scientific field of fracture mechanics. Many fracture-mechanical approaches capture crack propagation based on the energy absorption of the damaging material. This idea is based on the work of Griffith in 1921 [52] and was further developed by Irwin in 1948 [53]. Irwin additionally contributed to the development with his analysis of stresses and strains at crack tips to the understanding of crack growth [54].

The propagation of a crack in a pre-stressed material releases an amount of energy  $dE_{ela}$  per crack length  $da$  according to Equation (1.7). This energy release rate (ERR) depends on the crack length of  $a$  (with a width  $b$ ), the geometrical configuration of the specimen, and the applied load. In opposition to the released energy, the growth of a crack requires an amount of energy that is proportional to the newly created crack surface. This required energy per area is called critical energy release rate  $G_c$ . To analyze whether a crack grows, the required energy for crack propagation is compared with the potential energy being released by the softening of the specimen. The condition for crack propagation (1.8) is fulfilled when the actual energy release rate  $G$  exceeds the critical energy release rate  $G_c$ .

$$G = -\frac{dE_{ela}}{da} \frac{1}{b} \quad (1.7)$$

$$G > G_c \quad (1.8)$$

Following this idea, researchers tried to find a way of combining fracture mechanics with continuum mechanics. For that purpose, Kachanov developed the effective stress concept [55] that permits describing the state of stress in a cracked material element – the CDM. Then, Chaboche and Lemaitre [56, 57] proposed a damage model based on this concept, and Ladeveze provided further developments to apply CDM to composite materials [58, 59].

A crack represents a discontinuity in the material. The response of a cracked material element is that of a discontinuous material with three phases: two phases of material and one open crack phase, as shown in State 3 of Figure 1.8. Continuum mechanics cannot directly capture this discontinuity. A complete description of the physical material state would require an adaption of the specimen geometry during the analysis. This requirement presents a severe disadvantage, primarily because of the associated effort. The idea of the CDM is to overcome this disadvantage through a homogenized description of the crack. It idealizes all three phases in a single material element. This material element has to possess the effective properties of a black box around the real three-phase material.

The CDM concept of Chaboche relates the stiffness degradation to the reduced load carrying cross-section  $A_d = A_0 - A_{crack}$ . For the constitutive equation, only this reduced load carrying cross-section is relevant. But in the analysis  $A_0$  remains the reference surface of the stress in the constitutive equation. Thus, the ratio between those two values in equation (1.9) is the basic equation for the stiffness degradation. It is expressed by  $(1 - d)$ , where  $d$  works as damage variable, describing the damage status.



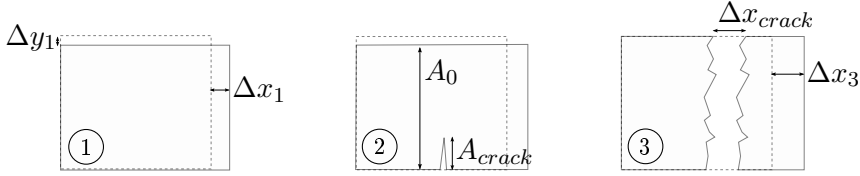


FIGURE 1.8: Schematics of a cracked material element according to the CDM.

$$(1 - d) = \frac{A_d}{A_0} \quad (1.9)$$

$$\hat{\sigma} = (1 - d) \sigma = (1 - d) E \varepsilon \quad (1.10)$$

### Damage evolution law

To describe the degradation path of the stress-strain curve, the fracture-mechanical concept of the ERR is applied to the CDM approach. The critical ERR as a material property defines the integral value of the stress-strain curve. However, no such fracture-mechanical material parameter defines the curve shape. A bilinear law is a well-conforming variant and used in many recent works [60, 61, 62]. This law is easy to handle, as it is analytically integrable. The integration results in Equation (1.11), expressing the specific energy absorption  $g_c$  that can be obtained through the critical ERR  $G_c$  and the volume of characteristic volume  $V_{char}$  of the homogenization approach. Accordingly,  $g_c$  is a volume-specific critical ERR. In reference to Equations (1.7) and (1.8), the cracked specimen has to provide at least this critical rate from its elastically stored energy in order to propagate the crack.

The remaining parameter in the constitutive law  $\varepsilon_u$  can be computed from the known input parameter  $G_c$ . Other evolution laws like exponential degradation [63, 64] usually require numerical integration of the stress-strain curve, which is computationally more expensive.

$$g_c = \frac{1}{2} \sigma_i \varepsilon_u = \frac{G_c}{\frac{V_{char}}{A_{crack}}} \quad (1.11)$$

The damage evolution is expressed through parameter  $d$  and described by the strain-driven evolution law in Equation (1.12). This equation determines the value of  $d$  depending on the damage initiation strain  $\varepsilon_i$  and the ultimate failure strain  $\varepsilon_u$ . The constitutive equation of the damage variable  $d$  characterizes the corresponding evolution law. As the CDM principle is independent of this law, the evolution equation (1.12) can easily be exchanged.

$$d(\varepsilon) = \frac{\varepsilon_u}{\varepsilon_u - \varepsilon_i} \left( 1 - \frac{\varepsilon_i}{\varepsilon} \right) \quad (1.12)$$

A problem occurs when an interactive failure condition is combined with a damage evolution law as in Equation (1.12). An interactive damage initiation criterion depends on more than one stress or strain component. However, a single strain value drives the evolution according to Equation (1.12). This problem is commonly resolved by an idealization called the concept of equivalent strain. A scalar equivalent strain and a scalar equivalent stress are calculated to feed the bilinear degradation law. A simple approach is the absolute value from the strain and stress vector of the associated fracture plane (Equations (1.13) and (1.14)). This strategy is applied by Gonzalez

[65], Falzon [60], Liu [62], and many other researchers. Alternatively, the strain  $\varepsilon_i$  in the fracture plane is computed by an equation analogously to the failure condition [66], or it is even expressed by the normal strain only [67]. Either way, one must be aware that all those approaches are an idealization, not capturing the true damage evolution path. In particular, a changing state of stress during the damage evolution will lead to distortion of the energy absorption.

$$\varepsilon_i = \sqrt{\langle \varepsilon_{nn} \rangle^2 + \varepsilon_{nl}^2 + \varepsilon_{nt}^2} \quad (1.13)$$

$$\sigma_i = \sqrt{\langle \sigma_{nn} \rangle^2 + \sigma_{nl}^2 + \sigma_{nt}^2} \quad (1.14)$$

Finally, the damage evolution equation (1.12) requires the strain value for full damage  $\varepsilon_u$ . Simple geometry provides its value: the integral of the bilinear law is the area of the triangle in Figure 1.9. Its calculation by Equation (1.15) requires the volume-specific critical ERR  $g_c$  from Equation (1.11) and the equivalent stress  $\sigma_i$  from Equation (1.14).

$$\varepsilon_u = \frac{2g_c}{\sigma_i} \quad (1.15)$$

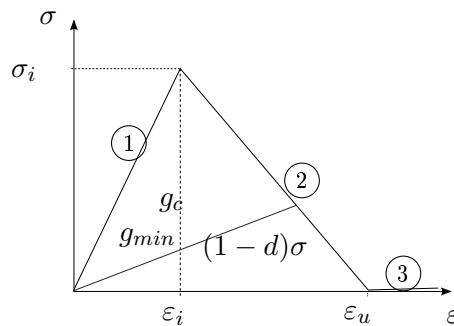


FIGURE 1.9: Bilinear damage evolution law with an elastic phase (1), a degradation phase (2), and a post-failure region (3).

### Degradation in three dimensions

For application to composite materials, the degradation must be applied to the stiffness tensor of orthotropic material. The CDM concept according to Equations (1.9) and (1.10) was adapted for this case by Matzenmiller [68]. The scalar damage variable is sufficient to describe the damage state in one predefined fracture plane: In three dimensions, several damage modes have to be taken into account. Those usually correspond with different fracture planes. Accordingly, at least one damage variable has to be introduced for each fracture plane. If compression and tension damage are distinguished and assumed not to influence each other, it is also possible to use two variables for each fracture plane.

Based on Matzenmiller's idea, many damage models for composite materials have been published [61, 62, 69]. The principle of effective stress from Chaboche is always the basic idea. Matzenmiller derived the degraded tensor  ${}_2\mathbf{C}^d$  from a degraded compliance matrix. This can be interpreted as degradation of Young's modulus and Poisson's ratio.

The degradation of the Poisson ratio is physically sound. The lack of stress in the load direction also prevents the lateral contraction effect. Instead, the crack will

merely open with two unstressed parts as illustrated in the third image of Figure 1.8. Orthogonal to the loading direction, the envelope of the cracked material element remains unchanged.

$${}_2\mathbf{C}^d = \begin{pmatrix} \mathbf{C}_{normal}^d & \mathbf{0} \\ \mathbf{0} & \mathbf{C}_{shear}^d \end{pmatrix} \quad (1.16)$$

$$\mathbf{C}_{normal}^d = \begin{pmatrix} \frac{(1-d_1)(1-\nu_{23}\nu_{32})(1-d_2)(1-d_3)}{\Delta E_{22}E_{33}} & \text{sym.} & \text{sym.} \\ \frac{(\nu_{21}+\nu_{31}\nu_{23})(1-d_3)(1-d_1)(1-d_2)}{\Delta E_{22}E_{33}} & \frac{(1-d_2)(1-\nu_{13}\nu_{31})(1-d_1)(1-d_3)}{\Delta E_{11}E_{33}} & \text{sym.} \\ \frac{(\nu_{31}+\nu_{21}\nu_{32})(1-d_2)(1-d_1)(1-d_3)}{\Delta E_{22}E_{33}} & \frac{(\nu_{32}+\nu_{31}\nu_{12})(1-d_1)(1-d_2)(1-d_3)}{\Delta E_{11}E_{33}} & \frac{(1-d_3)(1-\nu_{12}\nu_{21})(1-d_1)(1-d_2)}{\Delta E_{11}E_{22}} \end{pmatrix} \quad (1.17)$$

$$\mathbf{C}_{shear}^d = \begin{pmatrix} (1-d_1)(1-d_2)G_{12} & 0 & 0 \\ 0 & (1-d_1)(1-d_3)G_{13} & 0 \\ 0 & 0 & (1-d_2)(1-d_3)G_{23} \end{pmatrix} \quad (1.18)$$

$$\Delta = \frac{(1-\nu_{12}\nu_{21})(1-d_1)(1-d_2) - \nu_{13}\nu_{31}(1-d_1)(1-d_3) - \nu_{23}\nu_{32}(1-d_2)(1-d_3) - 2\nu_{21}\nu_{32}\nu_{13}(1-d_1)(1-d_2)(1-d_3)}{E_{11}E_{22}E_{33}} \quad (1.19)$$

To achieve a physically sound degradation, the damage variables  $d_i$  need to be further extended. The introduction of separate degradation variables  $d_{i+}$  for tension and  $d_{i-}$  for compression damage allows the separate consideration of both failure types. Depending on the current state of stress, the constitutive law picks the active degradation variables according to Equation (1.20). Three additional variables  $d_{i-shear}$  describe the shear degradation status. These are not independent but derived from the tension and shear variables [69]. This derivation results in a total of nine degradation variables, of which six are independent.

$$d_i = d_{i+} \frac{\langle \sigma_{nn} \rangle}{\sigma_{nn}} + d_{i-} \frac{\langle -\sigma_{nn} \rangle}{\sigma_{nn}} \quad (1.20)$$

### Degradation in oblique fracture planes

The material degradation in an oblique fracture plane is more complex than the previously introduced approach in Cartesian planes. In each Cartesian fracture plane, the influence of the crack on the stiffness entries in the tensor  ${}_4\mathbf{C}$  can be directly derived. However, an oblique fracture is not associated with a specific orthotropic component. A degradation in only one fracture plane of the material coordinate system would be incomplete, while a degradation of all matrix-driven normal and shear stiffness entries [70] would be too severe, because this would also affect the direction normal to the fracture plane, which can actually still sustain loads. Puck and Schürmann themselves suggest a method similar to this full degradation [38]. Without regarding the actual fracture angle, they diminish the parameters of matrix stiffness  $E_{22}$  and  $G_{12}$  by a factor  $\eta$ . However, they consider a two-dimensional case, in which the laminate thickness direction 33 is not included. This simplification does not necessarily require a full consideration of oblique fracture planes. The degradation might be too severe, but it makes the method suitable for the conservative prediction of failure.

Nevertheless, a conservative prediction alone is no guarantee for a physically plausible damage prediction. The effect of an oblique fracture plane on the deformation behavior of a material element has to be further analyzed. A pragmatic solution to

this problem is a quasi-one-dimensional workaround, which Tan et al. [60] and Liu et al. [62] use in their works. The degradation is not applied on the elasticity tensor but the stress tensor. For that purpose, the stress tensor  $\sigma$  is transformed from the material coordinates (1/2/3) to the fracture plane coordinate system (L/N/T). The coordinate systems are introduced in Figure 1.6 on page 11. As the fracture plane is always parallel to the fiber orientation, this transformation is a simple rotation around the 1-axis. In the next step the factor  $(1 - d)$  applies directly to the transformed stress components in the fracture plane  $\sigma_{NN}$ ,  $\sigma_{LN}$ ,  $\sigma_{NT}$ . The remaining three stress components  $\sigma_{LL}$ ,  $\sigma_{TT}$ ,  $\sigma_{LT}$  remain untouched. A complete description of the degradation status is provided by the fracture angle  $\varphi$  and the variable  $d$ . Transforming those values back to the material coordinates provides a set of degraded stresses. The one-dimensional equations can be expanded to a matrix multiplication of the stiffness matrix in Voigt notation and a degenerated degradation tensor  $\mathbf{D}$  as shown in Equation (1.22). The associated constitutive Equation (1.23) describes the introduced degradation method.

An analysis of Equation (1.23) shows a difficulty that arises from this approach. It leads to a non-symmetrical stiffness matrix as the expansion of  ${}_2\mathbf{C}^d$  shows in Equation (2.9) for the normal components. The degradation factor  $(1 - d)$  is located in the whole second row but not in the whole second column. Tan and Liu solve this issue through a symmetrification. The ratio of the degraded normal stresses  $\sigma_{ii}$  and the elastic stresses  $\hat{\sigma}_{ii}$  results in new values for the parameters  $d_{ii}$ . These modified parameters inserted in Equations (1.16) – (1.19) result in a symmetrical stiffness matrix.

$$\begin{aligned}\sigma_{NN} &= \hat{\sigma}_{NN} - d(\hat{\sigma}_{NN}) \\ \sigma_{LN} &= (1 - d)\hat{\sigma}_{LN} \\ \sigma_{NT} &= (1 - d)\hat{\sigma}_{NT}\end{aligned}\tag{1.21}$$

$${}_2\mathbf{D} = \begin{pmatrix} 1 & & & & \\ & (1 - d) & & & \\ & & 1 & & \\ & & & (1 - d) & \\ & & & & (1 - d) \\ & & & & & 1 \end{pmatrix}\tag{1.22}$$

$$\sigma = {}_2\mathbf{D}\hat{\sigma} = {}_2\mathbf{D}{}_2\mathbf{C}\varepsilon = {}_2\mathbf{C}^d\varepsilon\tag{1.23}$$

## 1.5 The finite element method

The finite element method (FEM) is an established procedure for solving the differential equations of motion. Closed-form solutions exist only for simple cases or if idealizations are applied. The FEM is an approach to provide a suitable numerical solution for complex cases, where no closed-form solution can be found with reasonable effort.

As the tensile bar illustration in Figure 1.10 shows, the FEM splits the target domain into subdomains, called finite elements. In these subdomains, simple shape functions  $N_{ij}$  approximate the solution. These functions are only defined in their subdomain. The degrees of freedom (DoF) are limited through a limited number of nodes in each subdomain. The shape functions meet the solution only at these nodes of the finite element. A minimization of the potential energy in the whole system leads to a system of equations. The number of unknown parameters is equal to the

degrees of freedom in the discretized finite element model. The displacement values at the nodes represent the unknown parameters. This approximation results in a discrepancy to the real solution.

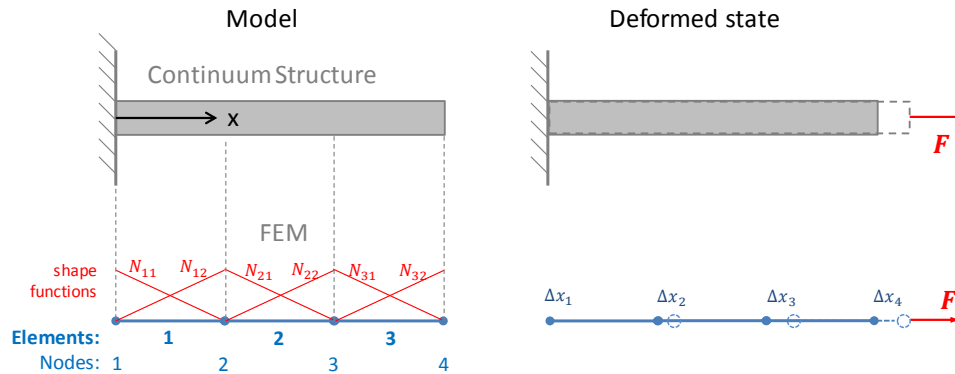


FIGURE 1.10: Sketch of the FEM applied to a tensile bar.

The underlying mathematical ideas of the FEM were already developed in the first half of the 20th century. Turner et al. [71] were in 1956 the first to describe a complete framework of the FEM. They conducted an analysis of structural stiffness. Other researchers quickly adopted the concept; important names include Argyris, Zienkiewicz, and Bathe, who contributed significantly to the further developments of the FEM [72, 73, 74]. The capabilities of the current FEM are strongly enhanced, and the development has continued [75, 76]. Today, the development often focuses on the modeling of damage. For application in impact analysis, the FEM basic methods, as well as advanced developments, are relevant.

### 1.5.1 Time integration

For solving dynamic problems like an impact, the equations of motions according to Equation (1.24) enlarge the solution space by the time domain. Inertia and damping are time-dependent effects that require a transient solution. To obtain this solution, the time domain is also discretized. With a step width of  $\Delta t$ , the deformation state is calculated at discrete points. Based on a set of initial conditions, the displacement solution is obtained in intervals with this step width. This work includes a brief introduction to the basics of time integration methods in Appendix B.1. The integration procedure can analogously be applied to a second-order differential equation, like the equation of motion.

$$\mathbf{M}\ddot{\mathbf{x}} + \mathbf{D}\dot{\mathbf{x}} + \mathbf{K}\mathbf{x} = \mathbf{f} \quad (1.24)$$

Transferred to the finite element solution of a structure, an explicit time integration requires only a matrix multiplication to obtain the displacement field at the next time point. In contrast, an implicit method results in a system of equations that has to be solved. Accordingly, the computational effort of explicit methods depends only linearly on the number of DoF, while this dependency is quadratic for implicit methods. The consequence concerning the computational effort is that explicit solutions become advantageous for large models with many DoF. However, it is important to remember that an explicit FEM does not compute a structural equilibrium state of internal and external forces. A deviation is always included and results in instability after a certain number of time increments.

**Maximum stable time increment:** The unstable character of an explicit time integration results in a limitation of the maximum possible time increment  $\Delta t_{max}$ . This limitation can be visualized by the speed of wave propagation in a structure. If waves propagate too quickly, the wave can run through a finite element within one time step. Within this time step, no counterforces antagonizing the wave's displacement are applied. Each time, counterforces are applied too late, resulting in an oscillation building up. The oscillation will increase for several increments until the solution completely diverges, and the point of instability is reached. For that reason, a sufficiently small time increment has to be ensured. This can be estimated through the ratio of wave propagation speed and the relevant minimal element length for that wave. According to the Courant condition [77] in Equation (1.25) the stable time increment proportionally increases with  $l_{crit}$ .

$$\Delta t_{stable} \sim \frac{l}{c_{wave}} \sim l_{crit} \sqrt{\frac{\rho}{E}} \quad (1.25)$$

As the Courant condition is not necessarily conservative, an additional reduction of the time increment is required to ensure stability. This reduction can be expressed by a safety factor  $s_t = \frac{\Delta t_{simulation}}{\Delta t_{stable}}$ , whose value is typically selected to be between 0.5 and 0.9 [78, 79, 80].

In addition, the Courant condition provides information about possible toeholds to increase  $\Delta t_{stable}$ : increasing the critical length, increasing the mass density or reducing the stiffness. The first of those reduces the approximation quality of the geometry. Changes in mass and stiffness are not physically grounded and affect the structural behavior; therefore, their adjustment has to be handled carefully. In the explicit FEM, adjustments of the mass density, called mass scaling, are common [79]. Mass scaling is useful, especially when only a few finite elements of a model determine the stable time increment. The mass in the corresponding elements increases, and the overall structural behavior is hardly affected. Primarily, the simulation can be carried out with a significantly larger time step, which leads directly to a lower computation time according to  $\frac{1}{\Delta t_{simulation}}$ . The physical soundness of the solution must always be monitored. The structural mass and the energy balance are important check values.

### 1.5.2 Composite modeling with the finite element method

Various options exist for modeling a composite laminate through finite elements. The significant difference in these options is the applied abstraction scale in the discretization [81]. On the macro-scale, the meshing can be performed on the laminate level as in Figure 1.11A. One single layer of elements represents the whole laminate stack. A laminate theory is required within each element to capture the deformation behavior of the composite. Having at least one integration point per layer ensures that the stresses and strains of each unique ply can be derived. Commonly, this method works with shell elements to capture the bending behavior of the laminate with a single element layer.

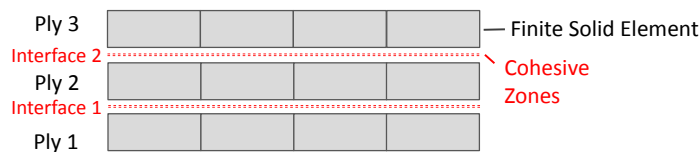
In further detail, the meshing can be conducted on the ply level through a meso-scale approach, as illustrated in Figure 1.11B. Each layer is modeled by at least one layer of elements. This mesh can consist of either solid or shell elements. The meshed layers are stacked upon each other and form the laminate. Neighboring layers share adjacent nodes, their degrees of freedom at the contact faces are coupled through tie constraints. Alternatively, a damage-capturing interface model connects the plies.

A very high computational effort results from the number of DoF, which multiplies by the number of layers in comparison with a macro-scale approach. In addition, the ply thickness  $t_{ply}$  drives the stable time increment in Equation (1.25).

Despite the large computational costs, this modelling strategy has been chosen in many recent works around the analysis of impact damage [65, 82, 60, 64, 62, 66].



(A)



(B)

FIGURE 1.11: Illustration of a composite layup model on the macro-scale (A) and on the meso-scale (B).

### 1.5.3 Contact formulation in the finite element method

A fundamental principle of physics, that objects cannot pass through each other [83], is not automatically valid in a finite element model. The underlying equation comprises the deformation behavior of a body. Its interaction with other objects has to be treated separately by modification of the external forces. Contact algorithms perform this modification. These algorithms also use the finite element mesh with its nodes and surfaces. Common contact algorithms prevent the penetration of nodes into surfaces. This aim can, for instance, be achieved through penalty stiffness [84] or Lagrangian multipliers, which work as a non-penetration constraint [85].

Accurate capturing of contact is crucial for the simulation of impact with the FEM. The contact between the striking body – the impactor – and the laminate is essential for the deformation.

### 1.5.4 Cohesive zone method

A key point of the laminate model on the meso-scale is the interface. While the out-of-plane modulus of the plies sufficiently describes the laminate compliance, the effects of occurring damage have to be considered separately. The cohesive zone method (CZM) is a suitable numerical method to approach fracture in interfaces. It describes the fracture as a “hard discontinuity” [81] in contrast to the CDM that describes only a “soft discontinuity”. De Lorenzis et al. [86] explain that “Simultaneously they permit the combination of stress- and energy-based crack descriptions”. Exceeding interfacial shear or normal strengths initiates the energy-based crack propagation.

These basic ideas of the CZM were developed by Dugdale [87] and Barenblatt [88]. Allix and Ladeveze [89] were the first to present a corresponding interface model to capture delamination damage.

In the initial state of the interface, the cohesive zone connects both interface partners elastically. This connection concerns three deformation modes that all lead

to a separation of the partners: the deformation mode in the normal direction and two out-of-plane-shear deformation modes. In each mode, a stiffness component  $K_{ij}$  and a relative displacement  $\delta_{ij}$  permit the calculation of a traction  $t_{ij}$  through Hooke's law in Equation (1.26). The stiffness components  $K_{ij}$  have the unit  $\frac{\text{N}}{\text{mm}^3}$  and stand for stress per separation. The tractions describe the state of stress in the interface zone, and a damage initiation condition can be evaluated. A failure criterion, as in Equation (1.27), is evaluated to determine the damage onset. After damage initiates, an energy-based damage evolution completes the fracture-mechanical traction separation, and the critical energy release rate  $G_i$  becomes the driving parameter. The constitutive formulation of the cohesive zone is comparable to that represented in the CDM model introduced in Subsection 1.4.

The whole formulation is either implemented in a specific element type (cohesive elements) or in a contact law (cohesive surfaces). Equation (1.26) represents the formulation for cohesive surfaces. Cohesive elements work with an additional constitutive thickness value  $T_0$  to compute strain values from the separations. The stiffness values  $K_{ij}$  respectively require a multiplication with this thickness to achieve the corresponding element stiffness  $e_{ij}$ :  $K_{ij}T_0 = e_{ij}$ .

$$\mathbf{t} = \begin{pmatrix} t_{nn} \\ t_{nl} \\ t_{nt} \end{pmatrix} = \begin{bmatrix} K_{nn} & & \\ & K_{nl} & \\ & & K_{nt} \end{bmatrix} \begin{pmatrix} \delta_{nn} \\ \delta_{nl} \\ \delta_{nt} \end{pmatrix} \quad (1.26)$$

$$f_{CZM} = \sqrt{\left(\frac{\langle t_{nn} \rangle}{X_{nn}}\right)^2 + \left(\frac{t_{nl}}{X_{nn}}\right)^2 + \left(\frac{t_{nt}}{X_{nn}}\right)^2} \quad (1.27)$$

For both cohesive elements and cohesive surfaces, the stiffness of the cohesive zone is a numerical and not a physical parameter. In order to maintain physical soundness, the stiffness has to be high enough not to influence the global laminate stiffness significantly. On the other side, too-high stiffness values would negatively affect the stable time increment of the simulation. For the derivation of a quantitative value for  $K$ , Turon [90] suggests the formula given in Equation (1.28). The reciprocal  $\frac{1}{\alpha}$  defines the ratio of the additional compliance introduced into the laminate by the cohesive zone. According to Turon, this value shall be 2% at the maximum.

$$K = \alpha \frac{E_{33}}{T_{ply}} \quad (1.28)$$

A cohesive zone prescribes the plane of possible crack development. For many cases of crack prediction, this would be a severe disadvantage, but delamination modeling is a predestined application. The interface is a known vulnerability in a laminate.

The required mesh density for cohesive zones does not depend on the minimal energy absorption, like the limits derived from the CDM. Instead, the cohesive zone length has to be significantly larger than the element length. This is the crack zone between the point of damage initiation and the point of full damage. In this zone, at least three elements are recommended to describe the crack-propagation behavior plausibly [90]. The cohesive zone length differs individually for each crack opening mode and depends on the critical energy release rate and the maximum allowable tractions. [91]

$$l_{cz} = ME \frac{G_c}{X_i^2} \quad (1.29)$$



According to Turon,  $M$  is a parameter that depends on the specific cohesive zone model. Turon lists several methods for its determination, resulting in values between 0.21 and 1.0.

To achieve a larger cohesive zone and thus a larger permitted element length, the strength parameter  $X_i$  is artificially decreased [90, 91]. The interface strengths  $X_i$  become purely numerical parameters, which are artificially reduced. During an impact, normal tensile stress in the out-of-plane direction is very low, and consequently a decrease of  $X_n$  is considered insignificant for the damage initiation. Either way, this method can result in physically implausible delamination damage close to the support of the specimen.

As shear stress initiates delamination, a similar adaption for Mode II is ineligible. Even though a plausible delamination damage result could still be achieved, the delamination threshold force of the impact event would not be met anymore.

### 1.5.5 Continuum damage mechanics in a finite element model

The basics of the CDM model were already explained in Section 1.4. Its application in the FEM requires some additional steps which this subsection briefly introduces.

#### Maximum element length

The approach in Equation (1.15) on page 14 relates the critical ERR of a failure mode to the constitutive law of the material degradation path. This equation works with a volume-specific energy release rate  $g_c$  with the unit  $[\frac{mJ}{mm^3}]$ . In contrast to that, the critical ERR as a material parameter is specific for the created crack surface, and the unit has to be area-specific  $[\frac{mJ}{mm^2}]$ . This requires normalization by a length value. A unit length would be the easiest possibility, but this would result in a severe deficiency of Equation (1.11) in the application on a finite element – a mesh dependency. A constant volume-specific value  $g_c$  makes the damage-induced energy dissipation dependent on the volume of the damaging finite element. In fact, the energy dissipation should depend on the element cross-section that represents the fracture plane.

The mesh dependency can be solved by normalization with the characteristic element length normal to the fracture plane [66]. In Equation (1.30)  $l_c$  represents this characteristic length. It is a function of the element dimensions, the failure mode, and the fracture angle. The normalization of the ultimate failure strain with the corresponding length value  $l_c$  is necessary to achieve mesh-independent energy absorption.

$$\varepsilon_u = \frac{2G_c}{l_c \sigma_i} \quad (1.30)$$

However, there is a mesh-dependent minimum energy absorption  $g_{min}$  defined by the elastic energy stored in an element when failure initiates. This appertains to the first half-triangle in the bilinear law, illustrated in Figure 1.9. The value is expressed in Equation (1.31). The ratio of critical ERR and minimal specific energy absorption results in the maximum allowable characteristic element length in equation (1.32). For practical application in an explicit simulation, an additional factor around 0.9 is recommended to prevent abrupt degradation and thus to ensure numerical stability. The mesh has to fulfill this requirement for each considered damage mode.

$$\frac{\sigma_i \varepsilon_i}{2} = \frac{\sigma_i^2}{2E} = g_{min} \quad (1.31)$$

$$\frac{G_c}{g_{min}} = \frac{2EG_c}{\sigma_i^2} = l_{max} \quad (1.32)$$

### Maximum degradation in the post-failure region

In theory, the damage parameters  $d_i$  range from zero (undamaged) to 1 (fully damaged). However, the upper limit of 1 is practically unsuitable. From the numerical point of view, a stiffness of zero results in a singular stiffness matrix. Deletion of the respective finite elements would solve this issue. However, this deletion causes other problems. Fully developed inter-fiber damage can occur with all fibers remaining intact. Deletion of the corresponding element would affect all directions and be physically inaccurate.

There are also physical reasons why a complete stiffness loss will not occur under compression or shear load. When compression damage occurs, the created crack does not open. The compression deformation pushes the damaged material together. In a laminate, this material cannot entirely move away or vanish. Residual stress will always remain. Some authors capture this stiffness by a stress plateau in the post-failure region [60].

## 1.6 Impact on composite structures <sup>2</sup>

Before the actual introduction to impact analysis methods, a further examination of the impact phenomenon itself is required. The technical term *Impact* actually describes a phenomenon that can emerge in very different ways. An important parameter for the impact characterization is the ratio of the impactor mass  $m_i$  and structural mass  $m_s$ . It determines which effects dominate the impact response. Olsson proposes distinguishing three different categories [92], as illustrated in Figure 1.12:

- In a *ballistic impact* with  $m_i \ll m_s$ , dilatational waves dominate the dynamic response.
- A *low-mass impact*  $m_i \approx m_s$  has a wide-band dynamic response in which many flexural eigenmodes of the structure participate.
- A *large-mass impact* with  $m_i \gg m_s$  results in a quasistatic structural response consisting of the impact system's fundamental flexural mode.

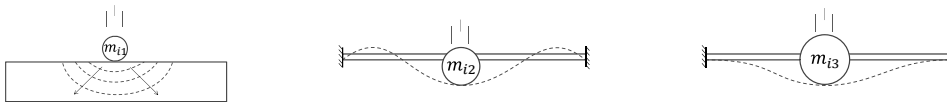


FIGURE 1.12: Categories of impact according to Olsson: ballistic impact, low-mass impact, and large-mass impact ( $m_{i1} < m_{i2} < m_{i3}$ ).

Thus, the impactor mass  $m_i$  characterizes the structural dynamic response. However, this parameter by itself does not drive the resulting impact damage. Both the impactor's velocity  $v_i$  and its mass  $m_i$  determine this damage. Figure 1.13 illustrates the relationship of impactor mass, impactor velocity, and damage. While a large-mass impact with high velocity causes destructive damage, its impact with low

<sup>2</sup>Parts of this section have been published by the author in [RB2].

velocity results in local damage to the laminate. The design-relevant BVID (compare with Section 1.3.3) belongs to this category. On the other side, low-mass impact with low-velocity causes negligible damage. The low-mass impact becomes interesting only in combination with a high impactor velocity. Even though this kind of damage was found to be “more detrimental to the integrity of a composite structure” [93], this damage is typically visible and not classified as BVID.

From this awareness, we derive the target domain of this work: large-mass impact with low velocity. This domain is commonly referred to as *low-velocity impact* – a definition that appears ambiguous, as it includes low-mass and large-mass impacts, which behave differently according to the above-mentioned categories specified by Olsson. The negligible small damage of low-mass impact with low velocity solves this ambiguity: it is not a common region of interest. In common sense, the term *low-velocity impact* refers to a large-mass impact with low velocity.<sup>3</sup>

Consequently, in the further course of this work, the term *low-velocity impact* refers to *large-mass impact with low velocity*.

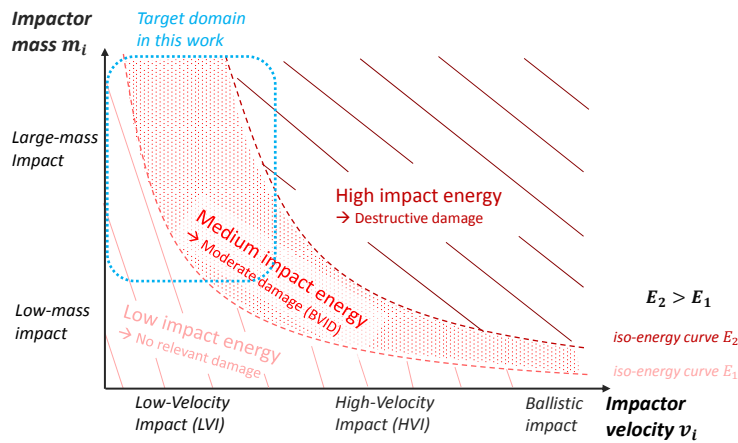


FIGURE 1.13: Characterization of impact scenarios through the impactor mass and velocity. The graph illustrates the target regions of interest (BVID) and validity (blue) of the models developed in the present work.

### 1.6.1 Overview of impact analysis methods

For reliable impact analysis, at least three basic physical principles must be understood: the vibration behavior of structures, the indentation of an object to a structure, and the damage of FRPs. The analysis of these principles is accompanied by analytical challenges in capturing these principles by mathematical equations – equations for which either closed-form solutions or approximate numerical solutions have to be found.

The approaches to impact analysis can be classified by their abstraction scale. The overview in Figure 1.14 comprises the most relevant classes of impact models. Simple analytic models describe an impact setup through springs and masses or a

<sup>3</sup>In contrast, the ambiguity of the terminology *large-mass impact* cannot be resolved. It may mean a large mass combined with low velocity or high velocity. The former is BVID-relevant, while the latter causes massive structural damage and must be analyzed in the context of crash analysis.

beam. Low-fidelity models on the macro-scale capture the structure on the laminate level. High-fidelity models require a resolution on the ply level of a laminate, leading to meso-scale approaches. Micro-mechanical modeling, distinguishing the constituent parts fiber and matrix as separate phases, represents the most detailed level. The increase of predictive capabilities came with a significant increase of the computational effort. Usually, the models aim at the prediction of the occurring damage, its onset, and its extent.

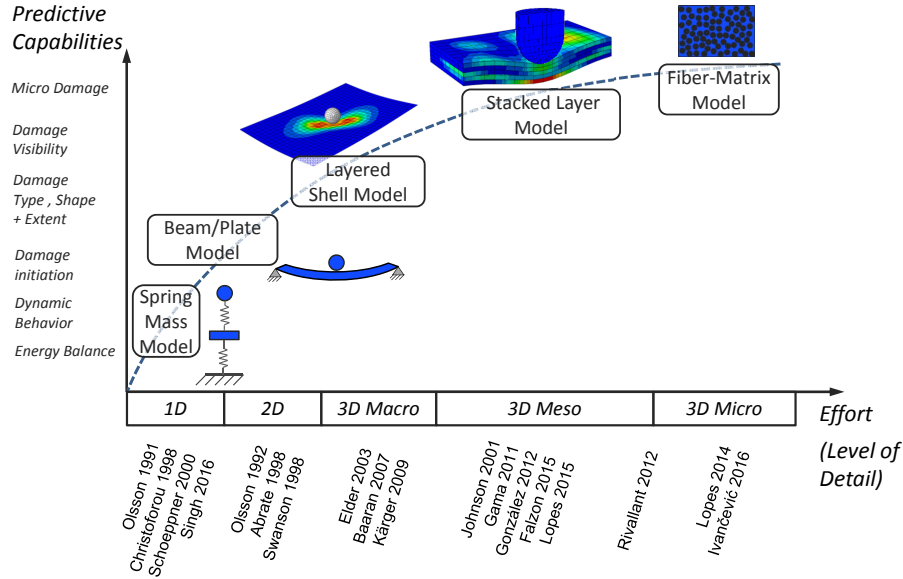


FIGURE 1.14: Overview of impact analysis methods on different abstraction scales.

Early analytical methods treat an impact system as a multi-body system in which springs connect one or more masses. Abrate published the first of such spring-mass models in 1991 [94], and later Christoforou [95] and others followed. These models capture an elastic impact response, taking into account the plate deformation of the structure and the local surface indentation. Based on a spring-mass model, Christoforou even developed a semi-analytical approach for analyzing impact by dimensionless constants, the so-called loss factor theory [96]. It allows achieving kinematic similarity of size-scaled impact scenarios. These analytical methods permit an estimation of impact duration, maximum contact force, and impactor displacement. Furthermore, Olsson developed an advanced spring-mass model [92, 97] that captures damage by a spring in series with the bending deformation. Singh and Mahajan [98] recently enhanced this idea through damage consideration in each deformation mode.

Static indentation problems of objects were first analyzed by Heinrich Hertz in the 19th century [99]. He developed an analytical contact law that is still important today, for analytical models or quick assessments of surface deformation by contact. Taking dynamic effects into account, Stepan Timoshenko provided the first solution for dynamic indentation of a beam, based on his famous static beam theory [19]. Incorporating the third dimension, Karl Karas investigated in his work from 1939 lateral shock to plates [100]. His work builds on both Hertz's contact law and Timoshenko's dynamic beam theory.

A plate approach comprises more eigenfrequencies of the impact system. Dobyns' development on the dynamics of orthotropic plates [101] forms the basis of these approaches. He provides an analytical description for "simply-supported orthotropic plates subjected to static and dynamic loading conditions". This description is founded upon pre-existing plate equations and an approximate dynamic solution by a series approach. All mentioned scientific works form historic landmarks for the analysis of impact on FRP. Although state-of-the-art methods go far beyond these historic developments, the knowledge provided in those works is still relevant today, especially to analytic solutions.

Building on the work of Dobyns, Olsson derived in 1992 the first impact model [102], based on Kirchhoff's plate equation. In addition, Swanson proposed an improved plate approach in 2005 [103] that is also valid for composite laminates [103]. Such plate models capture the undamaged dynamic behavior with higher accuracy than spring-mass approximations. The inclusion of material-specific nonlinearities, as proposed by Najafi in 2016 [104], even extends this capability.

Both spring-mass and plate models can be combined with an empirical or analytical prediction of damage threshold loads (DTL). Analytical estimations of the damage initiation and extent build on such DTL. For instance, Olsson, Schoeppner, and Abrate have proposed respective methods [92, 97, 105]. Damage threshold loads are usually derived using fracture mechanics, to predict the contact force that makes a delamination grow. To predict the damage extent, Jackson and Poe [106] proposed a force-based approach that calculates the largest delamination diameter.

Beyond the possibilities of analytical description, impact analysis can be conducted by the FEM in many variations. These variations are categorized in macro-, meso-, and micro-models, depending on the laminate's abstraction scale of the finite elements. Layered-shell approaches belong to the macro scale. As proposed by Elder et al. in 2003 [107], such models capture the kinematics of impact like a plate model. However, they permit the evaluation of failure conditions on the ply level and the corresponding stiffness degradation. Elder's model uses explicit simulations in LS-DYNA implementation; Baaran [108, 109] and Kärger [110, 70] have even developed a stand-alone-tool for impact analysis (CODAC<sup>4</sup>). By implicit time integration, combined FE analysis, and analytical equations, an efficient impact analysis was achieved.

An upgraded macro-scale model that even included a stacking of sublaminates was published by Johnson et al. in 2001 [111]. This stacking permits the authors to use an interface model between the plies. Johnson applies an interface model from Allix and Ladeveze [89] to capture delamination damage. This method still provides the basis for state-of-the-art meso-scale models. Considering the limited computational power compared to today's possibilities, Johnson reported reasonable results.

The increase of computational power permitted the application of Johnson's idea on the meso-scale: each ply is modeled with at least one layer of elements. The plies are equipped with a damage model based on CDM, and the CZM according to Allix [89] is used at the interface. A vast variety of meso-scale methods has been published – the interface model, the ply model, element types and meshing approaches are essential characteristics in which recent models differ. As a meso-scale model can work with any homogenized failure condition [32, 33].

In 2001, Borg et al. also published a cohesive element delamination model for composite laminates [112]. Based on this model, the research group presented a complete meso-scale model for impact analysis in 2004 [113]. In this model, an approach for determining the propagation direction of delamination was included. Published

---

<sup>4</sup>Composite Damage Tolerance Analysis Code, [www.dlr.de/FA](http://www.dlr.de/FA)

by Loikkanen et al., another meso-scale model followed in 2008 [114]. They applied the cohesive surface method in their impact analysis model.

Both Loikkanen and Borg report good delamination predictions. Borg additionally identified the necessity of improved ply-damage models. A correspondingly improved model was presented by Bouvet in 2010 [115] and by Gama in 2011 [63]. Later, several adapted configurations were developed by, for example, Ilyas in 2010 [116], Shi in 2014 [117], Gonzalez in 2012 [65] and Tan in 2015 [60]. Recent publications mainly provide incremental improvements, proposing better failure conditions [62], the inclusion of nonlinearities, the permanent deformation [60, 118, 64, 119] or the damage evolution [60, RB1] are proposed. Panettieri also identified additional relevant influence factors like the vibration behavior of the impactor [120]. Furthermore, Ehrich applied the meso-scale method for the analysis of impact on preloaded specimens [121].

Good results can be achieved with these methods, even though the computation effort is high and numerical difficulties have been reported. Recent improvements possibly provide a better solution accuracy, but they increase the computational effort rather than reducing it. Usually, user-defined material models are necessary for the CDM damage models. Especially if permanent indentation or nonlinear shear behavior is included, onboard materials of commercial FE codes do not provide the required features. Gama implemented a suitable material model for LS-Dyna and published it under the name Mat162 [69].

While normal meso-scale approaches capture intra-ply damage through CDM, Bouvet and Rivallant developed an alternative solution [115, 82, 122]. The mesh aligns with the fiber direction, and fiber-parallel cohesive zones are put inside each ply. In contrast to CDM, cracks are captured as real singularities in the ply. The corresponding failure mode is called *ply splitting* [115] and is a type of IFF. The simulation results of Bouvet show excellent agreement with experimental results on different laminates of unidirectional plies.

Furthermore, other variants to build a meso-scale model without CDM were tried. Nian [123] and Chen [124] considered the extended finite element method (XFEM) suitable for analyzing lamina damage, but Chen also mentioned difficulties with explicit time integration and the required computation effort. Other advanced methods like phase field theory [125], peridynamics [126], or discrete elements [127, 124] still do not provide the required maturity.

On the next level of detail, the prediction of IFF is conducted by a micro-mechanical model. Such a model needs to be coupled with a reference volume element (RVE) in a multiscale approach. The matrix damage is predicted on the micro-scale. Particularly for multiaxial loading, such a prediction is superior to homogenized models. Micromechanical failure criteria such as those proposed by Huang [128] or energy-based matrix failure conditions [129] can be used. The Mises yield criterion [29] for isotropic material is also a proper failure condition. It was applied in early works about micro-mechanical failure analysis [130] and is still applied in recent works [131]. Lopes et al. published the first impact model on this abstraction scale in 2014 [132]; later Ivančević et al. [133] and Liao et al. [134] proposed related approaches.

In summary, the present high fidelity models are able to capture impact damage with high accuracy, but these methods are numerically costly and partly require parameters that are not physically motivated. Simulation on the coupon level requires at least 100 central processing unit (CPU) hours [60, 61]. To achieve reductions of the physical testing effort, numerical methods should be reliable and sufficiently fast on the structural level. Efficient methods with the right balance between accuracy and computation effort have to be provided to make numerical impact analysis interesting for design applications.

### 1.6.2 Existing reviews

Many researchers already have conducted reviews about impact analysis methods. The compendium “Impact on Composite Structures” by Abrate [16] represents a review of the entire spectrum of analytical methods. The capabilities and the deficiencies of various spring-mass and plate models are analyzed and evaluated in this work. The first broadly based review was conducted by Elder et al. in 2004 [135]. Linear elastic fracture mechanics, macro-scale shell-models, and the damage threshold loads were tested. Among these, damage threshold evaluation lead to surprisingly good results, but the test cases were still far from possible impact use cases. For efficient aircraft design application, a need for further development and improved accuracy was recognized.

Reviews have also been published about recent high-fidelity models. A comparison of the predictive capabilities with different failure criteria was conducted by Liu et al. [62]. Their model is based on a stacked-solid approach with cohesive elements. According to their results, the Puck criterion leads to the most reliable results. Force history, energy dissipation, and damage initiation forces were plausibly predicted. Other criteria also lead to proper results. In consequence, it is appropriate to trade off between accuracy and computation effort for particular applications.

In 2015, Lopes et al. conducted another benchmark about impact simulation methods [64]. Four different meso-scale modeling strategies with varying mesh structures and cohesive zone models were presented and compared. Aligned meshing improved the prediction of the intralaminar failure and the delamination. Cohesive surfaces permitted the inclusion of the friction behavior of two delaminated plies and also lead to improvements in the overall results. Also, the work of Trouset 2014 work [136] provides a broad overview of the available impact analysis methods on different abstraction scales, according to Figure 1.14.

In addition to that, Jousset published a comparison of two different possibilities to employ a constitutive law in a cohesive zone [137]. A standard bilinear traction separation law was compared to a pressure-dependent elasto-plastic damage-model. An elastoplastic model had better behavior if the interface material showed significant plastic yield. May’s evaluation of cohesive laws [138] included strain-rate effects. He provided an overview of the required enhancements and identified strain rate effects as crucial only beyond LVI and quasistatic events. Abisset et al. proved in their work the equivalence of damage morphology between quasistatic indentation and LVI [139]. On the numerical side, the influence of cohesive parameters on the impact response was analyzed by Panettieri et al. [140].

The state-of-the-art modeling approach with a meso-scale model is also used beyond the analysis of LVI [60, 64, 141, 62]. Corresponding models for high-velocity impact were proposed by Pernas-Sanchez et al. [142] or by Heimbs et al. [143]. A comparable approach is also applied for crushing analysis [144] and for general damage modeling in composite structures [145].

### 1.6.3 Impact analysis on the structural level

Sufficiently accurate modeling strategies are available; the current challenge is the application of impact analysis on the structural level. While the predictive capabilities seem satisfactory, the corresponding computation effort is already very high for small coupon specimens. For coupon simulations of CAI impacts, Tan reports a computation time of 19 h on 32 CPUs [60], with Lopes even reporting 48 h on 40 CPUs, as a very fine mesh was applied. These numbers show that a blunt transfer of the same method

to the structural level would result in an inefficiently high computation effort. For some methods, also the modeling effort can also severely increase.

An excellent example for a structural application of a high-fidelity impact analysis was published by Schwab and Pettermann in 2016 [146]. The definition of a damage-prone area permits them to work with differently meshed zones. Riccio proposes in several publications a comparable approach [147, 148]. He also applies a local analysis approach with a damage-prone area and uses it at the coupon level in order to reduce the computational costs. Both Riccio and Schwab achieve good results with this local impact damage analysis. Additionally, Riccio presented the application of a meso-scale model on a substructural level [149]. Johnson works directly with a cut-out section of the actual structure [150]. Low-fidelity methods with a layered-shell mesh can directly be applied on the structural level as the number of DoF is significantly lower [110].



“Successful engineering is all about understanding how things break or fail.”

Henry Petroski, civil engineer and author (\*1942)

# 2

## The Numerical Prediction of Low-Velocity Impact Damage

### Scope of this chapter

In this chapter, I want to set up a physically sound impact-damage simulation. On the basis of the available of analysis methods introduced in Chapter 1, a particular impact analysis approach is selected through a trade-off. The selection process leads to a model on the meso-scale using the explicit FEM. The implemented model captures all laminate damage modes relevant to the impact analysis, in order to address the first research hypothesis from Section 1.2. The model is examined for its capabilities and deficiencies. Accordingly, I derive the required improvements.

The major improvement in this work is the degradation model for oblique fracture planes. A tensorial-based degradation approach provides the basis for this model. The damage result shows good agreement with experimental results and provides a better understanding of damage formation under impact load. Finally, the applicability and the required effort to analyze structural-level impact are examined.

(The developed tensorial-based degradation is not a necessary basis for the analytical method in Chapter 3. Parts of this chapter have been published by the author in [RB1] and [RB2].)

### 2.1 General considerations

When we consider all possibly relevant circumstances, several aspects of the impactor and the impacted structure determine how the impact damage emerges [22]. The generic Equation (2.1) summarizes the relevant aspects that affect the impact damage *DMG*.

These aspects are the impact energy  $E_i$ , the impactor properties *IMP* (size and shape), and the boundary conditions *BC*, including the deformation behavior of the surrounding structure around the impact region. All these provide a significant contribution to the dynamic impact response and the damage. Additionally, the material parameters *MAT* of the unidirectional plies and their interfaces are crucial to assess the deformation and intra-ply damage modes. Finally, the stacking sequence of the

layup  $LAY$  significantly determines the damage behavior of the laminate. A simulation model that is sensitive to each of these parameters is required to predict impact damage adequately.

$$DMG = DMG(E_i, IMP, BC, MAT, LAY) \quad (2.1)$$

## 2.2 Model building

### 2.2.1 System boundary of an impact setup

The system boundary determines where the zone of the numerical analysis ends. Force or displacement constraints describe the behavior of the further environment. An arbitrary system boundary with arbitrary boundary conditions suits a generic test case. However, the system boundary significantly determines how an impact use case or an experimental impact setup is transferred into a finite element model.

Several compression after impact (CAI) standards suggest an impact setup that is used for the most validation impacts in this work. The standards of the American Society for Testing and Materials (ASTM), Deutsches Institut für Normung (DIN; i.e., the German National Organization for Standardization), and Airbus Industries Test Method (AITM) [151, 152, 153] define this test in a similar manner. The Figure 2.1 shows a sketch of an example test equipment suggested by the Airbus standard AITM 1.0010. A  $150 \times 100 \text{ mm}^2$  specimen is centrally placed on a base plate with a  $125 \times 75 \text{ mm}^2$  window. Four rubber clamps hold the specimen in place. The impactor hits the clamped specimen centrally. The corresponding experiments are commonly conducted in a drop tower, as described in the Appendix A.1.

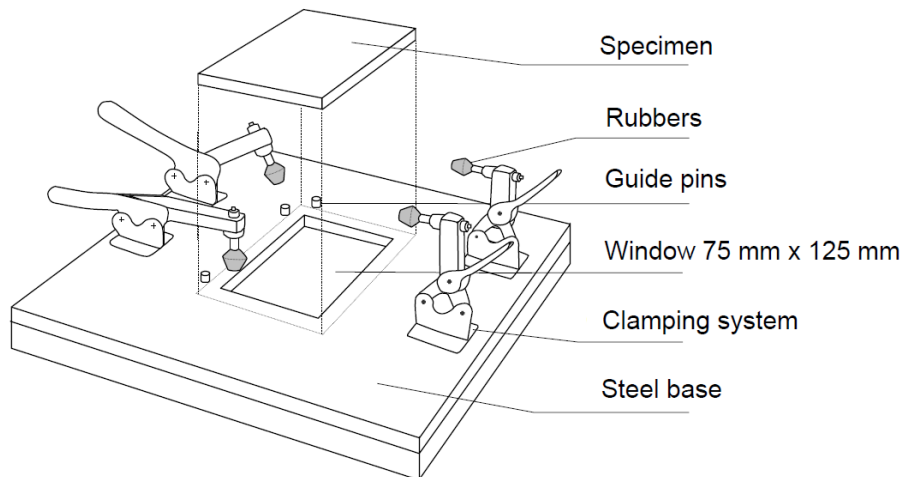


FIGURE 2.1: Impact test setup according to the CAI standard AITM 1.0010 [153].

Nearly all researchers who publish work about high-fidelity analysis methods explicitly model the test setup, including the support frame, the impactor, and the clamps [65, 122, 147, 62]. Panettieri et al. went even further and modeled the exact geometry of the impactor head and mass elements [120]. In that way, the vibration behavior of the impactor itself becomes part of the model. To assess the influence on the corresponding eigenmodes of the experiments conducted for this work, a modal analysis of the corresponding impactor is part of the Appendix A.1.

Contact phenomena drive the specimen support. For that reason, a simple replacement of the plate through clamped or simply supported boundary conditions is ineligible. Accordingly, a physically based finite element analysis requires a model of the impacted specimen and its real supporting conditions.

The rubber clamps apply an unknown preload to the specimen. This preload depends on the configuration of the impact setup and is hard to define precisely. However, it can be considered small in comparison to the load during the impact event and consequently not mandatory.

If a low-fidelity analysis method on the macro-scale model is applied, a contact model of the specimen and the base plate and the impactor can significantly increase the total computational effort of the model [RB2]. For that reason, it can make sense to accept reduced accuracy and avoid contact modeling. As low-fidelity models are generally less accurate, the accuracy decrease can be considered less severe. This makes the use of boundary conditions and analytical indentation models attractive, as suggested, for example, by Baaran and Kärger [109, 154, 70].

### 2.2.2 Abstraction scale of the laminate model

A finite element model can capture a composite laminate on various abstraction scales, as explained in Section 1.5.2. Its choice essentially influences the capabilities and the costs of an analysis model [RB2]. Consequently, the choice of the abstraction scale has to be well-considered.

As shown in the introduction, the development went from low-fidelity approaches on the macro-scale to advanced high-fidelity models on the meso-scale that can even be equipped with micro-scale failure analysis. As previously stated, a macro-scale model is usually a layered-shell approach, while meso- and micro-scale models are stacked-layer approaches. Therefore, the capabilities of a layered-shell and two stacked-layer approaches are analyzed in this section to form the basis for a trade-off decision on the way to a physically-sound impact analysis:

1. A *layered-shell* model with elements of the type S4R in Abaqus captures the whole laminate with a single element layer and one integration point for each ply.
2. A *stacked-shell* model includes each ply as an own layer of S4R shell elements. Tie constraints couple the adjacent surfaces of neighboring plies.
3. A *stacked-solid* model includes each ply as an own layer of C3D8R solid elements. Tie constraints couple the adjacent surfaces of neighboring plies.

All models have the same in-plane mesh density with a constant element length of 2 mm. Both element types S4R and C3D8R use reduced integration and tend to nonphysical deformation modes called *hourglassing* [79]. For their counterbalance the option *enhanced hourglass control* of Abaqus is employed. This method applies viscous and elastic forces to prevent artificial deformation. The thus-induced artificial energy has to remain small in comparison with the elastic energy in the model.

The evaluation of the available options requires their examination on a simple impact test case. Based on this case, we compare the analysis effort and the predictive capabilities. As stated above, such a numerical test setup can have an arbitrary configuration. For that purpose, a benchmark model according to Figure 2.2 has been set up with the following properties:

- a quadratic specimen with the outer dimensions  $100 \times 100 \text{ mm}^2$  and 4 mm thickness

- cross-ply laminate  $[0, 90, 0, 90]_s$  with  $t_{ply} = 0.5$  mm
- clamped boundary conditions on all four edges
- linear elastic material with the elastic properties provided for “Material 0” in the Appendix A.3
- spherical impactor with a nose diameter of 20 mm
- impact energy of 10 J at  $4 \frac{m}{s}$  impactor velocity

This test case differs in several points from a real impact configuration. The layup with very thick plies is especially generic. These thick plies facilitate the assessment of methods in this section. Fewer interfaces permit an easier assessment of the delaminations. To trigger all relevant laminate damage modes, the material properties in the test case differ from real properties. Mainly, the strengths and fracture toughness for FF are reduced.

In this test case (and all other models of this work), the  $x$ -direction of the global coordinates defines the  $0^\circ$  fiber orientation. An orientation of  $90^\circ$  stands for the corresponding  $y$ -direction. Furthermore, the commercial FEM software Abaqus is used for all models in this work.

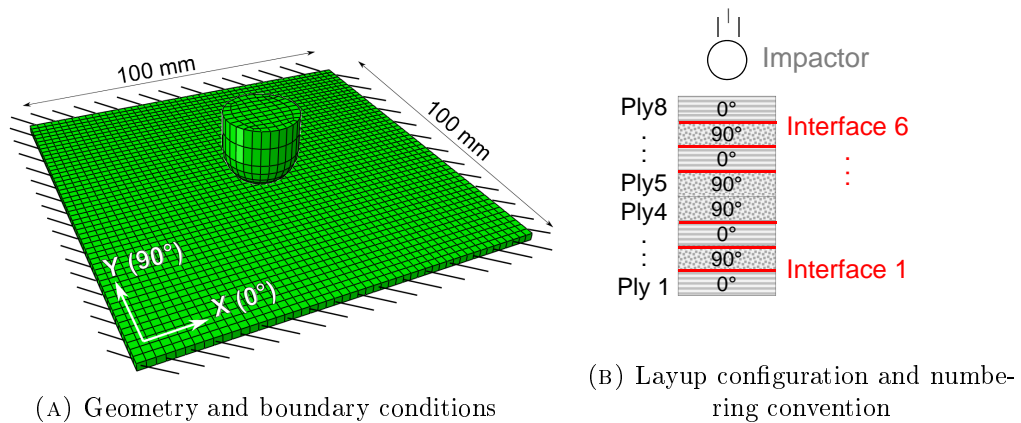


FIGURE 2.2: Test case for the assessment of methods and the trade-off analysis.

### Assessment of the elastic prediction

The basic requirement for a plausible damage prediction model is the capability to capture the elastic deformation under the impact load case. For examination of that capability, the test case was equipped with a linear elastic material.

Figure 2.3 shows the displacement plot of all three configurations at the time 0.8 ms. This time corresponds to a contact force between 10.4 kN and 10.6 kN. The contact force slightly varies between the models because of the slight differences in the predicted elastic response. As a reference, we consider the models’ static central deflection for a contact force of 10.6 kN. An implicit static analysis with a layered-shell model results in a central deflection of 2.035 mm.

The central deflection value of all three compared models hardly differs from the quasistatic solution, as the results in Figure 2.3 show. Moreover, all deflection results

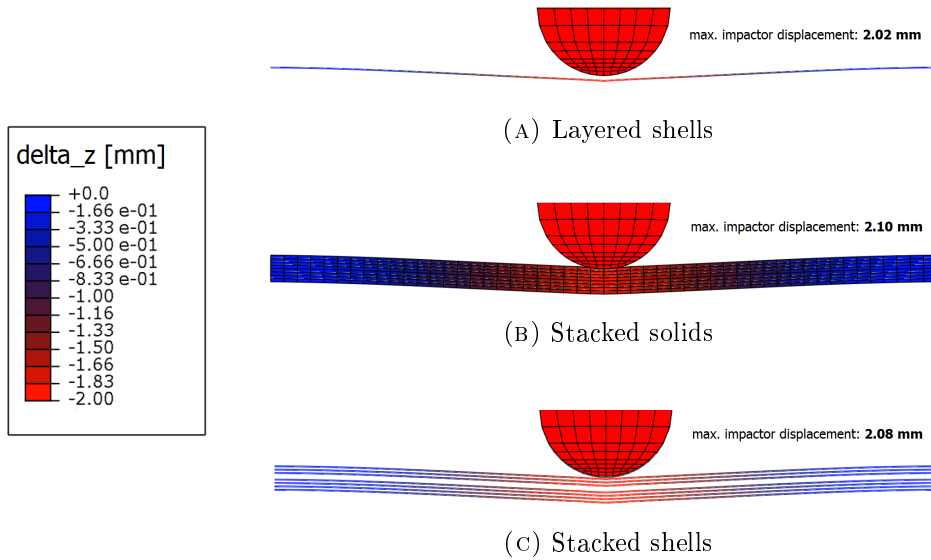


FIGURE 2.3: A central cross-section of three impact models shows the out-of-plane displacement  $\Delta z$  at  $t = 0.8$  ms.

are qualitatively equivalent. The deviation of the deformation value does not exceed 0.1 mm at any point of the specimen.

Qualitatively, the local surface indentation can be observed under the impact point of the stacked-solid model. The out-of-plane elasticity of the solid elements accordingly affects the deformation state, permitting a slightly larger indentation value. However, it hardly affects the global elastic response, as the force-displacement history in Figure 2.4 shows. The maximum contact force, the maximum impactor displacement, and the higher-order oscillation are nearly similar in the three elastic models. This similarity indicates the sufficiency of a simple macro-scale model to predict the transient elastic response of a structure under out-of-plane indentation.

### Assessment of the damage initiation prediction

The evaluation of failure criteria to predict the damage onset is conducted on the ply level of the composite laminate. As stated in Section 1.4, these criteria evaluate stresses or strains. Regarding the excellent agreement of the three models' elastic response, a satisfactory prediction of the stresses and strains can be expected for all tested methods. To prove that assumption, the stress distribution within the plies has to be checked to compare the stresses of all three elastic models. The static implicit solution provides maximum stresses for the laminate's top and its bottom according to Equation (2.2). To compare these values with the impact result, the elastic reference impact is evaluated at the time 0.8 ms and shown in Table 2.1.

$$\begin{aligned}
 \max(\sigma_{11-\text{ply}1}) &= 2260 \text{ MPa} \\
 \max(\sigma_{22-\text{ply}1}) &= 207 \text{ MPa} \\
 \min(\sigma_{11-\text{ply}8}) &= -1836 \text{ MPa} \\
 \min(\sigma_{22-\text{ply}8}) &= -176 \text{ MPa}
 \end{aligned} \tag{2.2}$$

Due to the bending effect under the out-of-plane load, the lowermost ply 1 sustains tensile load and the uppermost ply 8, compression load. The membrane deformation creates a field of tensile stress over all plies. The superposition of the bending and

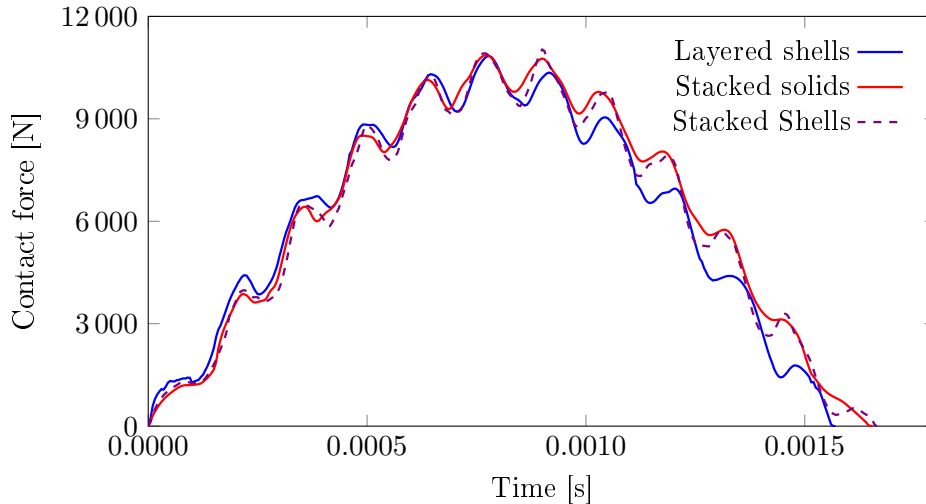


FIGURE 2.4: The force-displacement history of the elastic impact simulations with the three models on different abstraction scales.

the membrane deformation explains why the absolute values of the tensile stresses are higher than the absolute compression stresses.

Table 2.1 shows the plots of the in-plane stresses  $\sigma_{11}$  and  $\sigma_{22}$  for the lowermost and the uppermost ply in the test layup. These are average values for each ply; consequently, they are lower than the static reference stresses. Additionally, the failure index of a quadratic stress failure condition [Equation (1.2)] is presented for three selected plies.

The in-plane stresses of all three models are in good agreement. The deviations in ply 1 do not exceed 5%. The stress differs in the upper plies of the laminate only in the contact area with the impactor. Differences of up to 50% were found between the shell models and the stacked-solid approach. These differences are expectable, as the out-of-plane deformation of the solid elements also influences other stress components around the impact spot.

Nevertheless, the out-of-plane components are responsible for a significant difference between the models. The distribution of the failure index in the lowermost ply is similar for all three models. In-plane stresses dominate the state of stress in this ply. Out-of-plane stresses occur predominantly in the inner plies of the laminate [1]. The failure index in the plies 3 and 4 marks the mentioned effect on the damage occurrence. The stacked-solid model predicts a more extensive damage area, as it is the only one to consider the relevant out-of-plane stress component. In these inner plies, the shell models cannot provide an appropriate prediction.

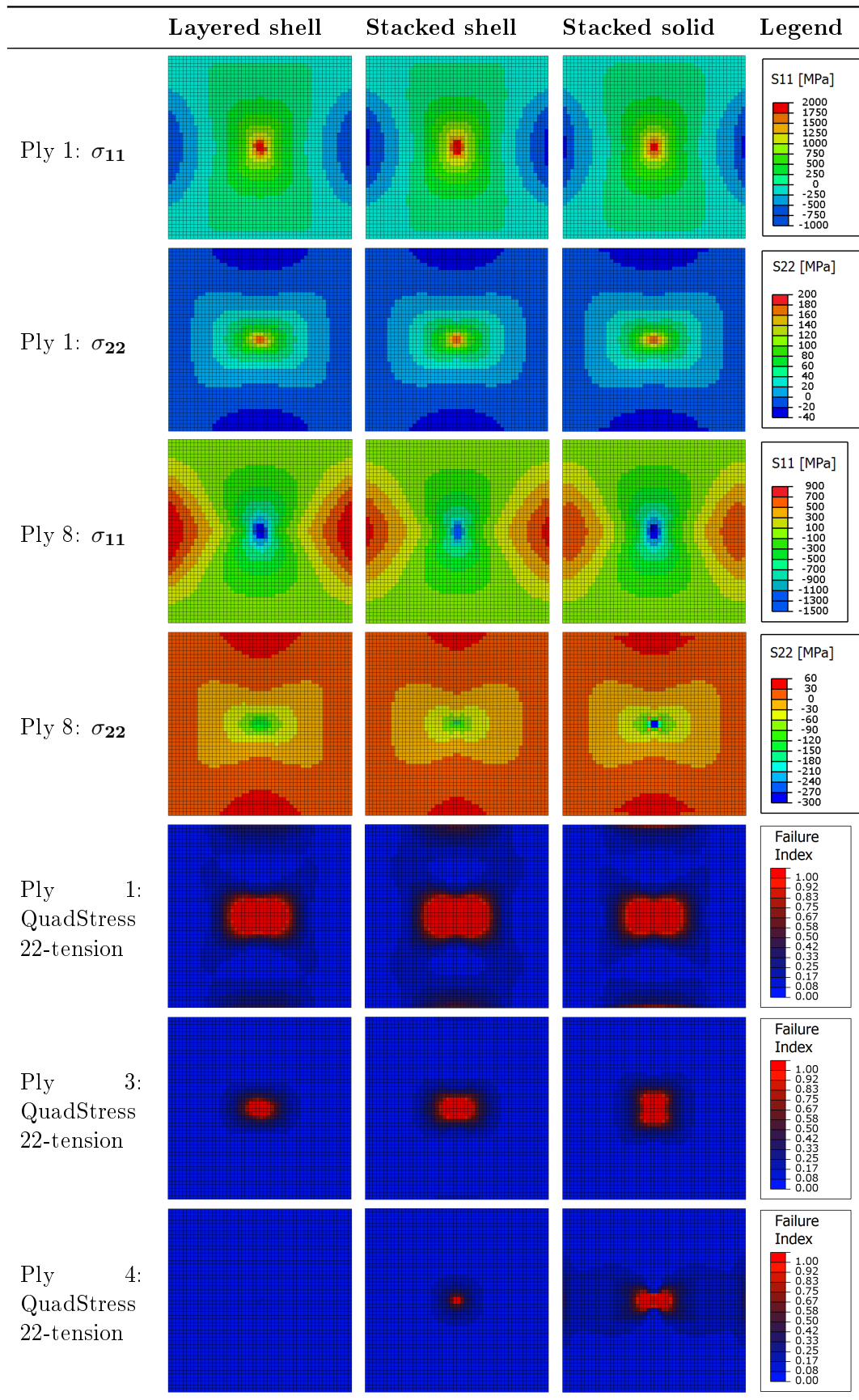


TABLE 2.1: Stress distribution and failure index for selected plies of the elastic impact test case at  $t = 0.8$  ms.

The out-of-plane stresses have to be part of a plausible damage prediction. Out-of-plane shear occurs under bending load. The ordinary shell elements do not capture the complete three-dimensional state of stress as it would be required for that purpose. Nonetheless, possibilities to resolve this deficiency exist. The extended two-dimensional method, as proposed by Rolfes and Rohwer [155, 156, 157] allows calculating transverse shear stresses based on the first-order shear deformation theory. Thus, the missing shear components could be considered for the evaluation of the failure criterion. As a result, a more plausible damage prediction in the inner plies of a laminate becomes possible with shell models.

Nevertheless, an extended shell model with the mentioned improvements would still neglect the out-of-plane compression stress  $\sigma_{33}$  in  $z$ -direction of the specimen. A significant contribution of this stress component can be expected in the laminate zone directly under the impactor. This stress can still not be considered in the failure condition. To estimate the influence of this component, an analytical estimation was conducted within this work. This estimation determines whether the stress  $\sigma_{33} = \sigma_{zz}$  can become relevant for the initiation of failure.

The principle of the analytical approximation is illustrated in the Figure 2.5. It is based on a plate under static indentation of an impactor. The composite plate is idealized with quasi-isotropic in-plane properties. The out-of-plane stiffness was chosen equal to the 22-stiffness of a unidirectional layer. An impactor of radius  $R_i$  indents the laminate with the force  $F_{impactor}$ . The static response of this setup is the subject of the analytical approximation.

A circular contact area between the impactor and the plate emerges [99]. The Hertzian contact law, according to Equations (2.3) and (2.4), provides the determination of the contact radius  $r_c$ . A circular section with this radius is cut free from the indented plate (center sketch in Figure 2.5).

$$r_c = \left( \frac{3FR_i}{4E_{hertz}} \right)^{\frac{1}{3}} \quad (2.3)$$

$$E_{hertz} = \left( \frac{1}{E_{33-impactor}} + \frac{1}{E_{33}} \right)^{-1} \quad (2.4)$$

The section force  $f_{radial-section}$  results from the equilibrium of forces with the contact force  $F_{impactor}$ .  $f_{section}$  is composed of a normal component  $n_{section}$  and a transverse component  $q_{section}$ . The decomposition of these components, according to Equations (2.5) and (2.6), requires the bending-angle  $w'$  at the radial location  $r_c$ . Taking into account the effective elastic properties, we can determine this angle analytically through the Kirchhoff theory of plates, which results in a value of  $0.7^\circ$  at a radial position of  $r_c$ .

$$\int_0^{2\pi} q_{section} d\theta = \cos(w') F_{impactor} \quad (2.5)$$

$$\int_0^{2\pi} n_{section} d\theta = \sin(w') F_{impactor} \quad (2.6)$$

The section force  $q_{section}$  corresponds to the integral of the shear stress  $\sigma_{rz}$  at the cutting edge. To evaluate this integral reversely, a distribution for this shear stress along the  $z$ -direction has to be assumed. For a plate under bending load, this distribution would be parabolic, with its maximum in the center of the laminate [8]. However, it is likely that the contact with the impactor still influences the out-of-plane



shear at the top of the laminate. The limiting case would be that the maximum occurs at the top of the laminate. This maximum leads to a half-parabolic distribution along the thickness. Both mentioned cases are considered in order to calculate an envelope of the stress distribution  $\sigma_{zz}(z)$ .

To calculate this stress distribution, the circular section is cut vertically, as shown on the right in Figure 2.5. In Equation (2.7) the equilibrium of  $z$ -forces is set up depending on the cutting position  $z$ .

$$\sigma_{zz}(z) = \frac{F_{\text{impactor}} - \int_0^{2\pi} \int_{t-z}^t \sigma_{rz}(z) dz d\theta}{\pi r_c^2} \quad (2.7)$$

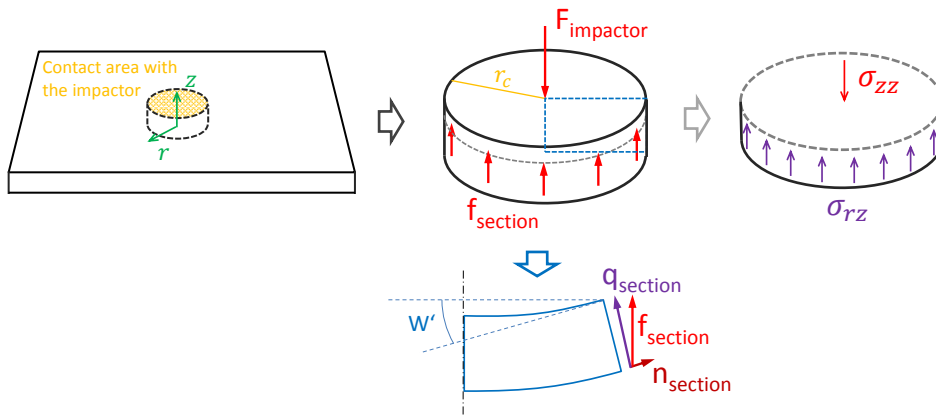


FIGURE 2.5: Sketch of the analytical derivation of out-of-plane stresses in a circular cross-section around the impact spot.

The distributions of  $\sigma_{zz}$  resulting from Equation (2.7) are plotted in Figure 2.6 for the two possible shear variants, the symmetric parabolic shear and the half-parabolic shear.

The results are compared to the numerical prediction based on the stacked-solid model. This comparison shows quantitatively and qualitatively a good agreement with the analytical estimations as the numerical prediction lies within the envelope of the two analytical variants. Qualitatively, the stress distribution based on the half-parabolic shear law is closer to the numerical prediction.

Based on the stress evaluation of the elastic impact models, we can assess the suitability of the three tested approaches for prediction of the damage onset. All models provide almost similar results for the in-plane stresses. These results indicate a good accuracy of the macro-scale model. However, out-of-plane stresses influence the damage initiation considerably in the contact zone with the impactor. Solid elements could improve the prediction of the damage initiation.

### Assessment of the damage propagation capabilities

For the analysis of impact damage, it is not sufficient to predict only its onset. A physically sound model has to capture the propagating damage during the whole impact event. Two factors drive this propagation: the damage evolution at a material level and the corresponding transfer of load after local degradation. The employed material law of degradation does not depend on the abstraction scale of the model. Therefore, it is not a selection criterion in the present trade-off. However, the capability to transfer load is crucial.

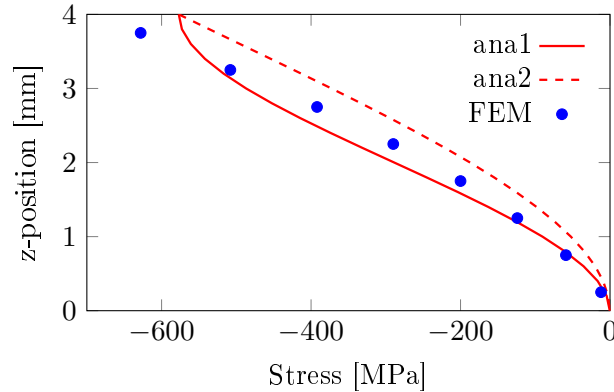


FIGURE 2.6: The stress distribution  $\sigma_{zz}$  over the laminate thickness predicted by the analytical models, with parabolic shear (ana1) and half-parabolic shear (ana2) and the numerical stacked-solid model (FEM).

To analyze the eligibility to predict damage propagation, we consider a generic test case of an eight-ply unidirectional laminate. Under tensile load in the fiber direction, the distribution of the stress and the strain along the thickness is analyzed with the layered-shell approach on the macro scale and the stacked-solid approach, which represents both meso-scale models in this trade-off. For the plot of stresses and strains in Figure 2.7, the distributions are normalized with the average stress along the laminate thickness and the average strain over the beam length, respectively.

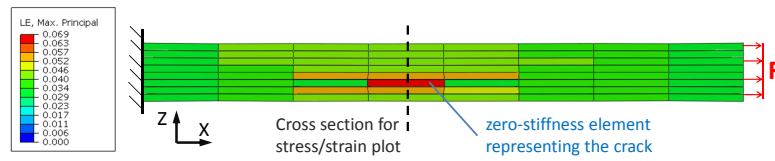
Figure 2.7A illustrates the test case and visualizes the strain distribution of the stacked-solid approach. A strain concentration at the crack and the adjacent plies is clearly visible. The diagram in Figure 2.7C shows the corresponding stress and strain over a cross-section at the crack location. The normalized stress and strain for each ply confirms a significant load transfer from the cracked layer to the adjacent plies. This load transfer encourages the propagation of damage to the concerned plies if there is a flaw in the laminate.

In contrast, the load transfer is insufficiently captured by the layered-shell model. The inclusion of a crack by setting the stiffness of the respective integration point to zero causes a stress and strain distribution as shown in Figure 2.7B. The DoF of the shell element link the strain for all plies. The stress is calculated depending on the individual stiffness of each ply. Consequently, the load transfer involves each ply comparably after one ply fails. No stress concentrations occur locally around the crack. This spread impedes both damage evolution and load transfer. Hence, the predicted propagation is not conservative. Underestimation of the stiffness degradation and the damage size is likely.

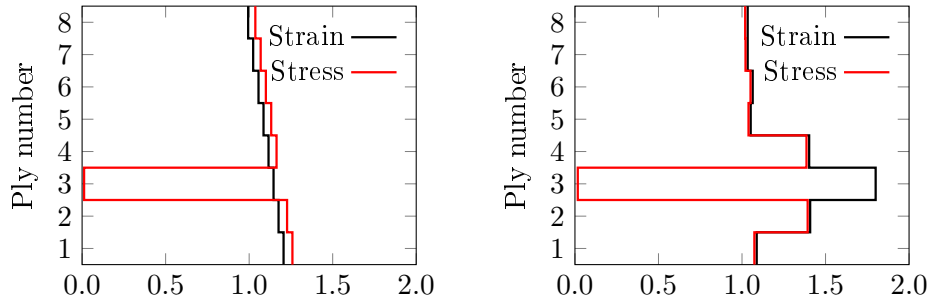
### Computation and modeling effort

The predictive capabilities of a layered-shell, a stacked-shell, and a stacked-solid approach were assessed in the previous three subsections. A brief consideration of the modeling and computation effort follows here.

In terms of the modeling effort, a layered-shell mesh is advantageous in comparison to a stacked-layer approach. A shell mesh on the laminate level requires only a mid-surface model of the structural geometry. The layup definition and the geometric modeling are uncoupled. In contrast to that, the stacked-layer approach describes the geometry on the ply level. Curvature, ply drop-off, and geometric particularities



(A) Layer-wise strain plot of a tension-loaded unidirectional laminate with a crack in the third ply (stacked-layer).



(B) Section plot of a layered-shell model (C) Section plot of a stacked-layer model

FIGURE 2.7: Load transfer behavior depending on the abstraction scale: layer-wise normalized stress and strain plots of a cross-section in a unidirectional laminate with a crack in ply three.

are difficulties to cope with. Therefore, layered shells are commonly preferred for the modeling of complex structures.

The computation costs for a numerical solution with each model depend essentially on several parameters of the FE model: the number of DoF the model has, the number of integration points, and the stable time increment. With regards to the laminate, the number of plies  $n_{plies}$  and the ply thickness  $T_{ply}$  drive these parameters.

Table 2.2 shows the normalized computation effort of the previously defined test case and its dependence on  $n_{plies}$  and  $T_{ply}$ . The layered-shell model is much faster than the stacked-shell or even the stacked-solid model. With an increasing number of layers  $n_{plies}$ , this difference increases because the number of DoF increases only in the stacked-layer models. With a decreasing ply thickness  $t_{ply}$ , the effect becomes more severe, too, as  $t_{ply}$  of solid elements affects the stable time increment according to the Courant Equation (1.25). For an impact analysis with a laminate consisting of thinner plies or more layers, the ratio of computation time can even increase to much higher values [RB2]. For example, a modified test case with a 4 mm configuration consisting of 22 plies of the material I or II (Appendix A.3) would multiply the computation effort of the stacked-solid model by a factor of 7.5. The effort of the layered-shell model would hardly be affected. The influence on the stacked-shell model is around factor three. However, a stacked-layer model always has to be combined with a damage-capturing interface model. This interface model also affects the stable time increment depending on the ply thickness  $t_{ply}$ ; therefore, the eventual effort of this model is larger than shown in Table 2.2.

	Layered shells	Stacked shells	Stacked solids
Normalized computation time	1	4.6	17.3
Laminate DoF	<i>const.</i>	$\sim n_{plies}$	$\sim n_{plies}$
Integration points	$\sim n_{plies}$	$\sim n_{plies}$	$\sim n_{plies}$
Stable time increment	<i>const.</i>	<i>const.</i>	$\sim t_{ply}^{-1}$

TABLE 2.2: Overview of the computational effort and its dependence on the number of plies  $n_{plies}$  and the ply thickness  $t_{ply}$  for each abstraction scale.

### Trade-off decision

Given consideration of the capabilities and the costs of each modeling strategy, Table 2.3 summarizes all addressed points. The first research hypothesis crucially demands an accurate prediction of the damage evolution behavior. Thus, the predictive capabilities are weighted higher than the required efforts. Consequently, a stacked-layer approach on the meso-scale abstraction is necessary to the specified needs. It plausibly captures damage in the plies and interfaces. Cracks can arise, open, and propagate. In addition, the formation of sublaminates is an important feature for the analysis of residual compression strength after the impact [158].

The proper prediction of damage initiation through three-dimensional failure conditions requires the model to capture the complete state of stress in the specimen. The out-of-plane components contribute significantly to the damage onset. This contribution is the strongest argument for the use of solid elements. Additionally, with regard to the surface indentation under the impactor, the meso-scale model with solid elements is superior to the shell model. For those reasons, I chose a *stacked-solid* approach as the baseline of this work.

	Layered shells	Stacked shells	Stacked solids
Modelling effort	++	–	–
Computation effort	+	–	--
Elasticity prediction	+	+	++
Damage initiation prediction	O	O	++
Damage evolution	--	++	++

TABLE 2.3: Summary of the trade-off between a layered-shell model, a stacked-shell model, and a stacked-solid model.

### 2.2.3 Impactor model and contact formulation

The indentation of the impactor into the laminate is a nonlinear process. A pure force or displacement boundary condition cannot capture it. Instead, either an analytical function or a contact formulation is required to include it in a numerical model.

The first mentioned option, an analytical model, is advantageous in terms of the computational effort but requires sophisticated integration into the FE model [109].

In addition, if the indentation model is elastic-based, it can hardly be adapted when surface damage occurs, and the contact behavior changes.

An FE contact model, in theory, provides these missing features. However, it increases the computational effort and is a possible source of instability to an explicit time integration. The additional computational effort has to be considered in relation to the total computational effort of the model. For the explicit layered-shell model, the contact formulation increases the computation effort by approximately 100%. This ratio can be even higher with implicit time integration [RB2]. In contrast to that, the computational effort of the stacked-solid model increases by only about 10%, as the contact's computational effort is less significant in comparison to the computational effort of the laminate model. This relationship makes the application of a contact model easy to justify for a high-fidelity analysis.

A contact model prevents the penetration of slave nodes into a predefined master surface through counteracting forces [79]. Instability can occur when those forces change irregularly. Usually, this change happens due to a master surface which is uneven or wobbly. The latter is likely to occur to the laminate surface under impact load. The ply elements are very thin in the thickness direction and relatively soft in two of three main directions, and their mass density is low. These properties can trigger uncontrolled vibration. Accordingly, the laminate surface must not be the master surface of the contact.

An impact analysis requires a pure master-slave contact formulation, where the impactor is considered the master surface, and the ply nodes represent the slave contact partner. This choice is very important for the stability of an impact simulation, as shown in Figure 2.8. Even the simple elastic model exhibits instabilities in the contact force if the contact model is inverted. The contact noise significantly disturbs the contact force history. This might cause a simulation to abort and makes the identification of damage-induced vibration difficult. The instabilities even persist if a double-sided contact model is applied. This contact formulation prevents the penetration of nodes from either contact partner into the other's surface.

One side effect of the pure master-slave contact shall be mentioned here. The impactor shape is convex. Accordingly, some impactor nodes will penetrate the element faces of the ply. However, if the impactor nodes were the slave partner, the penetration of the ply nodes into the impactor face would still be unlikely. Thus, the contact stiffness of the chosen contact formulation is less correct. The impactor appears a little undersized in the simulation result. However, the curves in Figure 2.8 show that the corresponding loss of stiffness is minimal, and the dynamic response of the elastic specimen remains similar. Therefore, I consider this effect negligible if the mesh is sufficiently fine. No further corrections are conducted.

#### 2.2.4 Interface model

The interface between two layers of different fiber orientations is a delamination-prone area. The corresponding damage-capturing interface model is a core element of a stacked-layer approach [89, 111]. The CZM is the current state of the art for such an interface model. In contrast to the fracture-mechanical standard method of virtual crack closure, the CZM, is capable of predicting damage onset and propagation, as stated in Section 1.5.4. The Equations (1.26) and (1.27) describe the constitutive behavior. Abaqus Explicit offers both variants. As the overview in Section 1.6.1 shows, both variants appear in the recent literature.

In this work, both variants were considered and assessed for their suitability. The stacked-solid model of the  $100 \times 100 \text{ mm}^2$  reference impact was equipped with each

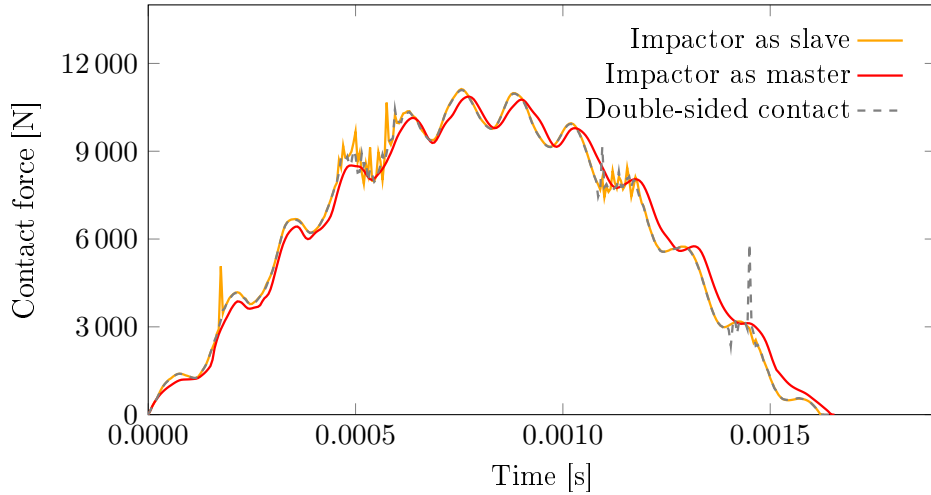


FIGURE 2.8: Force-displacement history of elastic impact simulations with three different contact formulations.

cohesive model. The Figure 2.9 shows the force history of the elastic stacked-solid model and its adaptations with cohesive elements and cohesive surfaces. According to the Equation (1.28), an interface stiffness of  $500\,000 \frac{\text{N}}{\text{mm}^3}$  was employed for both cohesive models. The constitutive thickness and the real thickness of the cohesive elements were selected equivalently to 0.01 mm. The strength and damage evolution properties of the cohesive zones are defined according to the generic data of “Material 0” from Appendix A.3.

During the initial phase of the impact, the force history of all three models is identical. This equality proves that the additional compliance by the cohesive interfaces hardly affects the impact response. After the damage initiation, the force history of the models with cohesive interfaces shows significant degradation. Cohesive elements and cohesive surfaces still behave similarly. Slight differences result from numerical effects like the finite thickness and the mass of cohesive elements. Additionally, the cohesive elements evaluate the traction-separation law at their integration points, while the cohesive surfaces evaluate the separation of the slave nodes.

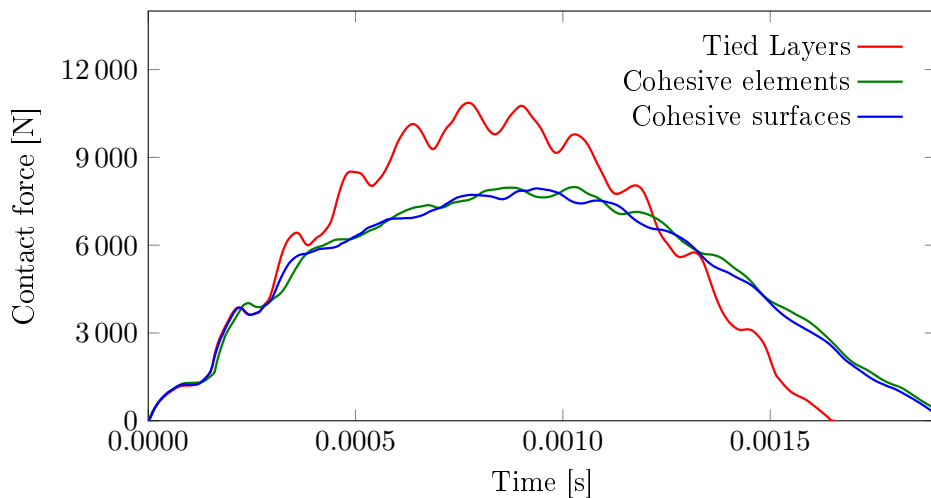


FIGURE 2.9: Force-displacement history of stacked-solid impact simulations with different cohesive zone methods.

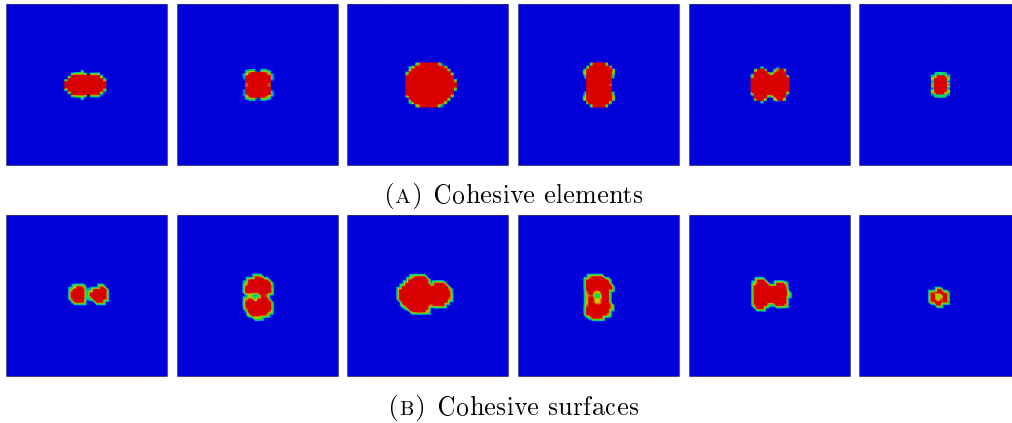


FIGURE 2.10: Predictions of the delamination results, beginning from the lowermost (left) interface to the uppermost (right).

As expected, both models with cohesive zones predict similar damage. Consequently, the required effort for modeling and computation is the driving factor for the selection. Concerning the modeling effort, cohesive surfaces are superior to cohesive elements. Cohesive elements require a geometrical thickness within the layup. This thickness makes the model building on the meso-scale more difficult. The geometrical thickness and the constitutive thickness are additional numerical parameters. Their influence might become relevant if inappropriately high or low values are chosen.

In comparison with the elastic model without cohesive zones, the computational effort of both models increases significantly. As Table 2.4 shows, the high number of DoF is a crucial reason for this increase. Additionally, the stable time increment of the simulation can decrease, depending on the elastic stiffness of the cohesive zone, as given in the Equation (1.28) on page 20. Cohesive elements also increase the number of integration points in the model; this increase is responsible for a higher computational effort for cohesive elements in direct comparison with cohesive surfaces.

Lopes et al. [132] describe an additional advantage of cohesive surfaces. The implemented contact formulation permits easily including friction between separated sublaminates. Through the consideration of static friction, they were able to obtain permanent indentation with such a model.

**Trade-off decision:** Due to the lower computational costs and the better modeling properties, I prefer the *cohesive surfaces* for the high-fidelity impact analysis in this thesis. Additionally, the consideration of post-failure friction is automatically included in the contact formulation and does not need to be considered separately for newly created crack surfaces. These circumstances make cohesive surfaces less complicated in their application and superior in their predictive capabilities.

	elastic	cohesive elements	cohesive surfaces
Normalized computation time	1	4.1	2.5
DoF	$(n_{plies} + 1) \times \frac{DoF_{ply}}{2}$	$n_{plies} \times DoF_{ply}$	$n_{plies} \times DoF_{ply}$
integration points	$I_{ply} \times n_{plies}$	$5I_{ply} \times n_{plies}$	$I_{ply} \times n_{plies}$

TABLE 2.4: Overview of the computational effort, degrees of freedom, and integration points for models with different cohesive zone methods.

Despite the mentioned advantages, a numerical issue impedes the application of cohesive surfaces in Abaqus Explicit. “An uneven master surface severely influences the damage behavior under compression load. Slave nodes that are close to a master element’s edge tend to separate immediately if compression load is applied. This results in large, physically unlikely delaminations. Stability problems of the simulation are probable. In consequence, coherent meshes in neighboring plies have to be avoided. We found two possible solutions to this issue. Firstly, the slave surface can be equipped with a denser mesh. However, this solution cannot be employed for laminates because each embedded ply is simultaneously master for its upper and slave for its lower ply. The second solution is an adaption of the mesh. In each second ply, the nodes were shifted by 0.2 mm in the in-plane directions” [RB2]. Even though both workarounds increase the modeling effort of cohesive surface models, the modeling effort is still smaller than for a cohesive element model.

In addition, cohesive surfaces cannot be combined with a double-sided contact model. Consequently, also the contact between neighboring plies requires a pure slave-master formulation. As a consequence, a known issue reoccurs here. The master-slave formulation of the impactor-laminate contact permits a slight indentation of the impactor into the laminate. For the same reason, the choice of the slave and the master influences the elastic stiffness of the numerical model: The laminate curvature under impact load can lead to severe penetrations of the plies if the inner contact partner forms the master surface as Figure 2.11 illustrates. In contrast, the master surface on the outer contact partner does not geometrically allow a penetration of the inner partner’s slave nodes.

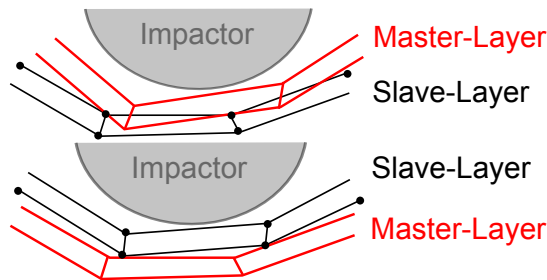


FIGURE 2.11: Penetration behavior of two adjacent plies depending on the master-slave choice of the contact partners.

### 2.2.5 Intra-ply damage model

Delamination usually dominates BVID. However, an interaction of the delamination with the intra-ply damage modes of the unidirectional plies is likely (compare to Section 1.3.2). For their consideration, an intra-ply failure model is employed according to the theory in Section 1.4. This model consists of the quadratic strain failure condition [Equation (1.2)] and a bilinear degradation law (Figure 1.9). Strength properties and critical ERR are adopted from the generic “Material 0” in Appendix A.3.

Figure 2.12 shows how intra-ply damage affects the force history. Analogously to the model considering only inter-ply damage, the elastic response in the initial phase remains unaffected. However, the damage initiates earlier, and the stiffness degradation is more significant, making the global response softer. The maximum contact force accordingly decreases, and the impact duration increases.

Additional *numerical difficulties* arise with the inclusion of an intra-ply damage model. As mentioned in Section 2.2.2, the elements with reduced integration (C3D8R)



are prone to hourglassing, which is a non-physical deformation. The hourglass control to counterbalance this deformation mode affects the energy balance in the model: artificial strain energy arises. This artificial strain energy is also part of the elastic impact model. Its value is below 4% of the total impact energy. An intra-ply damage model with a maximum degradation value of  $d_{i-max} = 0.999$  results in nearly 20%, which makes the simulation physically inconsistent.

Especially the compression in the 33 direction causes such unwanted behavior. Elements with full degradation  $d_{3-} = 0.999$  become heavily distorted and accumulate artificial energy. In the force history of Figure 2.12, this distortion causes the instability from the model  $d_i \rightarrow 0.999$ . For possible larger contact force or thinner plies, a simulation abort is likely.

The deletion of the respective elements from the model is a possible solution. Removing an element removes the stiffness components of all directions, however. Thus, it also affects the in-plane stiffness of a ply with out-of-plane damage. The key problem remains the element distortion resulting in instability.

For the mentioned reasons, degradation limits for the parameters  $d_i$  were introduced according to Equation (2.8). This limitation results in an hourglass energy of around 5%. The force response of the limited model also enables a significant gain of stability. Nevertheless, in Figure 2.12, two curves with different degradation limits also differ qualitatively. Thus, the numerically driven adaptation of the degradation limits is likely also to affect the damage result.

$$\begin{aligned}
 d_{1+} &\longrightarrow 0.999 \\
 d_{1-} &\longrightarrow 0.97 \\
 d_{2-}/d_{3-} &\longrightarrow 0.7 \\
 d_{shear} &\longrightarrow 0.99
 \end{aligned}
 \tag{2.8}$$

To understand how the intra-ply damage influences the impact damage behavior, we compare the damage behavior with a model that considers only inter-ply damage. To observe the damage initiation, the diagram in Figure 2.13 shows the energy history of the impact simulations. In particular, it shows the energy dissipation by damage. Firstly, we look at the dissipation by delamination, which is displayed in the value  $E_{dmg-interply}$ . Its course qualitatively differs between both models. The inclusion of intra-ply damage causes delamination to initiate earlier and reduces the delamination threshold force. This reduction indicates that intra-ply and inter-ply damage interact. The respective interactions were introduced in Section 1.3.2, and their occurrence is vital to a physically plausible impact simulation. In addition to the damage onset, the further development of the delamination energy differs between the two models.

Trivially, only the simulation that includes an intra-ply failure model can predict the energy absorption of the respective damage modes  $E_{dmg-intraply}$ . Small intra-ply damage initiates before the delamination onset. However, its final value is only around 40% of the energy absorbed by delamination.

Figure 2.14 shows the delamination results and the inter-fiber damage of the simulation that includes all damage modes. As FF did not occur, the corresponding result plots are not part of this figure.

Qualitatively, the delamination damage in Subfigure 2.14A differs only slightly from the results in Figure 2.10. The delamination in the lowermost interface is somewhat larger, and the delaminations in the middle of the laminate are smaller. Inter-fiber failure, as shown in Figure 2.14B, occurs in each ply in line with the fiber orientation. Due to the absence of FF, this result is plausible.

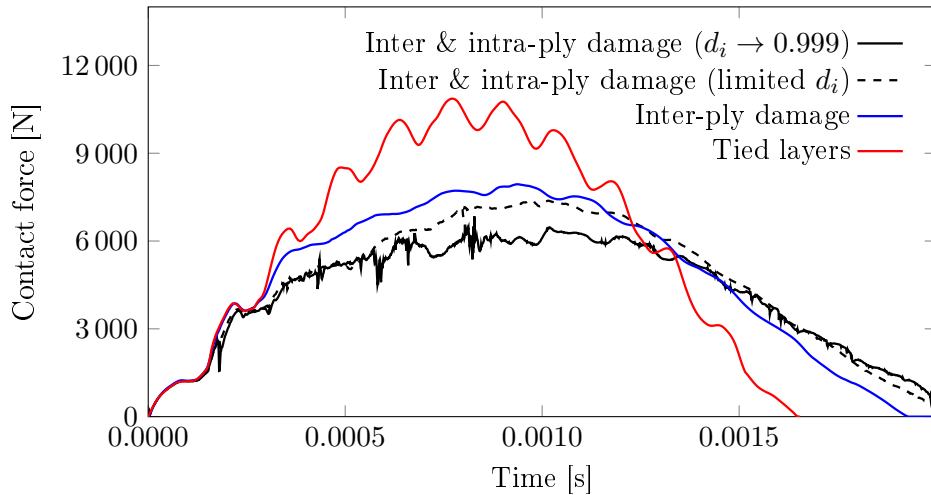


FIGURE 2.12: Force history of impact simulations with different activated damage modes.

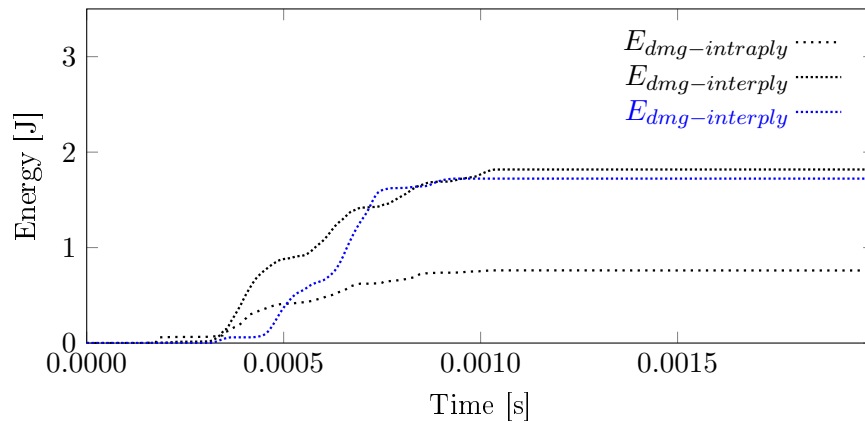


FIGURE 2.13: Damage energy dissipation history predicted with the model considering only delamination (blue) and the model taking into account intra-ply damage and delamination (black).

### 2.2.6 Analysis of the impact process

The model, as established so far, can now be applied to analyze the damage effects during an LVI. For this purpose the  $100 \times 100 \text{ mm}^2$  reference specimen is analyzed under a higher impact energy of 15.5 J. The energy increase shall cause FF, so all considered damage modes participate in the impact response. Figure 2.15 shows a combined plot of the resulting force history and the energy absorption of the damage modes. Figure 2.16 shows the corresponding damage predictions.

In comparison with the 10 J impact that was analyzed, the delaminations grew further. In the top ply, fibers fail under compression at a contact force of around 7000 N. At approximately 9000 N, tensile FF results in a sharp drop in the contact force.

The results of this coupon simulation provide information about the emerging damage during the impact event. Based on the corresponding damage thresholds, several phases of a low-velocity impact event can be identified. The phases differ in the predominant effects for the impact response and the damage propagation. We can analyze those effects with the help of the force history in Figure 2.15.

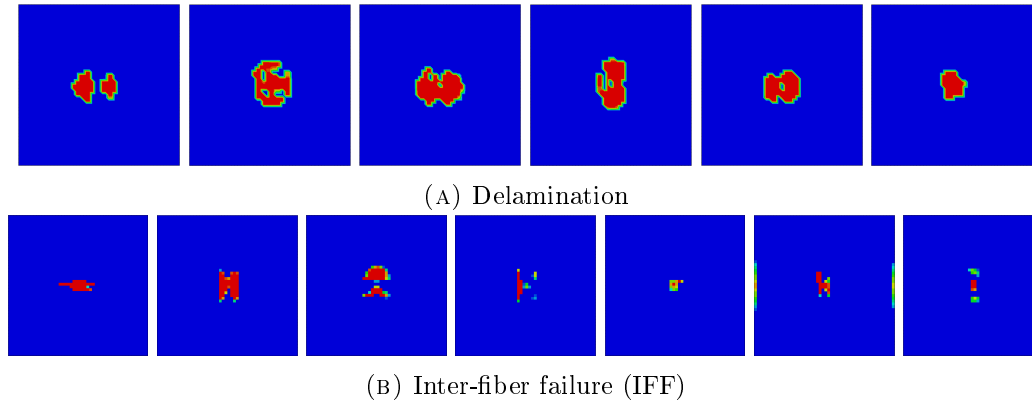


FIGURE 2.14: Predicted damage results of the numerical model with all damage modes.

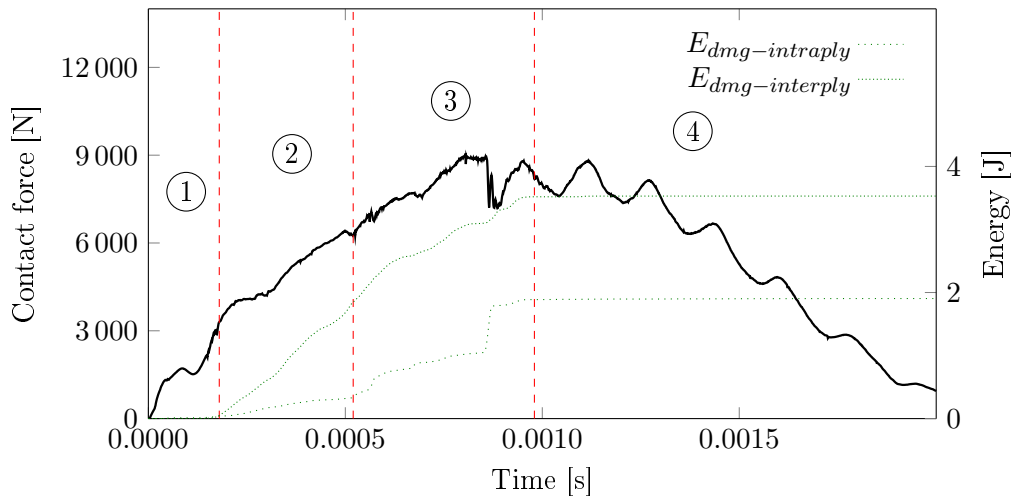


FIGURE 2.15: Phases of an impact illustrated in the force history (black) and the energy dissipation (green) of the reference impact simulation with increased impact energy (15.5 J).

1. The *initial phase* of the impact marks the region in which the impact response is driven by elastic deformation and effects of inertia in higher-order vibration modes. These can be observed in the oscillation of the force response. Damage hardly occurs and is limited to slight IFFs on the laminate surface.
2. The *delamination phase* of the impact begins with the delamination threshold. Delamination begins to propagate and quickly becomes the predominant damage mode, as the comparison of the energies  $E_{dmg-interply}$  and  $E_{dmg-intraply}$  shows. An impact scenario that reaches its maximum contact force in this phase mostly results in BVID. According to the FAA guidelines for composite aircraft [23], this is damage category 1 (of 5). Such damage has to be tolerated by the structure.
3. The *fiber damage phase* begins with the threshold force for FF on tension or on compression. When FF begins, a significantly larger amount of energy is dissipated by intra-laminar failure. This energy can even become larger than the energy absorption by delamination. It will result in FF becoming the predominant failure mode. An impact scenario that reaches its maximum contact force in this phase mostly results in visible impact damage (VID). According to the

FAA guidelines [23] this damage belongs to category 2 and has to be “reliably detected by scheduled inspections within specified intervals”.

4. The *relaxation phase* of the impact begins when the impactor indentation maximizes. This point can coincide with the point of maximum contact force or occur afterwards. This phase does not influence the damage size or shape. The energy balance proves that damage is already fully developed. However, the relaxation phase is essential if permanent deformation or the total energy absorption of an impact shall be predicted.

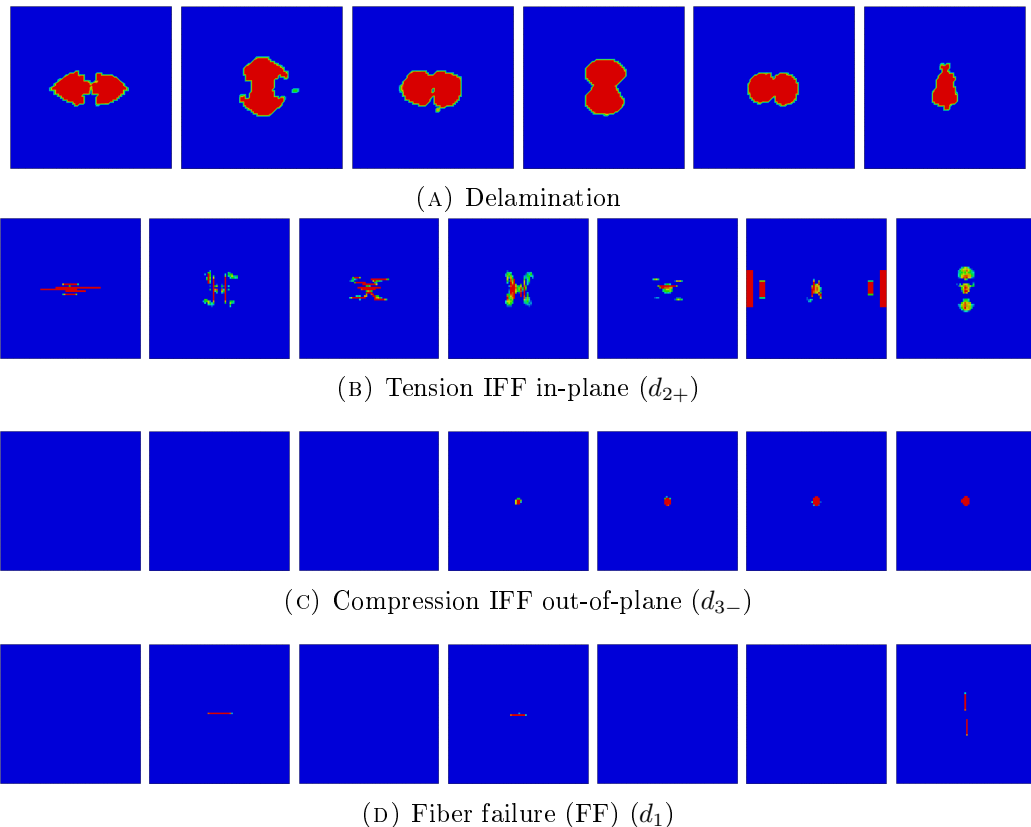


FIGURE 2.16: Predicted damage results of the numerical model with all damage modes.

### 2.2.7 Identification of required improvement

The selected numerical model is already eligible to compute the impact damage in composite laminates. So far, this model has no scientific novelty. However, the involved damage evolution works only in the three Cartesian planes of the material coordinates. Additionally, the stability of the explicit time integration remains a critical issue. Degradation of the out-of-plane compression stiffness was found to be the main cause of instability. The correction through a limitation of  $d_i$  affects the result.

On closer inspection, the compression damage model applies a severe idealization of the reality. Compression-caused matrix cracks in composite laminates commonly do not align normally to the load direction. Oblique fracture planes occur. The failure conditions of Puck [5], Camanho [7], or Catalanetti [48] take this effect into account. To establish a progressive damage model based on those criteria, a different damage

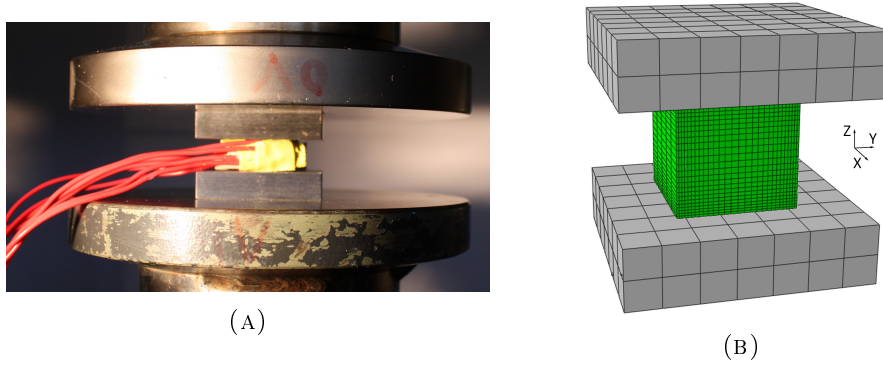


FIGURE 2.17: Experimental setup (A) and the corresponding FE model (B) of a compression cube specimen with a  $0^\circ$  unidirectional laminate.

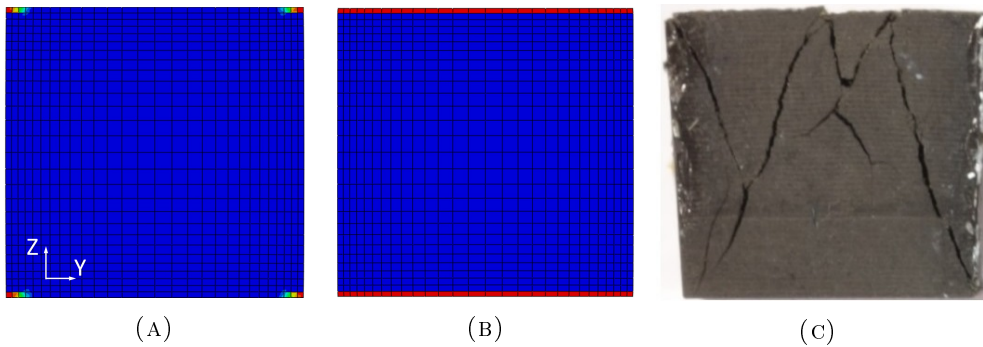


FIGURE 2.18: The predicted damage initiation (A) and the fully developed crack (B) of the compression specimen analyzed with a degradation mode in Cartesian planes in comparison with the experimental damage (C). The view is perpendicular to the fiber direction.

evolution approach has to be employed. It has to capture the degradation behavior of an obliquely cracked material element.

If the degradation is applied according to the principle of Matzenmiller, as explained in Section 1.4, a typical pattern of compression damage cannot be reproduced. To illustrate this deficiency, the damage result of a compression test with a cubical specimen is simulated (Figure 2.17). Such a test shall determine the out-of-plane properties of a composite laminate [159]. Two pressure disks compress a 10 mm cube of unidirectional material with an orientation of  $0^\circ$  (Material I in Appendix A.3). The prediction of the damage initiation and the fully developed crack are shown in Figures 2.18a and 2.18b in comparison with a test result.

Analogously to the experiment, the predicted damage initiates at the edges. The degradation of the out-of-plane stiffness in the corresponding elements transfers the load to the neighboring elements. Whether the damage criterion requires an oblique fracture plane or not; the fracture angle is unimportant to a degradation according to Equations (1.16) – (1.19). The variables  $d_i$  degrade the material either perpendicular or in line with the load direction. However, all those options result in a “flat crack” under compression load.

## 2.3 A tensorial-based progressive damage model

### 2.3.1 Material degradation in oblique fracture planes

A physically consistent approach for that case requires a more general description of  ${}_4\mathbf{C}^d$  than Matzenmiller's model provides. A fracture plane that is orientated obliquely to the describing coordinate system causes *coupling effects of shear modes and normal modes*. As stated in Section 1.4, Matzenmiller's stiffness matrix in Equations (1.16) – (1.19) contains a  $\mathbf{0}$  submatrix for shear-normal mode coupling. Consequently, the degraded stiffness matrix  ${}_4\mathbf{C}^d$  cannot be obtained through a reduction of existing entries with the factor  $(1 - d)$  from Equations (1.9) and (1.10).

The solution of Tan [60] and Liu [62] is better, as it considers some effects of an oblique fracture plane. However, the asymmetrical degradation of the stress tensor in the fracture plane has a disadvantage. The asymmetry affects the contribution of lateral strains  $\varepsilon_{11}$  and  $\varepsilon_{33}$  on the fracture plane's normal stress. The inverse influence of the fracture plane's normal strain  $\varepsilon_{22}$  on lateral stresses is not included in the degradation according to the Equations (1.21) – (1.23) on page 16. Nonphysical deformation behavior occurs. According to those equations, fully cracked elements still contract laterally. This effect can easily be shown with the stress history in a single element analysis under tensile load in Figure 2.19. Lateral contraction is omitted by the boundary conditions. This contraction leads to large lateral stress in the cracked element. This stress is physically non-existent.

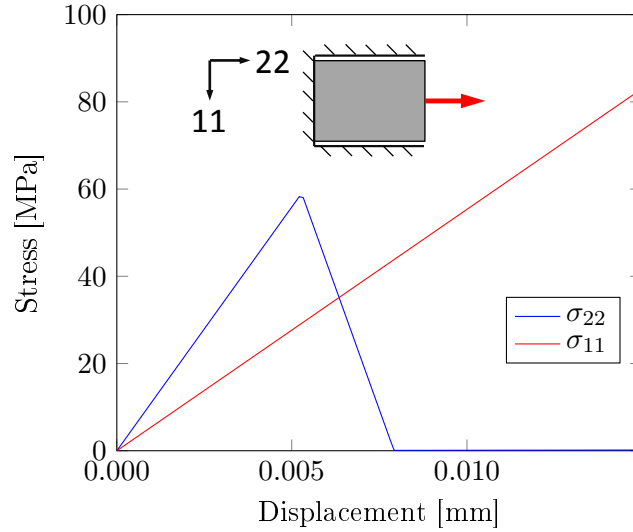


FIGURE 2.19: Force history of a single element under tensile load in 11-direction. After damage initiation, an asymmetrical material degradation is applied.

$$\mathbf{C}_{normal}^d = \frac{1}{\Delta} \begin{pmatrix} \frac{(1-\nu_{23}\nu_{32})}{E_{22}E_{33}} & \frac{(\nu_{21}+\nu_{23}\nu_{31})}{E_{22}E_{33}} & \frac{(\nu_{31}-\nu_{21}\nu_{32})}{E_{22}E_{33}} \\ \frac{(\nu_{21}+\nu_{23}\nu_{31})(1-d)}{E_{22}E_{33}} & \frac{(1-\nu_{13}\nu_{31})(1-d)}{E_{11}E_{33}} & \frac{(\nu_{32}-\nu_{31}\nu_{12})(1-d)}{E_{11}E_{33}} \\ \frac{(\nu_{31}-\nu_{21}\nu_{32})}{E_{22}E_{33}} & \frac{(\nu_{32}-\nu_{31}\nu_{12})}{E_{11}E_{33}} & \frac{(1-\nu_{12}\nu_{21})}{E_{11}E_{22}} \end{pmatrix} \quad (2.9)$$

The conducted demonstration example is valid for an orthogonal fracture plane in material coordinates. Non-symmetry occurs only for the modes of normal deformation. The shear modes are represented by a diagonal sub-matrix without coupling effects. In the fracture plane coordinate system, this representation changes. The asymmetry

also shows up in the previously mentioned shear coupling terms. It can easily result in a stability problem of an explicit simulation and convergence difficulties of implicit simulations. Both are critical disadvantages of asymmetrical material degradation. Tan and Liu's solution to this problem makes the degraded stiffness matrix of an oblique fracture plane symmetrical (compare to Section 1.4). Their approach involves some effects of an oblique fracture plane. However, the stiffness matrix  ${}_2\mathbf{C}^d$  still consists of only the original entries of the undamaged stiffness  ${}_2\mathbf{C}$ . New coupling effects between shear and normal deformation are still not part of the model.

### 2.3.2 Tensorial material degradation

To include the shear-normal coupling effects, the degraded stiffness tensor  ${}_4\mathbf{C}^d$  has to be derived in a more general manner. "A complete linear mapping of a rank  $n$  tensor requires a transformation tensor of rank  $2n$ . In consequence, a degradation tensor of eighth-order  ${}_8\mathbf{D}$  is required to map the undamaged fourth-order elasticity tensor  ${}_4\mathbf{C}$  to  ${}_4\mathbf{C}^d$  by Equation (2.10). This tensor has to provide both the degradation and the introduction of the newly created coupling effects.

$${}_4\mathbf{C}^d = {}_8\mathbf{D}{}_4\mathbf{C} \quad (2.10)$$

An oblique fracture plane, as shown in Figure 1.6, couples the normal deformations  $\varepsilon_{22}$  and  $\varepsilon_{33}$  with the shear mode 23. The belonging coupling entry  $C_{2223}$  exists neither in the undamaged elasticity tensor nor in the idealized variant of  ${}_4\mathbf{C}^d$ . It cannot be obtained by simple degradation of existing stiffness entries. Hence, the entry has to result from other stiffness components. Exactly this influence of any component in  ${}_4\mathbf{C}$  to any component in  ${}_4\mathbf{C}^d$  requires an eighth-order degradation tensor for its complete transformation to the degraded form.

To set up a suitable tensor, an approach by Kreikemeier is taken into account. He derived a second-order degradation tensor [160] based on the second-order identity tensor  $\mathbf{I}$  and on the direction of the largest principal stress. The degradation is defined by  $\tilde{\mathbf{D}} = (\mathbf{I} - \sqrt[4]{d}\mathbf{n} \otimes \mathbf{n})$ , where  $\mathbf{n}$  represents the direction of the maximum principal stress. The dyad of the second-order outer product  $\mathbf{n} \otimes \mathbf{n}$  subtracted from the identity tensor results in the degradation tensor. By the Rayleigh product of the degradation tensor and the stiffness tetrad  ${}_4\mathbf{C}$ , the stiffness  ${}_4\mathbf{C}^d$  is obtained. Regardless, this degradation is valid in the principle stress coordinates. Generally, this coordinate system is not equivalent to the fracture plane determined by the failure conditions of Puck or Camanho. Hence this degradation tensor still needs to be expanded to a more general form, taking into account a general state of stress.

For a degradation status of  $d = 0$  the degradation tensor must be able to map the stiffness tetrad to itself. Accordingly, Equation (2.11) remains a necessary condition for the degradation tensor.

$${}_8\mathbf{D}(d = 0) \stackrel{!}{=} {}_8\mathbf{I} \quad (2.11)$$

Thus, the eighth-order identity tensor defines the baseline of  ${}_8\mathbf{D}$  for the new degradation approach. The identity tensor  ${}_8\mathbf{I}$  is defined as follows:

$$I_{ijklmnop} = \delta_{im}\delta_{jn}\delta_{ko}\delta_{lp} \quad (2.12)$$

The expansion of Kreikemeier's approach to an eighth-order degradation tensor in the material coordinates requires an eighth-order dyad from the fracture plane normal vector  $\mathbf{n}$ .

$${}_8\tilde{\mathbf{D}} = ({}_8\mathbf{I} - d\mathbf{n}^{\otimes 8}) \quad (2.13)$$

Illustrated on an orthogonal fracture plane, this tensor's application in Equation (2.10) is equivalent to a degradation of the  $C_{2222}$  entry by  $(1-d)$ . The existence of this relation is correct, but it is only a single element of the complete tensor. The influence of other components on  $C_{2222}^d$  is also not yet included, nor is the inverse influence of  $C_{2222}$  to other components of  ${}_4\mathbf{C}^d$ . In addition to the  $N$ -direction that Kreikemeier used in his model, the tangential directions, in the fracture plane  $T$  and  $L$ , have to be considered for the outer product. In theory, there are  $3^8$  possible combinations of those vectors to form an outer product. Not all of those combinations require consideration in the subtraction from the identity tensor. Figure 2.20 shows how the degradation must affect the stress tensor and the influence of the strain tensor. A degradation shall be applied only if at least one basis vector of the corresponding entry is  $N$ . This principle can also be applied to the outer product of the vectors  $L$ ,  $N$  and  $T$ .

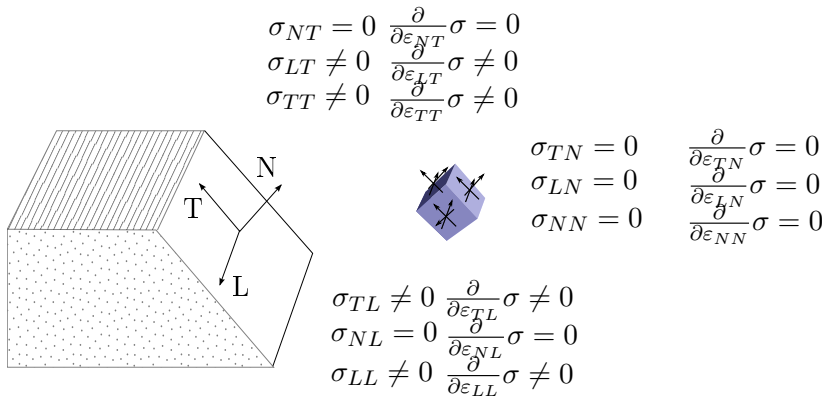


FIGURE 2.20: Overview of stress components and stress derivatives with respect to the strain of a fully developed material element with a crack.

To write the full tensor in one equation, the notation  $\mathbf{n}_1 = L$ ,  $\mathbf{n}_2 = N$  and  $\mathbf{n}_3 = T$  for the fracture plane base vectors is introduced. Those three directions are combined to eighth-order tensors in  $3^8$  outer products in Equation (2.14). The tensor  ${}_8\mathbf{\Omega}$  (2.14) is defined by a weighting factor representing the damage state in (2.15) and those outer products, providing the base system. The weighting factor's assembly follows a simple rule. Its entries are equal to the degradation parameter  $d$  if  $\mathbf{n}_2$  is part of the outer product. Otherwise, the value is zero. A nonzero weighting is applied only if the fracture plane's normal direction is represented by one of the eight vectors in the product. The multiplication of the outer products transforms the damage state in  $\mathbf{\Omega}$  to the fracture plane. With this condition the tensor  ${}_8\tilde{\mathbf{D}}$  can be set up by Equation (2.16). The execution of all eighth-order outer products in Equation (2.14) leads to an almost fully populated tensor  ${}_8\tilde{\mathbf{D}}$ .

$${}_8\mathbf{\Omega} = \Omega_{ijklmnop} \mathbf{n}_i \otimes \mathbf{n}_j \otimes \mathbf{n}_k \otimes \mathbf{n}_l \otimes \mathbf{n}_m \otimes \mathbf{n}_n \otimes \mathbf{n}_o \otimes \mathbf{n}_p \quad (2.14)$$

$$\Omega_{ijklmnop} = \min [d, d(\delta_{2i} + \delta_{2j} + \delta_{2k} + \delta_{2l} + \delta_{2m} + \delta_{2n} + \delta_{2o} + \delta_{2p})] \quad (2.15)$$



$${}_8\mathbf{D} = {}_8\mathbf{I} - {}_8\mathbf{\Omega} \quad (2.16)$$

While it requires a long process to obtain  ${}_8\mathbf{D}$ , the tensor itself can be simplified by using its three symmetry conditions [Equations (2.17) – (2.19)]. They result from the symmetry of the stiffness tetrad, accordingly, as a result of the symmetry in the stress and the strain tensor. These conditions reduce the number of independent components in  ${}_8\mathbf{D}$  from 6561 to 231.

$$D_{ijklmnop} = D_{mnopijkl} \quad (2.17)$$

$$D_{ijklmnop} = D_{klijmnop} = D_{ijklopnm} \quad (2.18)$$

$$D_{ijklmnop} = D_{jiklmnop} = D_{ijlkmnop} = D_{ijklnmop} = D_{ijklmnpo} \quad (2.19)$$

From the second and the third symmetry condition of  ${}_8\mathbf{D}$ , it directly follows that the degraded stiffness tensor is also symmetrical. In Equation (2.10),  $C_{ijkl}^d = D_{ijklmnop}C_{mnop}$  the first sub-symmetry in Equation (2.18) ensures the main symmetry of  ${}_4\mathbf{C}^d$ . The first two minor symmetries in Equation (2.19) result in the sub-symmetries of the stiffness tensor. Accordingly, the full linear mapping by an eighth-order tensor automatically keeps the symmetry of the stiffness tetrad. Appendix B.3 of this work includes a further outline of the symmetry properties of tensors.

The assembly of this eighth-order tensor for any fracture plane is a geometrical task. It depends only on the fracture angle  $\varphi$  and  $d$  from Equation (1.12) on page 13. The assembly through the proposed method is a long process for a general fracture plane. An implementation in a user subroutine of an FE code is possible, but the high number of operations in Equation (2.16) will seriously slow down the calculation. For development and demonstration, an implementation in SCILAB<sup>1</sup> was used. Best practice for visualization of the implemented degradation is a transcribed stiffness tetrad in Voigt notation.

### 2.3.3 Derivation of a simplified tensorial-based degradation

The damage tensor  ${}_8\mathbf{D}$  provides a general description of an arbitrarily cracked material element that depends only on the normal vector of the fracture plane and the damage evolution parameter  $d$  according to Equation (1.12). However, the evaluation of the product  ${}_8\mathbf{D}{}_4\mathbf{C}$  is numerically costly. The direct application of this equation in a numerical analysis would significantly slow down the computation. Accordingly, it makes sense to seek a simplification, considering not an arbitrary fracture but only fracture planes that occur with IFFs according to Puck [5]. Additionally, Cauvin and Testa have shown in their work from 1999 [161] that a degradation tensor of the eighth-order can be reduced to the fourth-order if the equivalent strain principle according to Chaboche [57] is applied. Even though the present work also uses the principle of Chaboche, Cauvin's reduction approach requires a set of several independent damage parameters. Therefore, its direct application to the material degradation based on a fracture angle and a scalar damage parameter  $d$  is not possible. However, the work of Cauvin indicates the possibility of further simplification of  ${}_8\mathbf{D}$ .

The direct derivation of  ${}_8\mathbf{D}$  is much easier if the fracture plane is orthogonal to the describing coordinate system. Therefore, a description in fracture plane coordinates is used to build the degradation tensor. In this case,  $L$ ,  $N$ , and  $T$  are unit vectors.

<sup>1</sup><http://www.scilab.org>

Each combination of them to an outer product leads to exactly one entry with the value 1 in the eighth-order tensor. The influence of the fracture angle is captured by a separate transformation of the stiffness tetrad to the fracture plane coordinate system. Rotation of a fourth-order tensor is performed by the Rayleigh product in Equation (2.21).

$$\mathbf{R} = \begin{pmatrix} 1 & 0 & 0 \\ 0 & \cos(\varphi) & \sin(\varphi) \\ 0 & -\sin(\varphi) & \cos(\varphi) \end{pmatrix} \quad (2.20)$$

$$C_{mnop}^r = R_{im}R_{jn}R_{ko}R_{lp}C_{ijkl} \quad (2.21)$$

After this transformation, the undamaged stiffness tensor is described by a system in which the fracture plane is normal to the 2-direction, now called  $N$  or  $n_2$ . In this system, setting up the degradation tensor becomes much easier. Figure 2.21 shows a sketch of the state of stress in a cracked material element. This state of stress sets the frame for the required degradation. The eighth-order degradation tensor represents a linear mapping, in which the influence of each component of  ${}_4\mathbf{C}$  on any component of  ${}_4\mathbf{C}^d$  can be taken into account. After the rotation, only components at the same position in both tensors can influence each other. Hence, in fracture plane coordinates, the  ${}_8\mathbf{O}^r$  is equal to  ${}_8\mathbf{\Omega}^r$ , as the outer product is equal to an identity transformation. Consequently,  ${}_8\mathbf{D}^r$  can be directly assembled based on the eighth-order identity tensor. Degradation has to be applied to any component that influences the strain or stress in the constitutive equation of the fracture plane. Therefore, the factor  $(1 - d)$  is applied to any Kronecker delta with index 2. No implicit summation is required in this definition, the Kronecker deltas define each component in  ${}_8\mathbf{D}^r$  by one combination of indexes.

$$D_{ijklmnop}^r = \delta_{im} (1 - d\delta_{2i}) \delta_{jn} (1 - d\delta_{2j}) \delta_{ko} (1 - d\delta_{2k}) \delta_{lp} (1 - d\delta_{2l}) \quad (2.22)$$

The tensor product of  ${}_8\mathbf{D}^r$  and  ${}_4\mathbf{C}^r$  gives the degraded stiffness tetrad  ${}_4\mathbf{C}^{dr}$  according to Equation (2.23).

$${}_4\mathbf{C}^{dr} = {}_8\mathbf{D}^r {}_4\mathbf{C}^r \quad (2.23)$$

$$\sigma = \underbrace{\mathbf{R}^T \mathbf{R}^T}_{{}_4\mathbf{C}^d} \underbrace{{}_8\mathbf{D}^r \underbrace{(\mathbf{R}\mathbf{R}{}_4\mathbf{C}^r\mathbf{R}^T\mathbf{R}^T)}_{{}_4\mathbf{C}^r}}_{{}_4\mathbf{C}^{dr}} \mathbf{R}\mathbf{R}] \varepsilon \quad (2.24)$$

In Equation (2.24), the full computation chain for the degraded stress is illustrated. The multiplication  ${}_4\mathbf{C}^{dr} = {}_8\mathbf{D}^r {}_4\mathbf{C}^r$  is computationally very expensive. However,  ${}_8\mathbf{D}^r$  is only filled with entries that exist in the identity tensor. Accordingly, a further simplification is possible. Only nonzero values of  ${}_8\mathbf{D}^r$  must participate in the multiplication of Equation (2.23). Thus, there are no coupling terms left in  ${}_8\mathbf{D}^r$ , and each entry of  ${}_4\mathbf{C}^{dr}$  can be derived directly from  ${}_4\mathbf{C}^r$ .

As mentioned before, the eighth-order degradation tensor  ${}_8\mathbf{D}^r$  is directly derived from the identity tensor in Equation (2.22). The degradation of existing stiffness entries works analogously to Matzenmiller's approach, presented in Equation (1.16). In

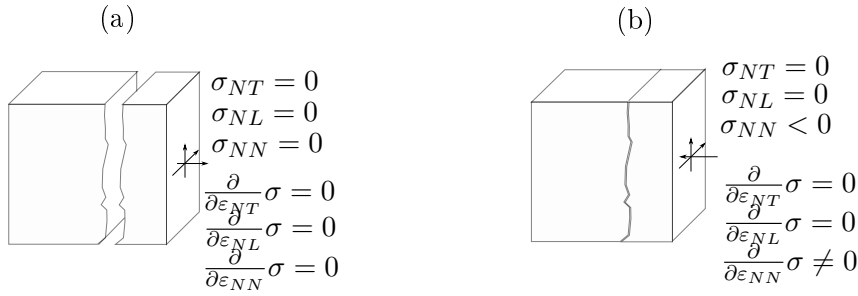


FIGURE 2.21: Existing stress components and derivatives of the stress with respect to the strain for an open crack (a) and a closed crack (b).

contrast to the original coordinate description, without shear-normal coupling terms, a fully populated matrix  ${}_4\mathbf{C}^r$  must be degraded now.

Following Figure 2.20, all stress components  $\sigma_{NN}$ ,  $\sigma_{NL}$  and  $\sigma_{NT}$  have to be degraded. In addition to that, the crack omits the influence of all strains in the fracture plane. Any stress component caused by the strain vector in the fracture plane needs to be degraded. Keeping the bilinear character of the damage evolution law, the factor  $(1-d)$  must be applied. However, this approach leads to the diagonal component being multiplied several times with this term. A power of  $\gamma$  occurs. A power of  $1/\gamma$  keeps the damage factor linear in Equation (2.26). Thus, the final degradation equation for an open crack is given in Equations (2.26) and (2.27).

$$C_{ijkl}^{dr} = [(1-d\delta_{fi})(1-d\delta_{fj})(1-d\delta_{fk})(1-d\delta_{fl})] C_{ijkl}^r \quad (2.25)$$

$$C_{ijkl}^{dr} = [(1-d\delta_{fi})(1-d\delta_{fj})(1-d\delta_{fk})(1-d\delta_{fl})]^{1/\gamma} C_{ijkl}^r \quad (2.26)$$

$$\gamma = \delta_{fi} + \delta_{fj} + \delta_{fk} + \delta_{fl} \quad (2.27)$$

In addition to this general degradation law, a difference between compression and tension in the fracture plane is required in a manner similar to Matzenmiller's in Equation (1.20). This relation does not directly fit the tensorial-based model because it works with a single damage evolution parameter for IFF. According to the Figure 2.21, the state of stress changes for open and closed cracks. The presented formula includes a degradation of the normal stresses. This is only valid for open cracks. If the crack is closed, compression can still be sustained. Based on Tan's model, where only shear stresses are degraded for compression load, Equation (2.28) serves as a branching condition for the degradation, to affect only shear components.

$$(1-d) = \begin{cases} 1 & \text{if } i = j \cup k = l \\ (1-d) & \text{if } i \neq j \cap k \neq l \end{cases} \quad (2.28)$$

## 2.4 Validation of the tensorial-based damage model

Two test cases are considered for the validation and the demonstration of the method's capability to describe cracks under compression and tension. The evaluation begins with the example of a minimal tensile specimen, as illustrated in Figure 2.22a. A displacement-controlled deformation is applied in the 2-direction of the material with free lateral contraction. The expected result is a sudden load drop in the force history and a localized crack band orthogonal to the loading direction. The force response

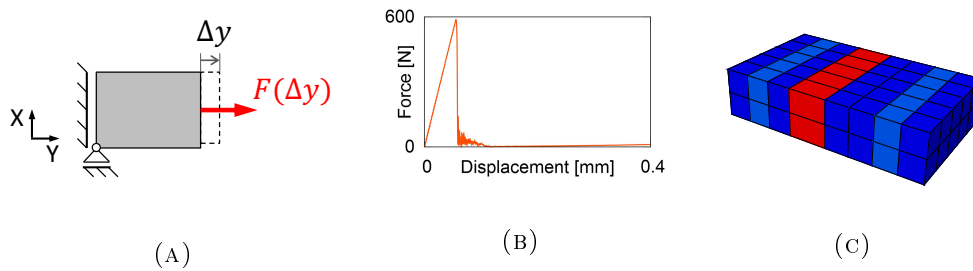


FIGURE 2.22: Sketch (A), force history (B), and damage (C) in a numerical minimal tensile test with the tensorial-based degradation.

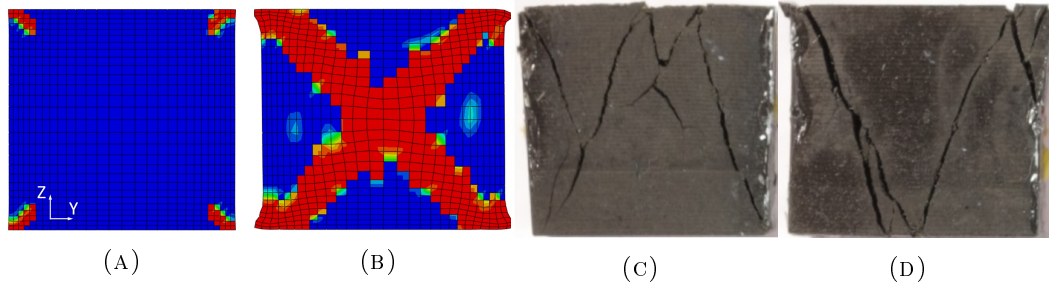


FIGURE 2.23: Application of the tensorial-based damage model for the prediction of the damage initiation (A) and the fully developed crack (B) under compression load in comparison with the experimental damage results (C) and (D).

in Figure 2.22b and the damage prediction in Figure 2.22c meet these expectations. Nevertheless, a degradation model in Cartesian fracture planes would also reproduce the results correctly. Consequently, this example suits only the demonstration of equivalence of the tensorial-based model and the previous damage model.

To show the gains of the tensorial-based model, an example with an oblique fracture plane and its effect on the post-failure deformation is necessary. The compression test on a cubical specimen, as illustrated in Section 2.2.7 (compare Figure 2.17), suits as such an example. The FE simulation is conducted with the new damage model.

Under compression, oblique fracture planes occur with a typical angle of  $53^\circ$  (compare to Section 1.4). The algorithm of Wiegand [39] and the failure condition of Puck [5] are employed to find this fracture plane.

As stated earlier, a coupling of normal and shear deformation forms the post-damage behavior. The result of the tensorial-based model for the cubical compression specimen is shown and compared to the experimental reference results in Figure 2.23. The damage criterion of Puck also predicts the damage onset at the edges of the cube (Figure 2.23a). In contrast to the Cartesian degradation, the crack propagates not orthogonally to the load direction but diagonally toward the center of the specimen (Figure 2.23b). The resulting crack pattern is a plausible prediction of the failure as it occurred in the experiment (Figures 2.23c and 2.23d). The deviation from the theoretical fracture angle results from the inhomogeneous state of stress caused by the hindered lateral expansion at the contact surfaces.

Despite the coupling effects of the oblique fracture plane, the solution is numerically stable, and a stability-driven limit of the degradation parameter  $d_{matrix}$  is not required. The limit value of 0.99 leaves only minimal residual stiffness.

With the presented tensorial-based method, the degradation can be performed in an arbitrary fracture plane that is parallel to the fiber direction 11. Nevertheless, a

more general approach for any fracture plane (in a different material) is possible by the same principle. This principle would require an appropriate transformation of the stiffness tensor into the coordinate system of the fracture plane. For example, this could be provided by three intrinsic or extrinsic Cardan rotations, as suggested by Davenport [162], or by quaternion rotation according to the development of Hamilton in 1844 [163]. The degradation of the stiffness tensor remains valid for any orthonormal transformation.

## 2.5 Validation of the impact model

### 2.5.1 Validation setup

The impact use case is the next-highest level of validation. This application to a real impact scenario additionally validates the capability of virtual impact testing with the high-fidelity model from Section 2.2. A set of five coupon experiments (CAI1.15, CAI1.30, CAI2.20, CAI2.40, B1) serves this validation purpose. All five cases are LVI scenarios with large impactor mass according to Figure 1.13 on page 23. Table 2.5 provides all relevant parameters for the impact cases, and Figure 2.24 shows the FE models of the test setups.

Briefly, three different laminates form the validation test series. Two of them are 4 mm CAI coupons. Both CAI configurations are tested on two different energy levels. The lower impact energy was chosen to trigger delamination but no significant FF. Thus, the impact scenario reaches its maximum contact force in the second phase according to the categorization in Section 2.2.6 shown in Figure 2.15. The second energy level was chosen higher to cause FF in addition to the delamination. Consequently, the third phase according to the conducted categorization, is reached. The last test case is a thin 2.2 mm laminate configuration. This thinner laminate configuration ensures that a pine tree pattern of delaminations occurs in the laminate [16]. Capturing this pattern, in particular, challenges an impact model as it requires a working interaction of intra-ply and inter-ply failure. In this case, the impact energy was chosen to reach the maximum damage size which is still classified as BVID. This level of damage is the maximum damage size that will probably remain undiscovered in a structure. The concerned structure still has to bear ultimate load, as shown in the DT diagram in Figure 1.3.

All specimens were made from unidirectional prepreg material. The specimens of configurations 1 and 3 consist of *Material I*; the specimen type 2 is made from *Material II* from the list in Appendix A.3, which provides the required set of material parameters for elasticity, strength, and damage evolution and mentions their origins. In-situ properties are applied for the strengths  $X_{22}$ ,  $X_{12}$ ,  $X_{13}$ , and  $X_{23}$  according to the method of Camanho et al. [164, 165].

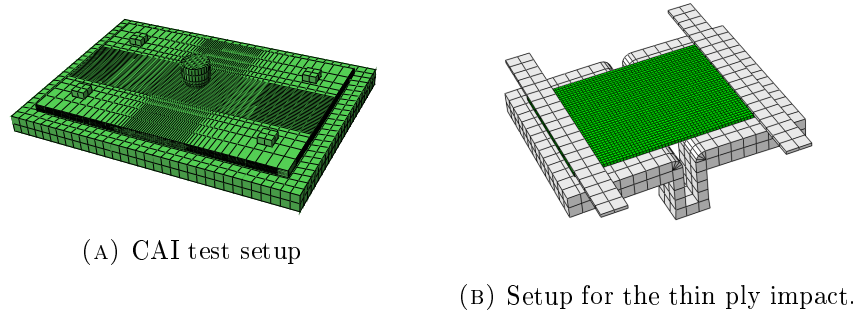


FIGURE 2.24: Virtual test setups for the validation of the high-fidelity impact analysis model.

Test case	CAI1.15, CAI1.30	CAI2.20, CAI2.40	B1
Type	CAI	CAI	thin coupon
Material	Material I	Material II	Material I
Layup type	quasi-isotropic	clustered	quasi-isotropic
Stacking sequence	[45,-45,0,90,45,-45,0,90,45,-45,0] <sub>s</sub>	[45,45,45,0,-45,-45,-45,90,-45,0,45] <sub>s</sub>	[45,-45,0,90,45,-45] <sub>s</sub>
Number of Plies	22	22	12
Delamination-prone interfaces	20	12	10
Nominal thickness	4 mm	4 mm	2.2 mm
In-plane geometry	150 × 100 mm <sup>2</sup>	150 × 100 mm <sup>2</sup>	160 × 110 mm <sup>2</sup>
Hole in support structure	125 × 75 mm <sup>2</sup>	125 × 75 mm <sup>2</sup>	125 × 75 mm <sup>2</sup>
Impact energies	A:15 J, B:30 J	A:20 J, B:40 J	25 J
Impactor nose diameter	16 mm	16 mm	20 mm
Impactor mass	3.95 kg	3.95 kg, 5.95 kg	3.99 kg

TABLE 2.5: Test parameters for the five validation experiments on three different laminates.

### 2.5.2 Validation results

To assess the quality of the numerical prediction, a direct comparison with the experimental results is presented in Table 2.6. The diagram in Figure 2.25 shows the force history curves. Finally, the Figures 2.26 and 2.27 show the delamination overlay plots and the fiber cracks in the top ply of each laminate.

All experimental data has to be seen in the context of the typical scatter of experimental impact damage [105, 166, 167]. The results table provides this context in the form of the standard deviation of the experimental results. Each diagram in Figure 2.25 includes the force history curves of at least three experiments. The plots of delamination and fiber cracks are also compared with three experimental results.

In addition to the known scatter, the measuring errors can occur in the record of the force history curves as described in Appendix A.1. Such errors can be observed for the configurations *CAI2.20* and *CAI2.40*, where the force measurement began with a delay, which causes a propagating error at the beginning of the test.

The tendency of the validation confirms a reasonable predictability of impact damage with the high-fidelity simulation. Nonetheless, we observe some qualitative and moderate quantitative deviation between the prediction and the experiments. The following breakdown to the relevant aspects of impact damage explains this general assessment:

- All predicted force-time and force-displacement history curves qualitatively accord with the experimental results concerning the first three phases of the impact event (compare to the Figure 2.15). Only the relaxation phase cannot be reproduced with the applied simulation model. The force-displacement plot especially reveals this discrepancy.
- The maximum contact force and the maximum indentation values are predicted with strong accuracy. The maximum values occur before the relaxation phase and that accuracy is not surprising.
- The prediction of the contact time involves the relaxation phase and is still reasonable. Thus, this parameter emerges as being insensitive towards slight mispredictions.
- The dissipation of energy is not correctly captured for any configuration. In all cases, the numerical prediction falls below the real dissipation.
- The damage threshold forces for delamination and fiber cracking are predicted to be slightly too low. The delamination threshold is marked by the first discontinuous load drop (well visible in the history plots of *CAI1.15*, *CAI1.30*, and *CAI1.40*). A larger load drop close to the force peak indicates the significant FF (observable on *CAI1.30* and *CAI2.40*).
- The qualitative damage pattern of delamination (Figure 2.26) and FF (Figure 2.27) is in four out of five test cases consistent with the experimental result. In the remaining case (*B1*), the lowermost and largest delamination is not predicted sufficiently well in the simulation.
- Quantitatively, we observe a tendency to an overestimation of the delamination damage. Especially for impact with low energy, the model significantly overestimates  $A_{dela}$ . This overestimation indicates a too-early delamination onset in the simulation based on the interface strengths. In consequence, the delamination threshold force is underpredicted.

With propagating damage, the discrepancy disappears. Thus, the energy-based damage evolution captures the experimental behavior plausibly. Case *B1* is an exception to this overestimation. However, the qualitative difference does not permit a quantitative comparison.

- The simulation provides accurate qualitative and quantitative predictions of the compression-induced fiber crack in the uppermost ply. All test configurations confirm these predictions. However, the numerical analysis of the test cases *CAI1.30* and *B1* also includes fiber cracking in the lowermost ply. This tensile crack did not emerge in any of the corresponding experiments.

As stated in the list above, the numerical and the experimental results are in strong agreement. However, at this point, we focus on the analysis of the deviating points and try to explain their causes.

Firstly, we look at the underprediction of the delamination threshold. Its cause is related to the artificial reduction of the interface strengths. The corresponding values do not represent the actual strength of the material. According to Equation (1.29) on page 20, the normal interface strength  $X_n$  is a numerical parameter. Its artificial reduction ensures enough elements in the cohesive zone. Nevertheless, the reduction is essential to allowing simulations with lower mesh density.

The second important difference we observed is the tensile FF in the lowermost ply of the impact specimens. In the case of *B1*, this FF is likely to cause a qualitatively faulty delamination pattern. Fibers break, instead of delamination further propagating in the interface. Afterwards, the fiber crack diminishes the load at the delamination crack tip, and the delamination pattern remains incorrect. A possible cause of the early FF can be found in the absence of a nonlinear shear model. As a typical shear response behaves degressively, the linearized model behaves stiffer than does the real response [168].

The good agreement of the experimental results and the numerical prediction affirms the model's suitability for virtual impact testing. This capability moves the physical testing effort to elaborate material characterization tests. Elastic parameters, strength values, and fracture-mechanical parameters have to be determined on the ply level in order to employ a high-fidelity impact simulation – a challenge to the user of a numerical impact model.

Test case		CAI1.15	CAI1.30	CAI2.20	CAI2.40	B1
$F_{max}$	[kN]	9.2 (8.6 ± 0.1)	12.7 (12.9 ± 0.1)	10.2 (9.9 ± 0.1)	12.6 (12.8 ± 0.3)	7.86 (8.0 ± 0.1)
$x_{max}$	[mm]	3.09 (3.19 ± 0.02)	4.41 (4.58 ± 0.02)	3.82 (-0%)	5.46 (-0%)	7.1 (7.39 ± 0.07)
$T_i$	[ms]	3.64 (3.70 ± 0.02)	3.87 (3.71 ± 0.02)	3.93 (3.85 ± 0.02)	5.06 (5.12 ± 0.16)	6.25 (6.36 ± 0.33)
$A_{dela}$	[mm <sup>2</sup> ]	391 (231 ± 15)	911 (762 ± 136)	864 (542 ± 31)	1344 (1450 ± 86)	280 (537 ± 60)
$l_{fiberack}$	[mm]	15 (12 ± 3)	28 (31 ± 8)	27 (26 ± 6)	40 (44 ± 8)	22 (18 ± 3)
$l_{matcrack}$	[mm]	10 ( <sup>a</sup> )	18 ( <sup>a</sup> )	29 (37 ± 3)	55 (72 ± 9)	24 (36 ± 3)
$E_{dis}$	[J]	3.6 (5.1 ± 0.1)	9.2 (11.4 ± 0.6)	5.1 (6.0 ± 0.5)	14.1 (24.6 ± 1.7)	5.2 (22.3 ± 1.6)

TABLE 2.6: Validation results of the numerical prediction in comparison with the experimental results (average and standard deviation) in brackets.

<sup>a</sup> No experimental data available.

### Energy dissipation

Finally, the underprediction of the energy dissipation  $E_{dis}$  marks an obvious deficiency of the numerical model in its present form. To understand its cause, we analyze which energies form full absorption  $E_{dis}$  according to Equation (2.29).

$$E_{dis} = E_{dmg} + E_{fric} + E_{rkin} + E_{res} \quad (2.29)$$



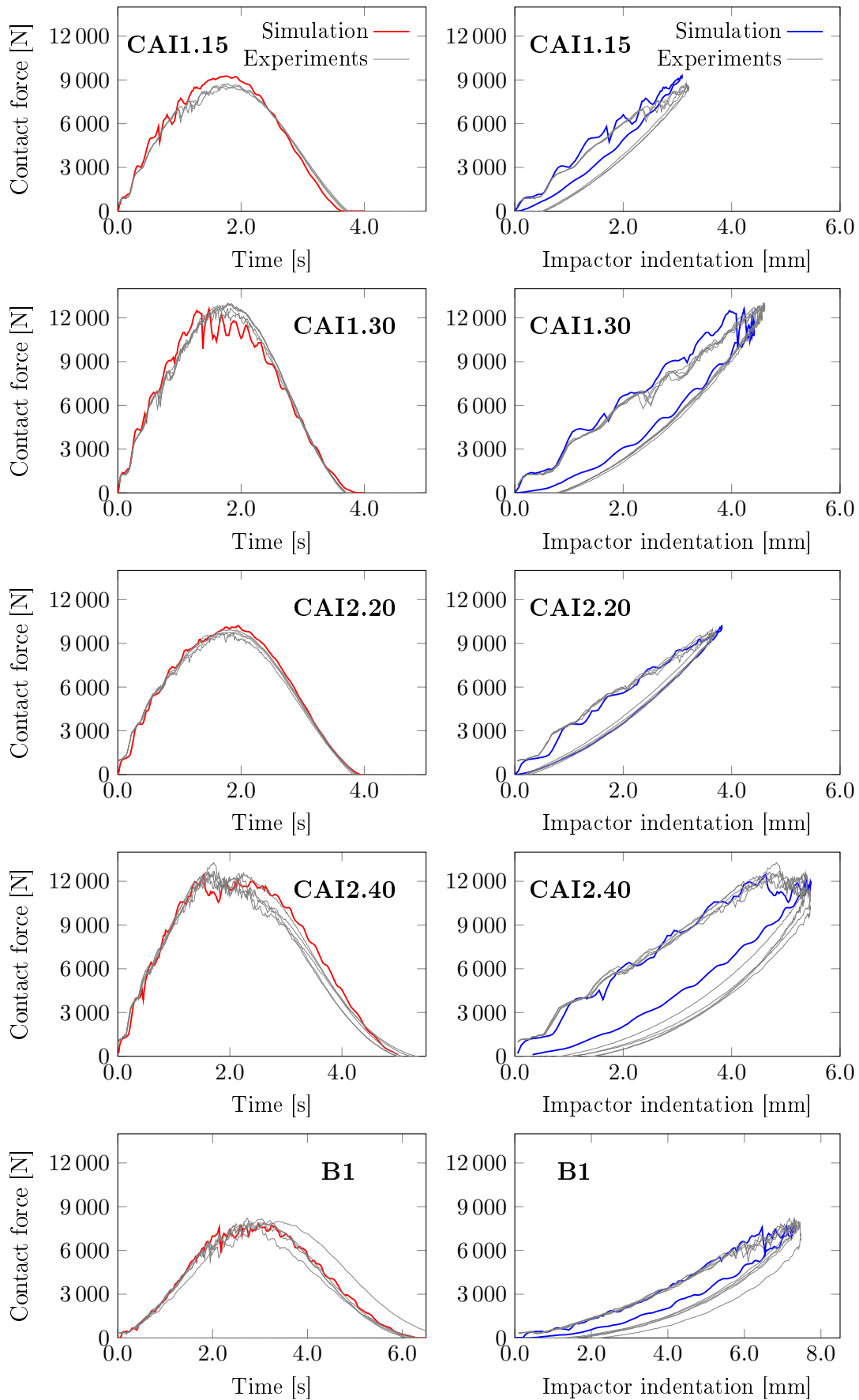


FIGURE 2.25: Numerical force time history (red) and force displacement history (blue) of the validation cases in comparison with the test results (grey).

The energy dissipation by damage  $E_{dmg}$  represents the actual absorption through the CZM and the CDM damage models. The numerical model should provide a reasonable prediction of this component. However, the present experimental data do not permit one to validate this model.

Frictional dissipation  $E_{fric}$  results from the contact friction and the material damping. The simulation includes these effects only partly, yet its value is far too small to explain the observed deviation from the experiment.

For the coupons under consideration, the remaining kinetic energy  $E_{rkin}$  in the specimen is also negligibly small. A modal energy analysis in the Section 3.3.3 of this work supports this assumption.

However, the calculated value of  $E_{res}$  is zero, while its experimental counterpart can be significant. The missing effects of permanent deformation explain this discrepancy. In reality, Matrix debris blocks open cracks, and during the relaxation these cracks cannot fully close [169]. They affect the relaxation path of the force-displacement curve and cause residual stresses in the unloaded laminate. The curve becomes bulgy and steep from the beginning of the relaxation. Good examples of this effect include the experimental history curves *CAI2.40*. A constitutive model not accounting for permanent indentation can neither correctly capture the relaxation phase nor the energy absorption.

The numerical prediction of the energy absorption represents the value  $E_{dmg}$  and not the full energy dissipation  $E_{dis}$ . As  $E_{dmg}$  increases only during the loading phase of the impact, its continuous evaluation is representative for all energy levels passed. The diagrams in Figure 2.28 show the thus-obtained correlation of the impact energy and the absorption through damage. The rise of these curves points out when damage grows. Steep increase indicates the exceedance of a damage threshold and plateaus at a phase without damage propagation.

### 2.5.3 Comparison with other methods

To classify the obtained results of the developed model, we have to consider how other damage models perform. As the most severe damage occurs in the test case *CAI2.40* with 40 J, this configuration serves as an example for the comparison. We consider the following four methods:

- An *unsymmetric degradation* as shown in Equation (1.21) is a simple degradation method that considers the effects of an oblique fracture plane by degradation of the fracture plane stresses. However, this degradation is equivalent to an asymmetrical stiffness matrix [Equation (2.9)] [RB1].
- A *symmetrified degradation* is a further development for the asymmetrical degradation of fracture plane stresses [60]. The model considers the effects of an oblique fracture plane but works with a degraded stiffness matrix according to Matzenmiller [Equations (1.16) – (1.19)].
- The *total degradation* concerns all resin-driven components in the stiffness after IFF occurs. This method considers oblique fracture only for the damage prediction. The degradation is conservative and was recommended by Puck [5] himself. It works according to the method of Matzenmiller [Equations (1.16) – (1.19)], with  $d_{22} = d_{33} = d_{matrix}$ .
- The *quadstrain model* combines the degradation according to Matzenmiller [Equations (1.16) – (1.19)] with the quadratic strain failure condition (1.2). Thus, it

does not take into account oblique fracture planes. Fracture is assumed to occur in the three Cartesian planes of the material coordinates.

Surprisingly, no significant difference between the models occurs in the force history of the impact. In Figure 2.29, we see the force-time and the force-displacement response. Both indicate, that all models lead to equal results before damage initiates at approximately 4000 N contact force. After damage initiation, the curves differ slightly. Only the quadratic strain model shows a tendency toward instability.

In order to assess the quality of the damage prediction, we take into account the delamination pattern. Figure 2.30 shows the results of all tested models and confirms that nearly all models provide a suitable predictions. The only exception that leads to a faulty result is the total degradation.

Remarkably, even the asymmetrical model predicts the correct result and does not become unstable – in spite of the physically inconsistent degradation (compare to Figure 2.19). This result becomes especially interesting as the degradation is easy to implement and computationally faster than any other model for oblique fracture planes.

Additionally, the good prediction of the quadratic strain model affirms that also a model with an elementary failure condition can lead to a suitable result [33]. The simplicity of this model facilitates the method's combination with theories for permanent deformation, residual compression stress or nonlinearities.

## 2.6 Critical assessment of the numerical impact analysis model

The developed damage model shows promising results in predicting impact damage. With delamination, IFF and FF, the model involves the essential damage modes and provides reasonable predictions. Importantly, it predicts compression failure in a physically plausible manner. Nevertheless, simpler degradation models were also shown to be capable to provide plausible predictions of impact damage. A consideration of the oblique fracture is not mandatory to achieve consistent results. The author has to admit, however, that oblique fracture is of minor importance to the damage morphology in a multidirectional laminate.

Notwithstanding the current development, several aspects of the chosen basis model emerge as questionable. The damage prediction by the failure condition of Puck provides a fracture angle in each finite element. This angle can differ from element to element. Consequently, the predicted crack pattern does not necessarily represent one continuous crack in the material. Also, the equivalent strain approach according to Equations (1.13) and (1.14) is an idealization, which becomes quantitatively incorrect when the state of strain changes during the damage evolution.

In addition, the tensorial-based degradation method further increases the computational effort of the numerical impact analysis. Thus, efficient applicability is limited to small coupons, and a simpler degradation model can still be the better choice if, for instance, efficiency is a crucial analysis requirement. Simpler degradation models were found to provide damage predictions of similar quality, as the benefits of the tensorial-based degradation seem merely relevant for impact damage.

Regarding the impact model as a whole, the cohesive zones require an artificial correction of the interface's normal strength in order to be applicable using a manageable element size. This artificial correction leads to inaccurate predictions if significant out-of-plane tensile stress occurs. The detected mesh dependency of the cohesive surfaces is also a possible source of analysis errors.

Finally, the constitutive material laws as applied in the CDM approach and the cohesive zones do not consider any effects of permanent deformation. Actually, the nonlinearity of the shear response results in significant residual strains after load removal [58]. Many state-of-the-art models include these effects in the material law [67, 115, 169, 170, 171]. In this work, they were intentionally left out. Firstly, such models increase the complexity of the constitutive laws. They are an additional source of uncertainty and require appropriate input parameters that were not available for the validation in this work. Secondly, this behavior affects mainly the relaxation phase of the impact, which is not mandatory for a plausible prediction of the damage. Eventually, the tensorial-based damage evolution and advanced constitutive laws for shear can be combined.

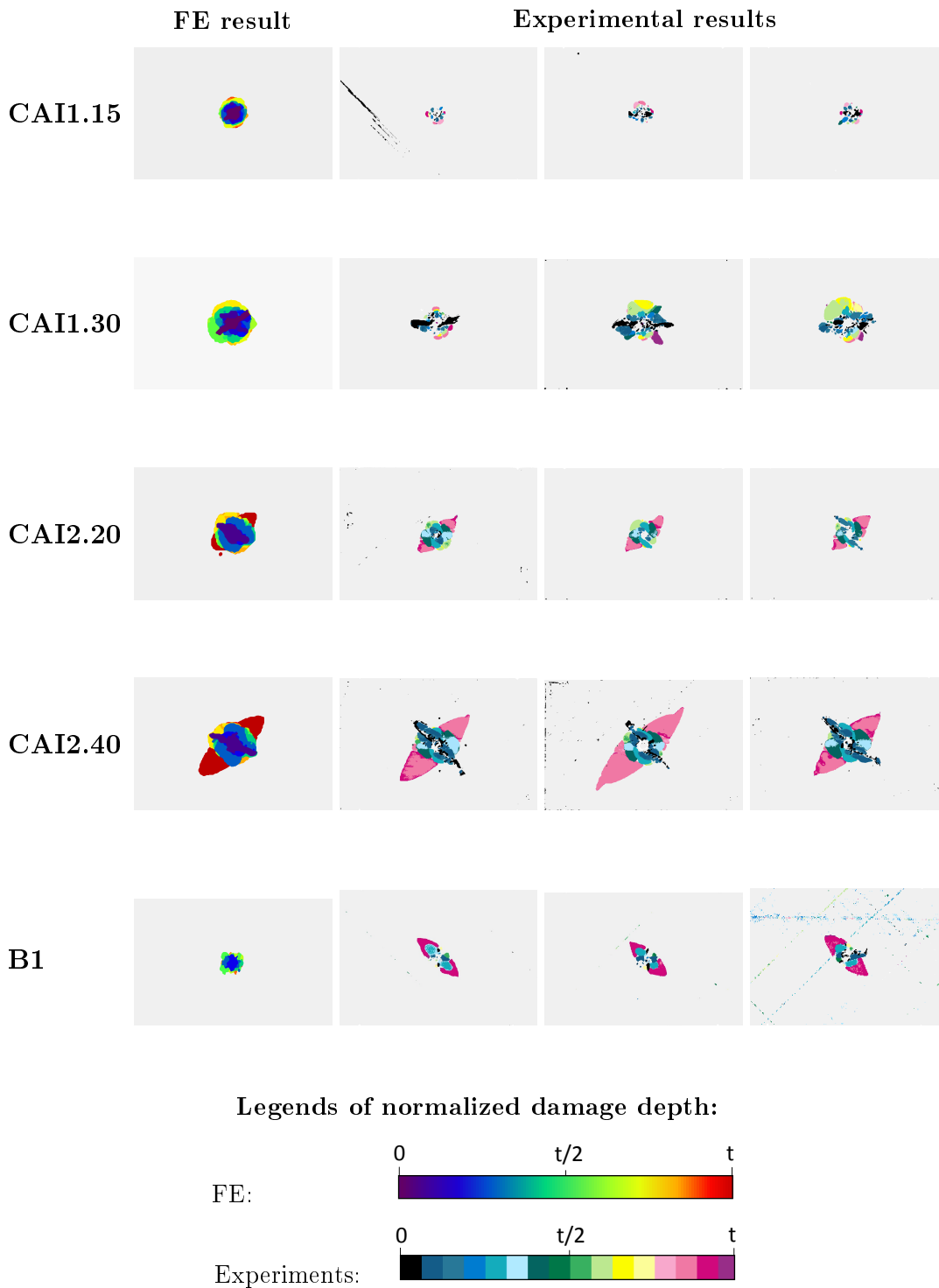


FIGURE 2.26: Comparison of the each predicted delamination overlay plot with the ultrasonic D-Scan results of three exemplary coupon tests.

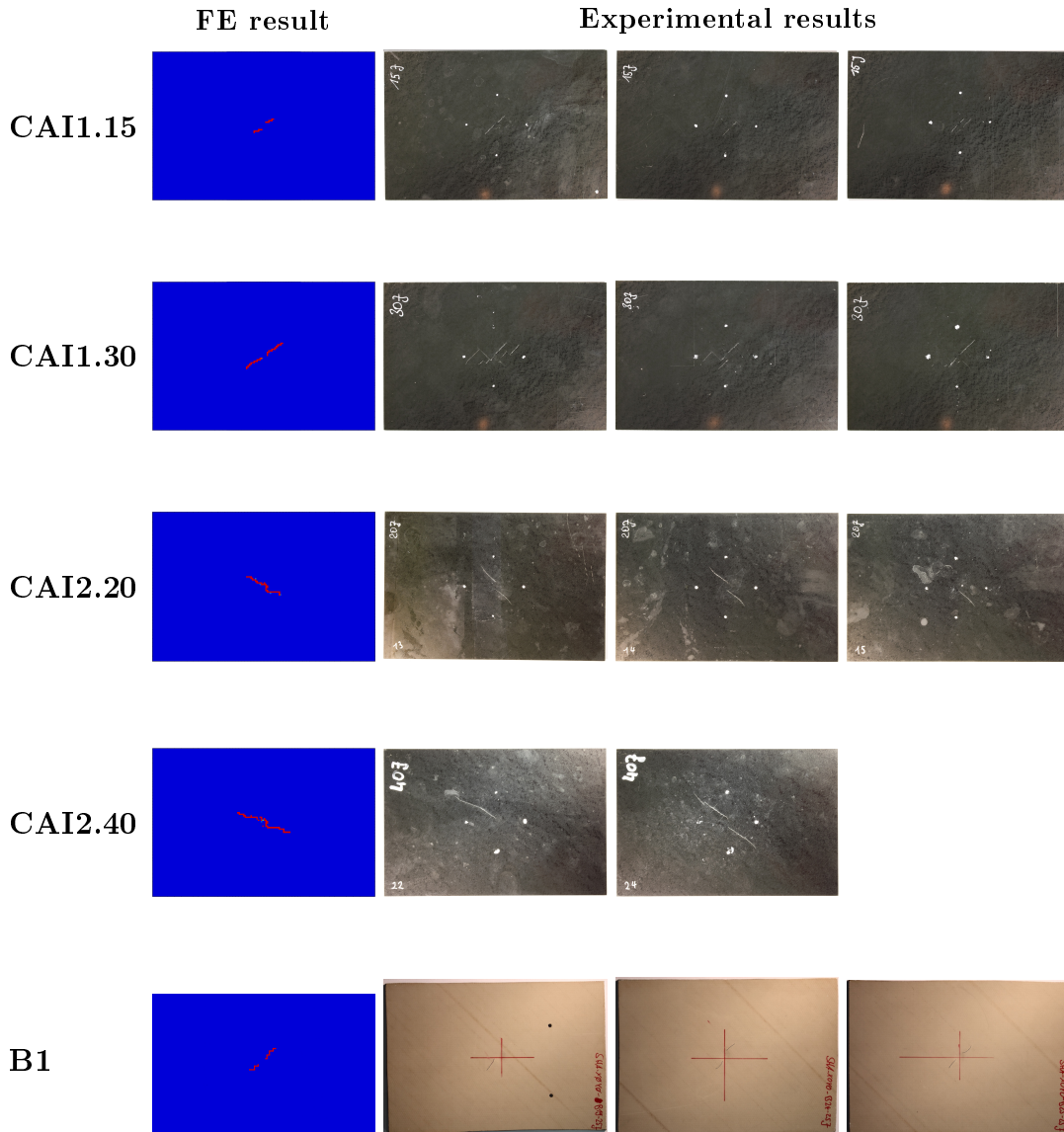


FIGURE 2.27: Comparison of the numerical prediction for FF in the top ply in comparison with the top view of three exemplary test coupons.

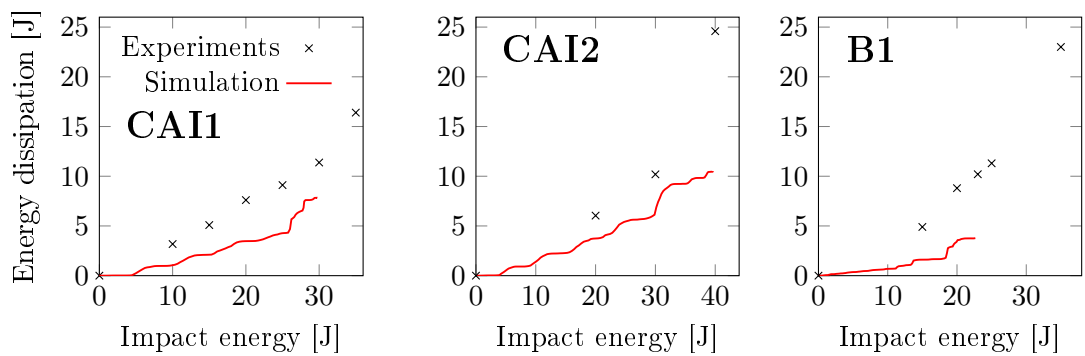


FIGURE 2.28: Energy dissipation by damage in comparison between the experiments and the high-fidelity simulation.

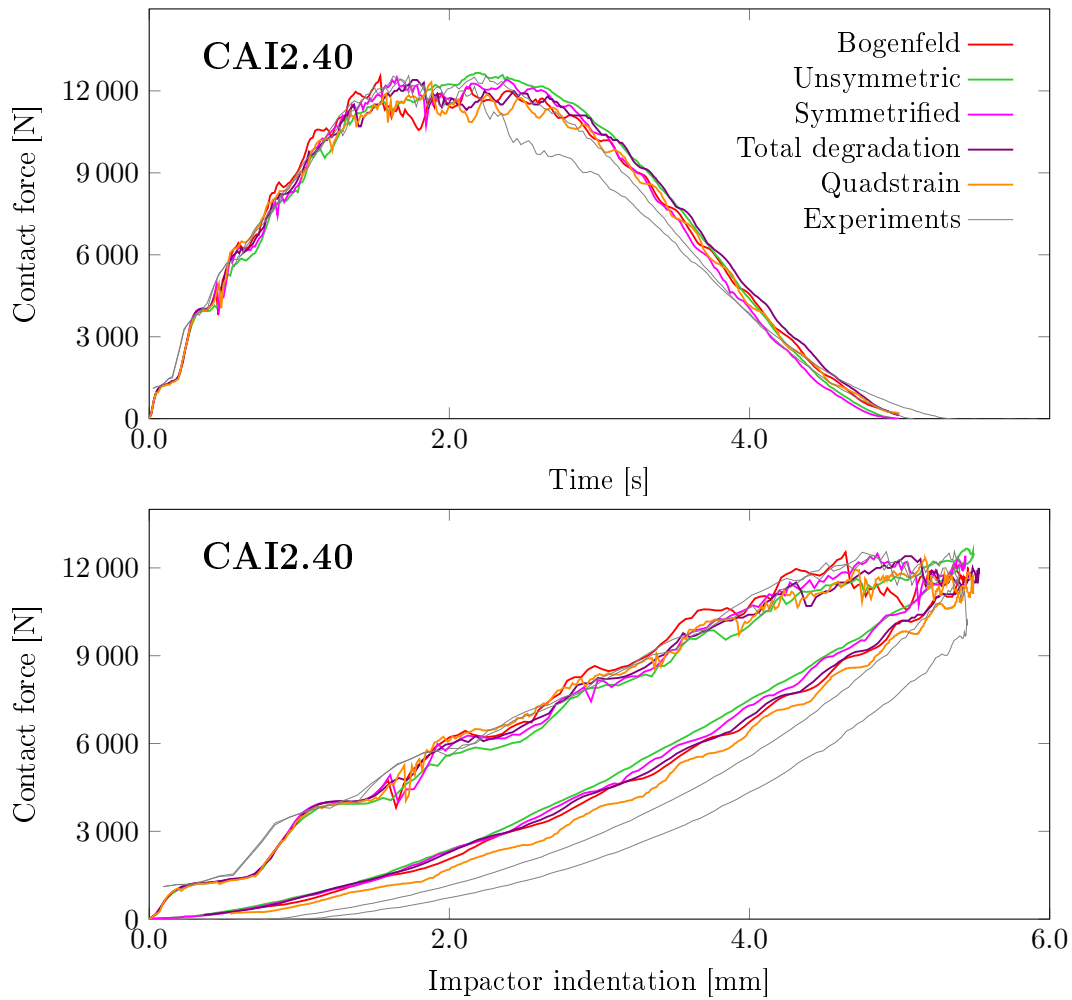


FIGURE 2.29: Comparison of different intra-ply damage models on the validation case CAI2.40.

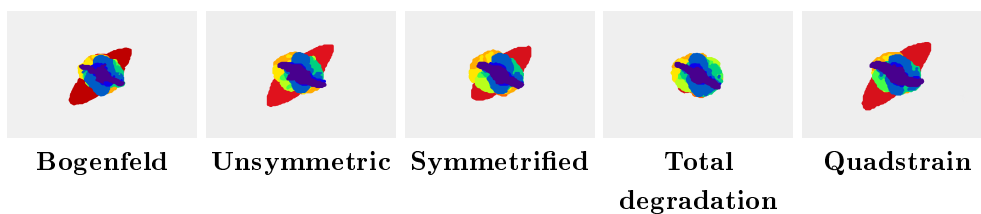


FIGURE 2.30: Comparison of the numerically determined delamination overlay plots with four different damage models (CAI2.40).





*“Abstraction forces you to reach the highest level of the basics.”*

Alan Soffer, artist

# 3

## Analytical Impact Scaling

### Scope of this chapter

The methods described in this chapter permit the efficient analysis of structural impact scenarios. Hence, the chapter addresses the second and third research hypotheses from Section 1.2. An analytical approach allows scaling the impact energy of a structural impact scenario to a reference impact scenario on the coupon level. The corresponding coupon represents a section of the actual structure. Thus, the numerical damage predictions through a high-fidelity method or coupon experiment can be transferred from the coupon to the structural level. A quasistatic analytical spring-mass model provides this transfer by capturing the specimen’s damage behavior and transferring it to any sufficiently similar impact scenario. In order to include the dynamic impact response in the transfer, a modal correction comprises the energy loss in higher-order modes.

A large set of impact experiments was conducted to validate the damage description by the analytical spring-mass model and the impact damage transfer. These experiments confirm the general validity of the method and depict its limitations for kinematically different scaling origins and targets.

The development described in this chapter is independent of the tensorial-based degradation in Chapter 2. Parts of this chapter have been published by the author in [RB3] and [RB4].

### 3.1 Analysis approaches for impact on the structural level

While the developed high-fidelity impact simulation model provides good results on the coupon level, its application on the structural level is economically inefficient [RB2]. A simulation of a coupon impact according to the Section 2.5 lasts approximately 100 CPU hours. Various authors have reported similarly high computation effort for their models [65, 169, 60]. Accordingly, a direct transfer of the method to the structural level does not make sense for an actual use case. There are two possible kinds of solutions to this issue: on the one hand, the simplification of the analysis model in order to become more efficient; and on the other hand, a limitation of the analysis area to permit reduction of the computational effort of a high-fidelity method. Such approaches are founded on the idea that the damage of LVI with large impactor

mass occurs locally around the impact spot [172]. Consequently, the full structure does not have to be analyzed for possible damage – only the damage-prone section. Four ways to allow structural impact analysis were considered for this research. These ways are described in the following list and illustrated in Figure 3.1.

- (A) The actual structural impact analysis is conducted through a layered-shell model as illustrated in Figure 3.1A. Comparative coupon analyses with a high-fidelity method validate or calibrate the low-fidelity model of each impact configuration, material, or laminate. This method is computationally very efficient and easy to apply. However, the trade-off analysis in Section 2.2.2 shows that a macro-scale model does not permit satisfactory damage evolution. Accordingly, this method cannot take advantage of accurate damage predictions through a model, as described in Chapter 2.
- (B) The easiest way to exploit the local characteristics of impact damage is a locally refined model of the structure, as Figure 3.1B illustrates. In this model, a high-fidelity mesh is embedded in a layered-shell model. Shell-to-solid couplings connect both meshes in the transition zone. A model of that type is suitable for predicting local impact damage on a structure. The computational effort only slightly exceeds the effort of a simple coupon simulation [RB2]. This level of effort makes the method attractive for a quick assessment of a single structural impact scenario. However, in practical application, this method faces a high modeling effort. The model-building effort reoccurs with each possible impact location on a structure as the damage-prone zone changes. Thus, the method is unattractive for application in a design process.
- (C) A global-to-local approach connects a global shell model and a local high-fidelity model. The principle behind this approach is comparable to a micro-meso multiscale method [132, 133, 134]. In this case, a multiscale formulation permits drawing the boundary conditions for the high-fidelity model from the global model. The reaction forces are mapped inversely. Figure 3.1C illustrates this method. The modular setup with two independent models allows working with a single structural model for all analyses. Different impact locations require only slight adaptations of the high-fidelity model. Accordingly, the approach is flexibly applicable, with a low modeling effort. The computation effort is comparable to approach B.
- (D) Figure 3.1D shows an unconventional approach. The impact analysis model is reduced to a small section around the damage-prone zone. For the actual impact analysis, this section is supported with arbitrary boundary conditions. Adapted impact parameters for this modified impact have to be calculated in order to obtain similar damage as it would occur in the original impact scenario. Whether and how such scaling can be performed is an interesting object of research and seems to offer possibilities beyond the locally refined analysis of an impact scenario. For these reasons, this approach was my focus in the development of an impact analysis method for composite structures.

### 3.1.1 General consideration of impact similarity

A scaling approach according to Figure 3.1d shall calculate the structural impact damage on a different specimen. Thus, the scaling has to ensure the similarity of the damage in those two impact scenarios. According to the general damage equation,

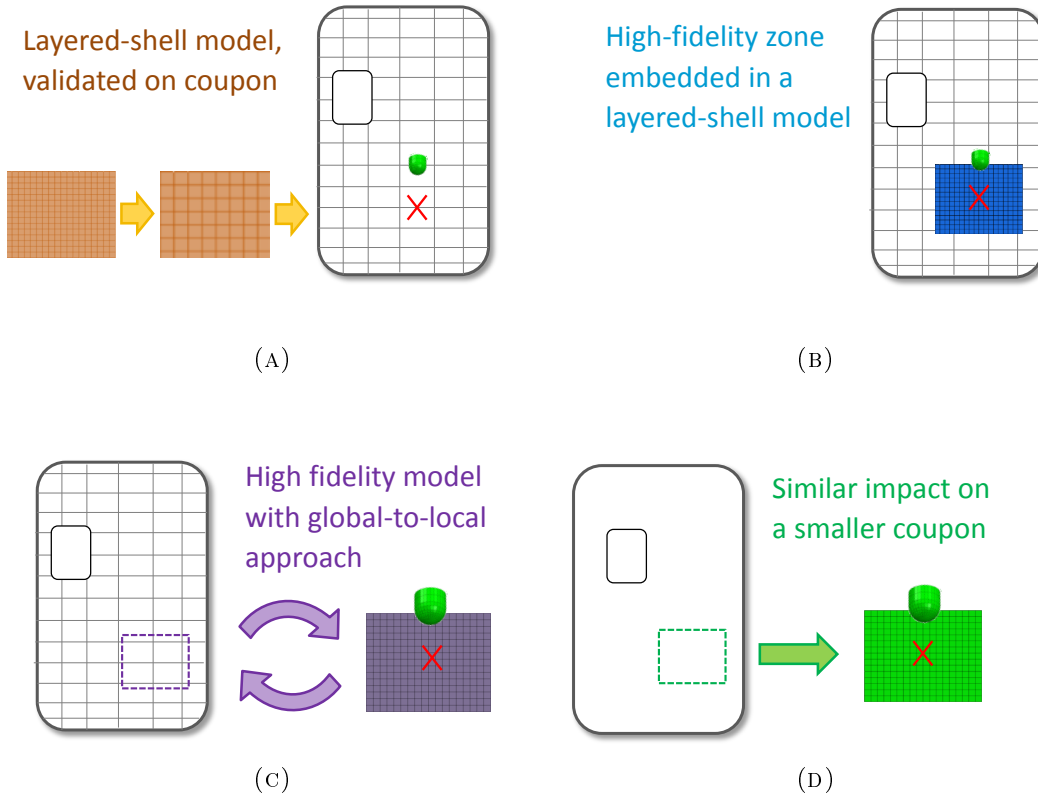


FIGURE 3.1: Graphical explanation of the considered options for impact analysis on the structural level.

Equation (2.1) on page 30, the impact damage depends on a set of generic parameters of the impactor and the impacted laminate.

To implement the idea of impact scenarios with similar damage, the equation is now modified to the new variant in Equation (3.1). Here, the energy  $E_i$  as the driving impact parameter depends on the boundary conditions  $BC$ . The expression  $E_i(BC)$  is a nonlinear normalization of the impact scenario. A damage description according to this general equation is objective regarding the boundary conditions or the impact location for similar impactor ( $IMP$ ), material ( $MAT$ ), and layup ( $LAY$ ). As the third research hypothesis of this work implies, it assumes the existence of an objective damage behavior from which the damage development of each specific impact scenario can be derived.

$$DMG = DMG [E_i(BC), IMP, MAT, LAY] \quad (3.1)$$

The suggested procedure seems analogous to the system description through dimensionless parameters as they are common in aerodynamics or thermodynamics (Reynolds number, Mach number, Nusselt number, etc.). Once the behavior of a single specific scenario is understood, the analysis with dimensionless parameters can transfer the behavior to an arbitrarily modified system. The first approach for impact damage could be to analogously determine dimensionless parameters.

With the help of Buckingham's  $\pi$ -theorem [173], Morton already in 1988 conducted such a dimensional analysis for impact on composite laminates [16, 174]. However, this method is linear, which makes it unsuitable for capturing the highly nonlinear impact effects. Another issue is that the scaling always affects the whole model. The scaling of the laminate and ply thickness especially disturbs the actual purpose of the

scaling between the structure and a reference coupon.

Beyond the dimensional analysis, Swanson also approached impact scaling [175, 176, 16]. To reduce the time and the costs of impact experiments, he intended to provide a method to scale impact between small laboratory specimens and large structures. This goal is already much closer to the need described in this work. He approached the scaling from the differential equation of orthotropic plates. This approach affects the geometry of the structure, the impactor, and also the laminate thickness, which prevents its application for the current purpose.

Additionally, Christoforou developed a methodology to scale the impact response of differently sized composite structures [95, 177, 178]. He discovered that “seemingly different impact situations may be similar in non-dimensional form and need not be duplicated” [95]. The similarity of the dynamic impact response drives the scaling approach. In this way, Christoforou derives the equivalence of actually different impact scenarios, when two dimensionless parameters are similar. This approach is already close to the objective of scaling an impact between two different scenarios of a similar laminate. However, the achieved similarity results from an equivalent normalized contact force. Thus, with the size of a structure, the damage scales with the size of the analyzed structure. This makes the purpose insufficient to define different impact scenarios with similar damage.

In summary, three different scaling approaches for impact on composite laminates are available. In particular, the works of Swanson and Christoforou show that it is possible to obtain similar damage for different boundary conditions. However, no method permits the analysis of a section from a structure. Consequently, the existing ideas had to be further developed to permit the transfer of impact damage between different scenarios. *My novel idea in this work is the use of a basic impact model that ensures the similarity of the damage in two different impact scenarios.* As formulated in the second research hypothesis in Section 1.2, this model has to capture the damage behavior of an impact event. It does not have to provide an elaborate damage prediction but only the transfer of predicted damage to a second impact scenario. Regarding the overview of impact analysis methods in Figure 1.14, a spring-mass model fits this need if an appropriate damage description can be provided.

## 3.2 Analytical impact analysis

### 3.2.1 Elastic spring-mass models

Spring-mass models describe an impact system in one dimension. They involve only the main vibration mode of the impact. In the case of LVI, this mode equals the quasistatic response. Thus, they suit the description of large-mass impact according to Olsson’s categories in Figure 1.12 on page 22. As long as the fundamental mode dominates the impact response, it can be captured through a spring-mass model with a single DoF. This limitation to the main vibration mode affects this work’s target domain in Figure 1.13 on page 23. It prohibits an extension toward the further BVID-relevant zone of higher impactor velocity and lower mass.

The response of an elastic structure is driven by several deformation effects which can all be captured through different springs, as Abrate showed [16]. These effects are bending, shear, and membrane deformation. Additionally, the local surface deformation needs to be considered. The illustration of the deformation modes in Figure 3.2 provides an overview of the mode shapes and the corresponding force-displacement relations.

Bending and shear deformation are connected in series ( $F_b = F_s = F_{bs}$ ), and membrane effects occur in parallel. Both depend on the global indentation  $w_{global}$ . The sum of their reaction forces forms the impactor contact force in Equation (3.2). Bending and shear forces are proportional to the global indentation  $w_{global}$ , whereas membrane forces are proportional to the third power of  $w_{global}$ , as Abrate [16] and Olsson [92] confirmed in their works about analytical impact models.

The fourth illustrated deformation mode in Figure 3.2 connects in series to  $w_{global}$  and is associated with the local surface indentation  $w_{local}$ . The contact law of Hertz [99] (or a comparable law) describes the indentation behavior. The sum of  $w_{global}$  and  $w_{local}$  forms the total impactor indentation  $w$ . The spring-mass model describing all these phenomena is shown in Figure 3.3 (B). It has three characteristic values,  $k_{bs}$ ,  $k_m$  and  $k_c$ , where  $k_{bs}$  summarizes bending and shear.

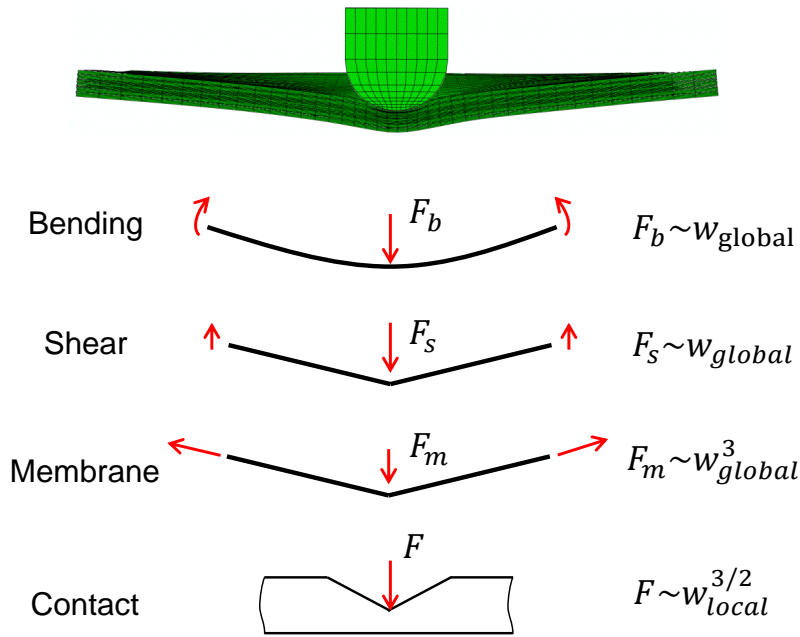


FIGURE 3.2: The elastic deformation under impact load is split up to a bending, a shear, and a membrane component.

$$F = F_{bs} + F_m \quad (3.2)$$

For common composite laminates, the local indentation is insignificant compared to the global indentation [Equation (3.3)]. The corresponding vibration mode has a very high frequency, which is negligible in the dynamic response. On account of that relation, we idealize the impact system by removing the surface indentation spring from the spring-mass model. This idealized spring-mass model is illustrated in Figure 3.3 (A). As we neglect the local indentation, a simple relation between contact force  $F$  and impactor displacement  $w$  can be established with Equation (3.4).

$$w_{global} \gg w_{local} \quad (3.3)$$

$$F(w) = w_{global} k_{bs} + w_{global}^3 k_m \quad (3.4)$$

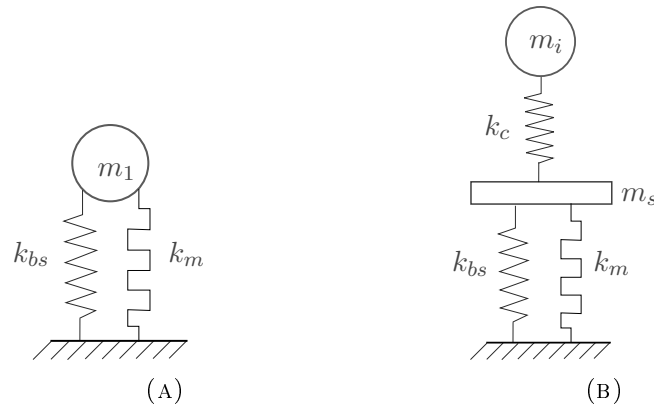


FIGURE 3.3: Elastic spring-mass models in the idealized version (A) and the variant accounting for local indentation (B).

The reduction of the model from two to one DoF changes the composition of the oscillating mass. The complete model 3.3 (B) consists of the impactor mass  $m_i$  and the modal mass of the specimen's first eigenmode. This mass  $m_s$  can be calculated in modal analysis. For a typical CAI specimen (as in the reference cases CAI1 and CAI2 in Section 2.5) the mass  $m_s = 0.04$  kg. The reduced model with only one DoF works with a combined mass  $m_1 = m_i + m_s$ , which approximates the modal mass of the impact system, with the impactor tied to the impact location.

In the next step, we test the suitability of Equation (3.4) for the description of elastic out-of-plane deformation. For this purpose, the force-displacement history of the FE model is evaluated. The parameters of the spring-mass model,  $k_{bs}$  and  $k_m$ , are fitted with a least squares method (LSQ) as explained in Appendix B.2. Eventually, the fit is compared to the original prediction of the FE model.

The FE model itself can be very elementary. In the model-building section, Section 2.2.2, a layered-shell model was found to suitably predict the elastic impact response. Thus, the result of an elastic impact analysis with layered shells serves for the determination of the elastic parameters  $k_{bs}$  and  $k_m$ .

To ensure the validity of the curve fit, a coefficient of determination for nonlinear fittings was evaluated [Equation (3.5)]. With this coefficient, a value of 1 indicates a perfect fit, with all measured values  $F_i(w_i)$  exactly on the interpolation curve. With a decreasing interpolation quality, the value approaches zero.

The finite element results for two different cases are given in the force-displacement diagram in Figure 3.4. The stiffer curve belongs to a  $150 \times 100$  mm<sup>2</sup> CAI specimen according to the standard AITM 1.0010 [153]. The second curve belongs to a stiffened panel section as it will be introduced in the validation section of this chapter.

In both of the demonstrated cases, the idealized model provides a good approximation of the global response. For all tested cases, the coefficient of determination was larger than 0.9, which indicates a good fit. The existing deviation from an ideal fit is caused by the oscillation in the dynamic indentation response rather than by a global divergence.

$$c_{det} = 1 - \sum_{i=1}^N \left[ \frac{F_i - w_i k_{bs} - w_i^3 k_m}{F_i * N} \right]^2 \quad (3.5)$$

In fact, the real system also responds with its higher eigenmodes. The spring-mass model does not include these modes. This restriction limits the validity of the

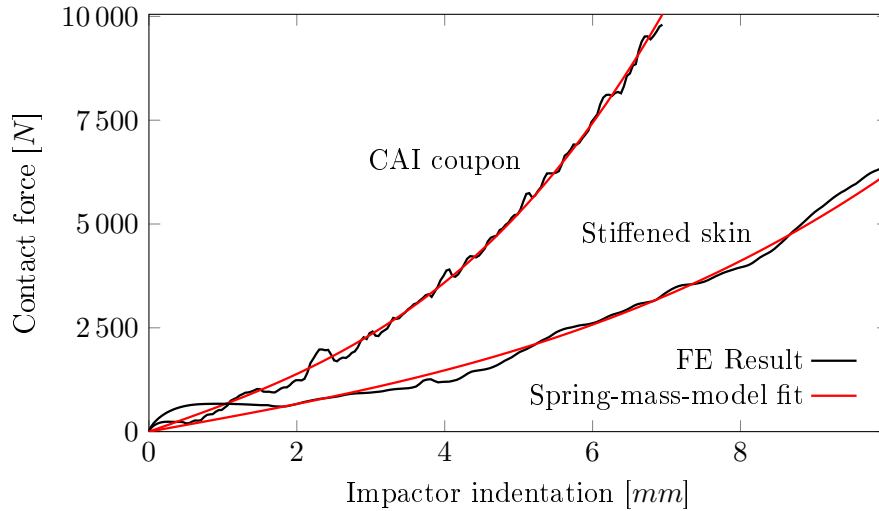


FIGURE 3.4: FE-predicted elastic force-displacement history and the spring-mass model fit for two test cases: a CAI coupon and a stiffened panel section.

model to LVI. The LVI response is similar to the quasistatic response, which again is represented by the first eigenmode of the impact system [92].

### 3.2.2 Damage description with spring-mass models

Elastic spring-mass models suit only the description of impact scenarios with hardly any damage occurring. The description becomes invalid as soon as the impact response leaves the initial phase according to the schematics in Figure 2.15 on page 47.

Usually, to include impact damage in analytic spring-mass models, the elastic models are upgraded. Springs in series to the elastic springs represent the softer behavior of a damaged structure. An entirely upgraded model recently published by Singh and Mahajan [98] considers damage in every deformation mode. According to them, bending damage, shear damage, membrane damage, and surface damage each require one additional damage element. Furthermore, Singh and Mahajan show analytical correlations between the damage parameters in the analytical model and the existing delamination damage in the laminate.

Earlier, Olsson proposed an elementary model [92], which works with a single additional damage element in the spring-mass system. This element is intended to capture the softening of shear and bending stiffness. The stiffness parameter of the newly introduced damage element is  $k_d$ . During the impact process, the value of  $k_d$  decreases monotonically. This results in the condition in Equation (3.6) for the derivative of  $k_d$ . Although  $k_d$  is a stiffness variable, it describes the additional *compliance by damage* in the impact system. As damage propagates in the structure during an impact event, the introduction of additional compliance is more demonstrative than a stiffness. This compliance by damage is mathematically described by  $c_d = \frac{1}{k_d}$ . From its initial value zero, it starts to increase monotonically with propagating damage. These conditions result in the boundary values of Equations (3.7) and (3.8) for  $k_d$ .

$$\dot{k}_d \leq 0 \quad (3.6)$$

$$k_d(t=0) \rightarrow \infty \quad (3.7)$$

$$k_d > 0 \quad (3.8)$$

The fundamental principle of additional compliance drives the progressive damage behavior of a spring-mass model. For this work, we idealized the spring-mass model of Olsson analogously to the elastic model in the previous section. The idealized version consists of three stiffness elements  $k_{bs}$ ,  $k_m$ , and  $k_d$ . The configuration is shown in Figure 3.5 (A).

In contrast to other works about analytical impact analysis, the aim of the present model is not the analytical prediction of impact damage but its description. A single scalar parameter is going to describe the impact-damage state in a structure. This state will later be utilized to achieve the same damage state on the structural level as on a reference coupon.

Equipped with the stiffness values of the elastic response and the force-displacement history of an actual impact event, the spring-mass model will capture the damage status in the laminate. The model of Olsson fits this need better than the complex variant by Singh, as a single damage parameter can directly be derived from the former. Consequently, the authors used the model of Olsson as a baseline for the first analysis. This model is physically sound for small impact damage without fiber cracking. It is not sufficient when the damage becomes larger, however. Problems arise with the appearance of the first fiber cracks. In Olsson's model, the membrane stiffness remains unaffected by the damage. The compliance by damage softens only the bending and shear forces. This results in very high membrane forces if the displacement increases. As there is barely any load in the bending shear load path,  $k_d$  may quickly lean toward zero. Even in the range of BVID, this inclination toward zero can lead to difficulties in the determination of  $k_d$  and physically unlikely behavior. For this reason, the model has been adapted to the current application.

The additional compliance by damage was moved to a series connection with the global bending, shear, and membrane deformation. This model is shown in Figure 3.5(B). The series connection with the global stiffness leads to a linear superposition of the elastic deflection  $w_{global}$  and the additional deflection by damage  $w_d$  [Equation (3.9)].

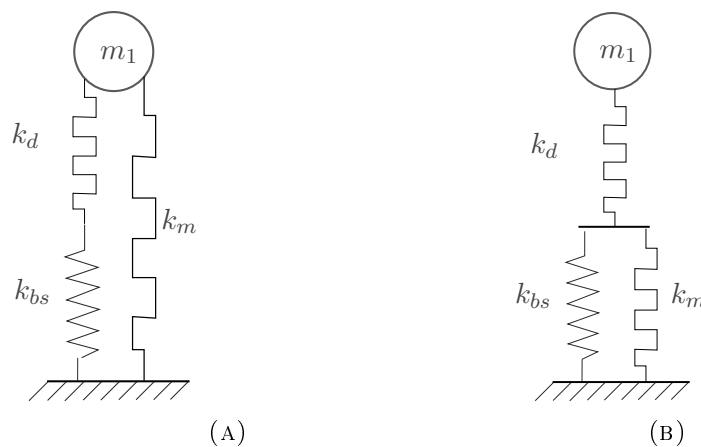


FIGURE 3.5: Sketches of damage-capturing spring-mass models: the idealized version of the model by Olsson (A) and the spring-mass model newly introduced in this work (B).



$$w = w_d + w_{global} \quad (3.9)$$

Equation 3.10 describes the relation between the contact force and the additional deflection by damage  $w_d$ . The relation of the force to the third power of the deflection is a preliminary assumption and will be evaluated in the course of this work. The assumption stands for a membrane behavior of the additional compliance by damage. It is based on a characteristic of delamination damage. The plies remain intact, but delamination separates them as sub-laminates. The bending stiffness of the laminate significantly decreases. The softening allows a larger indentation under similar force. In the delaminated region, the major part of the load is sustained by tensile stress in the angular fibers – a membrane effect. This assumption requires that the fibers sustaining tensile load remain intact. Thus, slight fiber damage on the impact side is tolerable. Broken fibers in the plies on the reverse side could thwart the validity of the spring-mass model.

$$k_d = \frac{F}{w_d^3} \quad (3.10)$$

The compliance by damage captures the progressive damage behavior of the impact by reducing the value of  $k_d$ . The elastic stiffness parameters remain untouched. This impact description is founded on the idea that the intact composite structure controls the elastic behavior. The major part of the structure is far enough removed from the location of impact not to experience any damage. It only stores elastic energy during the impact event. The damage barely affects this structural energy storage. Thus, the influence of local, impact damage on a relatively large structure is small enough not to be taken into account in the global elastic model. Instead, the deformation due to damage occurs locally on the laminate level.

The global elastic deformation and the deformation by damage are linearly superposed in the spring-mass model. This assumption is valid when the structure is significantly larger than the damage-affected part. An assumption that is true for this work's target domain of impact scenarios according to Figure 1.13 on page 23. This limitation prevents an extension of the target domain to large-mass impact with high velocity. The damage would affect the whole structure and require a more complex analytical degradation model, as proposed by Singh [98].

The stiffness value  $k_d$  integrally describes the local damage state of the laminate. In its function, this stiffness value is comparable to the projected delamination area. In contrast to this area, the stiffness parameter  $k_d$  is a parameter of the impact system. It can be evaluated at any point in the force-displacement history of an experimental impact or a finite element result. Correlating the stiffness  $k_d$  with the impact energy introduced to the specimen provides a function  $k_d(E)$ . This function represents the specimen-specific damage-propagation during the impact. Its determination is the baseline for the damage description by the newly introduced spring-mass model.

### 3.2.3 Determination principle for the damage parameter $k_d$

The determination of  $k_d$  based on a force-displacement history is a straightforward procedure. The global elastic displacement  $w_{global}$  is computed with the current contact force value by inverting Equation (3.4). The difference between the global elastic deflection and the total impactor displacement provides the additional deformation caused by the damage in the laminate.

The evaluation of an impact-force-displacement history for  $k_d$  is illustrated by the force-displacement diagram in Figure 3.6. It is possible to obtain the stiffness value for any point of the force-displacement history. A force-displacement history can be evaluated up to the point of maximum displacement, where the full impact energy is introduced into the laminate. The condition, that  $k_d$  needs to decrease monotonically, prevents a healing of the structure. However, prompt force drops always come along with dynamic effects. Inertial effects delay the elastic response of the structure and overshooting occurs. For this reason, the effects of high-frequent oscillations have to be eliminated by filtering the force history. Otherwise, prompt force drops would result in implausible drops of  $k_d$ .

This determination procedure for  $k_d$  provides information about the impact damage in the energy range between zero and the applied impact energy  $E_i$ . To exploit a simulation or a test maximally, a high impact energy  $E_i$  should be chosen. This energy needs to be chosen with care, as there is a validity limit for large impact damage that is dominated by fiber damage rather than by delamination.

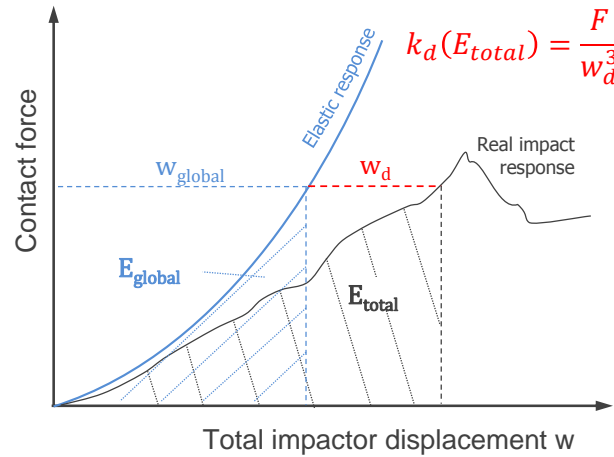


FIGURE 3.6: Determination of the damage stiffness parameter  $k_d(E)$  from the real impact response and the elastic response depending on the introduced energy  $E_{total}$ .

The model provides a scalar value for the energy dissipation by the damage that is easily obtained. The elastic energy in the global deformation modes, as shown in Equation (3.11), results from the integral of Equation (3.4). The subtraction of  $E_{global}$  from the total energy  $E_{total}$  provides the energy amount that was absorbed by the damage zone. Even this energy is not fully dissipated, however, as  $k_d$  also stores energy elastically. The elastic energy in the spring  $k_d$  needs to be subtracted from  $E_{total}$  then as well. This subtraction leads to the energy in Equation (3.12), defining the energy dissipation by damage.

However, the value of energy dissipation by damage is not equivalent to the full energy absorption during the impact. From Section 2.5.2, we know that during the relaxation phase, effects of permanent deformation absorb a significant amount of energy, so  $E_d < E_{dis}$ . Permanent indentation is not captured by the presented spring-mass model and is not required for the aspired goal, ensuring damage equivalency of a scaled impact between a structure and a reference coupon.

$$E_{global} = \frac{1}{2}k_{bs}w_{global}^2 + \frac{1}{4}k_m w_{global}^4 \quad (3.11)$$

$$E_d = E_{total} - E_{global} + \int_{w_d}^0 k_d \tilde{w}_d^3 d\tilde{w}_d = E_{total} - E_{global} - \frac{1}{4} k_d w_d^4 \quad (3.12)$$

**Evaluation of the spring-mass model** After the determination of the stiffness parameters, impactor mass, and initial impactor velocity, we can evaluate the spring-mass model to obtain the force response of an impact scenario. This evaluation is a straightforward procedure based on the time integration of the equation of motion of the point mass  $m_1$  [Equation (3.13)]. For the elastic spring-mass model, an analytical solution of this differential equation can be found through separation and integration [16]. This is equivalent to the damaged model with  $k_d \rightarrow \infty$ . However, the damage element  $k_d$  impedes an analytical solution. The course of  $k_d$  itself is not an analytical function but a discrete table of values. Thus the equation has to be solved through numerical time integration with a discrete step-width  $\Delta t$ .

$$\ddot{w} = \frac{F(w)}{m_1} \quad (3.13)$$

This integration and the initial condition  $\dot{w}(0) = v_0$  provide the history curves  $w(t)$ ,  $\dot{w}(t)$ , and  $\ddot{w}(t)$ . From these, the forces responses  $F(t)$  and  $F(x)$  derive directly.

### 3.3 Impact scaling

The developed spring-mass model is not intended to provide a stand-alone prediction of impact damage. The aim is to deduce the impact behavior of the scenario of interest from a simpler impact scenario with a predetermined result. The *transfer of the impact damage* shall be ensured through an equivalency of the damage parameter  $k_d$ . The *scaling of the impact energy* is conducted to achieve this equivalency. The key assumption behind this transfer of the damage behavior is that the damage behaves qualitatively equivalently in both cases. The local limitation of the impact damage suggests that this assumption is valid under specific conditions. The new spring-mass model describes the impact response as a superposition of the material behavior – which includes the damage – and the elastic structural behavior. Once the material behavior is known, the structural behavior becomes exchangeable. That way, we can deduce the structural impact response from the response of the reference coupon.

Usually, a reference coupon represents the origin of the transfer. The structure to be analyzed is the transfer target. The reference coupon crucially has to represent a segment of the structure. If connecting elements, stiffeners, or holes are part of the damage-prone area, these also have to be part of the reference coupon. The coupon has to comprise the entire damage-prone area. If nonlocal damage next to the impact spot occurs, this second hot-spot has to be part of the coupon.

The process to achieve an equivalence is illustrated by the flowchart in Figure 3.7. Firstly, the calculation of the elastic stiffness values on the origin side is necessary. This calculation includes an elastic FE analysis. Afterward, the damage parameter  $k_d$  of the transfer origin is obtained. In this step, a damage analysis by test or high-fidelity simulation needs to be conducted. An evaluation of the spring-mass model according to the determination process described in section 3.2.3 has to be conducted. An objective description of the damage is central to the transfer approach. From that point, the transfer to the target can be conducted. The elastic stiffness properties are the only necessary input from the target side. A curve of damage-equivalent impact

energy of the two scaling partners can be calculated. The damage parameter of the target can be determined for a given impact energy.

This scaling process considers only the force-displacement response and not the force-time response, which would additionally require an adaptation of the impact model mass  $m_1$ . The assumption of an LVI is that the quasistatic response drives the damage propagation. Thus, an equal impact duration is not a requirement for equivalent impact damage [RB2]. Additionally, the inclusion of the scaling for a similar force-time response would not extend the validity of the model according to the target domain in Figure 1.13. The model with adapted mass would consider only the first mode of the impact response, while the neglected vibration modes of higher order are damage relevant for low-mass impact with higher velocity.

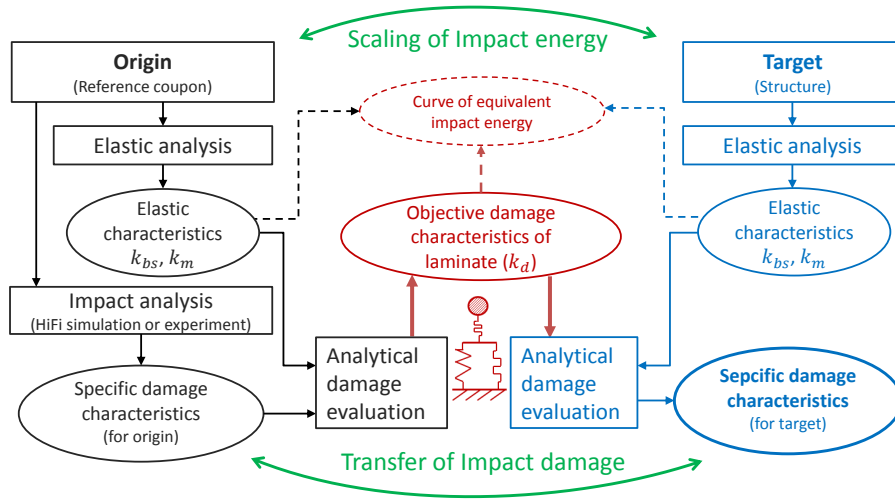


FIGURE 3.7: Flow chart for the scaling of the impact energy/ the transfer of impact damage between the origin and the target.

### 3.3.1 Scaling for equivalent damage or same impact energy

The determination of the *impact energy* for a given damage parameter  $k_d$  requires the inversion of the previously described determination method from section 3.2.3. This is made possible by an iteration over the total impactor displacement  $w$  on the target structure. The iteration starts with  $w = 0$  and proceeds with  $\Delta w$  according to Equation (3.14). Each iteration cycle  $n + 1$  begins with an evaluation of the analytical spring-mass model. Its input is the global elastic stiffness of the target and the current damage state  $k_{d\_n}$ . Equations (3.15), (3.16), and (3.17) form a nonlinear system of equations. It can be solved for its three variables  $F_{n+1}$ ,  $w_{global\_n+1}$  and  $w_{d\_n+1}$ . They provide the contact force and the division of the displacement in the new iteration cycle.

$$w_{n+1} = w_n + \Delta w \quad (3.14)$$

$$w_{n+1} = w_{global\_n+1} + w_{d\_n+1} \quad (3.15)$$

$$F_{n+1} = w_{d\_n+1}^3 k_{d\_n} \quad (3.16)$$

$$F_{n+1} = w_{global\_n+1}^3 k_m + w_{global\_n+1} k_{bs} \quad (3.17)$$

Afterward, the damage parameter needs to be updated. To ensure its objective description, a force-dependent function for  $k_d$  is used wherever possible. Depending on  $F_{n+1}$ , the new value  $k_{d\_n+1}$  is selected from the damage result of the scaling origin.

The force-displacement history of the target structure results directly from this procedure. The integral of the force-displacement curve provides the equivalent impact energy of the target structure for each value of  $k_d$ . In Equation (3.18), the integration of this force-displacement curve provides the temporary total impact energy of each iteration step.

$$E_{n+1} = \sum_{j=0}^n \frac{F_j + F_{j+1}}{2} \Delta w \quad (3.18)$$

When the aim of the analysis is to obtain the impact energy for similar damage on the target, the iteration stops as soon as the origin value of  $k_d$  is reached. This would indicate that the energy for a predefined damage state has been calculated: *if* ( $k_{d\_n} \leq k_{d\_aim}$ )  $\rightarrow E(k_{d\_aim})$ .

An alternative analysis approach is the *calculation of the damage state for a given impact energy* of the target. In this case, the iteration is conducted according to the same principle. Only the abort criterion changes. If the total energy exceeds the given impact energy, the associated damage state  $k_d$  represents the result of the analysis: *if* ( $E_n \geq E_{aim}$ )  $\rightarrow k_d(E_{aim})$ .

During the iteration process, the additional deflection by damage for each state of global elastic deflection is calculated. The variable  $k_d$  results directly from this indentation and the corresponding contact force. The relation in Equation (3.16) is not required to achieve the transfer. In the previous section, a cubic relation of contact force and damage indentation was postulated. This assumption does not affect the result of the conducted procedure so far. However, there are conditions in which the relation of both variables gains importance.

The transfer allows several deductions regarding the target structure. The first direct result is a prediction of its force-displacement curve. The integral of this curve provides the impact energy associated with each damage status. Thus, a correlation of the impact energy on the original structure and the target structure can be derived – a *curve of equivalent energy*. Figure 3.8 shows such a curve, for an origin and a target that serve as validation in the following section. Each instance of impact energy on the target structure is associated with an energy level at the origin. This correlation makes it possible to scale the impact energy for similar damage. A transfer could also be performed on the basis of equivalent elastic contact force by using only the elastic part of the spring-mass model. An explicit analytical correlation that results in the plotted curve can be derived from Equations (3.17) and (3.11). Yet, this approach does not take into account that the stiffness decreases with progressing damage. As such, the impact energy is overestimated when the transfer target is softer than the origin, as is the case in the example plot. However, an elastic-force-equivalent transfer might serve as an alternative approach if no experimental or numerical data concerning the impact event are available. In the energy range in which no damage occurs, both transfer methods provide the same result. The larger the damage size, the larger the error of force-equivalent scaling becomes.

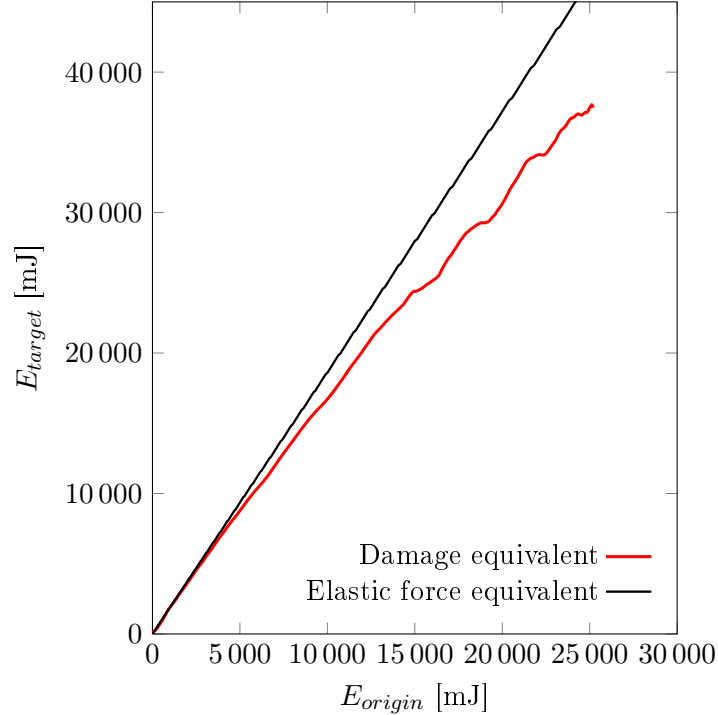


FIGURE 3.8: Curve of the damage-equivalent impact energy for the transfer origin and the target.

### 3.3.2 Unstable damage propagation

The problem of the method described in Section 3.3.1 is that the displacement function  $w(F)$  is mathematically not injective. Several displacement values  $w$  can correspond to same contact force. This multiplicity prevents a completely force-dependent objective damage description. A force-dependent damage description would limit the method to monotonically increasing force-displacement responses. Consequently, the case of decreasing contact force has to be distinguished. The decreasing force corresponds to unstable damage propagation. As Figure 3.9 shows, elastic energy is released when the force drops. This released energy further propagates the damage until a new equilibrium is reached.

To handle unstable propagation, the force history is split into injective and non-injective sections. Each injective section ends when  $\dot{F} < 0$ . A new injective section starts when the new equilibrium is reached. Further analysis steps are necessary to determine this new equilibrium state after unstable damage propagation.

A force drop releases energy from the global structure as illustrated in Figures 3.9 and 3.10. Equation (3.19) describes the released energy. For an equivalent force value, a compliant structure provides a larger energy reservoir than a stiff structure. The released energy is transferred to the damage element  $k_d$ , representing the compliance by damage in the spring-mass model. This energy transfer is illustrated in Figure 3.10. A part of the transferred energy is absorbed elastically. Further progression of  $k_d$  is also possible. This progression affects the contact force so that the released energy further increases.

$$E_{release} = \int_{w_g(F_{drop})}^{w_g(F_{up})} k_m w_g^3 + k_{bs} w_g dw_g \quad (3.19)$$

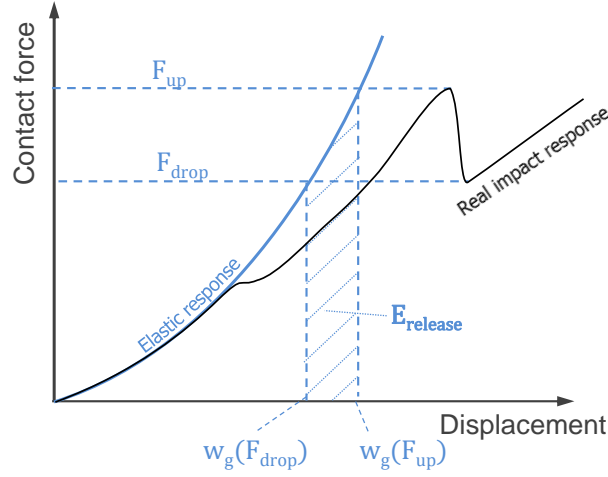


FIGURE 3.9: Released energy of the global elastic structure of an impact configuration when the contact force drops from  $F_{up}$  to  $F_{drop}$ .

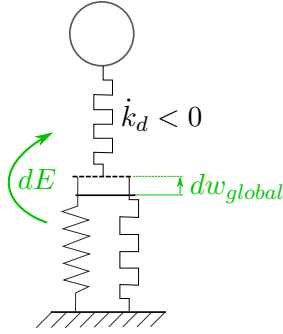


FIGURE 3.10: Spring-mass model illustration of the energy transfer during damage growth with decreasing contact force.

The damage growth is unstable as long as the structure releases more elastic energy than  $k_d$  can absorb elastically. If  $\frac{dE_i}{dk_d}$  exceeds  $-\frac{dE_d}{dk_d}$ , the damage propagates unstably. This criterion in Equation (3.20) evaluates the derivatives and compares the released energy and the absorbed energy with respect to  $k_d$  for unchanged total displacement  $\dot{w} = 0$ . The idea is analogous to the fracture-mechanical principle of energy release rates (compare to Section 1.4). The value  $-\frac{dE_d}{dk_d}$  stands for the critical ERR, while  $\frac{dE_i}{dk_d}$  is the damage- and load-specific ERR. The damage propagation remains stable as long as the released energy is smaller than the capability for elastic absorption. *This criterion is key to capturing force drops in the impact transfer.*

$$\frac{dE_i}{dk_d} < -\frac{dE_d}{dk_d} \quad (3.20)$$

Regarding the energy that can be absorbed elastically by  $k_d$ , the derivative of  $E_d$  with respect to  $k_d$  is a simple equation, Equation (3.21). Yet, according to the chain rule, this equation still requires the derivative of  $w_d$  with respect to  $k_d$ . The value  $w_d$  depends on four parameters –  $k_{bs}$ ,  $k_m$ ,  $k_d$ ,  $w$  – as shown in Equation (3.23). Among these, three are constant, and only  $k_d$  is undetermined.

The determination of  $\frac{dw_d}{dk_d}$  is approached by the equation of force equivalence, Equation (3.22), of the global elastic springs and the spring representing the damage.

It can be solved for  $w_d$  with a symbolic computing environment like Maple. The solution is a relatively long term that is differentiable with respect to  $k_d$ .

A similar procedure needs to be conducted for the derivative of the energy released by  $k_{bs}$  and  $k_m$ . This derivative depends only on the indentation  $w_g$ , which can easily be obtained after  $w_d$  is already known.

$$\frac{dE_d}{dk_d} = \frac{w_d^4}{4} + \frac{3}{4}k_d w_d^3 \frac{dw_d}{dk_d} \quad (3.21)$$

$$(w - w_d)k_{bs} + (w - w_d)^3 k_m = w_d^3 k_d \quad (3.22)$$

$$w_d = w_d(k_{bs}, k_m, k_d, w) \quad (3.23)$$

Under the precondition that consecutive values of  $k_d$  are available on sections of decreasing contact force, this theory can be implemented. With this data, the objective force-dependent damage description would be complete. However, the damage description method from section 3.2.2 provides values for  $k_d$  depending on either the energy or the impactor indentation. Therefore, an alternative evaluation for Equation (3.20) has to be conducted.

In the implementation, the derivative of  $E_d$  is obtained from the data of the origin side of the impact transfer. During the iteration process of the transfer approach, the derivative of  $E_d$  for the target structure is calculated. The criterion for a stable damage growth can be formulated by comparing these values in Equation (3.24).

$$-\frac{dE_d_{target}}{dk_d} > -\frac{dE_d_{origin}}{dk_d} \quad (3.24)$$

This modified criterion is weaker than the original formulation in Equation (3.20). Instead of a complete objective damage description, it provides only a comparison of the damage growth stability between the target and the scaling origin. In short, this means that if damage propagation is stable on the transfer origin and the elastically absorbed energy of the scaling target is equal or higher than at the origin, crack propagation on the target is stable, too. Yet, if the target can take less elastic energy than the origin, the behavior is undefined. This is an obstacle to overcome in the implementation. It requires the skipping of several iteration increments until the stability criterion is fulfilled. During those increments, it is assumed that the contact force remains temporarily on the drop value of the transfer origin. In reality, a force drop to a lower value would be expected. The solution would not include this drop, if a scaling is performed toward a stiffer target.

This procedure provides quasistatic scaling for impact scenarios with any force-displacement history. However, the quasistatic assumption still constricts the range of transferable impact scenarios.

### 3.3.3 Modal energy correction

The scaling approach, as presented so far, is founded upon a quasistatic, one-dimensional spring-mass model. As stated earlier in Section 3.2.1, this spring-mass model describes only the fundamental vibration mode of an impact. Thus, it is only valid for a quasistatic event, according to the categorization by Olsson in Figure 1.12 on page 22. The transfer method's range of validity lies within the limits of quasistatic solutions for LVI. Therefore, it strictly limits the target domain of the transfer model to very



large impactor mass and low velocity according to Figure 1.13 on page 23. An extension of the domain toward impacts with low mass and higher velocity would require a consideration of higher-order flexural modes.

Swanson already analyzed this issue in 1992 [179]. According to his work, a sufficient distance between the impact main frequency and the next-lowest eigenfrequency of the structure has to be kept. As a rule of thumb, he proposes that those two frequencies should differ by at least a factor of three. If the eigenfrequencies are closer, a significant ratio of impact energy goes into the higher-order eigenmodes. The energy ratio in the eigenmode is suitable as a measure for an impact's quasistatic character [RB2] because the influence of higher-order modes on the impact response marks the validity limit of a quasistatic solution.

In order to enlarge the range of validity for the scaling, the method has to take into account the energy in other modes. For quantification of that energy, the energy distribution over an impact system's eigenmodes is analyzed based on the modal impact response. This distribution permits derivation of the relevant energy fraction, the energy in the fundamental mode of the impact, for the quasistatic scaling.

However, the modal analysis requires a linearized idealization of the impact system, as Figure 3.11 illustrates. Any nonlinear effects are affected by that requirement. The model does not permit the inclusion of membrane effects, contact phenomena, or damage.

Accordingly, the linearization requires an elastic material model. As we analyze the distribution of energy at the beginning of the impact, this limitation is not a relevant restriction. As shown earlier in Figure 2.15 on page 47, no damage is caused in the initial impact phase. Membrane effects are also negligible, because the derivate  $\dot{F}_m(0)$  is zero according to Equation (3.4). Consequently, the linear behavior dominates the modal energy distribution.

Additionally, the linearized model needs tied contacts between the specimen and the impactor and the support structure, respectively. The impactor and the specimen are in contact during the whole impact process. This fact permits a straightforward procedure for the linearization. A point mass representing the impactor gets tied to the specimen.

The contact between the specimen and the support structure shows different behavior. Not all areas that are initially in contact keep that status during the impact process. Tying all possible contact zones together stiffens the model severely. Neglecting all contacts and using a statically determined support configuration results in a too-soft system. Eventually, this contact requires decisions to be made on a case-by-case basis. For example, tying two opposing edges with the other two edges left unsupported represents one option to achieve a plausible behavior.

The linearized system allows the description of the impact scenario as an initial value problem based on the equations of motion [Equation (1.24)]. The absence of external forces and the negligence of material damping reduces this equation to the homogeneous form in Equation (3.25). In the initial state, all DoF and nearly all velocity components are zero. The only exception is the impact point with the tied point mass, which begins with the initial impactor velocity  $v_i$ .

$$\begin{aligned} \mathbf{M}\ddot{\mathbf{x}} + \mathbf{K}\mathbf{x} &= \mathbf{0} \\ \mathbf{x}(t=0) &= \mathbf{0} \\ \dot{\mathbf{x}}(t=0) &= \dot{\mathbf{x}}_0 \end{aligned} \tag{3.25}$$

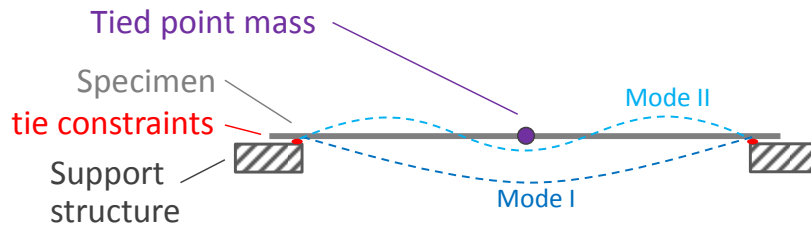


FIGURE 3.11: Model sketch of an impact system for a modal analysis.

A modal analysis [180] is the first step to calculate the modal energy distribution of the linearized impact system. It provides the linear independent vibration modes that can occur without coupling effects. Accordingly, the modal equations of motions, Equation (3.26), are independent of each other. These uncoupled equations result from a transformation of the equation of motion [Equation (1.24)] into the modal coordinates  $\xi$ . Each coordinate  $\xi_j$  stands for one eigenvector  $\hat{\mathbf{x}}_j$ . These coordinates and eigenvectors describe the dynamic response of the linear impact system with Equation (3.27). The value  $N_e$  describes the number of eigenmodes that the approximation considers. Its maximum value is equal to the number of DoF. The choice of a smaller value for  $N_e$  leads to the neglect of eigenmodes with high frequencies. This is a common procedure of model reduction, the dynamic condensation as it was proposed by Paz [181].

$$m_j \ddot{\xi}_j + m_j \omega_{0j}^2 \xi_j = \mathbf{0} \quad (3.26)$$

$$\mathbf{x}(t) = \sum_{j=0}^{N_e} \hat{\mathbf{x}}_j \xi_j(t) \quad (3.27)$$

Equation (3.28) transforms the initial velocity condition from the global to the modal coordinates. This equation is overdetermined when not all eigenmodes are considered, as there are more equations than free variables. Employing an LSQ method, as explained in the Appendix B.2, provides an approximate solution to obtaining the value for  $\dot{\xi}_{0j}$ . These initial velocities already give the energy distribution at the beginning of the impact. There is no elastic energy in the system as all DoF remain zero. Only the kinetic energy has to be evaluated, as Equation (3.29) shows.

$$\dot{\mathbf{x}}_0 = \sum_{j=0}^{N_e} \hat{\mathbf{x}}_j \dot{\xi}_{0j} \quad (3.28)$$

$$\hat{\mathbf{x}}_j \mathbf{M} \hat{\mathbf{x}}_j^T \frac{\dot{\xi}_{0j}^2}{2} = \frac{m_j \dot{\xi}_{0j}^2}{2} = E_j \quad (3.29)$$

The diagram in Figure 3.12 depicts the distribution of the kinetic energy over the first 50 eigenmodes of an impact system with 37 J. We recognize that the energy decreases with increasing mode number (and thus increasing eigenfrequency). The first few modes contain the bulk of the energy. This energy concentration permits the mentioned model reduction through neglect of very high-frequency eigenmodes. In this work, all modes below 10 000 Hz are taken into account. This limit is very conservative and was chosen arbitrarily. The low computational effort of the modal analysis does not demand a stricter approach.

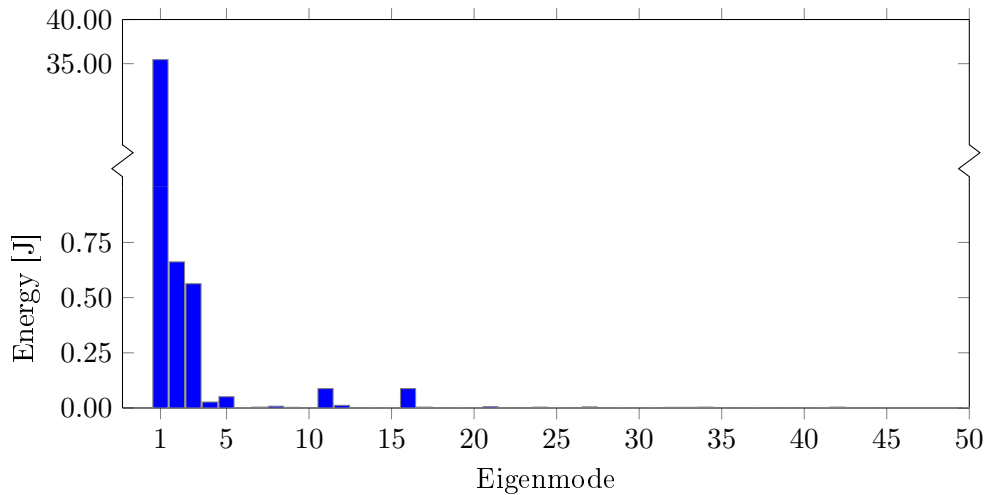


FIGURE 3.12: Distribution of kinetic energy over the first 50 modes of a linearized impact setup.

This energy-correction method quantifies the damage-relevant part of the impact energy. As LVI damage is driven by the first eigenmode, the energy in higher modes is considered as not relevant to damage. Two facts support this assumption. Firstly, the higher-order modes comprise little energy. The associated deformations are likely to occur elastically. This boundary determines whether an impact counts as large-mass impact and the corresponding limit of the target region in the impact overview diagram of Figure 1.13 on page 23.

Secondly, the material damping of carbon fiber material is sufficiently high to dissipate most of this energy before the turning point of the impact. In two independent works, Kottner et al. [182] and Oshima et al. [183] studied the damping behavior of carbon FRP. They provide approximate values for the logarithmic decrement ( $\Lambda = 0.02$ ) and the damping ratio ( $\zeta = 0.003$ ). These values are of similar orders of magnitude and can be used to estimate the decay behavior of higher-order modes during the impact event. The logarithmic decrement describes the amplitude ratio of two successive peaks  $\hat{\xi}(t_i)$  and  $\hat{\xi}(t_{i+n})$  with  $n$  full cycles between [Equation (3.30)]. The energy in an oscillation is proportional to the square of the amplitude. Accordingly, the energy decreases quadratically, and Equation (3.31) describes the energy dissipation over a number of cycles  $n$ . The maximum deflection and the maximum contact force mark the end of the damage propagation. Both maxima co-occur after a quarter of a first-mode-cycle. Thus, the number of oscillations during this quarter cycles is relevant for the decay of higher-order modes. This makes very high-frequency modes even more negligible, as they are completely damped when damage propagates in the specimen.

$$n\Lambda = \ln \frac{\hat{\xi}(t_i)}{\hat{\xi}(t_{i+n})} \quad (3.30)$$

$$E(t_i) \frac{1}{\exp 2\Lambda n} = E(t_{i+n}) \quad (3.31)$$

However, this whole dynamic correction captures only the energy distribution at the beginning of the impact event and would be valid during the whole process if the behavior were purely linear elastic. In reality, damage results in a force drop that can excite the impact system. This excitement relocates elastic energy from the

fundamental mode to higher-order modes. Accordingly, the modal energy estimation provides a minimum amount of energy that is lost to higher-order modes.

### 3.3.4 Obvious constraints and the characteristics of impact similarity

With quasistatic scaling and dynamic correction, the presented methodology permits the achievement of equal damage size in two impact scenarios. Several assumptions that were made to achieve the impact scaling result now in constraints. We distinguish these constraints in two categories: *general constraints* and *similarity requirements* for the origin and the target.

General constraints concern the validity of the spring-mass model or the choice of a reference coupon: Firstly, the damage has to only occur locally around the impact spot. Nonlocal damage that is located out of the reference coupon would not be recognized, using the scaling method. Secondly, fiber cracking must not be the predominant damage mode. Significant fiber cracking in the impact zone would erode the validity of the membrane stiffness approach in the damage element  $k_d$ . Finally, the damage size on the analyzed reference coupon determines the maximum predictable damage size on the target. Scaling can be performed toward smaller damage only. *Extrapolation to larger damage is not allowed.*

In addition, the origin and the target of the scaling have to fulfill several requirements of similarity. The equality is achieved based on several idealizations in a spring-mass model. The simplified damage description of this model entails several restrictions regarding its applicability. The restrictions concern all relevant parameters of the impact scenario:

- laminate stacking sequence in the damage-prone area
- ply material in the damage-prone area
- impactor shape and size
- dynamic impact response
- elastic deformation behavior in the impact zone

Based on this list, the similarity requirements for an impact transfer are formulated. The first three items in the list need to be fully equal. A different material or layup in the damage-prone area would change the qualitative damage behavior. Neither damage threshold forces nor the damage pattern of delamination would be comparable. Changing the impactor would have a similar effect and is also not permitted. Infringing the equality requirements would result in two different damages at origin and target, despite an equality in the value of  $k_d$ .

Even if the dynamic correction according to the Section 3.3.3 is applied, the dynamic impact behavior remains a possible source of uncertainty. If the range of LVI is left, the impact response contains significant higher-order vibration. The dynamic correction presented in this work extends the validity range for cases in which the range of LVI is left, but higher-order eigenmodes do not contribute to the propagation of damage in the laminate. However, these modes can become damage relevant if excited with sufficiently high energy. A study of the phenomenon showed that just 15% of the total impact energy in higher-order modes can affect the impact damage [RB2]. However, this value is valid only for the impact configuration from which it was derived (CAI impact). The energy threshold of a certain eigenmode to become

damage relevant can neither be determined as an absolute value nor as a ratio of the total impact energy. It is individual for each eigenmode and consequently unique to each impact system. And even a possible quantification of the relevant energy amount would not be sufficient to permit the scaling of this damage. The different formations of eigenmodes on the structural level and the reference coupon differently affect the damage. These circumstances impede the scalability if higher-order eigenmodes become damage relevant.

The last item in the list above is a soft condition, requiring only sufficient similarity. This soft demand is based on the principle of Saint Venant [184, 185]. The reagent forces in the support areas are sufficiently far removed from the damage-prone zone. Their exact distribution does not influence the damage. Only the deformation in the impact zone is responsible for shape and extent of the damage. The limits of this deformation need to be analyzed. For example, a long, slender specimen is unlikely to develop the same damage pattern as a quadratic plate. In addition, impact damage close to a supported edge will behave differently from a symmetrical impact. These geometric varieties primarily affect the damage pattern that is to be transferred. However, the force-displacement history can change as well. The development of  $k_d$  is especially influenced by the shifted threshold forces of delamination or fiber cracking.

In order to ensure a sufficient similarity of the deformation behavior, three check values,  $c_1$ ,  $c_2$  and  $c_3$ , are introduced in Equations (3.32) – (3.34). We obtain these values from the displacement gradients in four orthogonal directions around the impact point. The displacements are recorded during the out-of-plane indentation analysis in which the elastic response is determined. Four points with an even distance from the impact spot and a location on two orthogonal lines must be defined. All five points together form a cross, as depicted in the illustration in Figure 3.13.

In this work, a distance from the impact point of  $\Delta x = \Delta y = 5 \text{ mm}$  was chosen. The first two check values describe the deformation symmetry in two orthogonal directions. The stiffness ratio of these two directions is indicated by  $c_3$ . If the parameters of two different impact scenarios are all the same, full kinematic equivalence can be assumed. As long as there is sufficient similarity, a certain tolerance of the three values is permitted. During the validation, the check values were monitored for each transfer. By applying equation (3.35), the quadratic product of all check values can be used for a quick assessment of the deformation symmetry of an impact location. This check value permits the assessment of the similarity of an arbitrary impact location to a symmetrical (usually quadratic) reference coupon. The limit of validity cannot be expressed by a fixed value. It depends on the tracking distances  $\Delta x$  and  $\Delta y$ . In addition, it can vary depending on the material and the stacking. However, the quantitative derivation of appropriate limit values exceeds the scope of this work.

$$c_1 = \frac{w_i - w_{+x}}{w_i - w_{-x}} \quad (3.32)$$

$$c_2 = \frac{w_i - w_{+y}}{w_i - w_{-y}} \quad (3.33)$$

$$c_3 = \frac{w_i - w_{+x} - w_{-x}}{w_i - w_{+y} - w_{-y}} \quad (3.34)$$

$$c_{sym} = [\min(c_1, c_1^{-1}) \min(c_2, c_2^{-1}) \min(c_3, c_3^{-1})]^2 \quad (3.35)$$

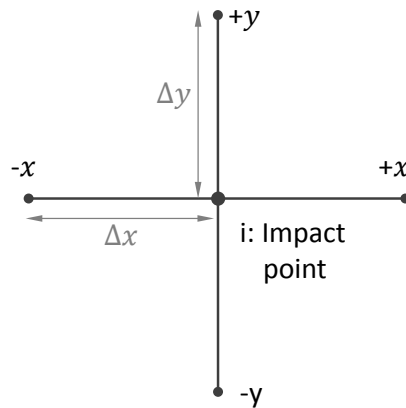


FIGURE 3.13: Location of the four reference points for the derivation of check values of deformation similarity.

### 3.4 Application and validation of the methodology

The validation of the presented models was performed through an extensive impact test campaign. The test campaign was tailored to serve three validation purposes, according to the schematics in Figure 3.14:

- The first validation (red arrow) concerns the damage description through the spring-mass model in which the additional compliance by damage is the damage parameter. The corresponding check is founded upon a test series of coupon impacts on different energy levels.
- The green arrow indicates the validation of the impact scaling method. This validation fully relies on experiments to prevent a possible bias of the virtual testing (for possible sources of errors check the critical assessment in Section 2.6). A large test series with differently sized impact specimens and impact locations was conducted in order to check the scaling capabilities under various conditions.
- The last validation step (blue arrows) consists of virtual tests using the high-fidelity model. The respective results are compared to a set of experimental tests. Those tests involved different laminates, boundary conditions, and energy levels. This calculation has already been made in Section 2.5 and is mentioned here only for the sake of completeness.

#### 3.4.1 Description of experimental impact damage through $k_d$

Based on the second research hypothesis, the modified spring-mass model with the stiffness  $k_d$  was developed to capture the damage state of an impacted composite laminate. This capability shall be validated.

A set of impacts on CAI coupon impacts according to the AITM 1.0010 was evaluated for this purpose. The testing campaign comprises 42 specimens with a quasi-isotropic layup of carbon-fiber prepreg with epoxy resin. We know this configuration *CAI1* from the validation of the numerical impact analysis in Section 2.5. Now, the impact energy of the full set of samples ranges from 10 J to 35 J.

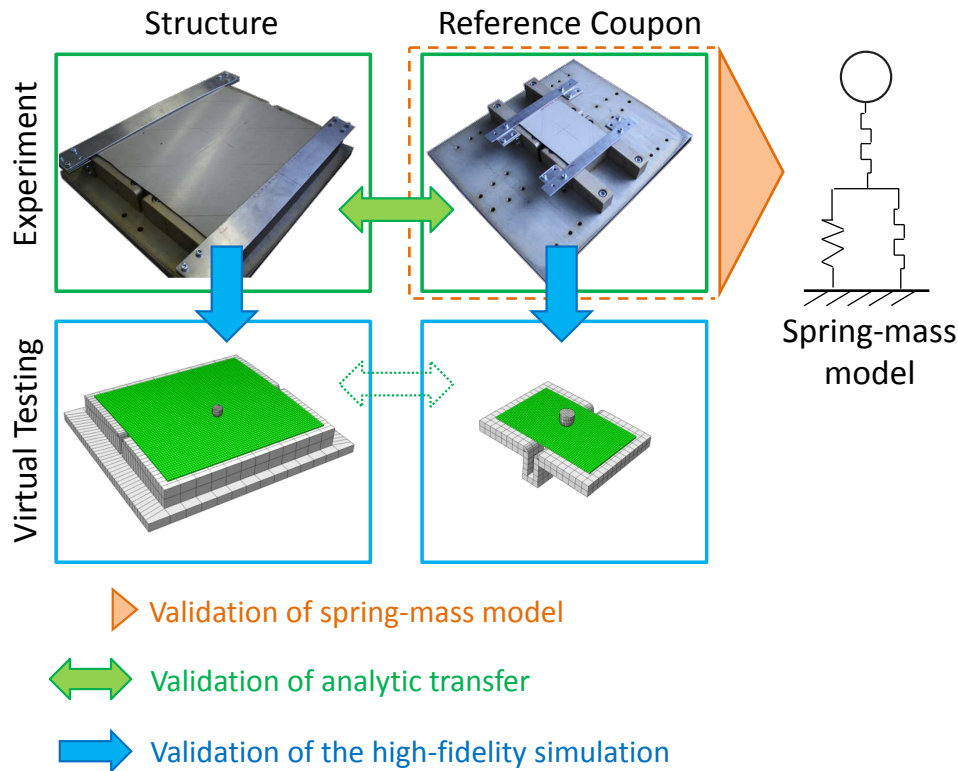


FIGURE 3.14: Validation schematics for the analytical spring-mass model, the impact scaling and the high-fidelity simulation.

The course of the damage parameter during an impact event is depicted in the diagram in Figure 3.15. The measured force-displacement history is plotted together with the history of  $k_d$ . Additionally, the elastic force-displacement curve of the specimen is part of the diagram, completing the source data from which  $k_d$  was derived. The derivation of  $k_d$  was conducted according to the determination principle presented in Figure 3.6. For this determination, the actual impact response curve can be a result of an experiment or an impact simulation. The elastic response is obtained from an elastic FE model.

Continuous evaluation of the damage parameter, as shown in Figure 3.15, allows the observation of the damage-progress during the impact event. Onset and propagation of damage soften the laminate stiffness. This softening is indicated by a drop of  $k_d$ . Flat periods of  $k_d$  indicate a temporary elastic behavior of the specimen.

With the spring-mass model set up from the relations in Figure 3.15, we can immediately verify the suitability of this model. Firstly, the force-displacement response has to be reproduced correctly. Secondly, the force-time history, which involves the effects of inertia should fit the test result. Figure 3.16 shows both curves as obtained through the numerical solution of the equation of motion, Equation (3.13). They affirm an excellent agreement of the analytical results with the experimental basis. From this result, we conclude that the developed model suits the description of an LVI response.

Beyond the impact response, the model shall describe the damage state of the impacted laminate. Therefore, the entire set of tested CAI specimens was evaluated for the final state of the damage parameter  $k_d$ . Figure 3.17 shows the results, including one complete  $k_d$ -curve of a single specimen. This curve was derived from a 30 J

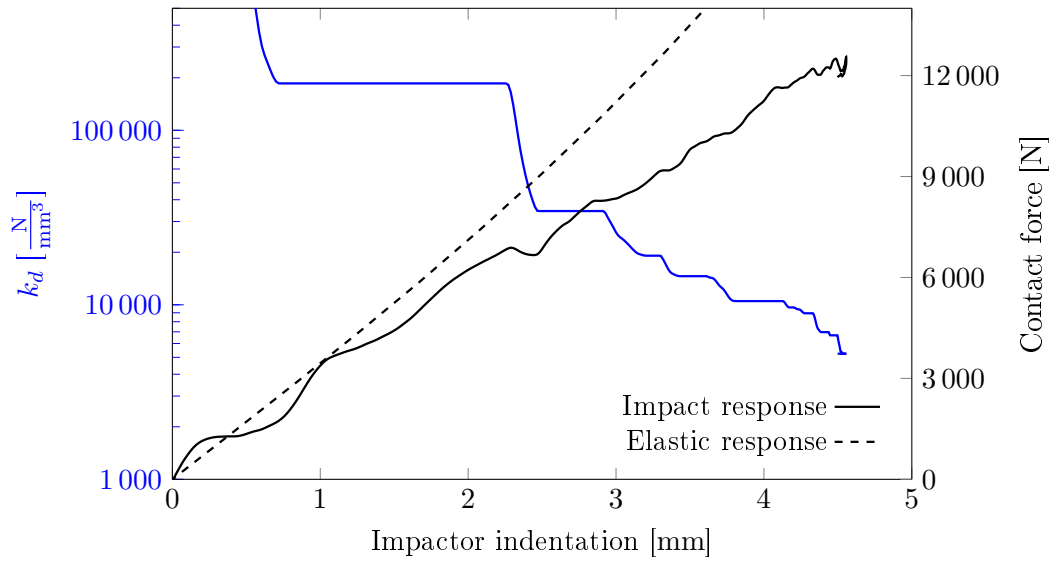


FIGURE 3.15: Development of the damage parameter  $k_d$  (blue) and the corresponding force-displacement history (black) on the example of a 30 J CAI impact (configuration *CAI1.30* in Section 2.5).

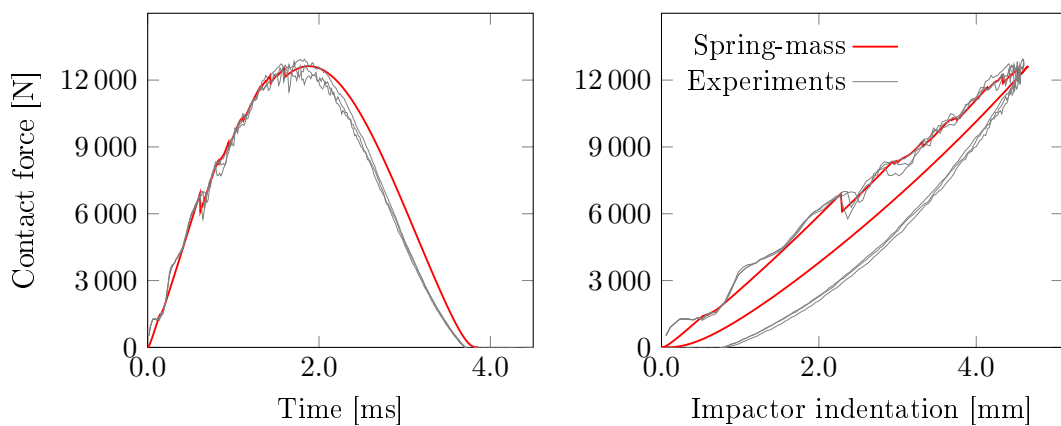


FIGURE 3.16: The spring-mass model's results for the force-time and force-displacement responses of a 30 J CAI impact (configuration *CAI1.30* in Section 2.5).



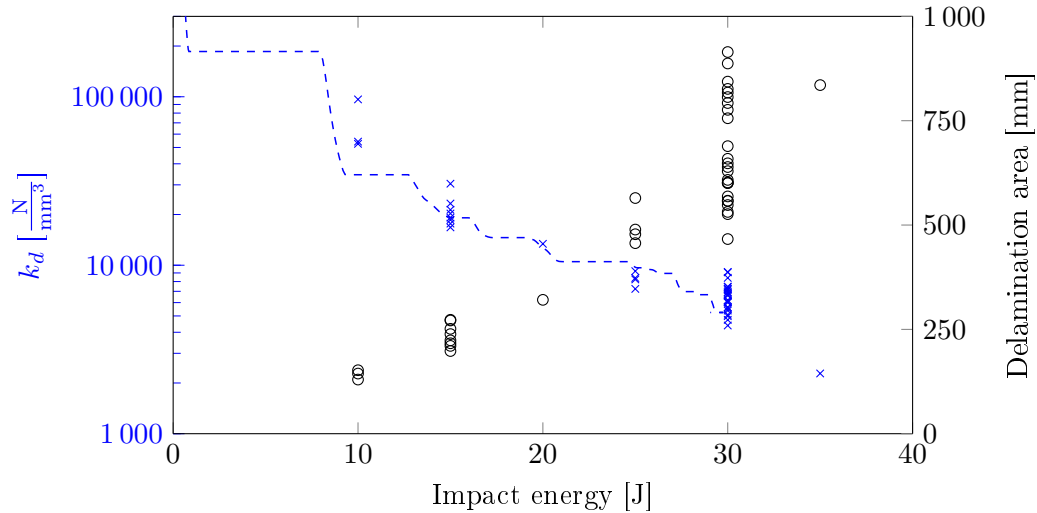


FIGURE 3.17: Comparison of the projected delamination area (black) with the values of  $k_d$  (blue) for a set of CAI experiments with the continuous course of one exemplary 30 J experiment (dashed line).

impact, permitting an evaluation in the energy range from 0 J to 30 J. The trend of the single specimen is in accordance with the data points of the test set. The damage compliance is presented here as a descriptive parameter of the damage status. Usually, the projected delamination area is used for the description of this damage status.

In order to prove the validity of the new description, the delamination area for each instance of impact energy is plotted in the same diagram. The  $k_d$  axis is logarithmic, as the range is between 100000 and 1000  $\frac{\text{N}}{\text{mm}^3}$ , and it exponentially decreases with an increasing impact energy. A significant scattering of  $k_d$  is detectable, in particular for high impact energy. Anyway, this scattering is qualitatively similar to the scatter of the delamination area. This similarity indicates that the scatter is not due to the descriptive model, but due to the real scattering of impact experiments, as it has also been reported in the literature [105, 166, 167].

The damage  $k_d(E)$  is a specific function for each impact configuration. Its ideal course without scattering in Figure 3.17 would be the same line for all specimens, each ending at the associated impact energy value. The line itself changes only if other parameters of the impact scenario are modified. These can be the shape or size of the impactor, the laminate configuration, or other modifications.

However,  $k_d(E)$  can also be affected by the specimen type, the location or the boundary conditions. In order to scale the impact parameters between different impact scenarios, the specific description of the compliance by damage must be replaced by an objective description. In general, objectivity concerning the elastic stiffness parameters  $k_{bs}$  and  $k_m$  is required.

### Energy dissipation by damage

As stated in Section 3.2.3, the analytical spring-mass model provides information about the energy dissipation  $E_d$  by damage. This dissipation results from the stiffness loss in the damage element  $k_d$ , and the function  $E_d(k_d)$  does not depend on the global stiffness parameters  $k_{bs}$  and  $k_m$ . The energy value  $E_d$  is an objective damage description comparable to  $k_d$ . Combined with the elastic stiffness parameters, the spring-mass model calculates the energy correlation  $E_d(E)$  according to Equation

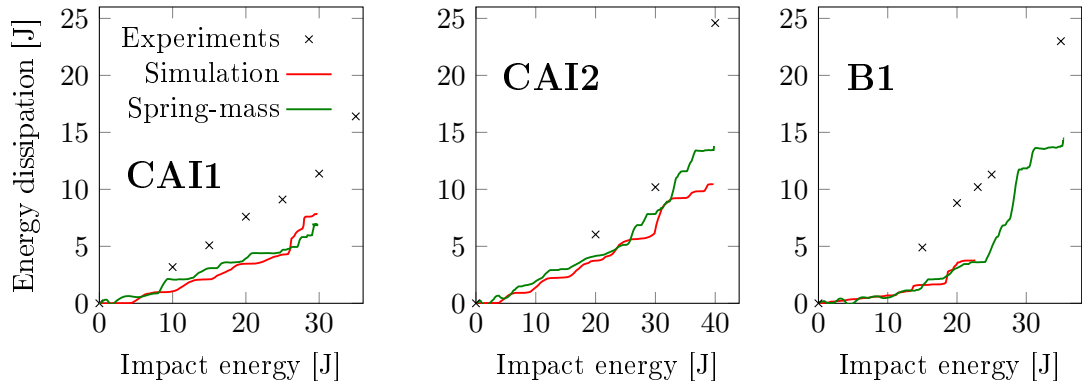


FIGURE 3.18: Energy dissipation by damage in comparison between the experiments, the high-fidelity simulation and the analytical spring-mass model.

(3.12) from page 79. The evaluation of this equation in each displacement increment of the iteration Equation (3.14) leads to a continuous history  $E_d(E)$ .

With that relation, we extend the previous relations of the impact energy and the energy dissipation (Figure 2.28 on page 66). In addition to the experimentally observed dissipation and the numerical prediction, we include the analytically obtained value from the spring-mass model in the diagram in Figure 3.18.

The dissipated energy of the model remains far below the experimental results. However, the trend is qualitatively similar. We observed the same effect for the numerically predicted energy dissipation. Even more, the notable agreement of the analytical and the numerical curve suggests a similar physical cause. Both curves are an extract of the full energy dissipation during an impact. However, this agreement is not a validation, as an experimental determination of energy in the damage modes was not conducted. The accumulated delamination area, fiber crack length, and inter-fiber crack length have to be determined in order to validate the energy absorption. So far, the agreement only *indicates* validity; it does not prove it.

### 3.4.2 Validation of the impact scaling

#### Test setup and impact configurations

For practical application, the impact scaling approach permits the analysis of a structural impact scenario on a reference coupon. For the purpose of validation, I define a different scaling scenario: *the result of a known coupon impact (reference coupon) shall be reproduced in various scaled impact scenarios*. These impact scenarios differ in the type and size of the specimen and the impact location. There are five different specimen geometries and a total of 18 different impact scenarios. The first of these is the reference impact configuration (REF). Based on the result of REF, different impact scenarios were defined to result in similar damage as on the reference coupon REF.

Under ideal conditions, similar damage would emerge in all 18 configurations. In contrast to the application scenario with different reference coupons, the chosen scenario is more convenient to evaluate. A direct comparison of the results of all configurations becomes possible and immediately shows deviations. Additionally, the

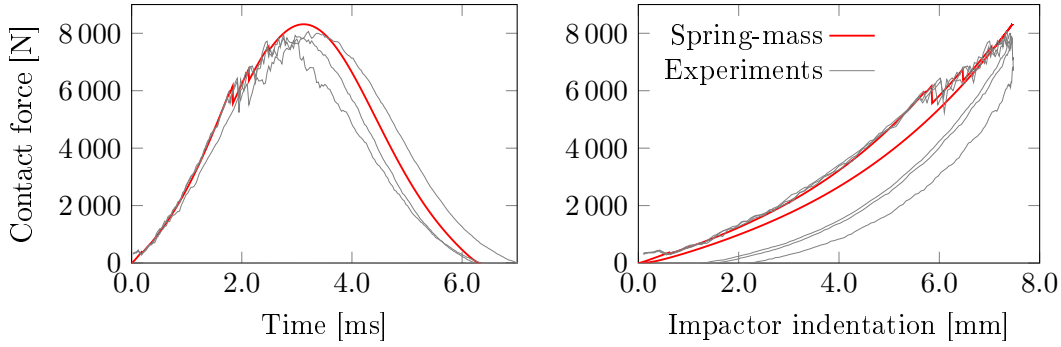


FIGURE 3.19: The spring-mass model’s force-time and force-displacement history of the reference impact “REF” (B1) with 25 J.

reduction to a single reference coupon reduces the number of required validation experiments. Otherwise each impact configuration would come along with its own reference impact. Despite this reduction, the full scaling methodology is conducted for each configuration. Thus, the approach suits the validation purpose.

All specimens have the same layup  $[45, -45, 0, 90, 45, -45]_s$ , consisting of plies from unidirectional carbon fiber prepreg material with a thickness of 0.184 mm (Material I in Appendix A.3). The geometries and impact locations are shown in Figure 3.20. The reference coupon is a small specimen of type “B” with an outer dimension of  $160 \times 110 \text{ mm}^2$ . The reference impact “B1” is placed in the middle of this specimen. The impact energy for this reference impact was determined in preliminary tests with this impact configuration. These tests aimed at finding the impact energy that leads to the maximum possible damage size that would still be classified as BVID. The visibility classification is based on a limit value of 0.3 mm permanent indentation. On average, this value was reached with an energy of 25 J. Under this impact load, a delamination-dominated damage with a projected damage area around  $500 \text{ mm}^2$  occurs. Inter-fiber fracture comes along with this damage and is mainly visible on the impact backside. Fibers already break in the uppermost ply at a length of approximately 20 mm. Based on our assumption of small impact damage, we consider this as still acceptable to be captured by damage variable  $k_d$  in the spring-mass model. As such, the 25 J configuration was chosen for the reference impact in this testing campaign.

We already know the described reference impact “B1” (REF) from the validation of the numerical impact simulation in Section 2.5. An elastic FE analysis provides the stiffness parameters  $k_m$  and  $k_{bs}$ . These parameters are combined with the experimental force response to build the corresponding spring-mass model of the scaling origin. Any scaling to be based on this spring-mass model necessitates the model’s validity for the scaling origin itself. The diagrams in Figure 3.19 verify this analytical description. Its force-displacement history fits well to the experimental basis. The force-time history also match the test result.

Apart from the reference coupon, there are four other types of test specimens for the scaling: one coupon of similar size as the reference but with the layup turned by  $90^\circ$ , two larger coupons of  $280 \times 160 \text{ mm}^2$  with and without a central stiffener, and finally a  $340 \times 310 \text{ mm}^2$  panel section with a central stiffener. The stiffeners measure 20 mm in height, consist of the same layup as the skin, and arise from the skin plies. Consequently, there is neither a stiffener foot nor a bonding interface.

All impacts were conducted under simply supported boundary conditions with clamping strips at two opposing edges. For that purpose, a special support fixture for these specimen types was used, as shown in the pictures in Table 3.1.

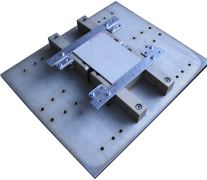
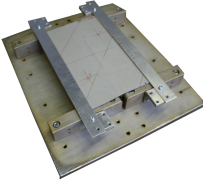
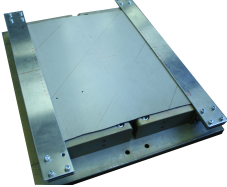
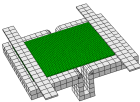
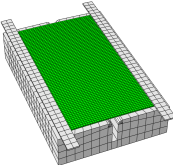
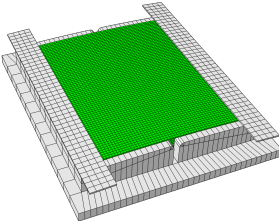
Coupon type	A,B	C,D	E
Test setup			
FE model			

TABLE 3.1: Test setups (upper row) and finite element models (lower row) for all specimen types of the transfer validation.

On each of these coupon types, several target impact locations were defined. To achieve the same damage for all configurations, the reference impact shall be scaled to each configuration. For that purpose, the reference coupon is always the scaling origin, while each new impact configuration forms a target. Consequently, an elastic indentation analysis has to be conducted for each target. For that purpose, the test setup was fully modeled with finite elements. Table 3.1 also shows the corresponding model for each test configuration.

The elastic finite element analyses with layered shells provides the elastic force responses for all configurations. In this analysis, it is crucial to apply consistent methods on the origin and on the target. This concerns mainly the prescribed indentation at the impact point, which has to be accomplished through the same method. For example, modeling the impactor is possible but not mandatory. The indentation can be achieved by a concentrated out-of-plane force at a single node representing the impact spot. This can save computation time as there is no numerical contact formulation between impactor and specimen. If the elastic simulation does not require contact modeling, an implicit solution can provide results very quickly. If the elastic model involves contact, an explicit time integration is more efficient.

The force response from this FE analysis forms the basis for the determination of the elastic spring parameters  $k_m$  and  $k_{bs}$ . The symmetry check values  $c_i$  are derived from it. To calculate the required impact energy, the impact response of the reference coupon is considered. For this calculation, the result of one reference impact was used.

This calculation did not include the modal energy correction to capture the dynamic energy loss. So, this set of experiments validates primarily the quasistatic scaling approach. Nevertheless, the eigenmode-based dynamic correction from Section 3.3.3 is employed later in the validation process, to explain deviations.

Table 3.2 presents the geometric configuration, the stiffness parameters, the symmetry conditions, and the calculated impact energy for all impact scenarios in the test set. Additionally, it shows the number of conducted tests. This number of tests depends on two factors: firstly on the number of available specimens of this type and secondly, on the result of the first test in this location. If the damage was qualitatively

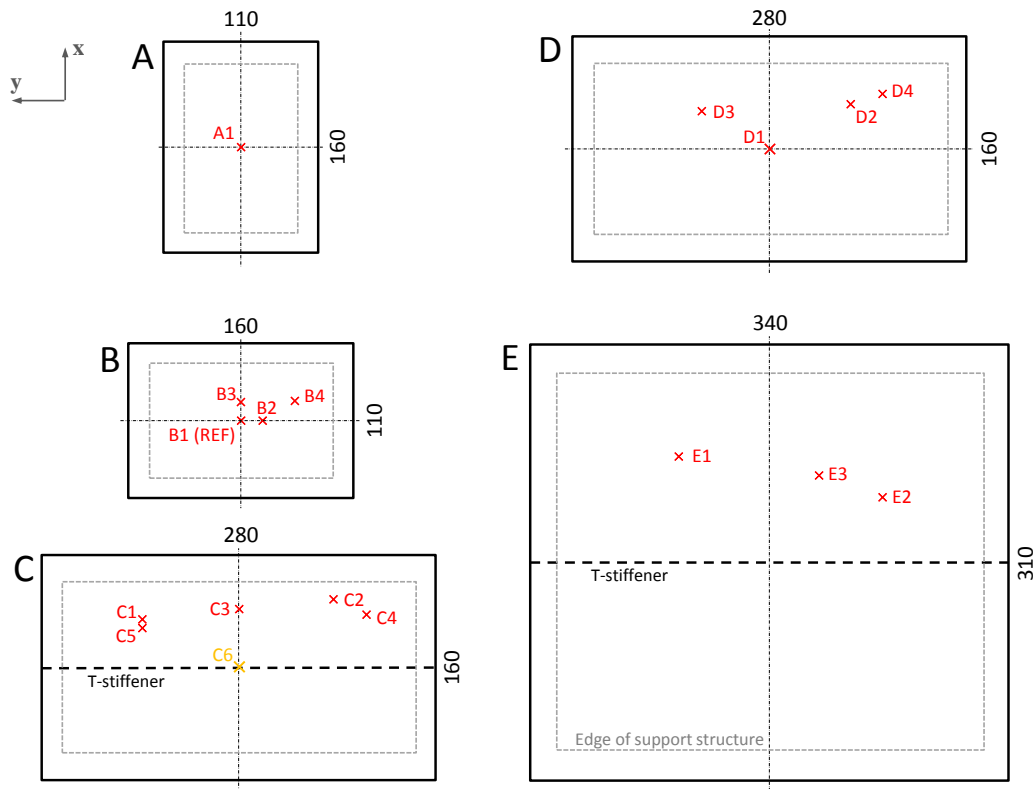


FIGURE 3.20: Geometry of all five validation specimen types and the 18 chosen impact locations.

different from the reference damage, the corresponding configuration was considered devalidated. In this case, the transfer is not valid. The different damage indicates that another reference coupon would be required to scale this impact location.

The impact positions were intentionally chosen to achieve impact scenarios that differ according to the following criteria:

- global indentation stiffness (and impact energy, respectively)
- symmetry conditions in various directions
- distance to a support structure
- distance to a stiffener
- ratio of membrane and plate deformations

As the reference coupon is small and stiff in comparison with most of the other impact configurations, nearly all transfers require a higher impact energy than did the reference coupon. The energy spectrum ranges from 21 J up to 39 J. The impactor mass remains constant at 3.99 kg. With this mass, the impact drop tower (Appendix A.1) can cover the required energy range.

### Validation results

The scaling procedure according to the flowchart in Figure 3.7 directly provides the force-displacement history of a scaling target. Therefore, this history curve is the

first result to be considered in this validation. The measured curve of the impact experiments is compared to the analytical curves derived from the spring-mass model. Figure 3.21 shows the force-displacement history of four exemplary impacts. The full set of diagrams is included in Appendix A.4.

The transferred force-displacement history curves in comparison with the experimental results are evidence of a very strong validity. The loading phase of all three test cases is well predicted. The damage onset thresholds also match. As a rule, the impact on the origin and the target have to exceed the same damage thresholds. This requirement leads to the side effect of similar maximum contact force values for similar damage. When the force before the threshold determines this maximum, the value is trivially similar. In addition, if the contact force exceeds the value of the last threshold, the maximum contact force is also similar for the target and the origin: the last section of the force-displacement curve is injective, and the spring-mass model provides a force-equivalent scaling. Thus, an equal maximum load is a necessary but not a sufficient condition for damage-equivalent impact scenarios.

Obviously, the oscillation behavior of the curve is not predicted, as it results from eigenmodes of a higher order. These are not part of the transfer as the spring-mass model is based on the first mode only. The result confirm the capability of the developed transfer method to predict the force-time history.

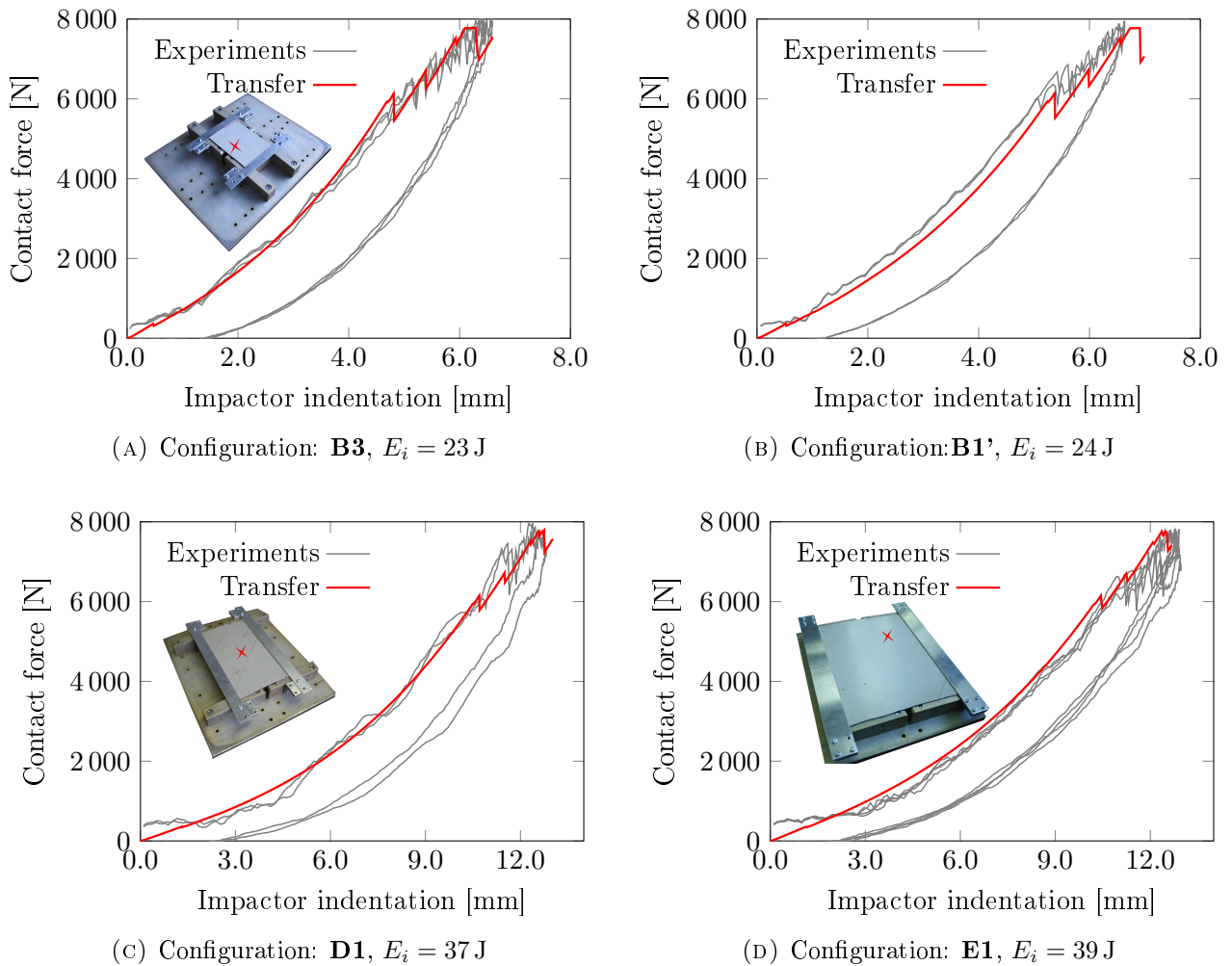


FIGURE 3.21: Force-displacement history of experimental impacts (grey) and prediction by the transfer (red) derived from the reference impact.

According to the conducted transfer of impact damage, all impact tests were designed to result in similar damage. I address this aim in the main step of the validation. Several metrics quantify the impact damage: the maximum contact force, the projected delamination area from the ultrasonic detection, the visible fiber crack length on the impact front side of the specimen, the visible inter-fiber crack length on the impact back side, and the energy absorption during the impact event. Additionally, each impact force provides a value for the damage parameter  $k_d$ . These results are also part of the validation, as  $k_d$  is the actual subject of the damage transfer. Consequently, it should be similar beyond the impact configurations.

- Similar *maximum contact force* is a necessary but not a sufficient condition for similar damage [RB3], as the same threshold forces have to be exceeded. However, in regions of decreasing contact force, differences in the damage propagation do not affect the peak force.

As visible in the first diagram of Figure 3.22, nearly all configurations fulfill the requirement of similar contact force. The only exceptions are the configurations B4, C4, D4, and E2. The deviation of these cases is visible but does not appear severe.

- The *delamination damage* is the predominant damage mode in BVID. The projected area is a common measure to assess this result. For the present validation, it is vital also to look at the qualitative delamination results as they are provided for all tests in Appendix A.4.

The second graph of Figure 3.22 compares the projected area of all configurations. We see a result that differs more. The configurations B4, C5, D3, and D4 deviate significantly from the reference range.

The qualitative delamination pattern also provides information about the similarity of the occurring damage modes. Indeed, most of the damage patterns are qualitatively similar. However, there are several configurations with very different damage. These are B4, C4, C5, D4, and E2.

- The lengths of the observable fiber cracks and the inter-fiber cracks on the specimens serve as measure for *intra-ply damage*. The third diagram in Figure 3.22 shows the respective crack lengths, measured for each configuration.

On the reverse side, tensile IFFs emerge. The crack aligns with the fiber orientation and does not branch. The same crack type also occurred constantly in nearly all impact configurations. A qualitatively different crack was observed in the asymmetric impact locations B4 and D4, where fiber cracking also occurred on the reverse side and the inter-fiber crack branches. Quantitatively, the damages of several configurations (C4, D3, E1, E2, E3) lie outside the range of scattering as observed on the reference coupon.

On the impact side of the specimen, compression-driven FF occurred. Two separate cracks initiate from the contact area with the impactor. The measured value in the diagram shows the accumulated length of both observed cracks. The behavior is comparable to what we observed for the IFF. Both B4 and D4 qualitatively differ from the reference coupon. In all E configurations, shorter fiber cracks emerged.

- The *energy absorption* during the impact is a parameter commonly related to the resulting damage size. Therefore, I also considered it an indicator of the similarity of the impact scenarios. However, this value emerged as an unsuitable

measure for that purpose. The energy absorption increases especially for soft impact spots that require high impact energy. Especially affected are the impacts on the specimen types D and C.

Several effects cause this increase. The significant energy absorption during the relaxation phase was described in the validation section of the high-fidelity model 2.5.2. Secondly, the dynamic energy loss to vibrations of a higher order was not taken into account for the energy calculation of the scaled impacts. However, the follow-up evaluation of the modal energy correction will later be used to explain the observed deviations.

- As damage parameter,  $k_d$  is the key to the impact scaling. Figure 3.23 shows the state of this parameter for all impact configurations. To provide an easier classification of the scatter and the deviations, the diagram includes two reference lines of 15 J and 35 J impacts on the reference coupon.

The results of  $k_d$  tend to an inverse distribution over the configurations as the projected delamination area. This tendency is plausible because smaller values of  $k_d$  stand for larger damage. However, there are some exceptions. In the impact configurations C4, D4, and E2, a small delamination area has small values of  $k_d$ .

The evaluation of the damage result supports the validation of the scaling method, but also suggests the devalidation of several test cases. Summarizing the results, we observe sufficiently similar damage for 9 of 17 conducted quasistatic transfers. The damages of the remaining eight configurations differ by at least one measure from the reference impact. The concerned configurations are B4, C4, C5, D3, D4, E1, E2, and E3.

These numerous potentially invalid transfers are not surprising, as the impact locations were specifically chosen to test the area of validity for the newly developed approach. The next validation step is to analyze whether these cases represent a violation of the area of validity or an actual devalidation. For that purpose, we consider the different phenomena that occurred on the above-mentioned impact transfers.

**Qualitatively different damage (B4, D4, C5):** Different damage modes were observed for three configurations. During the B4 and D4 impacts, fibers failed on the reverse side. This failure significantly affected the delamination size and its qualitative pattern. Both concerned impact locations are close to the edge of the specimen and have different symmetry characteristics than the reference impact. Thus, these locations indicate the limit of transferability for impact locations with a different deformation behavior. To resolve this issue, another reference impact that is comparably asymmetric has to be employed.

In addition, the C5 impact damage interacted with the stiffener on the skin. The delamination propagates under the stiffener, which significantly increases the delamination area. As the specimen was impacted 30 mm away from the stiffener mid plane, this behavior is hardly surprising. The impact damage with a length of 40 mm grows close to the stiffener edge. Under these circumstances, interaction with this stiffener is likely. A close look at two impacts of the configuration C1 shows already the beginning of this effect. The impact is located 36 mm away from the stiffener mid plane, and the lowermost delamination is slightly asymmetric. The half side that points to the stiffener becomes larger.

This second damage phenomenon indicates that the impact location requires a different reference coupon. This coupon has to include the stiffening element, and



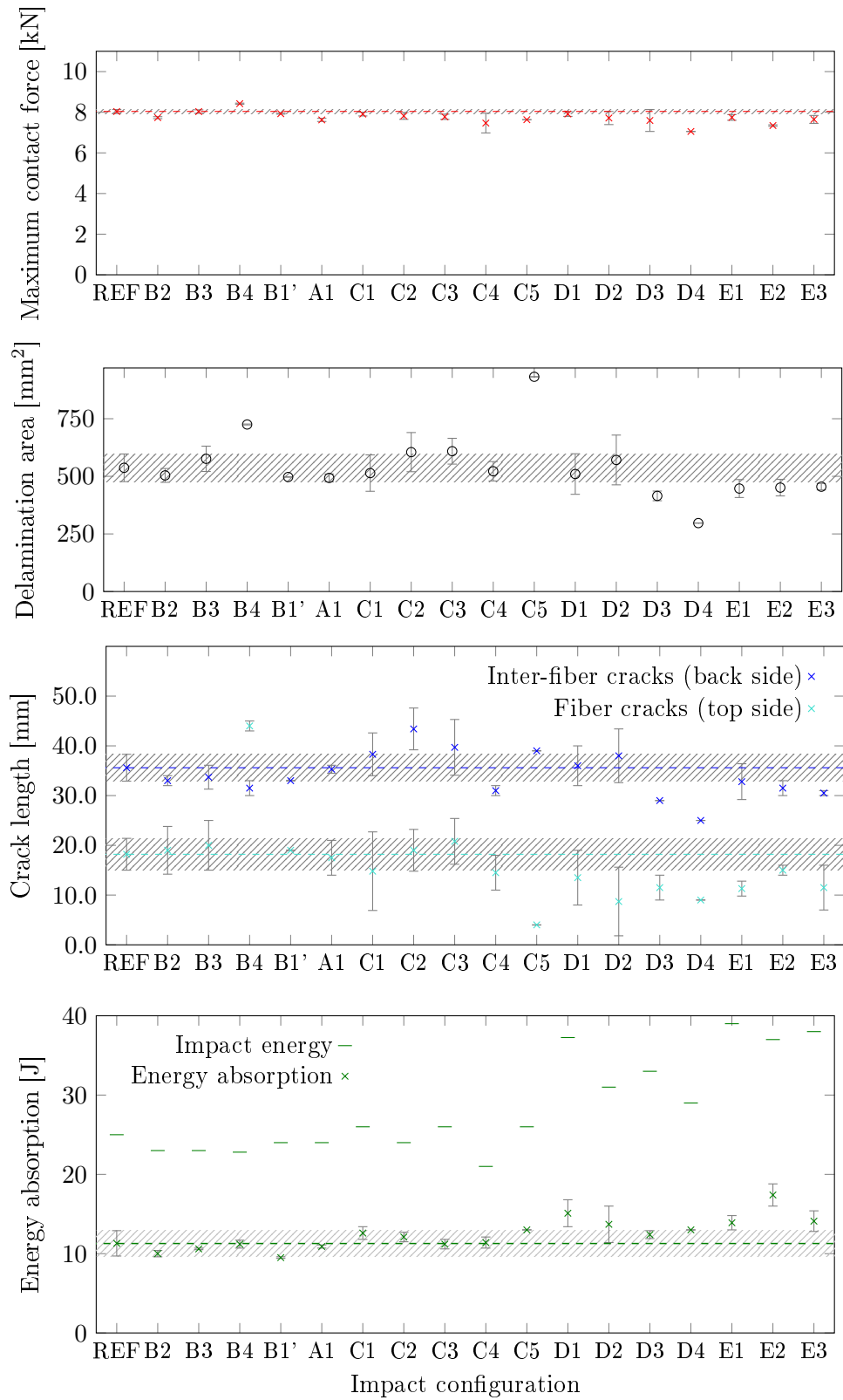


FIGURE 3.22: Maximum contact force, delamination area, crack length, and the energy absorption of all scaled impact experiments.

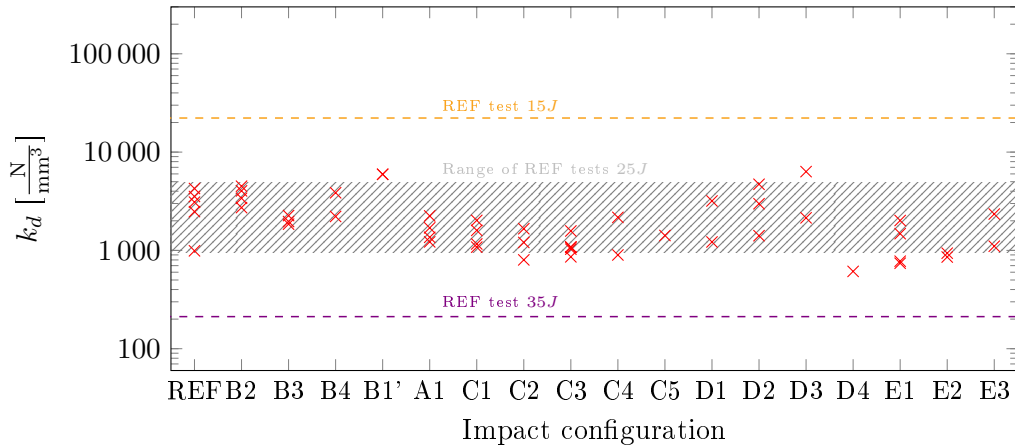


FIGURE 3.23: Experimentally determined values of  $k_d$  for all tested impact configuration that shall result in a similar damage as the reference coupon (REF).

the impact has to be placed at a distance equal to that of the structure, because the damage-prone area of the impact has to remain unchanged. The same requirement applies to impacts close to free edges, holes, or connecting elements; thus all these cases can be captured. However, the universal validity of such reference impacts is smaller than for monolithic impact locations.

**Non-local damage (C4 and E2):** Two configurations resulted in nonlocal damage occurring in addition to the main damage at the impact spot. The respective D-scan delamination results (Appendix A.4) show that additional delamination initiates at the ends of the stiffener. This stiffener was not part of the reference coupon. Accordingly, the transfer method as currently conducted would skip this second damage hot spot.

An appropriate solution to this problem has to be employed on the structural level. In the present approach, an elastic finite element model captures the behavior of the structure. A detection of a possible nonlocal damage hot spot can be performed during this elastic indentation analysis. If we consider Section 1.4, an appropriate prediction of damage initiation has to take into account the out-of-plane stresses. Therefore, a FEA with shell elements using the extended two-dimensional method [155, 156, 157] offers excellent possibilities. As I described in the model-building section, 1.4, a layered-shell model using this theory permits the combination of fast FEA with a reliable prediction of the damage onset. A degradation would not be required.

A special case of nonlocal damage is the impact scenario *C6*, where the impact was placed directly behind the stiffener, as Figure 3.20 shows. This impact position is the only one that was not intended to cause damage similar to the reference coupon. The obtained delamination result is also part of Appendix A.4. There are two damage-prone zones at the ends of the stiffener, but no local damage at the impact spot in the middle of the stiffener. This case represents the extreme example of nonlocal damage.

The transfer method would still be applicable for problems with nonlocal damage. However, the respective reference coupon has to be selected to be quite large.

**Quantitative deviation (D3, E1, E3):** Even if the observed damage modes are consistent with the reference, in some cases their size still differs from the intended

measure. The concerned impacts fulfill the similarity requirements as formulated in Section 3.3.4 of this chapter. In a different way from the nonlocal damage and the kinematically un-similar impact locations, the varying damage size could devalidate the methodology. Its purpose was to determine the energy quantity that results in a specific damage size under the premise of qualitatively equal damage behavior.

The mentioned cases all resulted in smaller damage than predicted. To find out why some damages emerged as smaller than the reference we try to track the causes. Three transfer configurations lead to smaller damage than predicted. These occurred without exceptions on larger coupons (D and E), where the indentation stiffness was significantly softer than the reference. However, their energy absorption of these configurations was larger. Apparently, this additional amount of energy did not yield to damage propagation. To explain this seeming paradox, the dynamic energy balance is the right point to consider. The observed loss of energy was the driving factor in establishing the modal energy correction according to Section 3.3.3. The diagram in Figure 3.24 shows the energy loss in vibrations modes of higher order and the ratio of damage-relevant energy (energy in the first mode). While all configurations on the small coupons have a negligible dynamic energy loss, losses of more than 1 J were calculated for all configurations on the specimen E. Therefore, the respective impact requires higher energy to cause damage that is similar to the reference. Nevertheless, the quantity seems to be too small to explain the smaller damage size. Indeed, this energy amount is not the full dynamic energy loss but an estimation of its minimum. The modal approach considers only the loss by the initial excitement of the specimen. The real loss will still be higher: each contact force drop re-excites the higher-order vibration in the specimen, as the oscillating contact force proves. So the currently suggested modal correction is capable of providing a tendency to improve the scaled impact energy. The impact damage on the reference coupons shows three significant drops of contact force. Assuming that each of these excitements is comparable to the initial excitement, a factor four would have to be considered for the dynamic energy loss in comparison with the calculated values in Figure 3.24. With this knowledge of modal correction and the remaining bias, we consider the concerned impact configurations to be validly scaled.

Eventually, the quasistatic scaling method conservatively predicts the impact damage size on the structure – even without any modal energy correction. The dynamic energy loss decreases the effective impact energy on the structure and cuts down the resulting damage size. Thus, the real damage on the structure would emerge as smaller than on the reference coupon.

### Summary of the experimental validation

Beyond the eight outliers, the validly scaled damage result range is larger than the scatter of REF. Impact damage reportedly varies in its dimension and failure modes, even if all test parameters are kept constant [105, 166, 167]. The impact transfer appears to increase this scatter even further. Each analysis step of the transfer procedure in the flowchart in Figure 3.7 on page 80 has a range of uncertainty: both elastic analyses, the interpolation of the elastic spring-mass model, the determination of the impact response, and the derivation of the objective damage behavior. The mathematical propagation of uncertainty can result in a significant increase of the scatter from the reference coupon to the transfer target.

Within the validation program, several causes of uncertainty were identified:

- The boundary conditions during the determination of the elastic indentation stiffness can be inaccurate. Idealized boundary conditions or missing preload

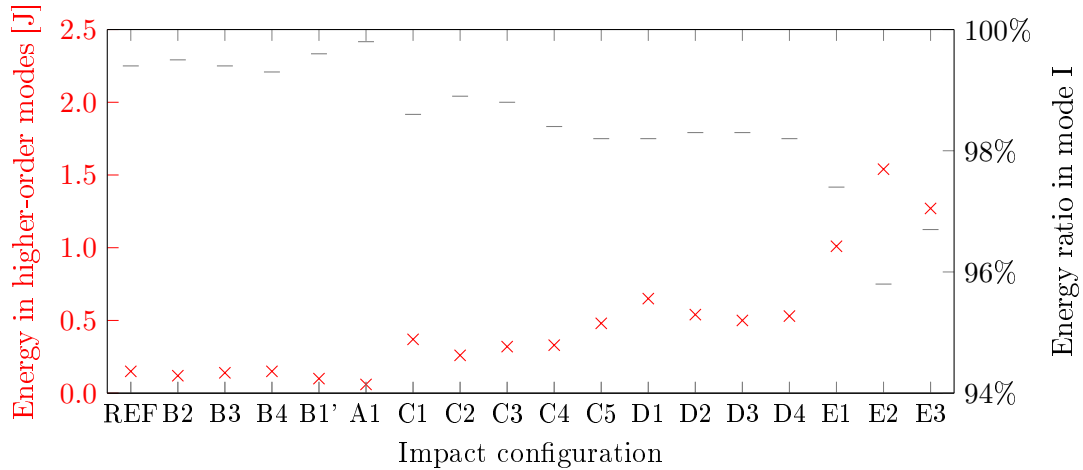


FIGURE 3.24: Dynamic energy dissipation by higher-order vibrations for each test configuration.

could result in flawed parameters  $k_m$  and  $k_{bs}$ . If contact phenomena are involved, the description of the elastic spring-mass model might be incapable of covering the full target range of contact force. Accordingly, this force range for the interpolation has to be chosen carefully.

The present test series is especially susceptible to such errors. Both the reference coupon and the transfer target are impacted on a support base that involves contact phenomena (images of the support structures can be found in Table 3.1). In contrast to that, the “artificial” boundary conditions of a numerical reference coupon can be chosen to be clear and constant – simply supported or clamped. A larger structure, where the boundary conditions are far from the impact point, is less affected by errors resulting from contact.

- Numerical issues in the determination of the elastic constants can also cause problems. The current method works through a force on a single node. This is an idealization of the contact zone with the impactor. The usage of an impactor and a contact model is a possible but computational costly solution. The implementation of an analytical contact law would be more use-case dependent but very efficient [109, 70].
- A single impact of REF was the basis for all conducted transfers. This impact is not necessarily representative of the average damage behavior of REF. The response is subjected to the usual scatter of impact experiments. The result of a single sample is unlikely to represent exactly the average; it could even be an outlier. Consequently, all transfers would be biased by the deviation of the single reference impact from the actual average damage behavior. To prevent this issue, the scaling origin has to be an average impact response. A sufficiently large set of reference experiments could provide this average. Alternatively, a set of simulations with varying material parameters could be used.

### 3.4.3 Quantification of the uncertainty through scaling

The results of the validation experiments indicate that the scaling causes an increase of the range of scatter. Thus, the uncertainty of the damage prediction rises accordingly.

The diagrams of the crack length and the delamination area in Figure 3.22 suggest this rise. Some scaled results exceed the reference and some remain below it. To quantify the effect, we can compare the rise of the scattering from the reference impact to the total of all validly scaled impacts. For that purpose, Table 3.3 contains the statistical results of two test groups: (1) the reference impacts, and (2) all validly scaled impacts. These consist of the mean value  $\bar{x}$  and the standard deviation  $s(x)$ .

A difference of the mean value between the reference impact and the total of all validly scaled impacts indicates a bias of the scaling method. Remarkably, none of the scaled mean values in Table 3.3 significantly differs from the reference. This result confirms that the scaling does not affect the results through a systematic bias.

The standard deviation behaves differently. As expected, the scaling causes an increase of this value, which is in numbers between 35% and 97%. The average increase of scatter is 75%. From these values, we conclude that the experimental uncertainty of impact damage results nearly doubles if the developed scaling method from this chapter is applied.

### 3.5 Critical assessment of the developed impact transfer method

The developed damage transfer provides a powerful tool to analyze structural impact scenarios on a local damage-prone zone. The validation prove that the transfer is applicable over a wide range of different impact locations as long as the qualitative damage behavior remains unchanged. Furthermore, the validation showed reasonable quantitative agreement of the scaled experimental impacts with their prediction through the transfer.

Nonetheless, the transfer method, due to its idealizations of the structure and the damage, represents an additional source of uncertainty. Hence, it increases the already large scattering range of impact experiments by a factor of nearly two. Deviations occur in both directions, toward larger and smaller damage, which makes a conservative damage prediction more difficult.

In addition to the scattering caused by idealizations, a systematic bias of the energy balance affects the scaling result. The dynamic energy loss was found to be not sufficiently predicted as the modal energy analysis captures only the excitement at the beginning of the impact. However, the damage progression can excite vibration modes of a higher order, and more energy gets dissipated. As a consequence, scaling from a coupon toward a softer target structure remains conservative, but impacts scaled into the other directions can occur larger than predicted by the transfer.

Concerning the qualitative impact damage, the whole transfer procedure does not take into account that the global structural response influences the state of stress in the impact zone. Due to the principle of Saint Venant, this influence is not relevant in most cases. Indeed, a change in the ratio of bending and membrane forces can significantly affect the damage initiation. While bending effects result in a linear stress distribution with a positive and a negative region, the membrane effect causes a field of pure tensile stress. Thus, a high membrane ratio in the impact response favors tensile cracking and impedes compression failure.

Finally, the conducted validation is limited to a single material, one layup configuration, and monolith impact locations. The applicability to different materials, fabric, or multimaterial or hybrid composites still has to be proven. Moreover, the consideration of impact damage involving fasteners, stiffening elements, or edges is currently hypothetical and still has to be investigated.

<b>Config.</b>	<b>B1 (REF)</b>	<b>B2</b>	<b>B3</b>	<b>B4</b>	<b>B1' (CAI)</b>	<b>A1</b>	<b>C1</b>	<b>C2</b>	<b>C3</b>
$\Delta x$ [mm]	0	15	0	15	0	0	36	45	40
$\Delta y$ [mm]	0	0	15	35	0	0	-60	-60	0
$k_{bs}$ [ $\frac{N}{mm}$ ]	671	720	909	1207	799	764	946	1085	960
$k_m$ [ $\frac{N}{mm^3}$ ]	17.10	18.80	28.0	34.57	19.90	16.90	17.19	21.86	12.97
$c_1$ [-]	1.0	0.96	0.93	0.9	1.0	1.0	0.95	0.59	0.88
$c_2$ [-]	1.0	1.0	1.0	1.0	1.0	1.0	0.84	0.87	1.0
$c_3$ [-]	1.02	1.02	0.99	1.0	1.03	0.98	1.07	1.09	1.08
$E_{impact}$ [J]	25	23	23	22	24	24	26	24	26
Number of tests	5	4	3	2	2	4	4	5	4

<b>Config.</b>	<b>C4</b>	<b>C5</b>	<b>D1</b>	<b>D2</b>	<b>D3</b>	<b>D4</b>	<b>E1</b>	<b>E2</b>	<b>E3</b>
$\Delta x$ [mm]	35	30	0	30	25	35	70	35	50
$\Delta y$ [mm]	-85	60	0	-60	50	-70	50	-65	-30
$k_{bs}$ [ $\frac{N}{mm}$ ]	1181	957	287	343	360	560	352	525	375
$k_m$ [ $\frac{N}{mm^3}$ ]	21.92	15.50	3.06	6.88	5.16	8.90	2.64	3.16	2.45
$E_{impact}$ [J]	21	26	37	31	33	29	39	37	38
Number of tests	2	1	2	3	2	1	4	2	2

TABLE 3.2: Overview of all 18 impact configurations, including the impact position from the specimen center, the elastic stiffness, the impact energy, and the number of conducted tests.

Parameter	Unit	Reference impacts	Validly scaled impacts
$\bar{F}_{max}$	[kN]	8.04	7.81
$s(F_{max})$		0.10	0.18
$\bar{A}_d$	[mm <sup>2</sup> ]	537	551
$s(A_d)$		60	81
$\bar{l}_{mc}$	[mm]	35.6	37.4
$s(l_{mc})$		2.7	5.2
$\bar{l}_{fc}$	[mm]	18.2	17.5
$s(l_{fc})$		3.2	6.3

TABLE 3.3: Average result values and the respective standard deviation the reference impacts and the total of all validly scaled impacts.





*“Aviation is the branch of engineering that is least forgiving mistakes.”*

Freeman Dyson, physicist

# 4

## Structural Assessment of Impact Damage

### Scope of this chapter

The combination of the impact scaling method and the numerical analysis has several possible application scenarios. A quick evaluation of structural impact damage can be achieved through a numerical reference coupon of minimal size. The minimal coupon size derives from a consideration of the elastic energy under impact load.

The numerical analysis of the coupon provides the impact response and the damage result, which the spring-mass model transfers to the structural level. Either the damage size for a given impact energy or the impact energy for given damage can be calculated. The damage parameter  $k_d$  correlates with the projected delamination area. The coupon result can be exploited for large areas of a structure that are sufficiently similar to the reference. This permits an areal assessment of the damage on an impact-prone structure.

Finally, this chapter includes how the proposed analysis procedures can be employed to a DT assessment during a design process. Parts of this chapter have been published by the author in [RB3] and [RB4].

### 4.1 Numerical impact analysis through a minimal reference coupon

#### 4.1.1 Determination of the minimal reference coupon size

The impact-analysis procedure of a structure on a reduced section raises the question how to choose this section. In general, the reference coupon can be of arbitrary size and geometry as long as it meets the similarity characteristics derived in section 3.3.4. For the computational efficiency of the simulation, the chosen size needs to be as small as possible. This requirement necessitates a reference coupon of minimal size. Beyond the efficiency, a minimal reference coupon matches another need: the quasistatic impact scaling to a target structure is conservative. As the minimal reference coupon represents the stiffest possible impact, the dynamic energy loss through higher-order modes is negligible. A scaling to target locations where dynamic energy loss exists always causes less damage than predicted on the reference, as supported by the validation results D3, E1, and E3 in Section 3.4.2.

Several factors possibly determine the size limit of the minimal reference coupon:

- the size of the damage-prone zone itself
- a possible damage initiation at the boundary conditions
- the validity limit of Saint Venant's principle

Among those limits, the size of the damage-prone zone is the smallest. However, in advance of the impact analysis, the extent of the damage remains unknown. Only, the impact analysis of the reference coupon is meant to determine the actual damage. The size of the coupon has to be defined beforehand.

For an approximate determination of the damage-prone zone, the elastic FE analysis of the reference coupon provides additional evidence: the laminate's damage-prone zone has to imply a sufficiently large energy reservoir for an existing crack to propagate. Hence, the laminate's energy released by the damage propagation has to exceed the critical ERR of at least one fracture mode. The damage can theoretically propagate into the area fulfilling this prerequisite.

The relevant limit value results from the lowest critical ERR. Commonly, this threshold is  $G_{Ic}$  for delamination or  $G_{m+}$  for tensile IFF. However, not all elastic energy gets released from the laminate when a crack propagates in one ply or interface. A simple approach would be to consider only the ply energy – simple but not conservative. The energy-supplying zone for a crack tip is not limited to the concerned ply.

At that point, we use the knowledge gained from the analysis of a flawed laminate in Section 2.2.2. The simulation result in Figure 2.7a and the following diagram suggests that a crack affects mostly three plies: the flawed ply itself and its two neighbors. Hence, it makes sense to assume that the energy in three plies drives the crack propagation. This assumption results in Equation (4.1), with the estimation of the limit value for the area-specific energy  $e_{laminate}$ .

$$\min(G_{Ic}, G_{m+}) = e_{laminate} \frac{3}{n_{plies}} \quad (4.1)$$

The elastic energy distribution of the indented specimen has to be analyzed for the limit value according to Equation (4.1). This border depends on the applied indentation force. For a conservative estimation, the chosen force has to be chosen at least as high as the expected maximum during the impact.

An analysis according to the procedure above has been conducted for the laminate of the validation series in Chapter 3. Figure 4.1a shows the energy distribution of the configuration REF under 8 kN. The limit value of  $2 \frac{\text{mJ}}{\text{mm}^2}$  results from the critical ERR  $G_{m+} = 0.5 \frac{\text{mJ}}{\text{mm}^2}$  divided through 12 plies multiplied by a factor of three. The resulting envelop has the dimensions  $55 \times 40 \text{ mm}^2$  – an estimate of the damage-prone zone.

This size represents a theoretical minimum for the reference coupon size. Additionally, the other two limiting factors of the coupon size also have to be considered. Such a small coupon is likely to trigger a damage onset at the edges, where the boundary conditions are applied. This secondary initiation of damage is caused only by an artificial, nonlocal damage-prone zone caused. In contrast to the nonlocal damages in the validation test series, this damage does not occur somewhere on the structure, but on the reference coupon. Nevertheless, the same method works for its compensation. During the elastic analysis of the indentation response, failure conditions have to be checked. If the extended two-dimensional method is used, a reliable prediction can be provided with an elastic shell model.

Even if damage does not initiate at the edges, it might propagate toward them. When the damage extent covers the whole length of the coupon in any direction, the damage interacts with the boundary conditions. Saint Venant's principle of locality is no longer applicable, and we reach the third size-limiting factor. The influence of the exact support configuration becomes relevant to damage propagation. Basically, if the impact damage shows an interaction with the boundary conditions, the reference coupon is too small. Such an interaction would be comparable to the effect observed on the impact configurations C1 and C5. At C1, the stiffener close to the impact location begins to affect the delamination shape. At C5, the delamination pattern differs entirely from the reference. A clamping or support can affect the damage in a similar manner.

An option to assess a possible invalidity also builds on the area-normalized energy distribution in the loaded impact specimen. In Figures 4.1b and 4.1c, the above-explained method to determine the damage-prone zone is applied to a potential minimal reference coupon. The energy distribution exhibits secondary hot spots at the edges. If there is a path with sufficiently high energy potential from the impact spot toward such hot spots, an interaction of the damage and the boundary conditions becomes likely.

Figure 4.1b shows a possible minimal reference coupon of a size  $110 \times 80 \text{ mm}^2$  loaded with 8 kN. The size results from the damage-prone area of the test coupon scaled by a factor of two. The analysis shows an isolated damage hot spot at the impact location. In contrast to that, Figure 4.1c shows the distribution for a smaller coupon, which is one and a half times the size of the damage-prone zone ( $80 \times 60 \text{ mm}^2$ ). On this coupon, the damage hot spot stretches to the edges – a possible path of damage propagation which has to be avoided. The analysis indicates that the reference coupon is too small. When different boundary conditions are applied, as in Figure 4.1c, the energy distribution changes. Generally, the minimal coupon size is larger for clamped than for simply supported edges.

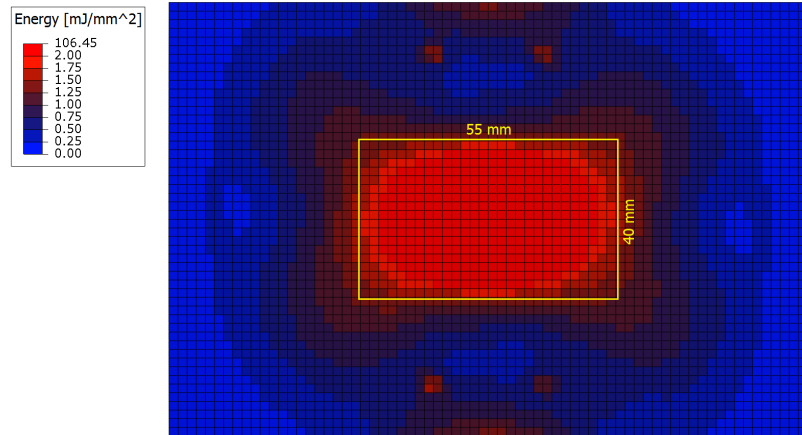
The conducted consideration of the energy-based approach does not provide the ideal size for a minimal reference coupon. It is an energy-based estimate, that is founded upon several idealizations. This estimate tells whether a reference coupon is safe to use. It does not ensure that this coupon is the smallest possible. As a rule of thumb, the coupon size should be twice as large as the damage or the damage-prone zone.

Appropriate boundary conditions are either clamped edges with free translatory in-plane DoF or simple support, fixing only the translational out-of-plane DoF. When the edges are fixed in-plane, significant membrane stresses emerge in the laminate. These stresses can influence the thresholds of FF and make a crucial assumption for the spring-mass model invalid, namely the qualitatively similar damage behavior. As such rigid attachment does not exist in a real structure.

#### 4.1.2 Numerical high-fidelity analysis of the minimal reference coupon

A simply supported virtual coupon with a size of  $100 \times 70 \text{ mm}^2$  shall now be used for damage prediction. The determination of the equivalent impact energy leads to a value of 25 J, with the stiffness parameters  $854 \frac{\text{N}}{\text{mm}}$  for  $k_{bs}$  and  $15.23 \frac{\text{N}}{\text{mm}^3}$  for  $k_m$ . Those parameters and the impact energy were determined through an elastic FE analysis.

The simulation result and the prediction by the transfer method are shown in Figure 4.2. Figure 4.3 shows the corresponding delamination damage. The qualitative damage pattern fits the original reference coupon, but the quantitative size is predicted to be slightly too large. The same applies to the trend of the force history, which



(A) Test coupon REF: the yellow frame marks the damage-prone area

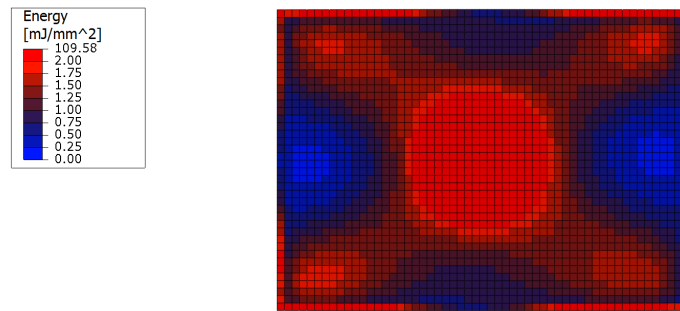
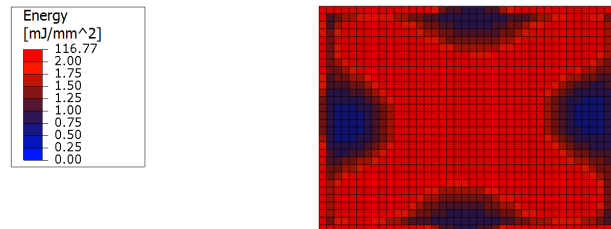
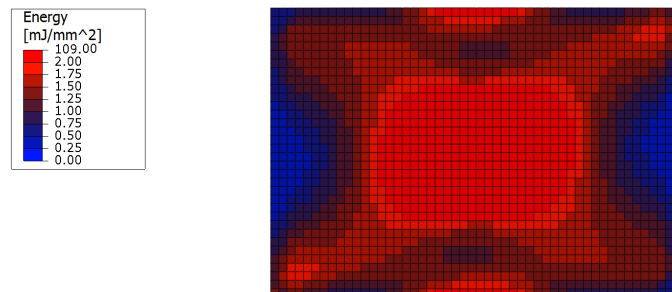
(B)  $110 \times 80 \text{ mm}^2$  numerical reference coupon clamped(c)  $80 \times 60 \text{ mm}^2$  numerical reference coupon clamped(D)  $100 \times 70 \text{ mm}^2$  numerical reference coupon simply supported

FIGURE 4.1: Laminate-level energy distribution of the validation laminate as calculated through an elastic analysis with 8 kN indentation force.

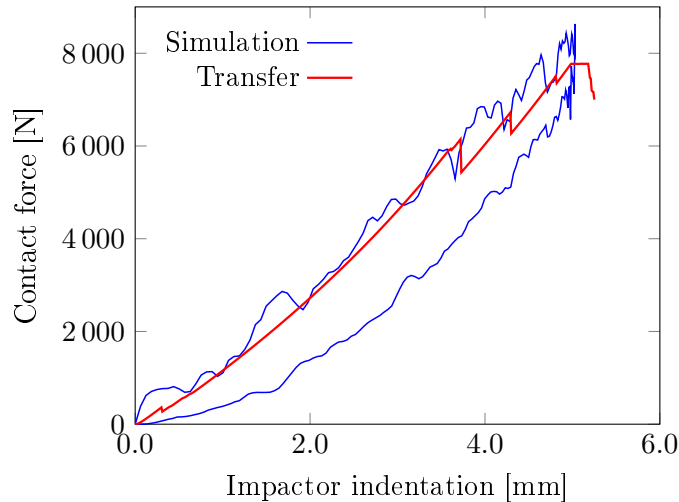


FIGURE 4.2: Numerical force-displacement history of the minimal reference coupon and its transfer prediction by the original reference coupon B1.

qualitatively meets the transferred prediction. However, the simulation apparently underestimates the force thresholds. In general, the accordance between the results is moderate. It meets the validation requirement for the scaling method, but further investigation and validation of the numerical simulation model would be useful.

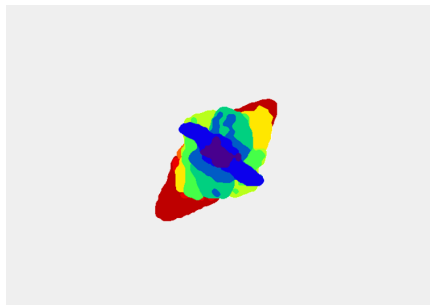


FIGURE 4.3: Delamination result predicted by the numerical analysis of the minimal reference coupon.

## 4.2 Integral assessment of impact-prone structures

The damage description through the spring-mass model is objective, as demanded in the general damage equation, Equation (3.1). The boundary conditions, the exact geometrical configuration, and the impact energy do not determine the qualitative damage behavior in an impact scenario. These findings offer a method to approach impact analysis on a structural level.

The major potential of the transfer method lies in the structural assessment of impact damage by a single high-fidelity analysis or coupon experiment. It is possible to obtain either the areal distribution of equivalent impact energy for a predefined damage or the areal damage distribution for a specific impact energy on the structure. The only analysis to be carried out on the structural level is the determination of global stiffness parameters. Each point of interest, representing one impact location, requires

its own analysis. If the analyzed points are sufficiently close, an interpolation in the area between these points is possible.

In the case of a given impact threat to a structure, this method provides the basis for an advanced DT assessment, taking into account the expected impact damage instead of the maximum possible BVID.

Figure 4.4 shows the results of an areal impact transfer analysis for the panel section E from the testing done in the previous chapter. The analysis, which has previously been conducted for a single point on the specimen, is now adopted to the full skin area. The distribution of equivalent energy still refers to the experimental reference coupon with a 25 J impact (from Section 3.4.2). As expected, the distribution is symmetrical to the stiffener. The largest values, around 40 J, are observed at the center of the free skin area. Moving closer to the stiffener or the supported areas leads to lower BVID-equivalent impact energies, below 20 J.

The third picture in Figure 4.4 shows the calculated damage distribution of  $k_d$  for a predefined impact energy threat of 30 J. Low values of  $k_d$  close to the edges indicate large damage, and high values in the center smaller damage. A remarkable feature of the damage distribution is its wide-spread uniformity. The explanation for this uniformity is the threshold-based character of the impact damage growth (compare Figure 3.15). After a threshold has been exceeded, the contact force drops, and the specimen can absorb some elastic energy without propagating the damage.

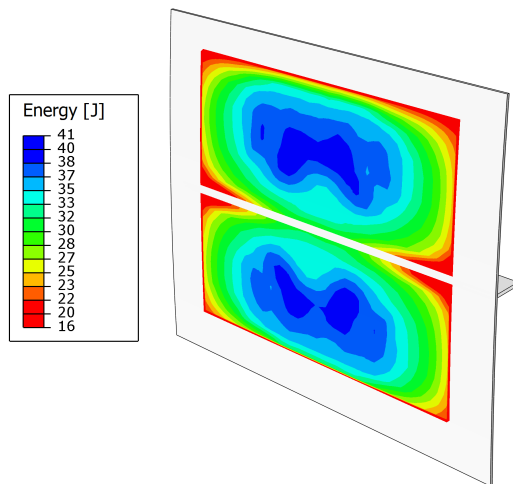
The predictable damage has a maximum, which marks the lower end of the scale. Damage larger than the final damage on the reference coupon cannot be recognized. An extrapolation is not permissible, as subsequent damage thresholds are unknown. Thus, it may be useful to analyze a reference coupon with very high impact energy, even though, this level of energy might violate the requirement of delamination-driven damage.

Finally, the damage of the 25 J-impact on the reference coupon was transferred to an arbitrary aircraft door section. This application of the scaling method should not be considered representative for an aircraft design but as a demonstration of the methodology developed in this doctoral thesis.

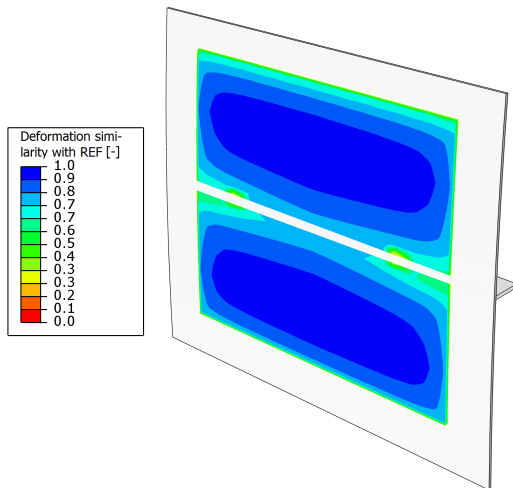
The door section includes three stiffeners and a frame structure behind the skin. The entire skin area is assumed with the same layout as the coupons in the validation in Section 3.4. Thus, a single reference coupon suffices to analyze a large zone of the skin area. Only the edges and the supported zones have to be excluded. As an impact in those areas would change the geometry of the damage-prone region, their analysis would require additional reference coupons. Each extra layout in a realistic skin structure would also need an additional reference coupon. A set of several reference coupons would be enough to cover the entire impact-endangered area.

Figure 4.5 shows the transfer results for the door section, the subfigure (a) shows the energy plot for similar damage as on the 25 J reference coupon, and the subfigure (b) provides the distribution of  $k_d$  for a 60 J impact scenario. The scale of the equivalent energy plot is cut off at the upper end at 60 J. This limit has been chosen based on the considered generic impact threat for the structural use case.

From the energy distribution, it can be concluded which areas require consideration of the maximum BVID in a DT analysis. This maximum size can arise, wherever the equivalent impact energy is smaller than 60 J. Here, the impact threat exceeds the required energy to produce the maximum BVID size. The equivalent impact energy in all blue regions is higher than 60 J. Hence, the actual impact threat is not able to cause damage in the size of the maximum BVID. The actual size of the damage resulting from the 60 J-impact is quantified by the damage parameter  $k_d$ .



(A) Equivalent impact energy for similar damage.



(B) Coefficient for deformation similarity according to equation (3.35)

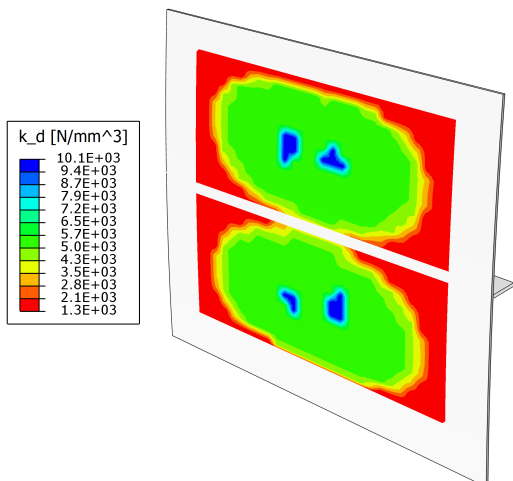
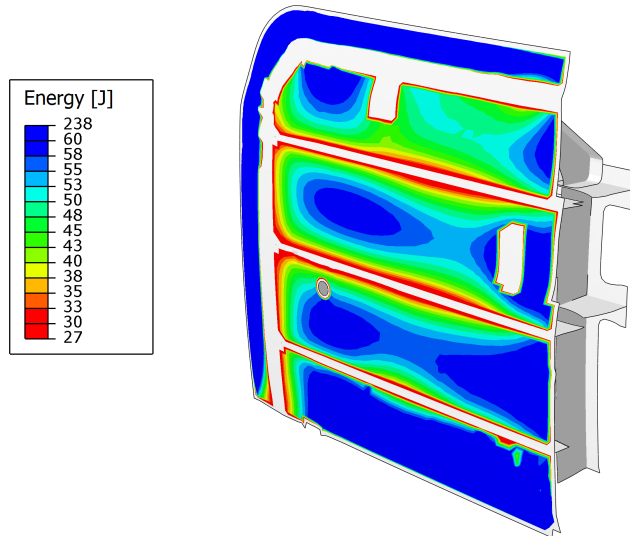
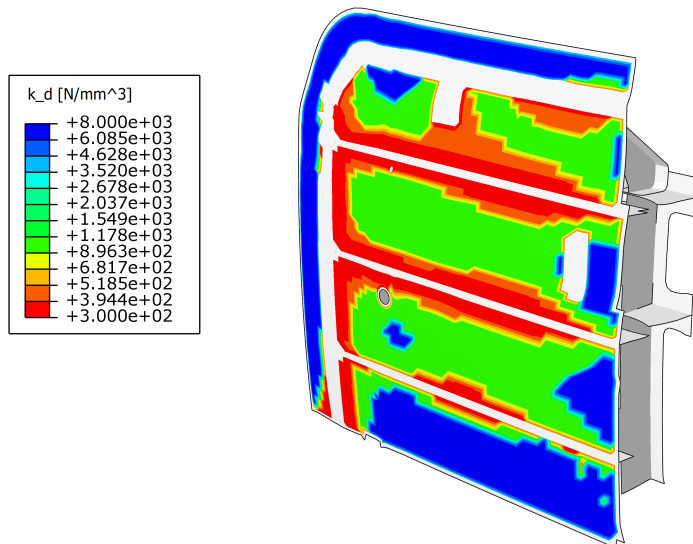
(C) Impact transfer damage parameter  $k_d$  for similar impact energy of 30J.

FIGURE 4.4: Areal impact transfer results for the stiffened panel section. The color scale is inverted, as small values of  $E$  and  $k_d$  indicate an impact-sensitive area (red) and high values an impact-firm zone (blue).

Subfigure (b) in Figure 4.5 shows the distribution of the damage parameter. In all areas where the damage does not reach the maximum BVID, this distribution defines the relevant damage size for a damage-tolerant design. In order to make this approach consistent to present analysis procedures in aviation, the projected delamination area and the damage parameter  $k_d$  can be correlated empirically. This correlation is individual for each laminate. Alternatively, existing approaches can analytically correlate the damage in a spring-mass model and the delamination size [106, 97, 98]. However, the accuracy of these approaches is usually low because the distribution of delaminations over the interfaces is not captured [RB2].



(A) Impact energy for damage similar to the 25J reference.



(B) Distribution of the damage value  $k_d$  for a similar energy of 60 J.

FIGURE 4.5: Areal impact transfer results for a generic aircraft door section. The color scale is inverted to emphasize that small values of  $E$  and  $k_d$  indicate an impact-sensitive area (red), high values stand for an impact-firm zone (blue).



### 4.3 Integration for structural design

The design of an impact-prone structure has to ensure that even the damaged structure sufficiently sustains the limit load according to the DT schematics in Figure 1.3 on page 8. In the case of BVID, even ultimate load has to be tolerated. The respective knock-down of the residual strength drives the sizing of the structure and accordingly its weight.

A common way to approach such a residual strength analysis would be the consideration of the maximum possible BVID. Whether or where this damage size can in fact emerge is not taken into account. At this point, the areal impact assessment provides a new tool for considering the actual impact threat for each location on a structure. Equation (4.2) expresses the design-relevant damage size in form of the damage parameter  $k_d$ . A damage of  $k_d(E_{threat})$  can result from the actual impact threat. If this damage is larger than the maximum BVID, it would be considered visible and not relevant to the DT analysis. Therefore, the maximum possible BVID sets an upper limit for the design-relevant damage size. This limit becomes a minimum in the damage parameter  $k_d$  because the  $k_d(max.BVID)$  decreases with increasing damage size.

In this way, the transfer method reduces the design-relevant impact damage size. In contrast to general knock-down factors for impact damage, this method enables the consideration of the actual damage threat to each point of the structure. It allows one to prove a higher residual strength or to derive possible weight reductions.

$$DMG_{DT} = \min [k_d(max.BVID), k_d(E_{threat})] \quad (4.2)$$

The above-explained principle represents an analysis strategy for impact damage tolerance on structures. This strategy has to take into account the actual threat to which the structure is exposed and accordingly provide knock-down factors for the design. The diagram in Figure 4.6 illustrates such a process. It involves the impact analysis through a high-fidelity method and an analytical transfer approach. In addition to that, the process has to employ a prediction method for residual strength or damage growth. The comprehensive analysis procedure combines these elements in the following chain:

1. The impact-prone structure forms the basis of the analysis. A set of reference coupons has to be derived from it. How many coupons a structure requires depends on the number of different layups, materials, and stiffener configurations in this structure.
2. Each reference coupon requires one impact analysis to determine the impact damage response and thus  $k_d$ . This experimental or numerical analysis provides both the impact force response and the damage result, including its characteristics of delamination, fiber cracking, and inter-fiber cracking.

A numerical or experimental residual strength analysis can possibly follow directly after this step [60, 186, 158].

3. The specific impact damage behavior of the reference coupons is now analyzed for the objective damage description. The analytical spring-mass model accomplishes this task. The procedure requires also an elastic response in addition to the impact response. Hence, the elastic indentation analysis also has to be conducted for each reference coupon. The respective analyses are conducted through a low-fidelity FE model.

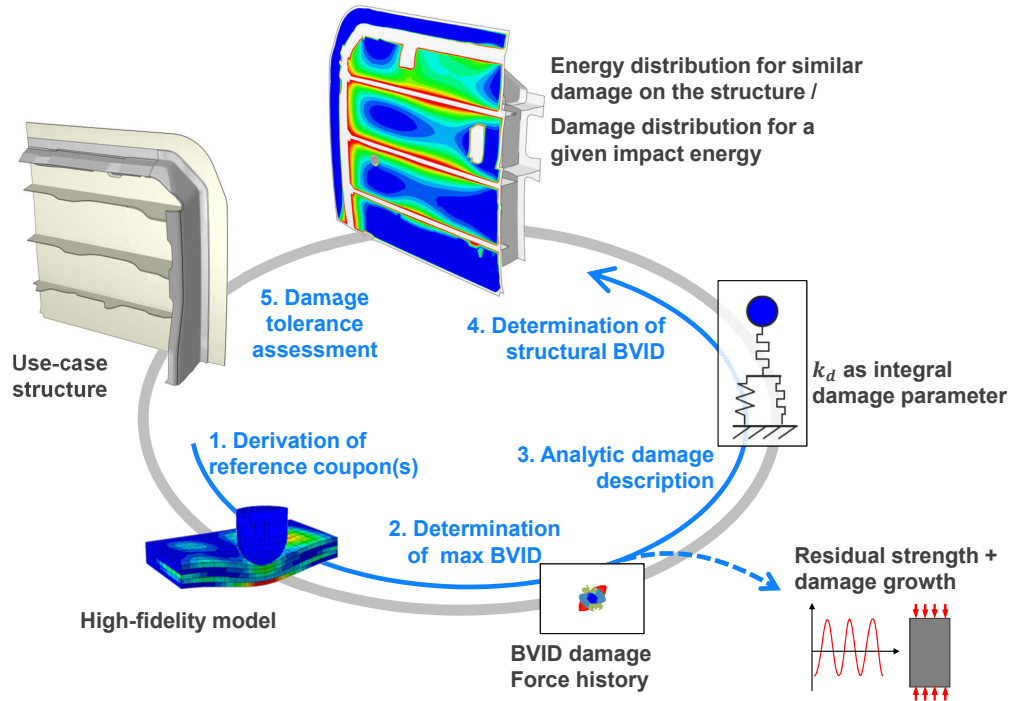


FIGURE 4.6: The proposed procedure for the assessment of impact damage tolerance with the methods in this work.

4. To derive the specific damage behavior of distinct locations on the structure, the spring-mass model is evaluated for the respective locations of interest. Therefore, the elastic indentation analysis has to be conducted through a low-fidelity FE model of the structure. In this regard, the damage-prone zones are also determined. An additional eigenfrequency analysis has to be conducted in order to apply the modal energy correction that captures the dynamic energy loss.
5. The final step is the actual DT assessment. One possibility is to compare the damage directly with an allowable reference. To comply with established procedures, it is helpful to correlate the damage parameter  $k_d$  and the projected delamination area. Knock-down factors can be derived from the correlation of the damage parameter  $k_d$  and the strength degradation on the coupon level. In order to efficiently calculate a knock-down factor, the residual strength can also be evaluated directly on the structural level through analytical methods [109, 70]. This procedure would be less conservative than deriving the residual strength from the reference coupons.

#### 4.3.1 Follow-up interface for residual strength analysis

Structures are commonly designed to sustain loads – impact-resistance as an end in itself is rarely the purpose. Accordingly, the prediction of residual strength or

damage growth has to be accomplished after successful impact analysis. Apart from an experimental investigation, two variants of this follow-up procedure exist. A numerical high-fidelity prediction [60, 186, 158, 65, 140] or analytically based estimations [109, 70, 187]. Both variants could be used to address the residual strength prediction in the above-proposed DT analysis process in Figure 4.6.

A simple option is to predict the residual properties using the same high-fidelity model as the impact simulation. A multi-step analysis chain of the impact analysis, a damping step, and the actual residual strength analysis have to follow one after another [60]. With all steps in one model, no mapping or transfer is required in-between them. Hence, the residual strength prediction is also performed through explicit simulation. The stability-driven limit of simulation time requires a massive increase of the numerical loading speed in comparison to the real experiment. Even though strain rate effects can just be left out of the material model, dynamic effects might influence the result [158]. Therefore, an explicit simulation of a quasistatic event has to be interpreted carefully. Regarding the process in Figure 4.6, such a numerical damage prediction has to be conducted on the reference coupon. On that level, knock-down factors have to be derived. When transferred to the structural level for DT assessment, such derivations are conservative. A coupon offers hardly any of the possibility for load transfer to other load paths as a structure does. Thus, the corresponding strength reduction affects the structure less than it does a coupon.

In order to conduct a less conservative analysis, the residual strength analysis has to be employed directly on the structural level. A high-fidelity analysis for the structure would require approximately the computational effort of an impact analysis on that level. Thus, the same issues concerning the structural analysis effort are also relevant to the residual strength analysis. With regard to the fast analytical impact transfer, a follow-up high-fidelity analysis cannot be a suitable approach. To make the follow-up analysis more efficient, analytical methods are a better choice. These methods idealize the impact damage or permit the use of a low-fidelity approach for the residual strength prediction. Eventually, they permit that the DT analysis chain according to Figure 4.6 can be employed as a comprehensively efficient procedure.



*“The problem in this business isn’t to keep people from stealing your ideas. It’s making them steal your ideas!”*

Howard Alken, pioneer in computing (1900-1973)

# 5

## Conclusion and Outlook

On the basis of three research hypotheses, I have developed a comprehensive analysis strategy for low-velocity impact on composite structures. An analytical spring-mass model permits one to scale a structural impact scenario to a representative reference coupon of much smaller size. The impact damage on this coupon is analyzable with a numerical high-fidelity model. The scaling approach transfers the damage result back to the structural level. Each of the involved methods uses a different abstraction scale of the impact system that has its own strengths and weaknesses:

- An explicit numerical high-fidelity simulation provides quantitatively and qualitatively plausible results for impact analysis. Furthermore, it enables an understanding of the damage processes within a laminate. The implemented finite element model confirms the first research hypothesis of this work.

However, the required analysis effort is high, because the high-fidelity model works with individual element layers for each ply in the laminate. Thus, the analysis is computationally costly. This high cost makes a direct application on the structural level inefficient.

- An analytical quasistatic spring-mass model can capture the elastic response and the damage of an impact system. Due to its analytical nature, a spring-mass model can be evaluated very quickly. This model confirms the second research hypothesis.

Nevertheless, due to insufficient sensitivity and accuracy, a spring-mass model can hardly predict damage on its own. The model also requires information about the elastic indentation stiffness, which has to be obtained beforehand.

- A numerical low-fidelity analysis enables the impact description through a spring-mass model and provides valuable information about the damage-prone zone of a structural impact scenario.

Even though a low-fidelity model is not sufficient to capture damage propagation appropriately, it predicts the elastic response accurately. A good prediction of the damage onset is also possible.

The combination of these three methods, according to the schematics in Figure 5.1, allows one to exploit the strength of each method while compensating for each’s

deficiencies. *The high-fidelity model analyzes the impact on the reference coupon.* This analysis is computationally the most costly part of the whole chain. As the reference coupon is much smaller than the actual use case structure, relocating the computation effort makes an impact analysis more efficient than an examination on the structural level. *Low-fidelity analyses of the structure and the reference coupon suit the determination of the stiffness parameters* for a spring-mass model. The elastic force responses provide input for an interpolation of the spring-mass model parameters.

Together with the coupon damage result, this *analytical spring-mass model transfers the damage result* to the structural level.

This combined analysis chain confirms the third research hypothesis of the present doctoral work. Structural impact scenarios become analyzable on a much smaller section: the reference coupon. Additionally, an areal assessment of impact damage becomes possible: once the blue analysis path in Figure 5.1 is known, many evaluations of the red path can be conducted for different but sufficiently similar impact locations on the structure. Hence, the impact damage for each possible location on the structure can be assessed, which is especially useful to employ a damage-tolerant design.

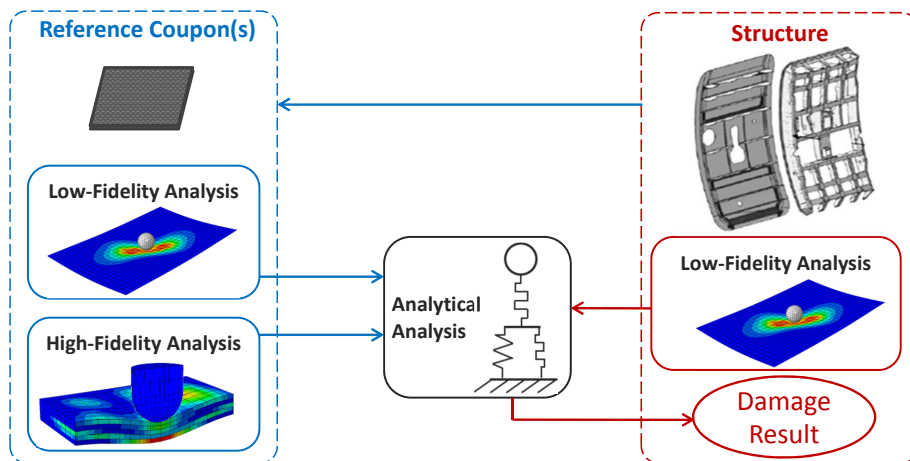


FIGURE 5.1: Schematics of the comprehensive analysis process of impact damage on composite structures.

The whole analysis chain was validated in several steps, handling the high-fidelity analysis, the spring-mass model, and the transfer of impact damage. The high-fidelity simulation provides plausible damage results for delamination, FF, and IFF. However, the application of such a model is challenged with regards to the determination of appropriate input parameters for that model, and the computational effort is very high. Furthermore, the scattering of impact results is currently not captured by that method. In the best case, the deterministic results represent the mean value of the experimental scattering. Otherwise, this scattering is a remaining reason for additional knock-down factors.

The spring-mass model describes the impact damage by the additional out-of-plane compliance in the laminate. This parameter similarly suits the damage description, as the projected delamination area does. The advantage of this measure is that it is provided by the spring-mass model as a property of the dynamic impact system. Accordingly, it can be determined on the basis of the dynamic impact response. The scatter of this compliance behaves similarly to the scatter of the projected delamination area.

The transfer through the spring-mass model provides a scaling of the impact energy for similar damage. This procedure was successfully conducted for a set of geometrically different impact experiments. This validation of the scaling showed good agreement of the prediction through the transfer and the tested impact configurations. However, a quasistatic energy transfer was found to be insufficient for some configurations. Dynamic energy dissipation has to be considered if the range of application is not strictly limited to the impact of very large masses with very low velocity. It was eventually discovered that the scaling even further increases the usual scattering of impact damage even further.

This work raises many questions that remain unanswered and demand further research. One particularly important point is the scatter of experimental impact damage and how to deal with it in numerical analysis. Obvious deficiencies of the homogenization in CDM and the CZM were accepted here. Those, of course, affected the analysis results but do not worsen the developed tensorial-based material degradation method. The occurrence of nonlocal damage as a possibly disturbing factor has to be further analyzed. A promising approach for such analysis could be based on the extended two-dimensional method for finite shell elements. Through this method, occurring non-local damage could be detected during the transfer procedure. Thus, the certainty of the transfer method can be further increased. The dynamic energy balance of an impact system is still not fully understood. The excitation of high-frequency vibration modes is not caused only by the initiation of the impact but also by each damage progression in the laminate. A quantification of the corresponding loss of energy can lead to more accurate scaling of the impact energy.

Beyond these open points, the application range of the developed method is extendable: different material systems and layup configurations are possible variations of monolith impact scenarios. Impact locations that involve fasteners, stiffening elements, and edges are also possible fields of application. However, all these specific scenarios are relevant to the design procedure of an aircraft. The research in this work might be adapted to conduct high-fidelity analysis for these cases, or it might be applied for quick determination of the design-critical impact scenarios, involving all possible scenarios. In any of these cases, more research challenges have to be confronted.

Finally, the presented research does not show how to build lighter aircraft structures, but it will contribute to the airworthiness of lighter structures in the future.





“An experiment is a question which science poses to Nature, and measurement is the recording of Nature’s answer.”

Max Planck, theoretical physicist (1858-1947)



## Experimental methods, results and material data

### A.1 Error analysis of the impact history data

All experimental impact testing in this work was performed with a Ceast drop tower as shown in Figure A.1. An impactor with a large mass is moved to a predefined height and dropped on the impact specimen. The height is computed based on the selected impact energy. Equipped with a piezo force sensor, a high-frequent measurement of the contact force between the impactor and the specimen is possible. This force represents the only value measured during the impact event. In combination with the known initial velocity, time integration of the histories of velocity and displacement is performed. There are several possible sources of error in this experimental setup. Their influence on the test results that are applied for validation of the numerical models is briefly investigated in this appendix section.

**Energy deviation:** Setting the impact energy by moving a mass to a predefined height is performed quite accurately. Nonetheless, the height does not comprise the deflection of the specimen during the impact. At its turning point, the impactor is located below the zero level by the length  $w_{max}$ . Additional energy according to Equation A.1 is introduced to the impact system. Depending on the impact parameters and the maximum deflection, this energy difference is less than 1 J.

$$\Delta w_{deflection} = g_0 \cdot m_i \cdot w_{max} \quad (\text{A.1})$$

**Oscillation in the impact system:** The oscillation behavior of the impactor can be important for the dynamic impact response of the whole system. The main cause is the impactor with its mass plates. The corresponding eigenfrequencies can reach as low as 500 Hz [120]. High-frequency oscillation in the contact force can be caused by excitation of these modes.

Following the conclusion in the work of Panettieri [120], an eigenfrequency analysis of the impactor was performed to find eigenmodes that are relevant for the dynamic response of the impact on a specimen. Figure A.2 shows the result. For an impactor



FIGURE A.1: Ceast Fractovis impact drop tower that was used to conduct the experiments for this work.

mass of 3.99 kg the eigenfrequencies associated with these modes were 1053 Hz and 2460 Hz.

**Error propagation to integrated history values:** Obtaining velocity and displacement information by integration of the force history is probably the most important source of error, as it propagates errors from the measurement of force  $\Delta F(t)$  and initial velocity  $\Delta v_0$ . In addition to that, a delayed triggering of the force measurement can cut off the first part of the force history.

$$v(t) = v_0 + \int_0^t g_0 - \frac{F(\hat{t})}{m} d\hat{t} \quad (\text{A.2})$$

$$w(t) = \int_0^t v_0 + \int_0^{\hat{t}} g_0 - \frac{F(\hat{t})}{m} d\hat{t} d\tilde{t} \quad (\text{A.3})$$

The influence of  $\Delta v_0$  is easy to analyze. It results in a constant bias of the velocity history and a linearly increasing bias  $\Delta v_0 \cdot t$  in the displacement. The error in the measured contact force  $\Delta F(t)$  is a random variable. The calibration of the sensor ensures its mean value to be zero. A normal distribution can be assumed, and the integral of the noise term becomes zero. Accordingly, there is no bias in the velocity and displacement history caused by the sensor noise.

$$\int_0^t \Delta F(\hat{t}) d\hat{t} = 0 \quad (\text{A.4})$$

The delayed triggering causes a cutoff in the force history and is described by Equation (A.5). The direct consequence is the same as described for the error term

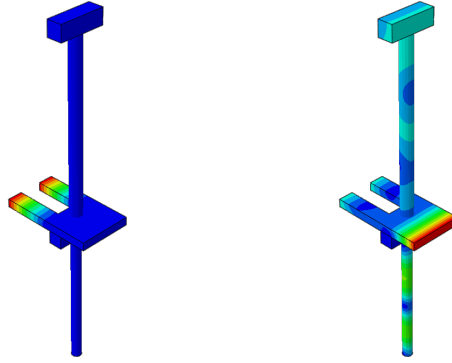


FIGURE A.2: Displacement magnitudes of the first two eigenmodes of the impactor that can participate in the impact.

$\Delta v_0$ , a constant bias in velocity and a linearly increasing bias in the displacement function.

$$\int_0^t g_0 - \frac{F(\hat{t})}{m} d\hat{t} = \int_0^{t_1} g_0 - \frac{F(\hat{t})}{m} d\hat{t} + \int_{t_1}^t g_0 - \frac{F(\hat{t})}{m} d\hat{t} \quad (\text{A.5})$$

In addition to the bias in the history values, associated values of force and displacement correlate incorrectly if the force record starts with a delay, because the force-displacement diagram creates a distorted abscissa. As the distortion factor is time-dependent, misinterpretation of the diagram is likely, even though the interpreter knows about the error. The integral value of the energy absorption and the turning point of the impactor are affected. For good experimental results, this error has to be avoided.

## A.2 Ultrasonic scanning methods

Ultrasonic scanning is the most important nondestructive testing method to assess delamination damage. The method is established for visualization of delamination damage in FRP materials [188]. The validation of numerical delamination prediction is based on ultrasonic images. Laminates are typically scanned with two techniques. To understand these techniques, we need to consider the basic principle of ultrasonic inspection. An ultrasonic sound wave is sent into the FRP laminate in the out-of-plane direction, as shown in Figure A.3. For that purpose, the laminate is put in an immersion tank under water. To obtain information about the damage state in the laminate, two characteristics of the wave can be exploited:

- The ultrasonic *C-scan* is a through transmission scan and the standard method to detect flaws in laminated structures. When the sound wave travels through a material, the material causes a damping of the signal amplitude. Damage, especially delamination, increases this damping. The C-scan method is founded on the evaluation of the echo signal from the reverse side of the immersion tank. An evaluation of the echo amplitude leads to the damage information. Figure A.3 shows, on the left, the principle of this method.
- The *D-scan* is a pulse echo evaluation and method provides more information about the laminate. When the material-phase changes (e.g. with delamination),

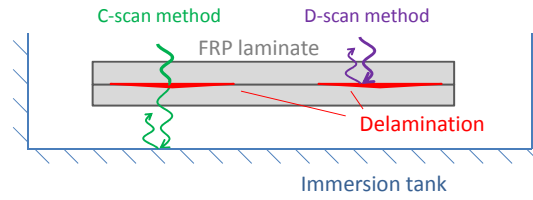


FIGURE A.3: Illustration of the evaluation of the sound waves for two ultrasonic scanning methods.

the sound wave reaches the plate's reverse side or the bottom of an immersion tank, and an echo of the sound wave occurs. The path of the sound wave is depicted on the right in Figure A.3. The D-scan method works with the wave reflections of the sublaminates, that arise with delamination. Considering the sound wave's time of flight, the out-of-plane location of the reflection point can be determined.

The information of a C-scan image is limited to the projected view through all interfaces of the laminate. In Figure A.4, three different delamination configurations are presented. Although the single delaminations quantitatively and qualitatively differ, they result in equal C-Scan images. The number of delaminations that leads to a drop of the echo signal does not result in a difference in the signal. Neither does the location of the delamination in the thickness direction.

The D-scan image provides further detail. The information of a delamination's depth in the laminate allows one to distinguish the three delaminations in case C. However, this method still does not contain information about the full damage state in the laminate. The shielding effect permits only an identification of the uppermost delamination at each in-plane position. Scanned from the reverse side, the example cases A and B would still lead to equal results. The additional delaminations in case A remain invisible. A scan from the top would show a different result, but the middle delamination in case A could still not be identified. In edge regions of the delamination, the echo signal might be weak or dispersive. Thus, the D-scan envelope of the damage is usually smaller than the C-Scan envelope. In the provided example images in Figure A.5, the D-scan envelope is approximately 13% smaller than the C-Scan envelope. In the C-scan an area is considered as damaged if the echo signal drop exceeds 5 dB. Accordingly, the green-blue transition marks the border between the damaged and undamaged area.

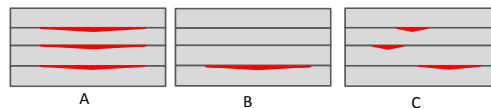


FIGURE A.4: Cross-section of three equivalent laminates with different delamination patterns.

A false-color scale, as shown in Figure A.6A, visualizes the actual depth of the detected delamination. The color distribution in this scale between the laminate top

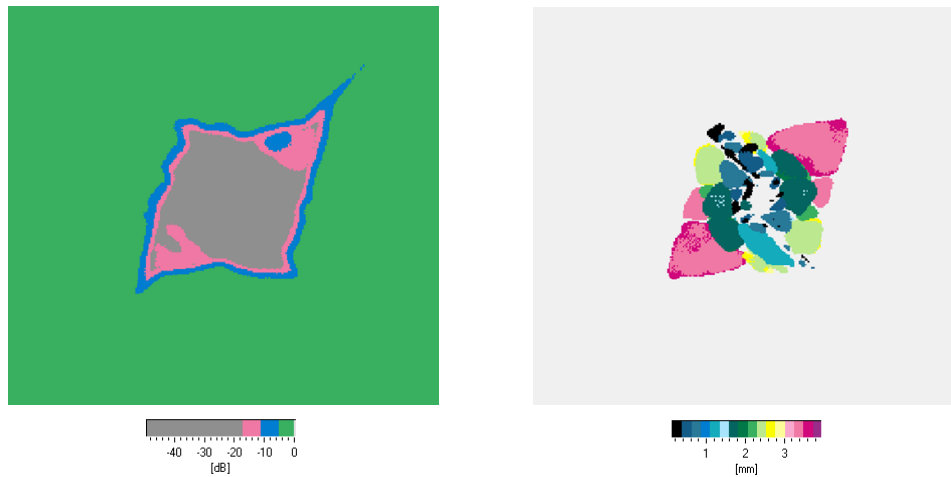
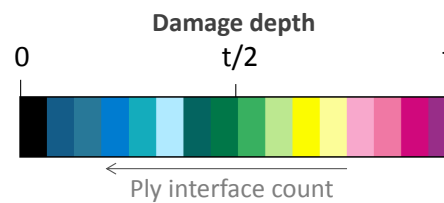


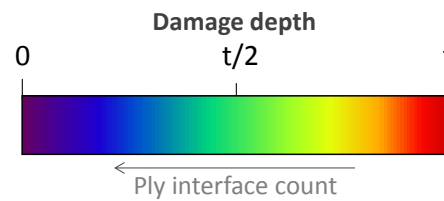
FIGURE A.5: C-Scan and D-Scan of the same impact damage.

(0) and the depth equal to the laminate thickness  $t$  is arbitrary. The scale for all experimental D-scan results in this thesis are based on a discrete 16-ary scale.

In contrast to an experimental investigation, a numerical prediction provides insight to all delaminations inside a laminate. In order to easily compare the numerical results with the experimental result, it is common to assemble the numerical results in a D-scan-equivalent plot. The false color scale of the overlay plot in the Figure A.6B is a continuous interpolation in accordance with the experimental color scale.



(A) Ultrasonic D-Scan



(B) Overlay plot of FE results

FIGURE A.6: Legends of the false color scale representing the depth of a delamination damage in the laminate.

### A.3 Material properties for numerical analyses

This section provides the material parameters for the numerical analyses conducted in the presented research. For that purpose, Table A.1 lists the parameters of three unidirectional materials. Among two real prepreg materials with carbon fiber reinforcement

and epoxy resin. The corresponding parameters result from material characterization tests in accompanying research projects around this thesis. Most of these experiments were conducted according to established standards. For any material parameter that does not result from a standardized test, Table A.1 references the source of literature where the test is described or the parameters are taken from.

The additional ‘‘Material 0’’ is a generic material. Its parameters were derived from the two real materials; however, some values were adapted for numerical reasons. These modifications allow that a simple impact example with an 8-ply laminate suffices to trigger all relevant damage modes. This simple model makes the development of a numerical impact model in Section 2 more tangible.

		Material 0 (generic)	Material I	Material II	Test standard / test method
Density	$[\frac{\text{kg}}{\text{m}^3}]$	1600	1580	1570	Manufacturer specification
Ply thickness	[mm]	0.5	0.184	0.184	Manufacturer specification
$E_{11t}$	[GPa]	159	167	170	DIN EN 2561 [189]
$E_{11c}$	[GPa]	159	151	150	DIN EN 2850 [190]
$E_{22t}$	[GPa]	8.6	8.8	8.8	DIN EN 2597 [191]
$E_{22c}$	[GPa]	8.6	9.0	9.4	DIN EN ISO 14126 [192]
$E_{33}$	[GPa]	8.6	8.6	9.0	Pellet test [159]
$G_{12}, G_{13}$	[GPa]	5.6	5.0	5.5	AITM 1-0002 [193]
$G_{23}$	[GPa]	4.5	3.0	4.5	Calculated transversely isotropic [194]
$\nu_{12}, \nu_{13}$	[-]	0.33	0.31	0.23	DIN EN 2561 [189]
$\nu_{23}$	[-]	0.48	0.48	0.48	Assumption based on resin properties [129]
$X_{11t}$	[MPa]	1600	3 000	2 700	DIN EN 2561 [189]
$X_{11c}$	[MPa]	800	1 450	1 590	DIN EN 2850 [190]
$X_{22t}$	[MPa]	50	60	105	DIN EN 2597 [191]
$X_{22c}$	[MPa]	205	230	252	DIN EN ISO 14126 [192]
$X_{33c}$	[MPa]	190	220	252	Pellet test [159]
$X_{12}, X_{13}$	[MPa]	115	110	105	AITM 1-0002 [193]
$X_{23}$	[MPa]	65	65	65	Obtained from $X_{22c}$ [5]
$G_{Ic}$	$[\frac{\text{mJ}}{\text{mm}^2}]$	0.8	0.5	0.5	AITM 1-0005 [195]
$G_{IIc}, G_{IIIc}$	$[\frac{\text{mJ}}{\text{mm}^2}]$	2.8	2.5	2.8	AITM 1-0006 [196]
$\eta$	[-]	2.8	2.1	2.1	ASTM D 6671 [197]
$G_{f+}$	$[\frac{\text{mJ}}{\text{mm}^2}]$	130	130	106	Literature: [60]
$G_{f-}$	$[\frac{\text{mJ}}{\text{mm}^2}]$	40	35	81	Literature: [60]
$G_{m+}$	$[\frac{\text{mJ}}{\text{mm}^2}]$	0.8	0.5	0.5	$= G_{Ic}$
$G_{m-}$	$[\frac{\text{mJ}}{\text{mm}^2}]$	4.6	4.1	4.6	$\frac{G_{m-shear}}{\cos \phi}$ [43]
$G_{m-shear}$	$[\frac{\text{mJ}}{\text{mm}^2}]$	2.8	2.5	2.8	$= G_{IIc}$
$X_{sh}$	[MPa]	55	87	87	DIN EN 2563 [198]
$X_n$	[MPa]	16	20	20	Obtained from $X_{22t}$ [90]

TABLE A.1: Material properties for the simulations in this work.

All strengths values in Table A.1 were determined for plies in a unidirectional laminate. Thus, their validity is also limited to that laminate type. However, embedded plies in a multidirectional laminate behave differently [164]. The actual strength value remains unchanged, but after the damage initiation, the laminate's fracture toughness prevents a crack propagation. Thus, even after the initiation of a crack, the stress further increases. This increase in stress leads to in-situ strength values, which are higher than the actual unidirectional ply strengths. This increase becomes stronger with decreasing ply thickness. According to the work of Camanho et al. from 2006 [164, 165], the in-situ strengths can be derived from the ply properties and the critical ERRs. For impact analysis, the application of this approach has already been validated [60].

For the numerical analysis in this research, in-situ values were applied for the strengths parameters  $X_{22t}^{is}$  and  $X_{12t}^{is}$ . The values are calculated according to Equations (A.6) and (A.7) and replace the corresponding value in Table A.1.

$$X_{22t}^{is} = \sqrt{\frac{4G_{Ic}}{\pi t_{ply}} (E_{22}^{-1} - \nu_{12}E_{11}^{-1})} \quad (A.6)$$

$$X_{12t}^{is} = \sqrt{\frac{8G_{12}G_{IIc}}{\pi t_{ply}}} \quad (A.7)$$

## A.4 Results of scaled impacts

This section contains all force-displacement diagrams of the validation impacts in Chapter 3. The prediction by the analytical scaling method is also included in the following diagrams in Figure A.7.

Furthermore, this section provides the raw delamination results for the validation experiments in Chapter 3. The ultrasonic D-scan results were obtained with the help of the analysis method as described in Appendix A.2.

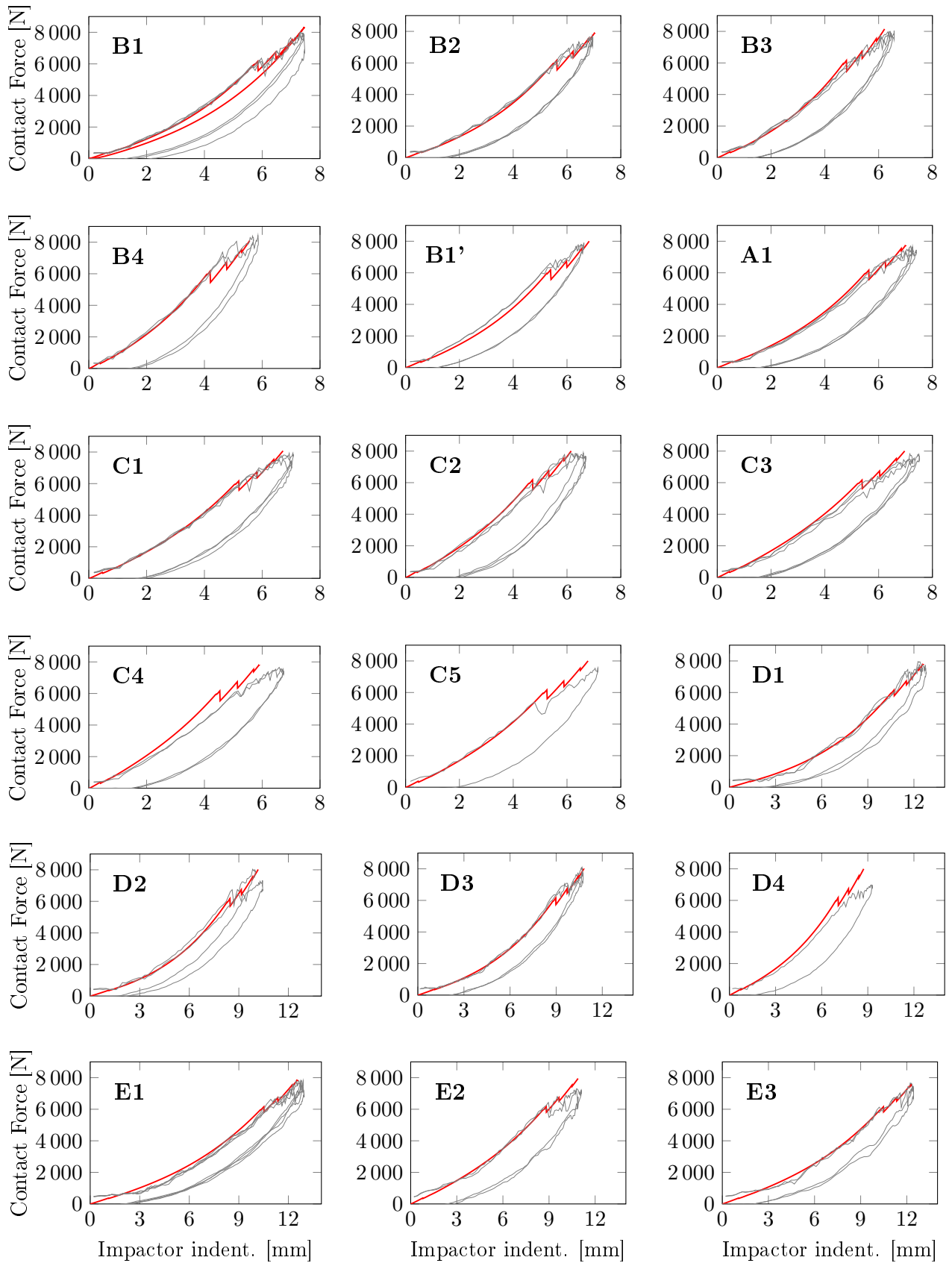


FIGURE A.7: The force-displacement curves of all impact configurations in the test campaign: comparison of the spring-mass model's prediction (red) and the experimental result (gray).



REF	B2	B3	B4	B1'
				
				
				
				
				
				
$537 \pm 60 \text{ mm}^2$	$504 \pm 30 \text{ mm}^2$	$567 \pm 55 \text{ mm}^2$	$725 \pm 2 \text{ mm}^2$	$497 \pm 3 \text{ mm}^2$

TABLE A.2: D-scan delamination results of the impact experiments on specimen type B.






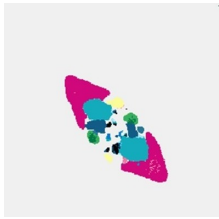



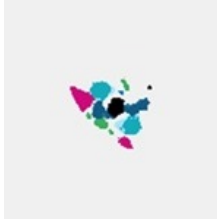
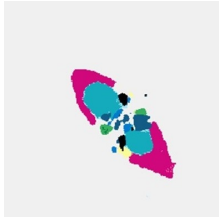
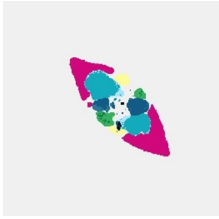


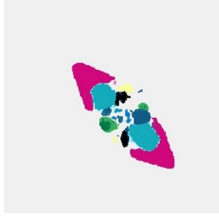

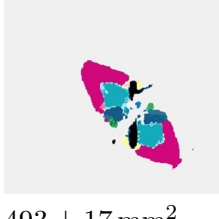
A1	D1	D2	D3	D4
				
				
				
				
				
$493 \pm 17 \text{ mm}^2$	$510 \pm 88 \text{ mm}^2$	$571 \pm 108 \text{ mm}^2$	$415 \pm 21 \text{ mm}^2$	$297 \text{ mm}^2$

TABLE A.3: D-scan delamination results of the impact experiments on specimen type A and D.

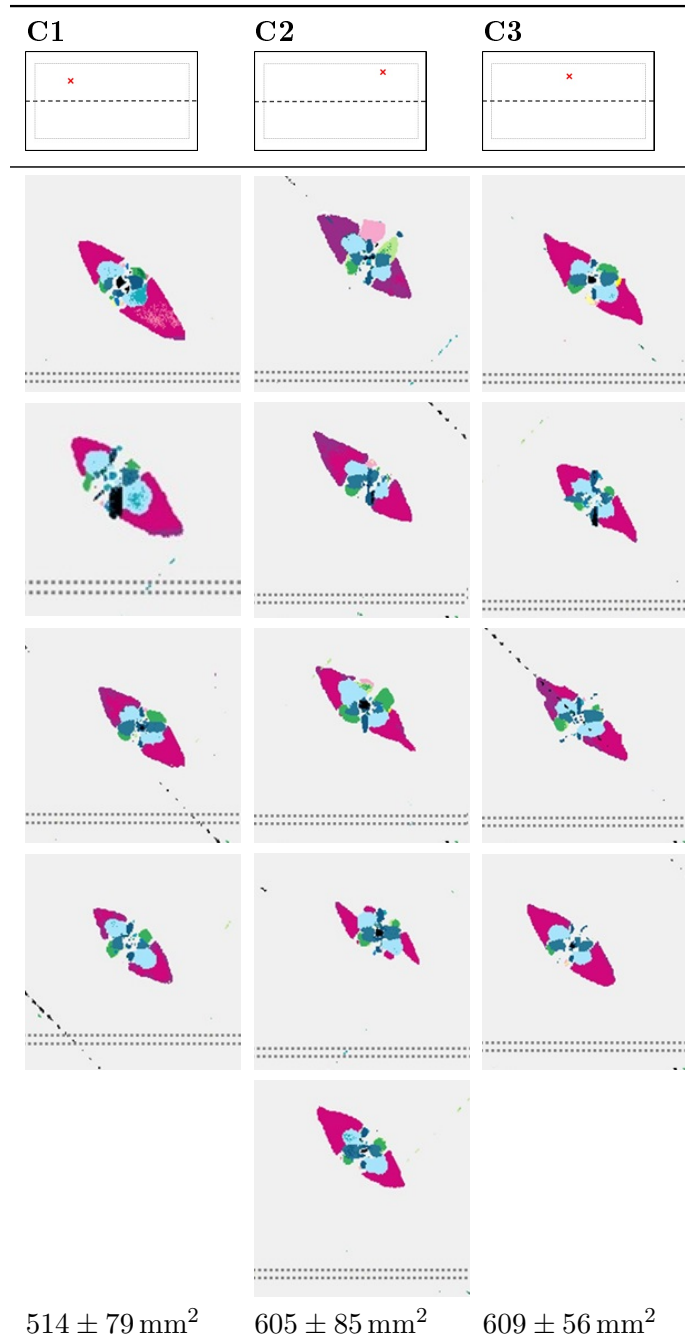


TABLE A.4: D-scan delamination results of the impact experiments on the specimen type C. The dotted double line indicates the position of the stiffener on the backside.

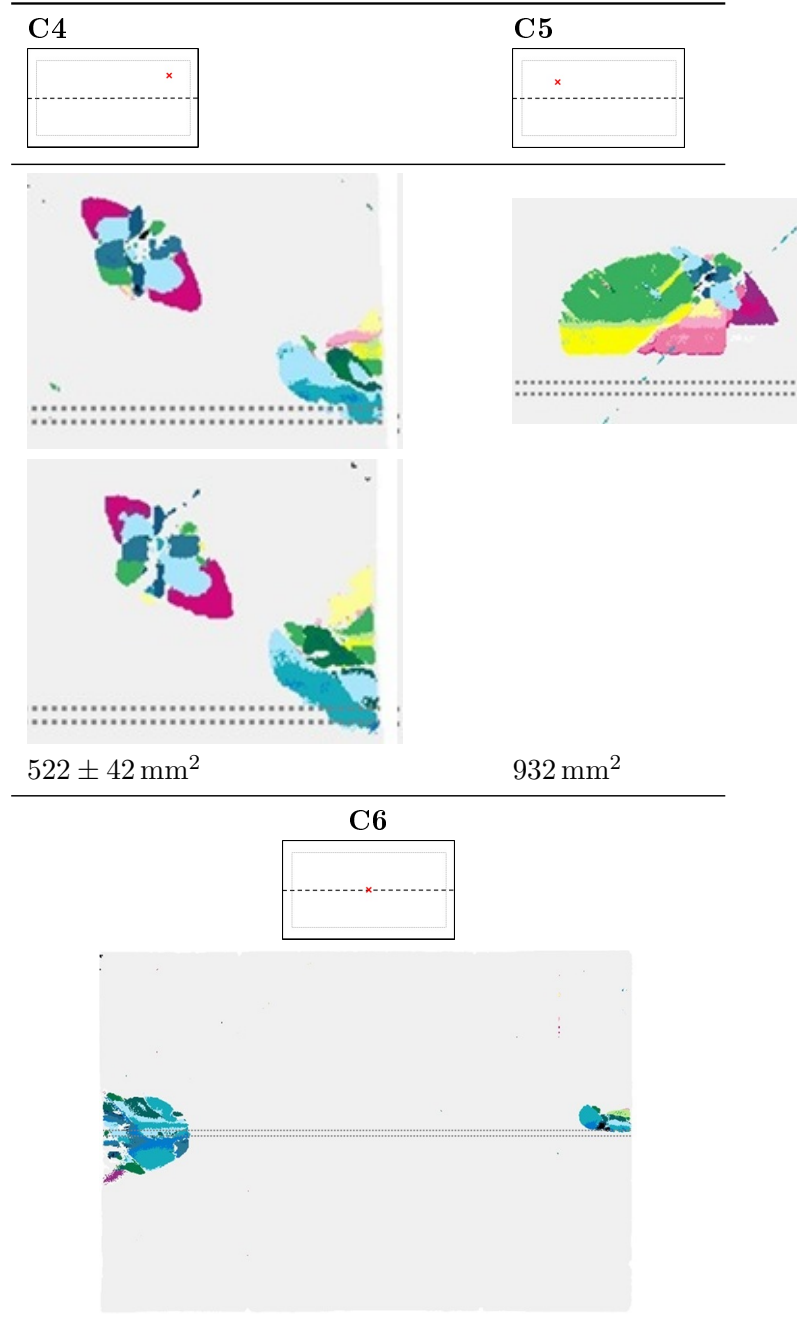


TABLE A.5: D-scan delamination results of the impact experiments on the specimen type C. The dotted double line indicates the position of the stiffener on the backside.

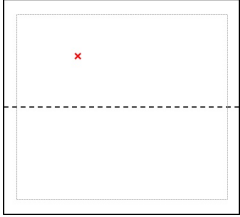
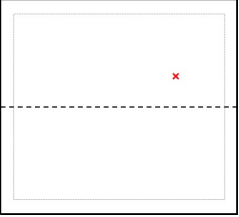
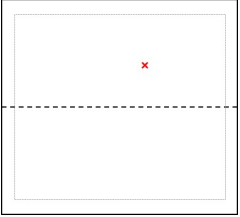
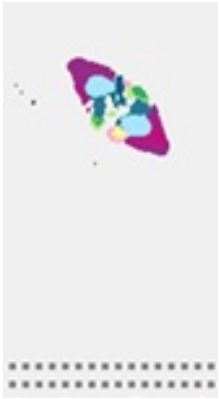

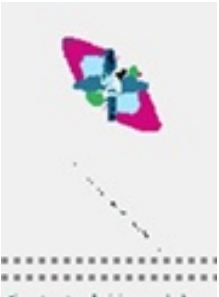

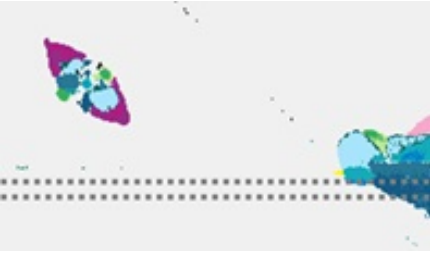
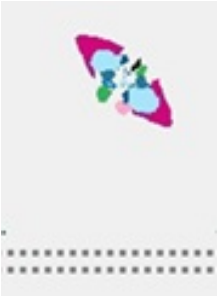






E1	E2	E3
		
		
		
		
		
$447 \pm 39 \text{ mm}^2$	$451 \pm 36 \text{ mm}^2$	$445 \pm 14 \text{ mm}^2$

TABLE A.6: D-scan delamination results of the impact experiments on the specimen type E. The dotted double line indicates the position of the stiffener on the backside.





# B

## Mathematical Methods

### B.1 Time integration methods

To solve an ordinary differential equation with a first-order time derivative like Equation (B.1), two main classes of time integration methods exist. These classes are the forward and the backward integration methods [199]. The so-called Euler methods are the most common and most simple representatives of both procedures. Beginning from a known time point  $t_n$ , the Euler forward method in Equation (B.2) uses the values  $x_n$  and  $t_n$  to compute the target function at  $t_{n+1}$ . This formulation is explicit, as it can be directly evaluated, requiring only the values of the current time increment.

In contrast, the Euler backward method in Equation (B.3) requires a value for  $x_{n+1}$ . Thus, apriori knowledge of the target time point is necessary, to calculate the target value at the time  $t_{n+1}$ . The new value  $x_{n+1}$  depends on itself, which requires an implicit solution by iteration. This iteration results in a much higher computational effort of the Euler backward method in comparison to the Euler forward method. However, the benefits of this increased effort are better accuracy and stability.

$$\frac{\partial x}{\partial t} = f(x, t) \quad (\text{B.1})$$

$$x_{n+1\_e} = x_n + \Delta t f(x_n, t_n) \quad (\text{B.2})$$

$$x_{n+1\_i} = x_n + \Delta t f(x_{n+1}, t_{n+1}) \quad (\text{B.3})$$

Figure B.1 shows a time-dependent function and illustrates explicit and implicit time integration. This illustration shows the disadvantage of an explicit method. The direct evaluation of the target function does not match the exact solution. The implicit solution is superior, as the iteration process results in the convergence to the exact solution value. The solution discrepancy of the explicit method increases with each time step and can lead to a full divergence of the approximation from the solution. To prevent this divergence, the chosen time increment  $\Delta t$  has to be chosen very small. Hence, the computational effort of an explicit model results from a high

number of increments, while the computation effort of the implicit solution results from the iteration effort.

This difference of the computationally costly part of the solution process leads to a significantly different behavior of the computation effort with both methods. The effort to employ an explicit time integration increases linearly with the number of DoF. In contrast, the effort of an implicit time integration increases quadratically. For that reason, an explicit solution is of particular interest for models with many DoF.

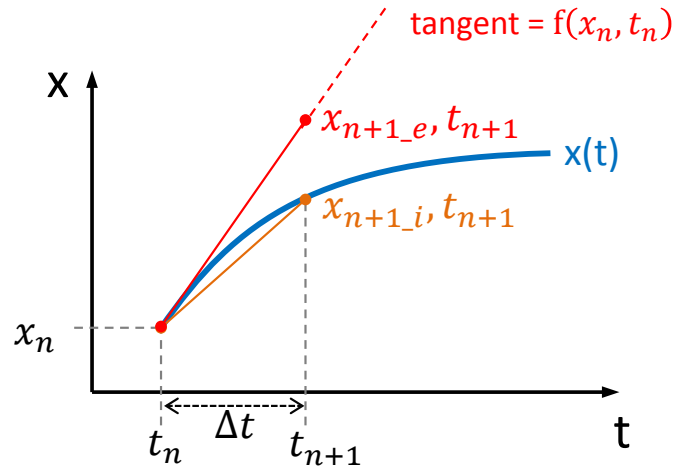


FIGURE B.1: Time integration by an explicit and an implicit procedure.

## B.2 Least squares (LSQ) function estimation

The LSQ estimation is a method to solve overdetermined linear systems of equations. This solution method applies, for example, when experimental data shall be used to fit a function with less free parameters than available data sets. Adrien-Marie Legendre was the first to describe it, at the beginning of the 19th century [200]. Today, it remains a commonly used tool for the evaluation of measured data [201].

Equation (B.4) shows a generic correlation between the result value  $y$  and the input values  $x_i$ . Both vectors are coupled through a set of parameters  $\mathbf{b}$ . When this correlation can be written in a linearized form to its unknown parameters  $\mathbf{b}$ , as Equation (B.5) shows, it can be interpolated by an LSQ estimation. The correlation between the parameters  $b_i$  and the function values  $\mathbf{y}$  has to be necessarily linear.

When a set of data is the basis of the interpolation, many equations like Equation (B.5) exist and can be rewritten, using a matrix notation. In this case,  $\mathbf{y}$  becomes the result vector and  $\mathbf{X}$  the matrix of input parameters.

$$y = f(x_i, b_i) \tag{B.4}$$

$$y = \sum_{i=1}^n x_i b_i \tag{B.5}$$



The system of equations has more equations than free variables and a solution for  $\mathbf{b}$  to meet all equations usually does not exist. The deviation of a solution is captured in the residuum  $\mathbf{R}$  as shown in Equation (B.6).

$$\mathbf{R}_{LSQ}(b) = \sum_{i=1}^n |y_i - \sum_{j=1}^m X_{ij}b_j|^2 = \|\mathbf{y} - \mathbf{X}\mathbf{b}\|^2 \quad (\text{B.6})$$

In order to obtain the best estimation, the LSQ method requests the minimum of the function  $R_{LSQ}(b)$  in Equation (B.7). This equation provides a set of parameters  $\hat{\mathbf{b}}$ , that produces the smallest residuum  $\mathbf{R}$  for the set of of input data  $\mathbf{X}$  and resulting values  $\mathbf{y}$ .

$$\hat{\mathbf{b}} = (\mathbf{X}^T\mathbf{X})^{-1} \mathbf{X}^T\mathbf{y} \quad (\text{B.7})$$

### B.3 Symmetry of tensors

A tensor of the dimension  $d$  and the order  $n$  has  $n^d$  entries. However, for symmetrical tensors, the number of independent entries is much smaller. This number of independent entries  $e$  can be determined through the exploitation of the tensor symmetry. Thus, the effort required for the assembly of the full tensor significantly decreases.

Let  $n\mathbf{T}$  be an  $n^{\text{th}}$ -order tensor of the dimension  $d$ . In that case, a second-order tensor  ${}_2\mathbf{T}$  has got  $d$  independent diagonal entries. Using the first symmetry  ${}_2\mathbf{T}_{ij} = {}_2\mathbf{T}_{ji}$ , the remaining entries appear twice. From Equation (B.8) we obtain the number of independent entries  $e(2, d)$  for a second-order tensor depending on the dimension  $d$ . The value  $e(2, d)$  results from number of diagonal values  $d$ . In addition, the subtraction of the number of diagonal entries from the total number of entries, and dividing them by two provides the number of additional independent entries.

$$e(2, d) = d + \frac{d^2 - d}{2} \quad (\text{B.8})$$

To understand the symmetry of higher-order tensors, we considering a tensor of the fourth order. We can express the major symmetry as  ${}_4\mathbf{T}_{ijkl} = {}_4\mathbf{T}_{klji}$ . The sub-symmetries are considered by the tensor consisting of  $d^2$  symmetric second-order tensors. This symmetry condition leads to Equation (B.9) describing the number of independent entries  $e(4, d)$  for a fourth-order tensor of the dimension  $d$ .

$$e(4, d) = e(2, d) + \frac{e(2, d)^2 - e(2, d)}{2} \quad (\text{B.9})$$

With a typical dimension of  $d = 3$  for a tensor in three-dimensional mechanics, the number of independent entries can be computed. A recursive formula in Equation (B.10) for the number of independent entries can be derived from that principle. Table B.1 shows the number of independent entries for for two-dimensional and three-dimensional tensor up to the eighth order.

$$e(2n, d) = e(n, d) + \frac{e(n, d)^2 - e(n, d)}{2} \quad (\text{B.10})$$

$n$	1	2	4	8
$e(n, 2)$	2	3	6	21
$e(n, 3)$	3	6	21	231

TABLE B.1: Number of independent entries  $e$  depending on the tensor order  $n$ .

A brief thought experiment helps to confirm the value  $e = 231$  for a three-dimensional eighth-order tensor. The Voigt notation for Hooke's law uses a two-dimensional matrix  ${}_2\mathbf{C}$  to write the fourth-order stiffness tensor  ${}_4\mathbf{C}$ . The stress and strain tensors are written as  $6 \times 1$  vectors. The  $6 \times 6$  matrix  ${}_2\mathbf{C}$  is also symmetrical. Consequently it consists of 21 independent entries (cf. Table B.1).

If we apply the same principle to the mapping of a fourth-order  ${}_4\mathbf{C}$  tensor through an eighth-order tensor  ${}_8\mathbf{D}$  a  $21 \times 1$  vector has to be multiplied by a  $21 \times 21$  matrix. This symmetrical matrix has 441 entries, of which 21 are located on the main diagonal. Due to the symmetry, the other 420 entries occur twice. Consequently, the tensor  ${}_8\mathbf{D}$  consists of  $21 + \frac{420}{2} = 231$  independent entries. The result of Equation (B.10) in Table B.1 provides exactly this value for  $e(8, 3)$ .

## Bibliography

- [1] H. Schürmann. *Konstruieren mit Faser-Kunststoff-Verbunden*. VDI-Buch. Springer Berlin Heidelberg, 2007, p. 672. ISBN: 9783540721901. URL: <https://books.google.de/books?id=8KQkBAAAQBAJ>.
- [2] W. J. Cantwell and J. Morton. “The impact resistance of composite materials - a review”. In: *Composites* 22.5 (1991), pp. 347–362. ISSN: 00104361. DOI: 10.1016/0010-4361(91)90549-V.
- [3] W. J. Cantwell and J. Morton. “The significance of damage and defects and their detection in composite materials: A review”. In: *J. Strain Anal. Eng. Des.* 27.1 (1992), pp. 29–42. ISSN: 0309-3247. DOI: 10.1243/03093247V271029.
- [4] E. S. Greenhalgh. *Failure analysis and fractography of polymer composites*. 1st ed. Woodhead Publishing Series in Composites Science and Engineering 27. Woodhead Publishing, 2009. ISBN: 978-1845692179.
- [5] A. Puck. *Festigkeitsanalyse von Faser-Matrix-Laminaten: Modelle für die Praxis*. Wien: Hanser, 1996, p. 210. ISBN: 9783446181946.
- [6] P. D. Ewins and A. C. Ham. “The nature of compressive failure in unidirectional carbon fiber reinforced plastics”. In: *AIAA Bull.* (1974). DOI: doi: 10.2514/6.1974-353.
- [7] S. T. Pinho et al. “Failure Models and Criteria for FRP Under In-Plane or Three-Dimensional Stress States Including Shear Non-linearity”. In: *Tm-2005-213530* February (2005), p. 68. DOI: NASA/TM-2005-213530.
- [8] W. M. Lai et al. *Introduction to Continuum Mechanics*. Elsevier Science, 2009, p. 536. ISBN: 9780080942520. URL: <https://books.google.de/books?id=1Ehh-hjG6EgC%7B%5C%7Dh1>.
- [9] D. Liu, E. Lansing, and L. E. Malvern. “Cracking in Impacted Glass / Epoxy Plates”. In: *J. Compos. Mater.* 21.July 1987 (1987), pp. 594–609.
- [10] M. Hosur et al. “Estimation of impact-induced damage in CFRR laminates through ultrasonic imaging”. In: *NDT E Int.* 31.5 (1998), pp. 359–374. ISSN: 09638695. DOI: 10.1016/S0963-8695(97)00053-4.
- [11] F.-G. Buchholz et al. “Delamination Analysis for Cross-Ply Laminates”. In: *Proc. Tenth Int. Conf. Compos. Mater. Fatigue Fract.* Woodhead Publishing, 1995, pp. 141–148.
- [12] C. Linder and B. of California. *New Finite Elements with Embedded Strong Discontinuities for the Modeling of Failure in Solids*. University of California, Berkeley, 2007. ISBN: 9780549611561. URL: <https://books.google.de/books?id=F6obZxoH0Q4C>.
- [13] X. Chen. *Advanced Fibrous Composite Materials for Ballistic Protection*. Woodhead Publishing Series in Composites Science and Engineering. Elsevier Science, 2016. ISBN: 9781782424840. URL: <https://books.google.de/books?id=7c4HBgAAQBAJ>.

- [14] M. F. Pernice et al. “Experimental study on delamination migration in composite laminates”. In: *Compos. Part A Appl. Sci. Manuf.* 73 (2015), pp. 20–34. ISSN: 1359835X. DOI: 10.1016/j.compositesa.2015.02.018.
- [15] L. K. Grunenfelder et al. “Acta Biomaterialia Bio-inspired impact-resistant composites q”. In: *ACTA Biomater.* (2014). ISSN: 1742-7061. DOI: 10.1016/j.actbio.2014.03.022.
- [16] S. Abrate. *Impact on Composite Structures*. Cambridge: Cambridge University Press, 1998. ISBN: 978-0521018326.
- [17] J.-H. Choi and F.-K. Chang. “A Model for Predicting Damage in Graphite/Epoxy Laminated Composites Resulting from Low-Velocity Point Impact”. In: *J. Compos. Mater.* 26.14 (Jan. 1992), pp. 2134–2169. ISSN: 0021-9983. DOI: 10.1177/002199839202601408.
- [18] Y. B. Shi and A. F. Yee. “Intraply crack and delamination interaction in laminate beams under transverse loading”. In: *Compos. Struct.* 29.3 (1994), pp. 287–297. ISSN: 02638223. DOI: 10.1016/0263-8223(94)90025-6.
- [19] S. P. Timoshenko. “On the correction for shear of the differential equation for transverse vibrations of prismatic bars”. In: *Philos. Mag. Ser. 6* 41.245 (1921), pp. 744–746. ISSN: 1941-5982. DOI: 10.1080/14786442108636264.
- [20] M. Radwańska et al. *Plate and Shell Structures: Selected Analytical and Finite Element Solutions*. Wiley, 2017. ISBN: 9781118934548.
- [21] E. McCurdy. *The notebooks of Leonardo da Vinci*. The Notebooks of Leonardo Da Vinci. Reynal & Hitchcock, 1938. URL: <https://books.google.de/books?id=qMoQAAAAIAAJ>.
- [22] G. Newaz and R. L. Sierakowski. *Damage Tolerance in Advanced Composites*. Taylor & Francis, 1995. ISBN: 9781566762618. URL: [https://books.google.de/books?id=%7B%5C\\_%7Dhr1Ys1toA4C](https://books.google.de/books?id=%7B%5C_%7Dhr1Ys1toA4C).
- [23] Federal Aviation Administration. *AC20-107B*. 2009. DOI: 10.1016/S0034-3617(11)70147-3. URL: [http://www.faa.gov/documentLibrary/media/Advisory%7B%5C\\_%7DCircular/AC20-107B.pdf](http://www.faa.gov/documentLibrary/media/Advisory%7B%5C_%7DCircular/AC20-107B.pdf).
- [24] H. K. Reddick Jr. “Safe-life and damage-tolerant design approaches for helicopter structures”. In: *Fail. Anal. Mech. Fail. Fibrous Compos. Struct.* 2278 (1983), pp. 129–151. ISSN: 01917811.
- [25] F. A. Administration. *Damage Tolerance Assessment Handbook*. Tech. rep. Cambridge, MA: U.S. Department of Transportation, 1993, p. 168.
- [26] J. Baaran. “Study on visual inspection of composite structures EASA.2007/3”. In: (2009).
- [27] J. Y. Mann and I. S. Milligan. *Aircraft Fatigue: Design, Operational and Economic Aspects*. Elsevier Science, 2013. ISBN: 9781483146454.
- [28] R. Hooke. *Lectiones Cutlerianæ, or A collection of lectures: physical, mechanical, geographical, & astronomical*. London, 1679.
- [29] R. von Mises. “Mechanik der festen Körper im plastisch deformablen Zustand”. In: *Nachrichten von der Gesellschaft der Wissenschaften zu Göttingen* 1 (1913), pp. 582–592.
- [30] W. J. M. Rankine. “On the Stability of Loose Earth”. In: *Philos. Trans. R. Soc. London* 147 (1857), pp. 9–27. ISSN: 0261-0523. DOI: 10.1098/rstl.1857.0003.

- [31] M. Hinton, P. D. Soden, and A. S. Kaddour. *Failure Criteria in Fibre-Reinforced-Polymer Composites*. Elsevier Science, 2004. ISBN: 9780080531571.
- [32] A. S. Kaddour and M. J. Hinton. “Maturity of 3D failure criteria for fibre-reinforced composites: Comparison between theories and experiments: Part B of WWFE-II”. In: *J. Compos. Mater.* 47.6-7 (2013), pp. 925–966. ISSN: 0021-9983. DOI: 10.1177/0021998313478710.
- [33] K. Rohwer. “Predicting fiber composite damage and failure”. In: *J. Compos. Mater.* 1.September (2014), pp. 0021998314553885–. ISSN: 0021-9983. DOI: 10.1177/0021998314553885.
- [34] P. P. Camanho. “Failure Criteria for Fibre-Reinforced Polymer Composites”. In: *Demegi, Feup Figure 1* (2002), pp. 1–13. URL: <http://paginas.fe.up.pt/%7B~%7Dstpinho/teaching/feup/y0506/fcriteria.pdf>.
- [35] S. W. Tsai and E. M. Wu. “A General Theory of Strength for Anisotropic Materials”. In: *J. Compos. Mater.* 5.1 (1971), pp. 58–80. ISSN: 0021-9983. DOI: 10.1177/002199837100500106.
- [36] C. Chamis. “Failure Criteria for Filamentary Composites”. In: *Compos. Mater. Test. Des.* STP460 (1969), pp. 336–351. DOI: 10.1520/STP49826S.
- [37] Z. Hashin. “Failure Criteria for Unidirectional Fiber Composites”. In: *J. Appl. Mech.* 47 (1980), pp. 329–334.
- [38] A. Puck and H. Schürmann. “Failure analysis of FRP laminates by means of physically based phenomenological models”. In: *Compos. Sci. Technol.* 62.12-13 Special Issue (2002), pp. 1633–1662. ISSN: 02663538. DOI: 10.1016/S0266-3538(01)00208-1.
- [39] J. Wiegand, N. Petrinic, and B. Elliott. “An algorithm for determination of the fracture angle for the three-dimensional Puck matrix failure criterion for UD composites”. In: *Compos. Sci. Technol.* 68.12 (2008), pp. 2511–2517. ISSN: 02663538. DOI: 10.1016/j.compscitech.2008.05.004.
- [40] Y. Shi, C. Pinna, and C. Soutis. “Modelling impact damage in composite laminates: A simulation of intra- and inter-laminar cracking”. In: *Compos. Struct.* 114 (2014), pp. 10–19. ISSN: 02638223. DOI: 10.1016/j.compstruct.2014.03.052.
- [41] R. G. Cuntze and a. Freund. “The predictive capability of failure mode concept-based strength criteria for multidirectional laminates”. In: *Compos. Sci. Technol.* 64.3-4 (2004), pp. 343–377. ISSN: 02663538. DOI: 10.1016/S0266-3538(03)00218-5.
- [42] P. Maimí et al. “A continuum damage model for composite laminates: Part I - Constitutive model”. In: *Mech. Mater.* 39.10 (2007), pp. 897–908. ISSN: 01676636. DOI: 10.1016/j.mechmat.2007.03.005.
- [43] P. Maimí et al. “A continuum damage model for composite laminates: Part II - Computational implementation and validation”. In: *Mech. Mater.* 39.10 (2007), pp. 909–919. ISSN: 01676636. DOI: 10.1016/j.mechmat.2007.03.006.
- [44] M. V. Donadon et al. “A progressive failure model for composite laminates subjected to low velocity impact damage”. In: *Comput. Struct.* 86.11-12 (2008), pp. 1232–1252. ISSN: 00457949. DOI: 10.1016/j.compstruc.2007.11.004.

- [45] A. Puck, J. Kopp, and M. Knops. “Guidelines for the determination of the parameters in Puck’s action plane strength criterion”. In: *Compos. Sci. Technol.* 62.3 (2002), pp. 371–378. ISSN: 02663538. DOI: 10.1016/S0266-3538(01)00202-0. arXiv: S0065-2156(08)70121-2.
- [46] R. G. Cuntze. “The predictive capability of failure mode concept- based strength criteria for multi-directional laminates – Part B”. In: *Stress Int. J. Biol. Stress* 1.2 (2004), pp. 976–1025. DOI: [http://dx.doi.org/10.1016/S0266-3538\(03\)00218-5](http://dx.doi.org/10.1016/S0266-3538(03)00218-5).
- [47] R. Basan. *Untersuchung der intralaminaren Schubeigenschaften von Faserverbundwerkstoffen mit Epoxidharzmatrix unter Berücksichtigung nichtlinearer Effekte*. 2011. ISBN: 9783981428131. URL: [http://www.bam.de/de/service/publikationen/publikationen%7B%5C\\_%7Dmedien/dissertationen/diss%7B%5C\\_%7D74%7B%5C\\_%7Dvt.pdf](http://www.bam.de/de/service/publikationen/publikationen%7B%5C_%7Dmedien/dissertationen/diss%7B%5C_%7D74%7B%5C_%7Dvt.pdf).
- [48] G. Catalanotti, P. P. Camanho, and a. T. Marques. “Three-dimensional failure criteria for fiber-reinforced laminates”. In: *Compos. Struct.* 95 (2013), pp. 63–79. ISSN: 02638223. DOI: 10.1016/j.compstruct.2012.07.016.
- [49] H. M. Deuschle. *3D Failure Analysis of UD Fibre Reinforced Composites: Puck’s Theory within FEA*. 2010. ISBN: 3930683997.
- [50] G. Lutz and V. Getriebebau. “The Puck theory of failure in laminates in the context of the new guideline VDI 2014 Part 3”. In: *Conf. damage Compos. ...* (2006), pp. 1–12. URL: <http://212.8.206.21/article/cdcm2006/papers/lutzii.pdf>.
- [51] C. E. Inglis. *Stresses in a plate due to the presnce of cracks and sharp corners*. 1913.
- [52] A. Griffith. “The Phenomena of Rupture and Flow in Solids”. In: *Philos. Trans. R. Soc. London* 221 (1921), pp. 163–198.
- [53] G. Irwin. *Fracturing of Metals*. Tech. rep. Cleveland, Ohio: American Society for Metals, 1947, pp. 146–166.
- [54] G. Irwin. “Analysis of Stresses and Strains Near the End of a Crack Traversing a Plate”. In: *J. Appl. Mech.* 24.September (1957), pp. 361–364. ISSN: 04306252.
- [55] L. Kachanov. *Introduction to continuum damage mechanics*. Mechanics of Elastic Stability. Springer Netherlands, 2013. ISBN: 9789401719575.
- [56] J. Lemaitre and J.-L. Chaboche. *Mechanics of solid materials*. Cambridge University Press, 1990, p. 584. ISBN: 978-0521328531.
- [57] J.-L. Chaboche. “Continuous damage mechanics - a tool to describe phenomena before crack initiation”. In: *Nucl. Eng. Des.* 64 (1981), pp. 233–247.
- [58] P. Ladeveze and E. LeDantec. “Damage modelling of the elementary ply for laminated composites”. In: *Compos. Sci. Technol.* 43.3 (1992), pp. 257–267. ISSN: 02663538. DOI: 10.1016/0266-3538(92)90097-M.
- [59] P. Ladeveze. “A damage computational approach for composites: Basic aspects and micromechanical relations”. In: *Comput. Mech.* 17.1-2 (1995), pp. 142–150. ISSN: 01787675. DOI: 10.1007/BF00356486.
- [60] W. Tan et al. “Predicting low velocity impact damage and Compression-After-Impact (CAI) behaviour of composite laminates”. In: *Compos. Part A Appl. Sci. Manuf.* 71 (Apr. 2015), pp. 212–226. ISSN: 1359835X. DOI: 10.1016/j.compositesa.2015.01.025.

- [61] E. V. González et al. “Simulation of drop-weight impact and compression after impact tests on composite laminates”. In: *Compos. Struct.* 94.11 (2012), pp. 3364–3378. ISSN: 02638223. DOI: 10.1016/j.compstruct.2012.05.015.
- [62] P. F. Liu et al. “Finite element analysis of dynamic progressive failure of carbon fiber composite laminates under low velocity impact”. In: *Compos. Struct.* 149 (2016), pp. 408–422. ISSN: 0263-8223. DOI: 10.1016/j.compstruct.2016.04.012.
- [63] B. A. Gama and J. W. Gillespie Jr. “Finite element modeling of impact, damage evolution and penetration of thick-section composites”. In: *Int. J. Impact Eng.* 38.4 (Apr. 2011), pp. 181–197. ISSN: 0734-743X. DOI: <http://dx.doi.org/10.1016/j.ijimpeng.2010.11.001>.
- [64] C. Lopes et al. “Physically-Sound Simulation of Low-Velocity Impact on Fibre Reinforced Laminates”. In: *Int. J. Impact Eng.* (2015), pp. 1–15. ISSN: 0734743X. DOI: 10.1016/j.ijimpeng.2015.05.014.
- [65] E. V. González et al. “Simulation of drop-weight impact and compression after impact tests on composite laminates”. In: *Compos. Struct.* 94.11 (Nov. 2012), pp. 3364–3378. ISSN: 02638223. DOI: 10.1016/j.compstruct.2012.05.015.
- [66] L. Raimondo et al. “A progressive failure model for mesh-size-independent FE analysis of composite laminates subject to low-velocity impact damage”. In: *Compos. Sci. Technol.* 72.5 (2012), pp. 624–632. ISSN: 02663538. DOI: 10.1016/j.compscitech.2012.01.007.
- [67] A. Faggiani and B. Falzon. “Predicting low-velocity impact damage on a stiffened composite panel”. In: *Compos. Part A Appl. Sci. Manuf.* 41.6 (2010), pp. 737–749. ISSN: 1359835X. DOI: 10.1016/j.compositesa.2010.02.005.
- [68] A. Matzenmiller, J. Lubliner, and R. L. Taylor. “A constitutive model for anisotropic damage in fiber-composites”. In: *Mech. Mater.* 20 (1995), pp. 125–152.
- [69] B. Z. Haque. *A progressive damage model for unidirectional and woven fabric composites*. Tech. rep. May. Delaware: University of Delaware Center for Composite Materials, 2014.
- [70] L. Kärger et al. “Evaluation of impact assessment methodologies. Part I: Applied methods”. In: *Compos. Part B Eng.* 40.1 (Jan. 2009), pp. 65–70. ISSN: 13598368. DOI: 10.1016/j.compositesb.2008.06.003.
- [71] M. J. Turner et al. “Stiffness and Deflection Analysis of Complex Structures”. In: *J. Aeronaut. Sci.* 23.9 (1956), p. 20.
- [72] J. H. Argyris. *Energy Theorems and Structural Analysis: A Generalised Discourse with Applications on Energy Principles of Structural Analysis Including the Effects of Temperature and Nonlinear Stress-strain Relations*. Butterworth’s scientific publications Teil 2. Butterworth, 1960.
- [73] O. C. Zienkiewicz and Y. K. Cheung. *The finite element method in structural and continuum mechanics: numerical solution of problems in structural and continuum mechanics*. European civil engineering series Bd. 1. McGraw-Hill, 1967.
- [74] K. J. Bathe and E. L. Wilson. *Numerical methods in finite element analysis*. Prentice-Hall civil engineering and engineering mechanics series. Prentice-Hall, 1976. ISBN: 9780136271901.

- [75] K. J. Bathe and P. Zimmermann. *Finite-Elemente-Methoden*. Springer, 2002. ISBN: 9783540668060.
- [76] G. Dhatt, E. Lefrançois, and G. Touzot. *Finite Element Method*. ISTE. Wiley, 2012. ISBN: 9781118569702.
- [77] R. Courant, K. Friedrichs, and H. Lewy. *On the Partial Difference Equations of Physics*. Tech. rep. New York: New York University, 1956, p. 92.
- [78] J. Peraire et al. “Finite element Euler computations in three dimensions”. In: *Int. J. Numer. Methods Eng.* 26.10 (1988), pp. 2135–2159. ISSN: 10970207. DOI: 10.1002/nme.1620261002.
- [79] Simulia. *Abaqus Analysis User’s Guide*. 2015.
- [80] J. Plešek, R. Kolman, and D. Gabriel. “Estimation of critical time step for explicit integration”. In: *18th Int. Conf. Eng. Mech.* (2012), pp. 1001–1010. DOI: 10.1016/j.arthro.2012.06.001.
- [81] C. A. Rose, C. G. Dávila, and F. A. Leone. “Analysis Methods for Progressive Damage of Composite Structures”. In: *NASA Langley Res. Cent. NASA/TM-20. July 2013* (2013).
- [82] S. Rivallant, C. Bouvet, and N. Hongkarnjanakul. “Failure analysis of CFRP laminates subjected to compression after impact: FE simulation using discrete interface elements”. In: *Compos. Part A Appl. Sci. Manuf.* 55 (2013), pp. 83–93. ISSN: 1359835X. DOI: 10.1016/j.compositesa.2013.08.003.
- [83] Archimedes. *The Works of Archimedes*. Cosimo, Incorporated, 2007. ISBN: 9781602062528. URL: <https://books.google.de/books?id=6nPDFR89HhwC>.
- [84] K. Willner and L. Gaul. “A penalty approach for contact description by FEM based on interface physics”. In: 17 (1998), pp. 589–598.
- [85] J. C. Simo, P. Wriggers, and R. L. Taylor. “A perturbed Lagrangian formulation for the finite element solution of contact problems”. In: *Comput. Methods Appl. Mech. Eng.* 50.2 (1985), pp. 163–180. ISSN: 00457825. DOI: 10.1016/0045-7825(85)90088-X.
- [86] L. De Lorenzis and G. Zavarise. “Cohesive zone modeling of interfacial stresses in plated beams”. In: *Int. J. Solids Struct.* 46.24 (2009), pp. 4181–4191. ISSN: 00207683. DOI: 10.1016/j.ijsolstr.2009.08.010.
- [87] D. Dugdale. “Yielding of steel sheets containing slits”. In: *J. Mech. Phys. Solids* 8.2 (1960), pp. 100–104. ISSN: 00225096. DOI: 10.1016/0022-5096(60)90013-2. arXiv: 0021-8928(59)90157-1 [10.1016].
- [88] G. I. Barenblatt. “The Mathematical Theory of Equilibrium of Crack in Brittle Fracture”. In: *Adv. Appl. Mech.* 7 (1962), pp. 55–129. ISSN: 00652156. arXiv: S0065-2156(08)70121-2.
- [89] O. Allix and P. Ladevèze. “Interlaminar interface modelling for the prediction of laminate delamination”. In: *Compos. Struct.* 22 (1992), pp. 235–242.
- [90] A. Turon et al. “An engineering solution for mesh size effects in the simulation of delamination using cohesive zone models”. In: *Eng. Fract. Mech.* 74.10 (2007), pp. 1665–1682. ISSN: 00137944. DOI: 10.1016/j.engfracmech.2006.08.025.
- [91] P. W. Harper and S. R. Hallett. “Cohesive zone length in numerical simulations of composite delamination”. In: *Eng. Fract. Mech.* 75.16 (2008), pp. 4774–4792. ISSN: 00137944. DOI: 10.1016/j.engfracmech.2008.06.004.



- [92] R. Olsson. “Analytical prediction of large mass impact damage in composite laminates”. In: *Compos. Part A Appl. Sci. Manuf.* 32.9 (2001), pp. 1207–1215. ISSN: 1359835X. DOI: 10.1016/S1359-835X(01)00073-2.
- [93] W. J. Cantwell and J. Morton. “Comparison of the low and high velocity impact response of CFRP”. In: *Composites* 20.6 (1989), pp. 545–551. ISSN: 00104361. DOI: 10.1016/0010-4361(89)90913-0.
- [94] S. Abrate. “Impact on Laminated Composite Materials”. In: *Appl. Mech. Rev.* 44.4 (Apr. 1991), pp. 155–190. ISSN: 0003-6900. URL: <http://dx.doi.org/10.1115/1.3119500>.
- [95] A. P. Christoforou and A. S. Yigit. “Effect of Flexibility on Low Velocity Impact Response”. In: *J. Sound Vib.* 217.3 (Oct. 1998), pp. 563–578. ISSN: 0022460X. DOI: 10.1006/jsvi.1998.1807. URL: <http://linkinghub.elsevier.com/retrieve/pii/S0022460X98918077>.
- [96] A. P. Christoforou. “Impact dynamics and damage in composite structures”. In: *Compos. Struct.* 52.2 (2001), pp. 181–188. ISSN: 02638223. DOI: 10.1016/S0263-8223(00)00166-5.
- [97] R. Olsson. “Analytical model for delamination growth during small mass impact on plates”. In: *Int. J. Solids Struct.* 47.21 (2010), pp. 2884–2892. ISSN: 00207683. DOI: 10.1016/j.ijsolstr.2010.06.015.
- [98] H. Singh and P. Mahajan. “Analytical modeling of low velocity large mass impact on composite plates including damage evolution”. In: *Compos. Struct.* 149 (2016), pp. 79–92. ISSN: 02638223. DOI: 10.1016/j.compstruct.2016.04.009.
- [99] H. Hertz. “Ueber die Berührung fester elastischer Körper”. In: *J. für die Reine und Angew. Math.* I.92 (1881), pp. 156–171. ISSN: 14355345. DOI: 10.1515/crll.1882.92.156.
- [100] K. Karas. “Platten unter seitlichem Stoß”. In: *Ing. Arch.* 10 (1939), pp. 237–250.
- [101] A. L. Dobyns. “Analysis of Simply-Supported Orthotropic Plates Subject to Static and Dynamic Loads”. In: *AIAA J.* 19.5 (1981), pp. 642–650. ISSN: 0001-1452. DOI: 10.2514/3.50984.
- [102] R. Olsson. “Impact response of orthotropic composite plates predicted from a one-parameter differential equation”. In: *AIAA J.* 30.6 (1992), pp. 1587–1596. ISSN: 0001-1452. DOI: 10.2514/3.11105.
- [103] S. R. Swanson. “Contact deformation and stress in orthotropic plates”. In: *Compos. Part A Appl. Sci. Manuf.* 36 (2005), pp. 1421–1429. ISSN: 1359835X. DOI: 10.1016/j.compositesa.2004.11.011.
- [104] F. Najafi, M. H. Shojaeefard, and H. Saeidi Googarchin. “Low-velocity impact response of functionally graded doubly curved panels with Winkler-Pasternak elastic foundation: An analytical approach”. In: *Compos. Struct.* 162 (2016), pp. 351–364. ISSN: 0263-8223. DOI: <http://dx.doi.org/10.1016/j.compstruct.2016.11.094>.
- [105] G. Schoeppner and S. Abrate. “Delamination threshold loads for low velocity impact on composite laminates”. In: *Compos. Part A Appl. Sci. Manuf.* 31.9 (2000), pp. 903–915. ISSN: 1359835X. DOI: 10.1016/S1359-835X(00)00061-0.

- [106] W. C. Jackson and C. C. Poe. *The Use of Impact Force As a Scale Parameter for the Impact Response of Composite*. Tech. rep. Hampton, Virginia: NASA Langley Research Center, 1992, p. 28.
- [107] D. Elder, R. Thomson, and M. Scott. “Comparison of composite damage predictions between a 2D, 3D LS-Dyna simulation and experimental results for a low speed impact event”. In: *Proc. Tenth Aust. Int. Aerosp. Congr.* Brisbane, 2003.
- [108] J. Yap et al. “Composite stiffened panels impact damage simulation and parametric studies”. In: *Proc. Tenth Aust. Int. Aerosp. Congr.* Brisbane, 2003.
- [109] J. Baaran, L. Kärger, and A. Wetzel. “Efficient prediction of damage resistance and tolerance of composite aerospace structures”. In: *Proc. Inst. Mech. Eng. Part G J. Aerosp. Eng.* 222.2 (2008), pp. 179–188. ISSN: 0954-4100. DOI: 10.1243/09544100JAERO278.
- [110] L. Kärger, J. Baaran, and J. Teßmer. “Efficient simulation of low-velocity impacts on composite sandwich panels”. In: *Comput. Struct.* 86.9 (May 2008), pp. 988–996. ISSN: 00457949. DOI: 10.1016/j.compstruc.2007.04.029.
- [111] A. F. Johnson, A. K. Pickett, and P. Rozycki. “Computational methods for predicting impact damage in composite structures”. In: *Compos. Sci. Technol.* 61.15 (2001), pp. 2183–2192. ISSN: 02663538. DOI: 10.1016/S0266-3538(01)00111-7.
- [112] R. Borg, L. Nilsson, and K. Simonsson. “Simulation of delamination in fiber composites with a discrete cohesive failure model”. In: *Compos. Sci. Technol.* 61.5 (2001), pp. 667–677. ISSN: 02663538. DOI: 10.1016/S0266-3538(00)00245-1.
- [113] R. Borg, L. Nilsson, and K. Simonsson. “Simulation of low velocity impact on fiber laminates using a cohesive zone based delamination model”. In: *Compos. Sci. Technol.* 64.2 (2004), pp. 279–288. ISSN: 02663538. DOI: 10.1016/S0266-3538(03)00256-2.
- [114] M. Loikkanen, G. Praveen, and D. Powell. “Simulation of Ballistic Impact on Composite Panels”. In: *10th Int. LS-DYNA Conf.* (2008), pp. 1–12. DOI: 10.15632/jtam-pl.53.2.263.
- [115] C. Bouvet, S. Rivallant, and J. J. Barrau. “Modelling of Impact Damage and Permanent Indentation on Laminate Composite Plate”. In: *14th Eur. Conf. Compos. Mater.* June (2010), pp. 1–10.
- [116] M. Ilyas. “Damage modeling of carbon epoxy laminated composites submitted to impact loading”. PhD thesis. L’Université de Toulouse, 2010, p. 261. URL: <http://oatao.univ-toulouse.fr/4272/>.
- [117] Y. Shi, C. Pinna, and C. Soutis. “Modelling impact damage in composite laminates: A simulation of intra- and inter-laminar cracking”. In: *Compos. Struct.* 114 (Aug. 2014), pp. 10–19. ISSN: 02638223. DOI: 10.1016/j.compstruct.2014.03.052.
- [118] C. Bouvet et al. “Discrete Impact Modeling of Inter- and Intra-laminar Failure in Composites”. In: *Dyn. Fail. Compos. Sandw. Struct.* 192 (2013), pp. 339–392. DOI: 10.1007/978-94-007-5329-7.

- [119] A. Riccio et al. “Characterisation of the impact induced damage in composites by cross-comparison among experimental non-destructive evaluation techniques and numerical simulations”. In: *Proc. Inst. Mech. Eng. Part C J. Mech. Eng. Sci.* (2016), p. 0954406216681595. ISSN: 0954-4062. DOI: 10.1177/0954406216681595.
- [120] E. Panettieri et al. “Low-velocity impact tests on carbon/epoxy composite laminates: A benchmark study”. In: *Compos. Part B Eng.* 107 (2016), pp. 9–21. ISSN: 13598368. DOI: 10.1016/j.compositesb.2016.09.057.
- [121] F. Ehrich. “Low Velocity Impact on Pre-Loaded Composite Structures”. PhD thesis. 2013.
- [122] N. Hongkarnjanakul, C. Bouvet, and S. Rivallant. “Validation of low velocity impact modelling on different stacking sequences of CFRP laminates and influence of fibre failure”. In: *Compos. Struct.* 106 (Dec. 2013), pp. 549–559. ISSN: 02638223. DOI: 10.1016/j.compstruct.2013.07.008.
- [123] G. Nian et al. “Failure analysis of syntactic foams: A computational model with cohesive law and XFEM”. In: *Compos. Part B Eng.* 89 (2016), pp. 18–26. ISSN: 13598368. DOI: 10.1016/j.compositesb.2015.10.044.
- [124] S. Chen et al. “Numerical analysis of impact failure of automotive laminated glass: A review”. In: *Compos. Part B Eng.* 122 (2017), pp. 47–60. ISSN: 13598368. DOI: 10.1016/j.compositesb.2017.04.007.
- [125] G. Molnár and A. Gravouil. “2D and 3D Abaqus implementation of a robust staggered phase-field solution for modeling brittle fracture”. In: *Finite Elem. Anal. Des.* 130.November 2016 (2017), pp. 27–38. ISSN: 0168874X. DOI: 10.1016/j.finel.2017.03.002.
- [126] S. Silling. “Reformulation of elasticity theory for discontinuities and long-range forces”. In: *J. Mech. Phys. Solids* 48.1 (2000), pp. 175–209. ISSN: 00225096. DOI: 10.1016/S0022-5096(99)00029-0.
- [127] M. Hahn. “Lebensdauerabschätzung von metallischen Strukturen mittels der Diskrete-Elemente-Methode im gekoppelten thermo-mechanischen Feld”. Doctoral thesis. University of Stuttgart, 2012. ISBN: 9783942807012.
- [128] Y. Huang, L. Xu, and S. Kyu Ha. “Prediction of three-dimensional composite laminate response using micromechanics of failure”. In: *J. Compos. Mater.* 46.June (2012), pp. 2431–2442. ISSN: 0021-9983. DOI: 10.1177/0021998312449888.
- [129] D. Krause. “A physically based micromechanical approach to model damage initiation and evolution of fiber reinforced polymers under fatigue loading conditions”. In: *Compos. Part B Eng.* 87 (2016), pp. 176–195. ISSN: 13598368. DOI: 10.1016/j.compositesb.2015.10.012.
- [130] G. V. G. Rao, P. Mahajan, and N. Bhatnagar. “Micro-mechanical modeling of machining of FRP composites - Cutting force analysis”. In: *Compos. Sci. Technol.* 67.3-4 (2007), pp. 579–593. ISSN: 02663538. DOI: 10.1016/j.compscitech.2006.08.010.
- [131] L. Wang et al. “Progressive failure analysis of 2D woven composites at the meso-micro scale”. In: *Compos. Struct.* 178 (2017), pp. 395–405. ISSN: 02638223. DOI: 10.1016/j.compstruct.2017.07.023.
- [132] C. Lopes et al. “Multiscale Simulation Strategy for Low-Velocity Impact on FRP”. In: *Proc. Am. Soc. Compos. - 29th Tech. Conf. Compos. Mater.* Ed. by H. Kim. DEStech Publications, Inc, 2014, pp. 59–78.

- [133] D. Ivančević and I. Smojver. “Explicit multiscale modelling of impact damage on laminated composites – Part I: Validation of the micromechanical model”. In: *Compos. Struct.* 145 (2016), pp. 248–258. ISSN: 02638223. DOI: 10.1016/j.compstruct.2016.02.048.
- [134] B. B. Liao et al. “Multi-scale modelling of dynamic progressive failure in composite laminates subjected to low velocity impact”. In: *Thin-Walled Struct.* 131:July (2018), pp. 695–707. ISSN: 02638231. DOI: 10.1016/j.tws.2018.07.047.
- [135] D. J. Elder et al. “Review of delamination predictive methods for low speed impact of composite laminates”. In: *Compos. Struct.* 66.1-4 (2004), pp. 677–683. ISSN: 02638223. DOI: 10.1016/j.compstruct.2004.06.004.
- [136] E. Troussset. “Prévision des dommages d’impact basse vitesse et basse énergie dans les composites à matrice organique stratifiés”. In: (2014).
- [137] P. Jousset and M. Rachik. “Comparison and evaluation of two types of cohesive zone models for the finite element analysis of fracture propagation in industrial bonded structures”. In: *Eng. Fract. Mech.* 132 (2014), pp. 48–69. ISSN: 00137944. DOI: 10.1016/j.engfracmech.2014.10.018.
- [138] M. May. “Numerical evaluation of cohesive zone models for modeling impact induced delamination in composite materials”. In: *Compos. Struct.* 133 (2015), pp. 16–21. ISSN: 02638223. DOI: 10.1016/j.compstruct.2015.07.032.
- [139] X. Sun, M. Wisnom, and S. Hallett. “Interaction of inter- and intralaminar damage in scaled quasi-static indentation tests: Part 2 - Numerical Simulation”. In: *Submitt. to Compos. Struct.* 136 (2015), pp. 712–726. ISSN: 02638223. DOI: 10.1016/j.compstruct.2015.09.061.
- [140] E. Panettieri, D. Fanteria, and F. Danzi. “Delaminations growth in compression after impact test simulations: Influence of cohesive elements parameters on numerical results”. In: *Compos. Struct.* 137 (2016), pp. 140–147. ISSN: 02638223. DOI: 10.1016/j.compstruct.2015.11.018.
- [141] H. Singh and P. Mahajan. “Modeling damage induced plasticity for low velocity impact simulation of three dimensional fiber reinforced composite”. In: *Compos. Struct.* 131 (2015), pp. 290–303. ISSN: 02638223. DOI: 10.1016/j.compstruct.2015.04.070. URL: <http://www.sciencedirect.com/science/article/pii/S0263822315003761>.
- [142] J. Pernas-Sánchez et al. “Numerical analysis of high velocity impacts on unidirectional laminates”. In: *Compos. Struct.* 107 (2014), pp. 629–634. ISSN: 02638223. DOI: 10.1016/j.compstruct.2013.08.035.
- [143] S. Heimbs et al. “High velocity impact on preloaded composite plates”. In: *Compos. Struct.* 111.1 (2014), pp. 158–168. ISSN: 02638223. DOI: 10.1016/j.compstruct.2013.12.031.
- [144] H. a. Israr et al. “Finite element simulation of 0°/90° CFRP laminated plates subjected to crushing using a free-face-crushing concept”. In: *Compos. Part A Appl. Sci. Manuf.* 62 (2014), pp. 16–25. ISSN: 1359835X. DOI: 10.1016/j.compositesa.2014.03.014.
- [145] B. Falzon and P. Apruzzese. “Numerical analysis of intralaminar failure mechanisms in composite structures. Part I: FE implementation”. In: *Compos. Struct.* 93.2 (2011), pp. 1039–1046. ISSN: 02638223. DOI: 10.1016/j.compstruct.2010.06.028.

- [146] M. Schwab and H. E. Pettermann. “Modelling and simulation of damage and failure in large composite components subjected to impact loads”. In: *Compos. Struct.* 158 (2016), pp. 208–216. ISSN: 02638223. DOI: 10.1016/j.compstruct.2016.09.041.
- [147] A. Riccio et al. “Modelling the simulation of impact induced damage onset and evolution in composites”. In: *Compos. PART B* 66 (2014), pp. 340–347. ISSN: 1359-8368. DOI: 10.1016/j.compositesb.2014.05.024.
- [148] A. Riccio et al. “A Joint Numerical-Experimental Study on Impact Induced Intra-laminar and Inter-laminar Damage in Laminated Composites”. In: *Appl. Compos. Mater.* 23.3 (2016), pp. 219–237. ISSN: 15734897. DOI: 10.1007/s10443-015-9457-0.
- [149] A. Riccio et al. “Numerical Investigation of a Stiffened Panel Subjected to Low Velocity Impacts”. In: *Key Eng. Mater.* 665 (2015), pp. 277–280. ISSN: 1662-9795. DOI: 10.4028/www.scientific.net/KEM.665.277.
- [150] A. F. Johnson, N. Toso-Pentecôte, and S. Kilchert. “Validation of damage modelling in composite fuselage structures under high velocity impact”. In: *CEAS Aeronaut. J.* 4.3 (2013), pp. 253–264. ISSN: 1869-5582. DOI: 10.1007/s13272-013-0071-2.
- [151] ASTM. *ASTM D7136 - Standard Test Method for Measuring the Damage Resistance of a Fiber-Reinforced Polymer Matrix Composite to a Drop-Weight Impact Event*. 2005. DOI: 10.1520/D7136.
- [152] D. I. für Normung. *DIN EN 6038 - Bestimmung der Restdruckfestigkeit nach Schlagbeanspruchung*. Berlin, 1996.
- [153] *AITM 1-0010 Determination of Compression Strength After Impact*. Blagnac, 2005.
- [154] L. Kärger, J. Baaran, and J. Teßmer. “Rapid simulation of impacts on composite sandwich panels inducing barely visible damage”. In: *Compos. Struct.* 79.4 (Aug. 2007), pp. 527–534. ISSN: 02638223. DOI: 10.1016/j.compstruct.2006.02.012.
- [155] K. Rohwer. “Application of higher order theories to the bending analysis of layered composite plates”. In: *Int. J. Solids Struct.* 29.1 (1992), pp. 105–119. ISSN: 00207683. DOI: 10.1016/0020-7683(92)90099-F.
- [156] R. Rolfes and K. Rohwer. “Improved transverse shear stresses in composite finite elements based on first order shear deformation theory”. In: *Int. J. Numer. Methods Eng.* 40.1 (1997), pp. 51–60. ISSN: 00295981.
- [157] K. Rohwer, R. Rolfes, and H. Sparr. “High-order theories for thermal stresses in layered plates”. In: *Int. J. Solids Struct.* 38.21 (2001), pp. 3673–3687. ISSN: 00207683. DOI: 10.1016/S0020-7683(00)00249-3.
- [158] C. P. Diemel and T. Qaimari. “A Finite Element Study on the Influence of Delamination Shape on Residual Compressive Behavior of Single and Multiple Delaminated Composite Structures”. In: *Proc. 5th Int. Work. Aircr. Syst. technoplogies*. Hamburg: Shaker Verlag Aachen, 2015, pp. 335–344.
- [159] B. C. Kim et al. “Through-thickness compressive strength of a carbon/epoxy composite laminate”. In: *Compos. Struct.* 92.2 (Jan. 2010), pp. 480–487. ISSN: 02638223. DOI: 10.1016/j.compstruct.2009.08.032.

- [160] J. Kreikemeier. “A Two Scale Finite-Element-Approach to Analyse the Damage State of Composite Structures”. PhD thesis. Otto-von-Guericke-Universität Magdeburg, 2011, p. 145.
- [161] A. Cauvin and R. B. Testa. “Damage mechanics : Basic variables in continuum theories”. In: *Int. J. Solids Struct.* 36.5 (1999), pp. 747–761. ISSN: 00207683. DOI: 10.1016/S0020-7683(98)00044-4.
- [162] P. B. Davenport. “Rotations about nonorthogonal axes”. In: *AIAA J.* 11.6 (1973), pp. 853–857. ISSN: 00011452. DOI: 10.2514/3.6842.
- [163] W. R. Hamilton. *On quaternions, or on a new system of imaginaries in algebra*. Tech. rep. 1844. DOI: 10.1080/14786444408644923.
- [164] P. P. Camanho et al. “Prediction of in situ strengths and matrix cracking in composites under transverse tension and in-plane shear”. In: *Compos. Part A Appl. Sci. Manuf.* 37.2 (2006), pp. 165–176. ISSN: 1359835X. DOI: 10.1016/j.compositesa.2005.04.023.
- [165] P. P. Camanho and S. R. Hallett. *Numerical Modelling of Failure in Advanced Composite Materials*. Woodhead Publishing Series in Composites Science and Engineering. Elsevier Science, 2015. ISBN: 9780081003428. URL: <https://books.google.de/books?id=Z1qZBQAAQBAJ>.
- [166] N. Uda, K. Ono, and K. Kunoo. “Compression fatigue failure of CFRP laminates with impact damage”. In: *Compos. Sci. Technol.* 69.14 (2009), pp. 2308–2314. ISSN: 02663538. DOI: 10.1016/j.compscitech.2008.11.031.
- [167] S. Xiao, P. Chen, and Q. Ye. “Prediction of damage area in laminated composite plates subjected to low velocity impact”. In: *Compos. Sci. Technol.* 98 (2014), pp. 51–56. ISSN: 02663538. DOI: 10.1016/j.compscitech.2014.04.016.
- [168] *ASTM D 5379 Standard Test Method for Shear Properties of Composite Materials by the V-notched Beam Method*. West Conshohocken, 2005.
- [169] C. Bouvet, S. Rivallant, and J. J. Barrau. “Low velocity impact modeling in composite laminates capturing permanent indentation”. In: *Compos. Sci. Technol.* 72.16 (2012), pp. 1977–1988. ISSN: 02663538. DOI: 10.1016/j.compscitech.2012.08.019.
- [170] D. Fanteria, G. Longo, and E. Panettieri. “A non-linear shear damage model to reproduce permanent indentation caused by impacts in composite laminates”. In: *Compos. Struct.* 111.1 (2014), pp. 111–121. ISSN: 02638223. DOI: 10.1016/j.compstruct.2013.12.017.
- [171] W. He et al. “Prediction of permanent indentation due to impact on laminated composites based on an elasto-plastic model incorporating fiber failure”. In: *Compos. Struct.* 96 (2013), pp. 232–242. ISSN: 02638223. DOI: 10.1016/j.compstruct.2012.08.054.
- [172] M. Schwab et al. “Simulation of the Intermediate Velocity Impact Behaviour of Woven Composite Laminates Applying”. In: *20th Int. Conf. Compos. Mater.* July. Copenhagen, 2015, pp. 19–24.
- [173] E. Buckingham. “On Physically Similar Systems; Illustrations of the Use of Dimensional Equations”. In: *Phys. Rev.* 4.4 (1914), pp. 345–376. DOI: 10.1103/PhysRev.4.345.
- [174] J. Morton. “Scaling of impact-loaded carbon-fiber composites”. In: *AIAA J.* 26.8 (1988), pp. 989–994. ISSN: 0001-1452. DOI: 10.2514/3.10001.

- [175] S. R. Swanson. “Scaling of impact damage in fiber composites from laboratory specimens to structures”. In: *Compos. Struct.* 25.1-4 (1993), pp. 249–255. ISSN: 02638223. DOI: 10.1016/0263-8223(93)90171-L.
- [176] S. R. Swanson. “Interpretation of Scaling of Damage and Failure in Fiber Composite Laminates”. In: *J. Thermoplast. Compos. Mater.* 7.2 (1994), pp. 155–164. ISSN: 15307980. DOI: 10.1177/089270579400700207.
- [177] A. P. Christoforou, A. A. Elsharkawy, and L. H. Guedouar. “An inverse solution for low-velocity impact in composite plates”. In: *Comput. Struct.* 79.29-30 (2001), pp. 2607–2619. ISSN: 00457949. DOI: 10.1016/S0045-7949(01)00113-4.
- [178] A. P. Christoforou and A. S. Yigit. “Scaling of low-velocity impact response in composite structures”. In: *Compos. Struct.* 91.3 (2009), pp. 358–365. ISSN: 02638223. DOI: 10.1016/j.compstruct.2009.06.002.
- [179] S. R. Swanson. “Limits of quasi-static solutions in impact of composite structures”. In: *Compos. Eng.* 2.4 (1992), pp. 261–267. ISSN: 09619526. DOI: 10.1016/0961-9526(92)90009-U.
- [180] R. W. Clough and J. Penzien. *Dynamics of structures*. Dynamics of Structures Ray W. Clough, Joseph Penzien. McGraw-Hill, 1975. ISBN: 9780070113923. URL: <https://books.google.de/books?id=UdxRAAAAMAAJ>.
- [181] M. Paz. “Dynamic Condensation”. In: *AIAA J.* 22.5 (1984), pp. 724–727. ISSN: 0001-1452. DOI: 10.2514/3.48498.
- [182] R. Kottner, J. Vacík, and R. Zemčík. “Improvement of the damping properties of carbon-fibre-reinforced laminated plastics using damping layers”. In: *Mater. Tehnol.* 47.2 (2013), pp. 189–193. ISSN: 15802949.
- [183] N. Oshima, D. Inui, and T. Fukuda. “Improvement of Damping Property of CFRP Composite Beam Interleaved with Shape Memory Polymer Using CFRP Laminate as a Heater”. In: *Mem. Fac. Eng. Osaka City Univ.* 38 (1997), pp. 1–6.
- [184] B. de Saint-Venant. *Memoire sur la torsion des prismes*. S.L., 1853, p. 586. URL: <https://books.google.de/books?id=iMELAAAAYAAJ>.
- [185] R. Toupin. “Saint-Venant’s Principle”. In: *Arch. Ration. Mech. Anal. Springer Verlag* 18.2 (1965), pp. 83–96.
- [186] C. P. Diemel. “Modeling the Behavior of Impact Induced Multiple Delaminations under Compressive Load”. In: *Proc. Am. 29th Tech. Conf. Compos. Mater.* 1. San Diego, USA: American Society for Composites, 2014. ISBN: 9780874216561. DOI: 10.1007/s13398-014-0173-7.2. arXiv: arXiv:1011.1669v3.
- [187] F. Esrail and C. Kassapoglou. “An efficient approach to determine compression after impact strength of quasi-isotropic composite laminates”. In: *Compos. Sci. Technol.* 98 (2014), pp. 28–35. ISSN: 02663538. DOI: 10.1016/j.compscitech.2014.04.015.
- [188] C. Scarponi and G. Briotti. “Ultrasonic technique for the evaluation of delaminations on CFRP, GFRP, KFRP composite materials”. In: *Compos. Part B Eng.* 31.3 (2000), pp. 237–243. ISSN: 13598368. DOI: 10.1016/S1359-8368(99)00076-1.

- [189] Deutsches Institut für Normung. “DIN EN 2561 - Kohlenstofffaserverstärkte Kunststoffe - Unidirektionale Lamine - Zugprüfung parallel zur Faserrichtung”. In: (1995).
- [190] Deutsches Institut für Normung. *DIN EN 2850 - Kohlenstofffaserverstärkte Kunststoffe - Unidirektionale Lamine - Druckprüfung parallel zur Faserrichtung*. 1995.
- [191] Deutsches Institut für Normung. *DIN EN 2597 - Kohlenstofffaserverstärkte Kunststoffe - Unidirektionale Lamine - Zugversuch senkrecht zur Faserrichtung*. 1998.
- [192] Deutsches Institut für Normung. *DIN EN ISO 14126 - Bestimmung der Druckeigenschaften in der Lamineebene*. 2000.
- [193] Airbus Industrie. *AITM 1-0002 - Fiber reinforced plastics - Determination of in-plane shear properties*. 1998.
- [194] P. Sandorff. *Transverse shear stiffness of T300/5208 graphite-epoxy in simple bending*. Tech. rep. Burbank: Lockheed California Company, 1981.
- [195] Airbus Industrie. *AITM 1-0005 Carbon fiber reinforced plastics Determination - Determination of interlaminar fracture toughness energy*. 1994.
- [196] Airbus Industrie. *AITM 1-0006 Carbon fiber reinforced plastic - Interlaminar fracture toughness energy Mode II*. 1994.
- [197] *ASTM D 6671 - Standard Test Method for Mixed Mode I-Mode II Interlaminar Fracture Toughness of Unidirectional Fiber Reinforced Polymer Matrix Composites*. 2013. DOI: 10.1520/D6671.
- [198] D. I. für Normung. *DIN EN 2563 - Bestimmung der scheinbaren interlamina- ren Scherfestigkeit*. 1997.
- [199] J. C. Butcher. *Numerical Methods for Ordinary Differential Equations*. New York: John Wiley & Sons Inc, 2003, p. 440.
- [200] A. M. Legendre. *Nouvelles méthodes pour la détermination des orbites des comètes*. Paris: F. Didot, 1805.
- [201] A. Björck. *Numerical Methods for Least Squares Problems*. Society for Industrial and Applied Mathematics, 1996. ISBN: 9780898713602.

#### Own publications by the author:

- [RB1] R. Bogenfeld and J. Kreikemeier. “A tensorial based progressive damage model for fiber reinforced polymers”. In: *Compos. Struct.* 168 (2017), pp. 608–618. ISSN: 02638223. DOI: 10.1016/j.compstruct.2017.02.006.
- [RB2] R. Bogenfeld, J. Kreikemeier, and T. Wille. “Review and benchmark study on the analysis of low-velocity impact on composite laminates”. In: *Eng. Fail. Anal.* 86 (2018), pp. 72–99. ISSN: 13506307. DOI: 10.1016/j.engfailanal.2017.12.019.
- [RB3] R. Bogenfeld, J. Kreikemeier, and T. Wille. “An analytical scaling approach for low-velocity impact on composite structures”. In: *Compos. Struct.* 187.March 2018 (2018), pp. 71–84. ISSN: 02638223. DOI: 10.1016/j.compstruct.2017.12.012.
- [RB4] R. Bogenfeld, J. Kreikemeier, and T. Wille. “Validation of the low-velocity impact damage prediction through analytical scaling”. In: *Compos. Struct.* 209.November 2018 (2019), pp. 715–726. ISSN: 02638223. DOI: 10.1016/j.compstruct.2018.11.011.